

A STUDY OF NATURAL SPIN-PARITY STRANGE MESON
RADIAL EXCITATIONS IN $K^- p \rightarrow K^- \pi^+ n$ AT 11 GeV/c*

-- Lloyd Stanley Durkin

Stanford Linear Accelerator Center
Stanford University
Stanford, California 94305

December 1980

Prepared for the Department of Energy
under contract number DE-AC03-76SF00515 -

Printed in the United States of America. Available from the National
Technical Information Service, U.S. Department of Commerce, 5285 Port
Royal Road, Springfield, VA 22161. Price: Printed Copy A13;
Microfiche A01.

* Ph.D. dissertation.

ABSTRACT

Results are presented from a high statistics study of the reaction $K^-p \rightarrow K^-\pi^+n$ at 11 GeV/c. This data was selected offline from an ~ 1000 event/ μb K^-p experiment run on the Large Aperture Solenoid Spectrometer (LASS) at SLAC which triggered on essentially the total inelastic cross section. This $K^-\pi^+n$ sample, after cuts, contained $\sim 42,000$ events in the $K\pi$ invariant mass region from 0.65 GeV to 2.30 GeV, and $|t'| < 0.2$ GeV².

In this thesis, a spherical harmonic angular moments analysis of this data is presented, as well as an energy independent partial wave analysis (PWA) of these angular moments. The nearly uniform acceptance characteristics of this data allowed a detailed analysis, which yielded information on natural spin-parity strange meson resonances in the $K\pi$ invariant mass range from 0.65 GeV to 2.30 GeV. In this study the well established $K^*(895)$, $K^*(1430)$, and $K^*(1780)$ are observed, and clear evidence is presented for a $J^P=4^+$ strange meson state at a mass of 2.08 GeV.

Furthermore the $K^-\pi^+$ elastic scattering partial waves extracted in this PWA show unambiguous evidence for a relatively narrow S wave resonance near 1.42 GeV in the $K\pi$ invariant mass. This state is a confirmation of the $0^+ \kappa(1500)$ seen in previous PWA's. A new higher S wave resonance is clearly seen unambiguously near 1.90 GeV. In addition unambiguous evidence is presented for a relatively wide P wave resonance

in the 1.70 GeV region. A second new P wave resonance also is seen in two of four ambiguous partial wave solutions in the 2.10 GeV region.

These resonance states are discussed within the framework of a simple harmonic oscillator quark model. In particular three of the underlying resonances are discussed as possible natural spin-parity strange meson radial excitations.

ACKNOWLEDGEMENTS

This experiment and my thesis were made possible by the joint efforts of a number of people to whom I offer my deepest thanks.

I wish to thank the following physicists, who were integral to the preparation, running, and analysis of the experiment: R. Carnegie, P. Estabrooks, T. Fieguth, R. Hemingway, A. Honma, D. Hutchinson, W.B. Johnson, P. Kunz, T. Lasinski, D.W.G.S. Leith, R. McKee, W. Meyer, G. Dakham, B. Ratcliff, S. Shapiro, S. Suzuki, and J. Va'Vra.

My special thanks are extended to R. Bierce for his invaluable assistance in processing the endless tapes of data from this experiment. I would also like to commend the following SLAC Group B staff members for expert technical support of the spectrometer hardware, data acquisition systems, and various LASS programs: M. Gravina, H. Hannerfeld, F. Holst, A. Kilert, D. McShurley, G. Oxoby, and W. Walsh.

I am grateful to Dr. Blair Ratcliff for his assistance with and discussions about the physics analysis and to my advisor, Prof. David Leith, for the patience and guidance he has provided throughout. I am also indebted to my good friend and colleague, Alan Honma, who shared equally in the hard work that went into the greater part of this analysis.

Finally, my wife Madeline and my parents, Stan and Adele Durkin, have my love and gratitude for their cheerful support, and unwavering enthusiasm throughout this long endeavor.

TABLE OF CONTENTS

	Page
I. Introduction	1
II. Experimental Apparatus	11
A. Overview	11
B. Beamline	16
C. Target	20
D. Magnets	23
1. Solenoid Magnet	23
2. Dipole Magnet	24
E. Cylindrical Spark Chambers	24
F. Capacitative Diode Spark Chambers	28
G. Proportional Wire Chambers	30
1. Beam Chambers	32
2. Cylindrical Chamber	32
3. Plug Chambers	32
4. Full Bore Proportional Chambers	33
5. Trigger Chambers	35
6. JHxy	35
7. JHup and JHdown	36
8. PWC Readout	37
H. Magnetostrictive Spark Chambers	38
1. MS1T and MS2T	38
2. MS1D-MS4D	40
I. Scintillation Counters	43
J. Particle Identification Systems	45
III. Triggering and Data Collection	48

	Page
A. Fast Logic and Electronics	48
1. Beam Logic	48
2. Trigger Logic	50
3. Gating Logic	53
4. Scalers	56
5. CAMAC	57
B. Data Acquisition System	58
1. Triplex Computer System	59
2. IBM 1800	62
IV. Track Reconstruction and Fitting	64
A. Unpacking	66
B. Match Points	68
C. Beam Track Finding	69
D. Dipole Track Finding	71
E. Solenoid Track Finding	73
F. Vertex Finding	76
G. Geometrically Constrained Track Fitting	77
H. Alignment	79
I. Calculation of Plane Sigmas	83
V. Data Processing and Selection	85
A. Data Processing	85
B. Kinematical Variables	92
C. Selection of the Final $K\pi\pi$ Event Sample	96
D. Raw $K\pi\pi$ Data Distributions	98
E. Track Resolution Cuts	105
VI. Momentum Calibration, Backgrounds, and Normalization	107
A. Momentum Calibration	107

	Page
B. Backgrounds	110
C. Normalization	113
VII. Angular Moments Analysis	118
A. Angular Moments Fitting Methods	119
1. Moments Fitting Method	122
2. Maximum Likelihood Fitting Method	125
B. Monte Carlo	128
1. Overview	128
2. Event Generation	130
3. Geometrical Tracking	131
4. Event Reconstruction	134
5. Track Resolution	135
6. Monte Carlo Output	139
7. Monte Carlo Checks	140
8. Spectrometer Resolution	142
9. Spectrometer Acceptance	143
C. Calculation of the Acceptance Moments	145
D. Angular Moments Fits	149
1. Final Angular Moments Presentation	151
E. Fits to the Leading K^* Resonances using the Angular Moments	165
F. Checks on the Angular Moments Fits	172
VIII. Energy Independent Partial Wave Analysis	180
A. Discussion of the Exchange Model	180
B. Multiple t' Bin Partial Wave Analysis	186
C. Integrated t' Partial Wave Analysis	197
1. Fitting Method	197

	Page
2. Ambiguities and Solution Classification	202
3. Final $K^-\pi^+$ Elastic Scattering Partial Waves	208
a) S Wave Solutions	223
b) P Wave Solutions	230
c) D Wave Solutions	231
d) F Wave Solutions	232
e) G Wave Solutions	232
D. Leading K^* Resonance Fits using the Partial Waves	233
E. Future Isotopic Spin Decomposition of the Partial Waves .	235
F. Resolution of the Barrelet Zero Ambiguities	237
IX. Summary and Conclusions	240
A. Summary of the Results	240
B. A Simple Quark Model Interpretation of the Observed States	253
C. Radial Excitations in the Natural Spin-Parity Strange Mesons	260
D. Conclusions	265
References	266

LIST OF TABLES

	Page
1. Beamline running conditions	21
2. Cylindrical Spark Chamber radii, efficiencies, and resolutions	27
3. Capacitative Diode Spark Chamber efficiencies, and resolutions	31
4. Proportional Wire Chamber efficiencies, and resolutions	39
5. Magnetostrictive Spark Chamber efficiencies, and resolutions	42
6. PASSMC cuts	99
7. Normalization corrections	114
8. The final $K^-p \rightarrow K^-\pi^+n$ acceptance corrected angular moments as a function of mass	160
9. Breit-Wigner resonance parameterization with a Blatt-Weisskopf barrier factor	167
10. Resonance parameters from Breit-Wigner fits to the angular moments	169
11. Parameterization for the D, F, and G waves for the energy dependent fit to the t_{60} , t_{70} , and t_{80} angular moments	171
12. Resonance parameters from the energy dependent fit to the t_{60} , t_{70} , and t_{80} angular moments	174
13. The number of events fitted in each t' bin for the multiple t' bin PWA in the mass bin .92 GeV < $M(K\pi)$ < .96 GeV	187

14. Chi-square per 31 degrees of freedom for the multiple t' bin partial wave fits as a function of mass bin and η	192
15. Production parameter fit values	195
16. The Barrelet zero solution classifications	209
17. Partial wave phases for the S and P waves in the elastic region	215
18. $K^-\pi^+$ elastic scattering partial wave magnitudes and phases in the inelastic region	216
19. Number of partial waves used and angular moments fitted in the integrated t' bin PWA	219
20. Resonance parameters from Breit-Wigner fits to the partial wave amplitudes	222
21. Comparisons of the two different types of Breit-Wigner fits performed in this analysis to the Particle Data Group table values	236
22. Estimated parameters for the underlying resonances	246

LIST OF FIGURES

	Page
1. A schematic diagram of a quark-antiquark meson system	4
2. A level diagram of the expected quark model meson states ...	5
3. The known meson states before this analysis	6
4. The LASS spectrometer	13
5. The LASS solenoid	14
6. The beam transport system	17
7. The liquid hydrogen target	22
8. The Cylindrical Spark Chambers	25
9. The Proportional Wire Chambers	34
10. The HA-HB scintillation hodoscope	44
11. The Time of Flight and Quad scintillation hodoscope	46
12. The beam logic	49
13. The trigger logic	52
14. The gating logic	54
15. The data acquisition system	60
16. The REALTIME data management network	61
17. The data processing chain	86
18. The software filter	88
19. The definition of the t-channel helicity or Jackson angles .	94
20. A histogram of the $K^-\pi^+$ invariant mass	100
21. A projected three dimensional plot of $\cos\theta_j$ vs the $K^-\pi^+$ invariant mass	102
22. Eight $K^-\pi^+$ invariant mass histograms in consecutive $\cos\theta_j$ slices	104

23. The missing mass squared spectrum with a Monte Carlo fit superimposed	109
24. The missing mass squared spectrum with a folded missing mass squared spectrum superimposed	111
25. A sample of total exclusive cross section measurements for the reaction $K^-p \rightarrow K^-\pi^+n$ versus K^- beam momentum	116
26. An acceptance contour plot in the variables $M(K\pi)$ and $\cos\theta_j$.	144
27. A comparison of the final angular moment fits to the data ..	152
28. The final $m=0$ acceptance moments as a function of mass	153
29. The final $m=1$ acceptance moments as a function of mass	154
30. The final $m=2$ acceptance moments as a function of mass	155
31. The final $m=0$ acceptance corrected angular moments as a function of mass	157
32. The final $m=1$ acceptance corrected angular moments as a function of mass	158
33. The final $m=2$ acceptance corrected angular moments as a function of mass	159
34. The t_{90} and t_{100} angular moments	164
35. Leading resonance fits to the t_{2j0} angular moments	168
36. The energy dependent fit to the t_{60} , t_{70} , and t_{80} angular moments	173
37. Angular moments comparisons in the mass bin $1.40 \text{ GeV} < M(K\pi) < 1.44 \text{ GeV}$	176
38. Angular moments comparisons in the mass bin $1.76 \text{ GeV} < M(K\pi) < 1.80 \text{ GeV}$	177
39. Angular moments comparisons in the mass bin $2.04 \text{ GeV} < M(K\pi) < 2.12 \text{ GeV}$	178

40. The angular acceptance moments as a function of t' in the mass bin $0.90 \text{ GeV} < M(K\pi) < 0.94 \text{ GeV}$	188
41. The acceptance corrected angular moments as a function of t' in the mass bin $0.90 \text{ GeV} < M(K\pi) < 0.94 \text{ GeV}$	189
42. The production parameters γ_a , γ_c , and b as a function of mass	196
43. The $K^-\pi^+$ elastic scattering partial waves in the 1.40 GeV to 1.60 GeV mass region with and without an $n\pi$ cut imposed	199
44. The Barrelet zeros	206
45. The four ambiguous $K^-\pi^+$ elastic scattering S wave magnitudes and phases	210
46. The four ambiguous $K^-\pi^+$ elastic scattering P wave magnitudes and phases	211
47. The four ambiguous $K^-\pi^+$ elastic scattering D wave magnitudes and phases	212
48. The four ambiguous $K^-\pi^+$ elastic scattering F wave magnitudes and phases	213
49. The four ambiguous $K^-\pi^+$ elastic scattering G wave magnitudes and phases	214
50. Argand diagrams for the $K^-\pi^+$ elastic scattering partial waves of solution A	224
51. Argand diagrams for the $K^-\pi^+$ elastic scattering partial waves of solution B	225
52. Argand diagrams for the $K^-\pi^+$ elastic scattering partial waves of solution C	226
53. Argand diagrams for the $K^-\pi^+$ elastic scattering	

	Page
partial waves of solution D	227
54. An Argand diagram of the isospin $1/2$ $K^-\pi^+$ elastic scattering S wave	229
55. Partial wave Breit-Wigner fits to the leading K^* resonances	234
56. Real and imaginary projections of the S wave Argand diagrams	248
57. Real and imaginary projections of the P wave Argand diagrams	249
58. Real and imaginary projections of the D wave Argand diagrams	250
59. Real and imaginary projections of the F wave Argand diagrams	251
60. Real and imaginary projections of the G wave Argand diagrams	252
61. A Chew-Frautschi plot of the leading natural spin-parity strange mesons	254
62. A quark model level diagram showing the known strange meson states	258
63. A quark model level diagram showing the known $c\bar{c}$ states	261
64. A summary of the known and possible strange meson radial excitation mass splittings	264

Chapter I

INTRODUCTION

In the past few years the discovery of the J/ψ particle and the multiple associated $c\bar{c}$ resonances in e^+e^- collisions has heralded in a new era in our understanding of meson spectroscopy. The success of the quark model in classifying the myriad of $c\bar{c}$ states has been quite phenomenal. For more than ten years the the quark model has provided a clean way of classifying the known baryon resonances, but this success in explaining the "charmonium" spectrum has confirmed the model for mesons in a very clear manner. Discoveries in the experimental study of light quark meson spectroscopy have not been as rapid due mainly to the difficulty of producing and studying these states.

Conceptually meson-meson ($K\pi, \pi\pi$) elastic scattering has always been attractive as a possible source of information for this study of light quark meson spectroscopy. A straight forward partial wave analysis of such a simple reaction would lead to an easily interpreted spectrum of natural spin-parity meson states. Unfortunately nature has not provided us with any means of maintaining real meson targets. The study of light quark meson spectroscopy has been confined to the study of various production reactions ($K^-p \rightarrow K^-\pi^+n$, $\pi^-p \rightarrow \pi^-\pi^+n$, etc.).

The lack of real meson targets can be circumvented in the analysis of these production reactions. The most fruitful approach in these analyses has been to use a simple exchange parameterization to isolate the

single pion exchange contribution to the given production reaction. Once this single pion exchange contribution has been isolated, one then extrapolates to the pion pole ($t = \mu^2$). The end point of such analyses are $K\pi$ or $\pi\pi$ elastic scattering partial waves as a function of mass. This idea of extrapolating to the pion pole is not a new one ¹, but such analyses by their very nature require: 1) full angular information on the production reaction, 2) good spectrometer acceptance, and 3) high statistics; as well as a good phenomenological understanding of the exchange mechanisms involved. In the last ten years various experiments have been run with high enough statistics to perform such analyses and the theoretical tools needed have become available as well. These experiments have made, and will make substantial progress in our understanding of light quark natural spin-parity meson spectroscopy ².

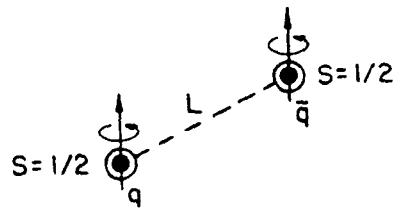
In this paper such an energy independent partial wave analysis will be presented for the specific reaction $K^-p \rightarrow K^-\pi^+n$. The end point of this analysis was $K^-\pi^+$ elastic scattering partial waves as a function of the $K\pi$ invariant mass. These partial waves then yielded information on natural spin-parity ($P = (-1)^J$) strange meson resonances.

Before outlining the experiment and the analysis presented in this thesis, it is convenient to review the present status of K^* spectroscopy. In order to discuss the known K^* states, it is necessary to present a framework within which to classify these states. The quark model has proven so successful in describing the $c\bar{c}$ spectrum that a simple central potential quark model based loosely on a simple harmonic oscillator potential will be used here. In this model, a meson is represented by two spin 1/2 quarks ($q\bar{q}$) bound in a central potential (see

figure 1). In this model the quantum numbers of the associated mesons follow from addition of the internal quantum numbers of the two bound quarks.

Shown in figure 2 (known as a Grotrian plot) is the spectrum of states predicted by this simple model. On the left hand side of this plot, predicted states with quark spins antiparallel are shown. For orbital angular momentum between the $q\bar{q}$ pair of $L = 0, 1, 2,$ and 3 ; a series of mesons is predicted with $J^P = 0^-, 1^+, 2^-,$ and 3^+ respectively. On the right hand side of this plot, predicted states with quark spins antiparallel are shown. Here vector addition of L and S in a simple harmonic oscillator potential predicts degenerate triplet levels. In this diagram for convenience these triplets are plotted as though this degeneracy had been broken by an $L.S$ coupling. On both sides of the plot, higher mass states within a given column represent radial excitations of the lowest state within that column. It should be remembered that in studying the $K^-p \rightarrow K^-\pi^+n$ reaction in this analysis, only the natural spin-parity ($P = (-1)^J$) states were accessible as a consequence of parity conservation. These states are located on the right hand side of this Grotrian plot, and do not include the middle state in each triplet. This model presents a convenient means of classifying the known K^* states ($s\bar{d}$), but the details of the predicted level structures should not be taken too seriously.

Presented in the Grotrian plot of figure 3 are the known K^* resonances ³ previous to this present analysis. States listed with a solid bar represent states whose parameters are rather well known. Where a question mark is listed next to a state, this particular state



$$J = L + S$$

$$P = (-1)^{L+1}$$

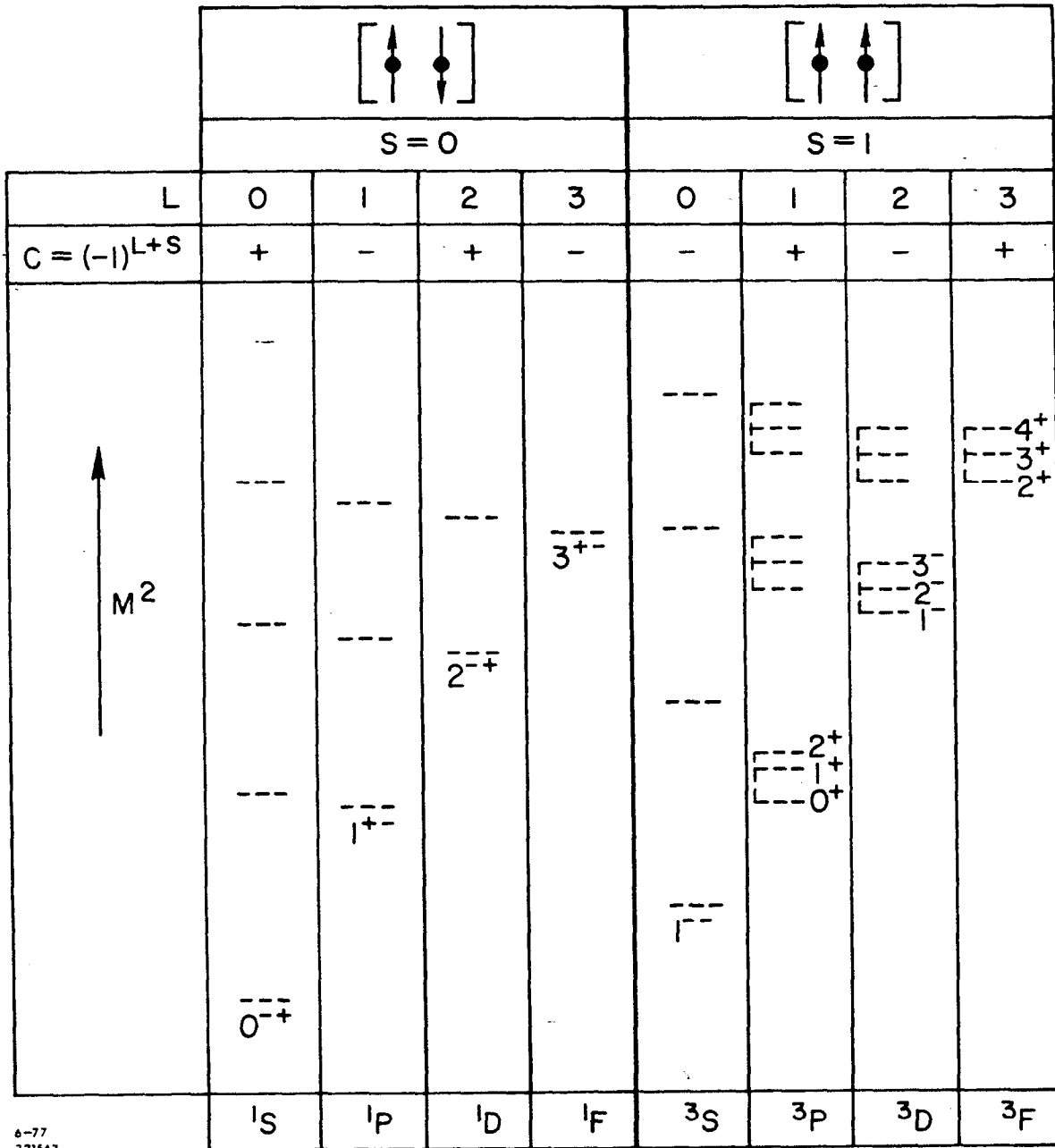
$$C = (-1)^{L+S}$$

$$G = (-1)^{L+S-1}$$

10-80
3942 A 57

FIG. 1--A schematic diagram of a quark-antiquark meson system.



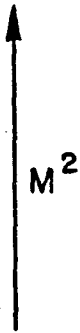
($q\bar{q}$ LEVEL SCHEME)



6-77
3215A7

FIG. 2--A level diagram of the expected meson states from the simple quark model described in the text.

($q\bar{q}$ LEVEL SCHEME)

									
	S = 0				S = 1				
L	0	1	2	3	0	1	2	3	
$C = (-1)^{L+S}$	+	-	+	-	-	+	-	+	
	0^{-+} K(494)	1^{+-} Q _B (1350)	2^{-+} L(1800) ?		1^{--} K*(895)	0^{+-} K(1650) ?	0^{+} K(1500)	1^{+} Q _A (1340)	2^{+} K*(1435)
		1^{+-} K*(1400)						1^{-} K*(1780) L(1800) ? K(1650) ?	
	1S	1P	1D	1F	3S	3P	3D	3F	

1-81
4011A3

FIG. 3--A quark model level diagram showing the known strange meson states before this analysis.

has been seen ambiguously (the state's existence is still in question). The other states listed on this plot are reasonably solid states which could use further study, and confirmation. Where a state has been listed twice, in different positions on this plot, this signifies that the classification of this state within the quark model is presently ambiguous. Looking at this diagram it is quite remarkable how little is known about the strange mesons after twenty years of effort. In fact only one solid state is seen above 1.50 GeV. Certain successes stand out in this experimental effort though. In this plot a well established triplet is seen although the properties of the two underlying states in this triplet need further study and confirmation. Orbital excitations are also seen in both the natural and unnatural spin-parity states. There is a marked scarcity of information on radial excitations. The $K'(1400)$ is the only solid evidence for a radial excitation in these strange meson states, but the properties of this state are not well known.

Looking in particular at the natural spin-parity states, three leading resonances ($K^*(895)$, $K^*(1430)$, $K^*(1780)$) are listed, along with two underlying states (the $\kappa(1500)$, and the questionable $K'(1650)$). These three leading resonances have been studied in multiple previous experiments, and the properties of these states are now rather well known³. The only evidence for the two underlying states comes from a partial wave analysis by Estabrooks et al.⁴ in a previous 13 GeV K^-p experiment run by SLAC group B, SLAC experiment E-75⁵. This experiment was run at SLAC on a forward dipole spectrometer, and severe acceptance cutoffs (inherent in any forward dipole spectrometer) restricted this analysis

to the $K\pi$ invariant mass region from 0.65 GeV to approximately 1.70 GeV, and the acceptance was seen to drop rapidly above 1.5 GeV. The analysis presented in this thesis will extend this analysis region up to a $K\pi$ invariant mass of 2.3 GeV, and thus will allow the investigation of high mass natural spin-parity K^* resonances. With this high mass extension one would also hope to see some of the notably missing natural spin-parity strange meson radial excitations. This extension was possible due to the nearly 4π acceptance, good resolution and high statistics capabilities of the Large Aperture Solenoid Spectrometer (LASS) at SLAC on which this data was taken.

The SLAC experiment E-132⁶, of which this data and analysis are a part, was a collaborative effort of SLAC experimental group B and an experimental group from Carleton University; Ottawa, Canada. This 11 GeV/c K^-p experiment was run on the Large Aperture Solenoid Spectrometer (LASS) facility. This experiment was triggered on practically the entire K^-p inelastic cross section. During the data taking phase of this experiment nearly 40 million K^-p triggers were written to high density magnetic tape.

The physics goals of this experiment are much broader than the simple experimental study of the natural spin-parity kaon resonances in the reaction $K^-p \rightarrow K^-\pi^+n$ which will be presented here. This experiment will make an extensive experimental study of natural and unnatural spin-parity meson resonances with one or two strange quarks. In particular this spectrometer's ability to fully analyse high multiplicity events will allow a systematic study of both natural and unnatural spin-parity kaon resonances using $K\pi$, $K\pi\pi$, and $K\pi\pi\pi$ final states. Since the two

prong $K\pi$ final state analysis did not require the complex particle identification and multiprong vertex finding of the other multiprong channels, the decision was made to software select and thus quickly process a two prong data sample while the fine tuning of the multiprong analysis routines was taking place. It is the analysis of this two prong data sample, specifically in the reaction $K^-p \rightarrow K^-\pi^+n$, with which this thesis will deal.

In the following chapters, a description will be given of each step in the data taking, data selection, data processing, and analysis of this $K^-p \rightarrow K^-\pi^+n$ data. Specifically chapter II will present a description of the beam and spectrometer hardware used in collecting this data sample. The trigger logic and data acquisition system will be discussed in chapter III. Chapters IV and V will deal with the software filter selection, event reconstruction, and kinematical selection of a final $K^-p \rightarrow K^-\pi^+n$ data sample from these 40 million events written to magnetic tape in this experiment. Chapter VI will discuss: 1) momentum calibration of the spectrometer, 2) backgrounds in the final $K^-p \rightarrow K^-\pi^+n$ data sample, and 3) experimental normalization. Chapters VII and VIII will form the bulk of this thesis, and will deal with the analysis of this final $K^-p \rightarrow K^-\pi^+n$ data sample.

This analysis is most easily discussed in two steps. Chapter VII presents a study of the acceptance corrected angular distributions of this data sample. The endpoint of this step in the analysis was a set of fitted acceptance corrected angular moments which completely described the angular dependence of this data. In this chapter the Monte Carlo used to calculate the spectrometer's acceptance will be discussed,

as well as the fitting methods used to obtain the final acceptance corrected angular moments. To end this chapter, these angular moments are presented as a function of $K\pi$ invariant mass, and the leading K^* resonance structure visible in these moments are discussed. Fits to these angular moments which yielded resonance parameters for these leading states are then discussed.

Chapter VIII will then present an energy independent partial wave analysis (PWA) of these angular moments. The endpoint of this PWA was a set of $K^-\pi^+$ elastic scattering partial waves as a function of $K\pi$ invariant mass. The first part of this chapter will present the simple exchange model used to isolate the single pion exchange portion of the $K^-p \rightarrow K^-\pi^+n$ reaction. The method used to isolate the single pion exchange portion of this reaction, extrapolate to the pion pole, and thus obtain the $K^-\pi^+$ elastic scattering partial waves will then be discussed. These partial waves will then be shown as a function of mass, and the resonance structures visible in these waves will be discussed. To end this chapter fits to the leading K^* resonances using these partial waves will be presented.

In the last chapter of this thesis, a summary will be given of the results from this angular moments analysis, and the PWA. These results will be discussed and compared with those from previous experiments. The resonances seen will then be classified within the framework of the simple harmonic oscillator quark model presented in this chapter. Finally a discussion of the evidence for radial excitations in the natural spin-parity strange mesons will be given.

Chapter II

EXPERIMENTAL APPARTUS

A. Overview

The data analysed in this thesis was selected offline from an 11 GeV/c K^-p experiment (SLAC E-132) run on the Large Angle Solenoid Spectrometer (LASS) at SLAC. Preliminary data taking in this experiment took place during June of 1977, and the final data taking between December of 1977 and March of 1978. Both the preliminary and final data taking periods were each preceded by approximately a month of low beam rate checkout running. This experiment triggered on essentially the entire K^-p inelastic cross section. During this experiment $\sim 4.5 \times 10^8$ K^- particles were incident on the LASS liquid hydrogen target. This gave an experimental sensitivity of ~ 1000 events/ μb in almost all inelastic channels, and resulted in approximately 40 million events being written to magnetic tape.

Interactions in this experiment were furnished by an 11 GeV/c K^- beam incident on a 90 centimeter long liquid hydrogen target. These beam kaons were produced, selected, and focused in the rf separated SLAC beamline 20/21. Particle identification in this beamline was provided by two Cerenkov counters, $C\pi$ and CK . The final momentum, position, and angular measurements of beam particles was supplied by various scintillation counters, and a set of beam proportional chambers.

The outgoing particles from a K^-p interaction in the LASS liquid hydrogen target were tracked, measured, and identified in the LASS spectrometer. Shown in figures 4-5 are schematic diagrams of this spectrometer. The LASS spectrometer consisted of two large momentum measuring magnets combined with various associated detectors.

The first of the LASS magnets was a large superconducting solenoid filled with a nearly uniform 23 kilogauss magnetic field pointing along the incident beam direction. Outgoing particles from interactions in the liquid hydrogen target, situated at the upstream end of this solenoid, traveled with near helical trajectories through this solenoid field. Charged particles with large angles and relatively low momentum were bent strongly in this magnetic field, and thus could be well measured.

Several types of detectors filled the interior of the solenoid in order to measure the trajectories of charged interaction particles. Surrounding the liquid hydrogen target were fifteen planes of CD readout cylindrical spark chambers, and a single cylinder of proportional wires. These chambers gave positional information on tracks traveling sideways out of the target. Interaction particles traveling downstream * of the target were measured in multiple planar CD readout spark chambers, and several proportional wire chambers (PWC's). Covering the exit to the

* The cartesian coordinate system used in this experiment was defined with its z axis pointing along the incident beam direction. The y axis was then defined as the vertical normal to the horizontal plane. Lastly the x axis was defined relative to the y and z axis in order to complete an orthogonal right handed coordinate system. The term 'upstream' in this coordinate system refers to the negative z direction, while the term 'downstream' refers to the positive z direction.

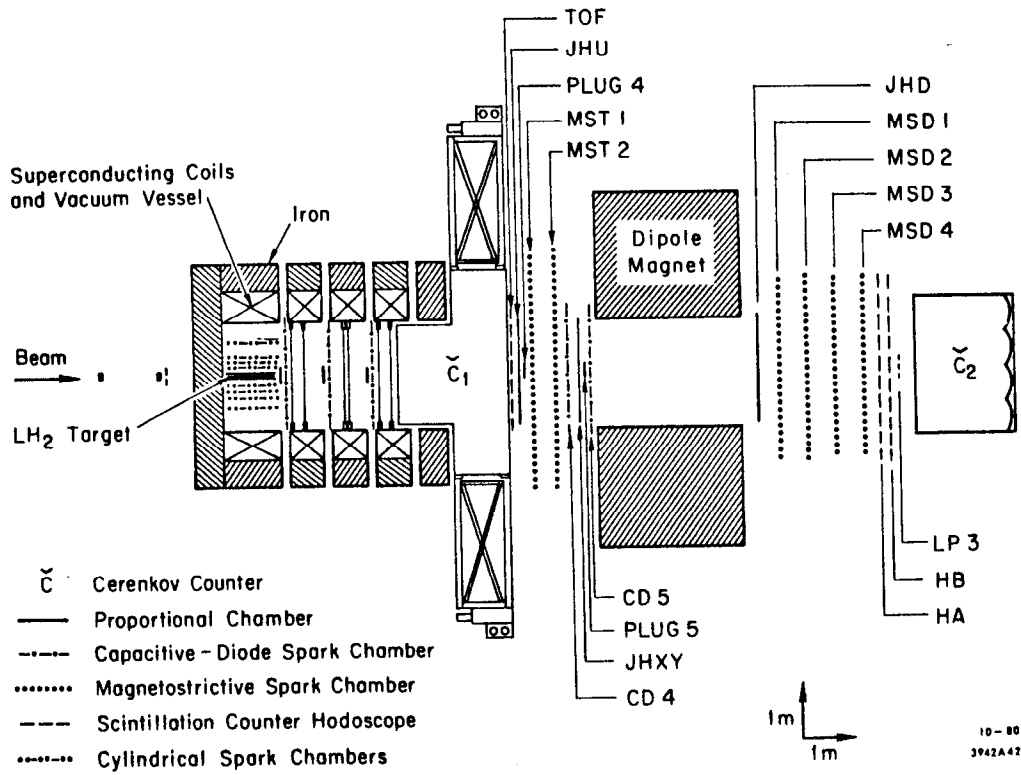
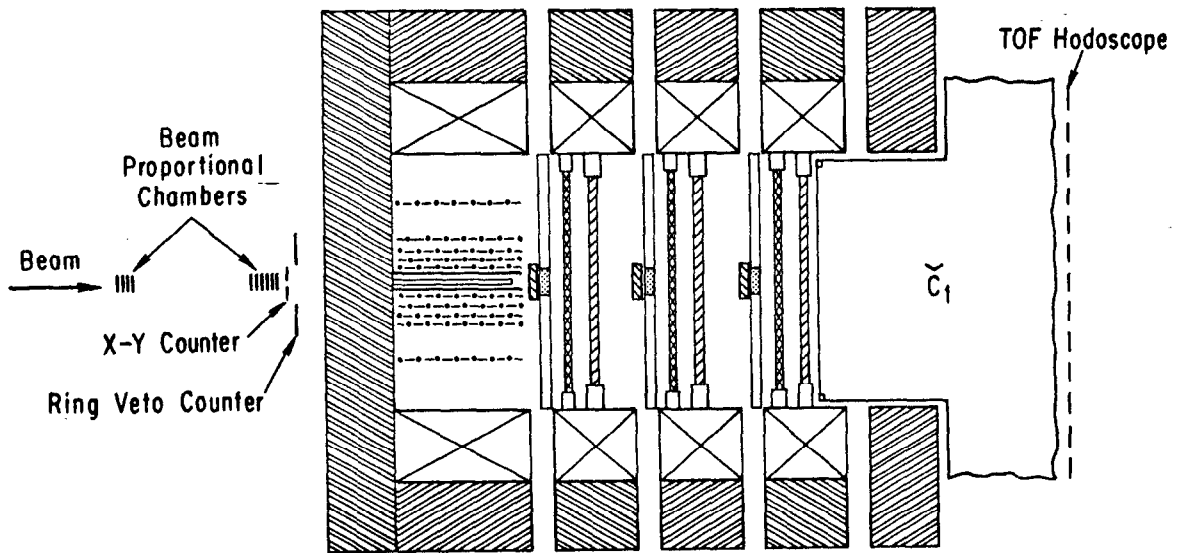


FIG. 4--An overhead plan view of the LASS spectrometer.



- | | |
|--|--|
| LH ₂ Target | Cylindrical Proportional Chamber |
| Plug Proportional Chamber (Plug 1,2,3) | Full Bore Proportional Chamber (1.5, 2.5, 3.5) |
| Tracking/Trigger Chamber (Trig A,B,C) | Cylindrical C-D Chamber |
| Capacitive-Diode (CD) Chamber (CD 1-3) | Polyurethane Foam Plugs |

10-80
1947A-03

FIG. 5--An overhead detail of the LASS solenoid magnet and associated detectors.

solenoid was a thirty eight celled partitioned atmospheric Cerenkov counter C1, and mounted on the downstream end of this Cerenkov counter were twenty four segmented scintillation time of flight counters. Four more conventional scintillation counters called the quad counters, were located at the center of this TOF array. Both the Cerenkov counter, and the TOF counters provided particle identification of particles exiting the solenoid.

The second of LASS's two magnets was a conventional water cooled dipole with a maximum integrated magnetic field of 30 kilogauss-meters in the vertical direction. Charged forward interaction particles with high momentum, which could not be well measured in the solenoid, were bent strongly and thus could be well measured in this dipole field.

Knowing the entrance and exit trajectories of particles traveling through the LASS dipole allowed a very accurate momentum measurement of these particles. In this analysis the region upstream of the dipole, between the two magnets, was referred to as the 'twixt' region. In the twixt region a number of planar CD readout spark chambers, and planar PWC's served to measure the trajectories of particles entering the dipole. The region downstream of the dipole was known as the 'downstream' region. In the downstream region the exit trajectory of a particle leaving the dipole was measured by four planar MS readout spark chambers, and a single planar PWC. Downstream of these chambers was a full coverage scintillation counter array (HA-HB) which provided positional as well as timing information for 'downstream' particles. The last device in this spectrometer was a large eight celled unpartitioned pressurized Cerenkov counter, C2, used to provide particle identification of particles exiting the dipole.

The LASS solenoid dipole configuration gives this spectrometer nearly 4π acceptance with good resolution in almost all regions of longitudinal and transverse momentum. The LASS beamline, target, and spectrometer hardware will be described in greater detail in the rest of this chapter.

B. Beamline

Shown in figure 6 is a schematic diagram of SLAC beamline 20-21. This system produced, selected, collimated, focused, and measured the 11 GeV/c K^- beam particles used in this experiment. A detailed description of this beamline system is given in reference 7, so that only a brief description will be given here.

The K^- beam particles used in this experiment were produced by steering the 20 GeV/c SLAC electron beam onto a water cooled primary target (.22 radiation lengths Be preceded by .86 radiation lengths Cu). The current of the electron beam hitting this target was kept at ~25 mA during this experiment. Steering of the electron beam incident on the target was checked by monitoring the pulse heights of two secondary emission monitors (SEM's), and the electron current at I-40 was also monitored throughout this experiment (see diagram).

The secondary beam had a production angle of one degree. All negatively charged particles produced within ± 3.85 milliradians of this angle were then collected, and focused into an achromatic focus, F1. Here various movable collimators were used to collimate the beam. The beam momentum was selected by moving these collimators to have a

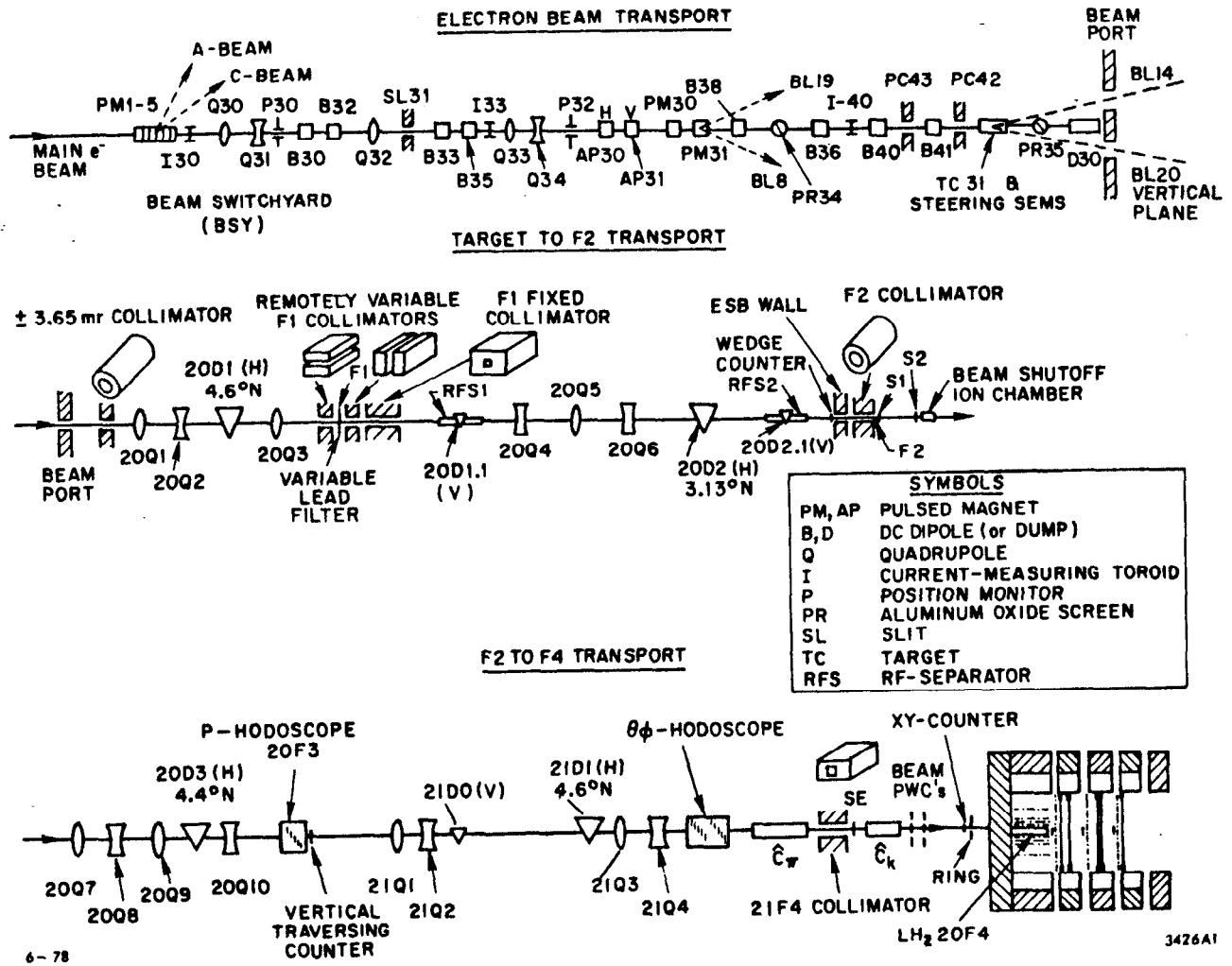


FIG. 6--A layout of the beam transport system.

dispersion, dP/P , of $\sim 2.5\%$ (FWHM). One $1/8$ " lead filter was also placed in the beamline at F1 in order to remove unwanted electrons from the beam.

The main SLAC electron beam was produced in $1.6 \mu\text{sec}$ spills 180 times a second. Within each $1.6 \mu\text{sec}$ spill period, the SLAC electron beam hit the BeCu target for 5 psec every 350 psec. There was thus a spatial separation of unlike same momentum particles a few meters downstream from the collimation point at F1. Two rf separators were located in this beamline downstream of F1 to make use of this spatial to remove unwanted particles from the beam. In this experiment the second rf separator's y electric field (2856 MHz) was tuned to be at a minimum when pions passed through the rf cavity, and at a maximum when kaons passed through this same cavity. Unwanted pions were thus swept from the beamline. Only the second rf separator was needed in this experiment since at 11 GeV/c e's, π 's, and p's were all 180 degrees out of phase with beam kaons. Thus this one rf separator removed most unwanted particles from this beam. The π/K contamination was measured in this experiment to be $\sim 1/40$, and the p/K contamination was $\sim 1/550$. These two ratios were monitored carefully throughout this experiment.

The third focus of this beam transport system was a dispersive focus (F3). Located at this focus was an array of six overlapping scintillation counters (P-hodoscope). These scintillation counters formed eleven .64 cm wide vertical bins, which were used to measure the momentum of the incident beam particles. Using this scintillation array, the momentum of these incident beam particles could be measured to an accuracy of .25 %.

The final focus of our beam transport system, F4, was located a few centimeters in front of the LASS liquid hydrogen target. Final kaon identification of our beam particles was furnished by two Cerenkov counters, C π and CK. The first counter, C π , was five meters long, and was filled with hydrogen gas at a pressure of 25 psig. This gas and pressure was chosen so that 11 GeV pions emitted light in the Cerenkov counter, but protons and kaons did not. The second Cerenkov counter, CK, was one meter long, and was filled with CO₂ to a pressure of 55 psig. This pressure and gas were chosen so that 11 GeV/c kaons and pions emitted light in this counter, but protons did not. The output of these two Cerenkov counters were thus used to define pions (C π .CK), protons ($\overline{\text{C}\pi}$. $\overline{\text{CK}}$), and kaons ($\overline{\text{C}\pi}$.CK) in this experiment.

The final position and direction of kaons entering the target were measured by a scintillation counter hodoscope ($\theta\phi$), an upstream beam PWC, and a downstream beam PWC. The $\theta\phi$ hodoscope was positioned 13.7 meters upstream of the LASS liquid hydrogen target. This hodoscope consisted of an array of 24 1/2" wide scintillation counters; twelve placed in a vertical plane, and twelve placed in a horizontal plane. An upstream beam PWC was located approximately 215 cm upstream of the target. This chamber consisted of four planes of 64 proportional wires with 1.016 mm spacing. The first two planes gave X and Y readout, and the second two planes were rotated ± 45 degrees with respect to the x axis to give E and P readout. One meter downstream of this PWC was the downstream PWC. This chamber consisted of five planes of sixty four proportional wires space 1.016 mm apart. The first two planes once again gave X and Y readout, and the fifth plane was rotated ± 45 degrees

with respect to the vertical to give E readout. The second two planes were displaced .5 mm with respect to X and Y wires respectively giving X' and Y' readout. This offset served to halve the x and y position resolution of this downstream PWC.

A large 4"x4" square scintillation counter (SE) in the beam provided beam timing information for both our trigger and TOF systems (see figure 6). The XY and ring scintillation counters located downstream of the beam PWC package were used in this experiment to provide double rejection in the beam. The XY counter was 1 1/4" in diameter, and was segmented into four equal pie shaped pieces. Each separate segment was equipped with its own individual phototube. Two large ring shaped counters (R, BR) completely surrounded the XY counter providing beam halo rejection.

Table 1 shows typical beam parameters during the data taking in this experiment. Control of magnet currents was performed by the Yard-mux computer system. This system controlled and monitored magnet currents to at least 1 % on all beamline magnets during this experiment (some magnets were monitored to .1 %).

C. Target

The LASS liquid hydrogen target used in this experiment measured 91.4 cm in length and 5.7 cm in diameter. The target cell consisted of two long concentric mylar cylinders (see figure 7). A thin mylar head capped the downstream end of the outer cylinder. The downstream end of the inner tube was also capped by a mylar window. Liquid hydrogen was

TABLE 1

Beamline Running Conditions	
K ⁻ Beam Momentum	11.0 GeV/c
Momentum Bite	2.5 % FWHM
Primary e ⁻ Beam Energy	20.5 GeV
Primary e ⁻ Beam Current	25 ma
K/pulse	≈2.5
π/K	2.5 %
p/K2 %
Spot Size (σ) at F4	
Horizontal	5 mm
Vertical	5 mm
Angular Dispersion at F4 ^a	
dX/dZ	7.6 mrad FWHM
dY/dZ	8.0 mrad FWHM

^a F. Winkelmann, SLAC Report No.160 (1973)

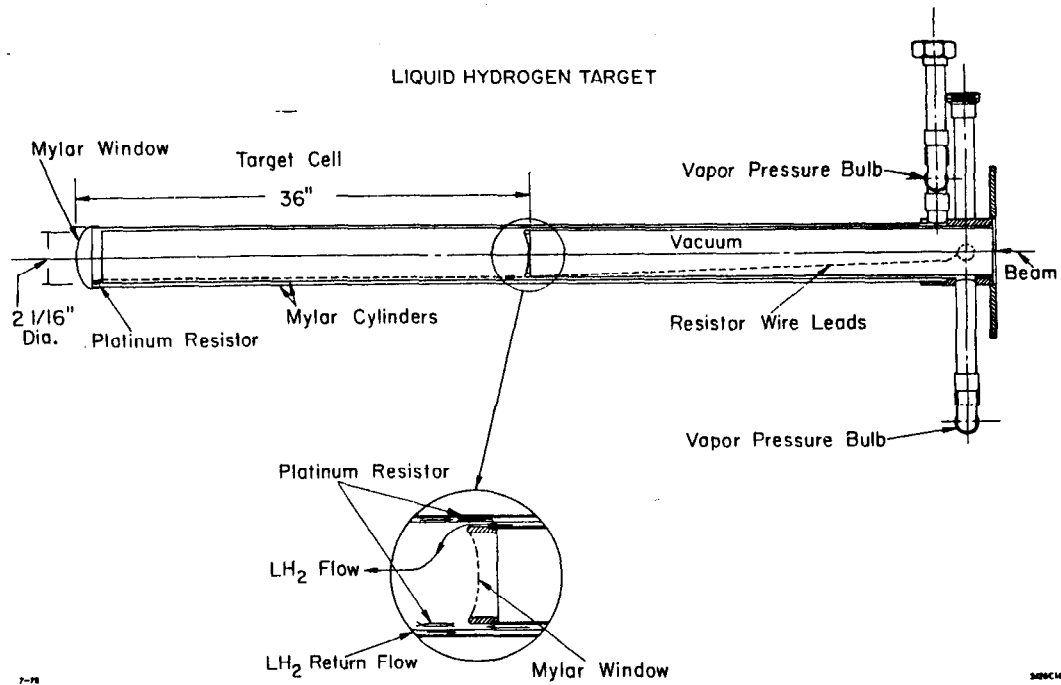


FIG. 7--The LASS liquid hydrogen target.

continuously flowed through this target during this experiment. The cryogenic system filling the liquid hydrogen target was of the condensing type. In this system liquid hydrogen at near atmospheric pressure was in equilibrium with gaseous hydrogen. Thus a single temperature, or pressure measurement determined the liquid hydrogen density. Our hydrogen density in this experiment was monitored by four vapor pressure bulbs located at the entrance and exit to the target, and three resistors located inside the target cell. The use of these monitors will be described in the normalization section. The hydrogen density was kept constant to ~1 % throughout this experiment. Near the end of the data taking in this experiment, a chemical analysis was performed on the liquid hydrogen in the cell. No notable DH or D_2 contamination was found.

D. Magnets

1. Solenoid Magnet

The superconducting solenoid used in this experiment was comprised of four large separate superconducting coil assemblies. Each coil assembly consisted of a large stainless steel vacuum container with superconducting copper coils bathed in liquid hydrogen at the center. Six inch gaps were designed between these assemblies for inserting the solenoid planar CD chambers, as well as the proportional plug chambers. Flux return iron was located on the outside of each coil assembly, and an iron flux return plate was situated at the upstream face of the

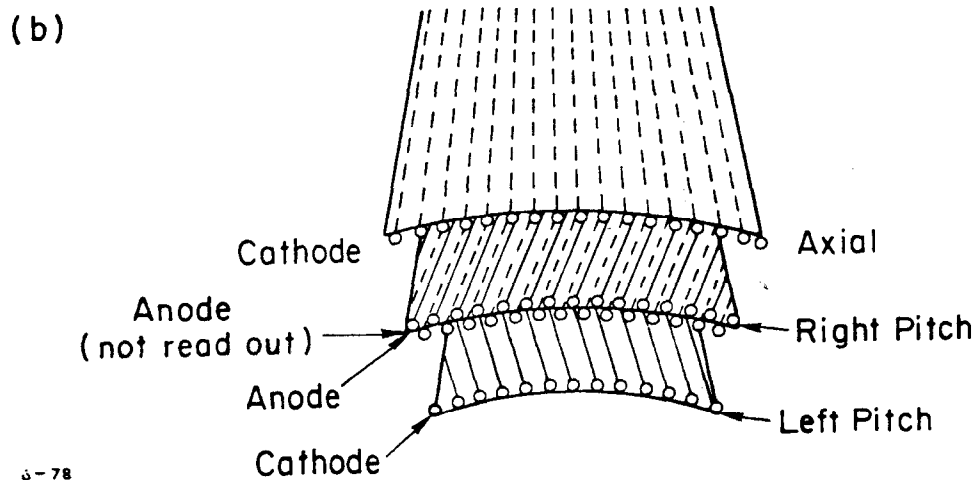
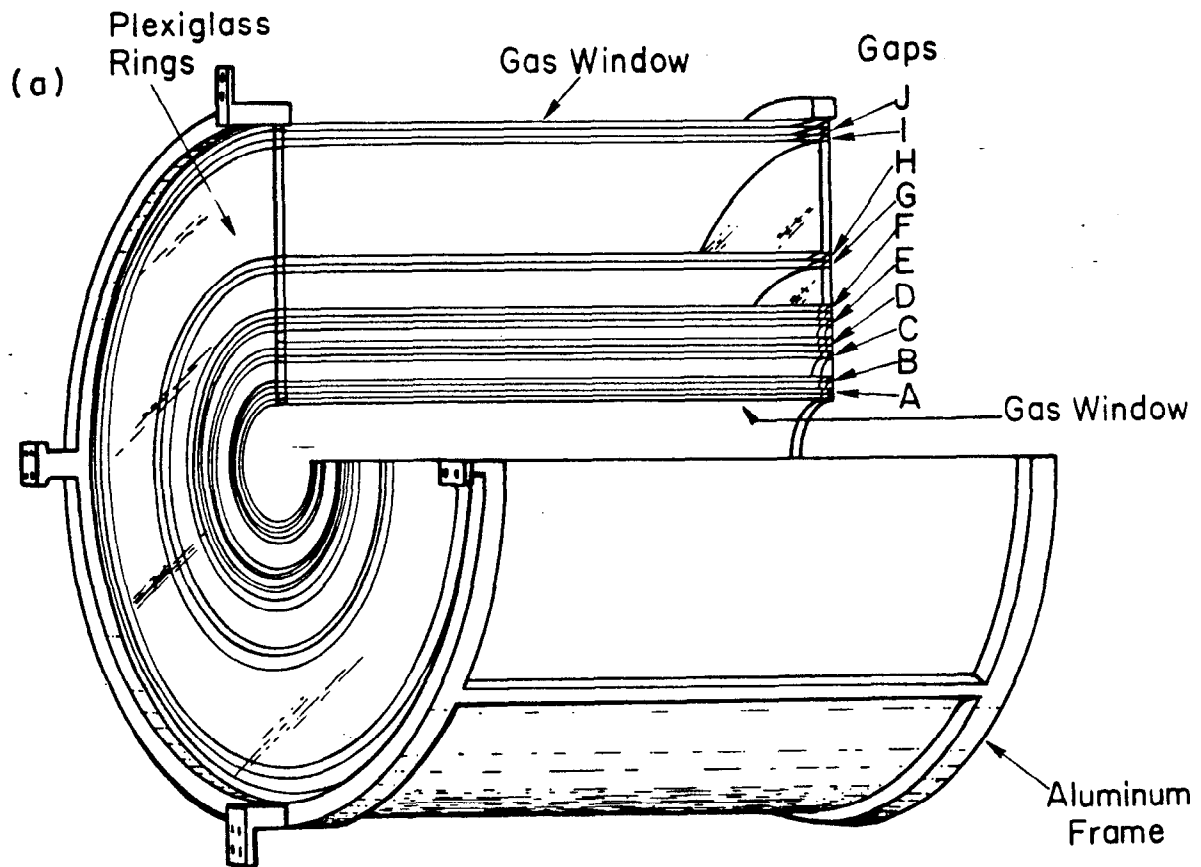
solenoid. A circular hole in the center of this iron plate allowed the insertion of the LASS liquid hydrogen target into the solenoid. In addition an iron flux return ring was located at the downstream end of the solenoid. These flux returns served to make the solenoid field uniform, as well as reducing the magnetic flux outside the magnet. During this experiment 1600 Amps were run through the superconducting coils providing a nearly uniform 22.4 kilogauss z magnetic field over the 465 centimeter long, and 185 centimeter diameter solenoid interior.

2. Dipole Magnet

The dipole magnet used in this experiment was a conventional water cooled magnet with a maximum magnetic field of 16 kilogauss in the vertical direction. During this experiment the dipole was run at a current of 7050 Amps providing this maximum field strength. The uniform field region in this dipole measured 2 meters in x , 2.4 meters in z , and its gap height was 1 meter. The maximum integrated field strength of this magnet was 30 kilogauss-meters, and typically a particle needed at least 1.5 GeV/c forward momentum in order to cross this magnet without being swept into its sides.

E. Cylindrical Spark Chambers

A diagram of the cylindrical spark chambers is shown in figure 8. The cylindrical spark chambers consisted of ten separate cylindrical spark chamber gaps surrounding the LASS liquid hydrogen target. The



6-78

3426A2

FIG. 8--The Cylindrical Spark Chambers;
 a) a cutout view of the chambers
 b) a detail of two chamber gaps

gaps had cylindrical axis nearly identical to the cylindrical axis of the target. The chambers had an active area of 90 cm in length, and the radius of these ten gaps is given in table 2. Two distinct types of gaps alternately made up these ten gaps.

The first type of gap consisted of a low voltage inner cylinder of left slanting wires (left screw sense), and a high voltage outer cylinder of right slanting wires (right screw sense). Both left and right slanting cylindrical wires made a stereo angle of θ ($\tan\theta = 1/10$) with the z direction. Readout of both the high and low voltage wires gave measurements of azimuthal (ϕ) angles, and z positions of intersecting tracks. The gap spacing between the high and low voltage wires was 1 cm. Wire spacing in the first four gaps of this type was 2 mm, while the fifth gap had a wire spacing of 4mm.

The second type of spark chamber gap consisted of a high voltage inner cylinder of slanting wires, and a low voltage outer cylinder of straight wires. The low voltage wires made a zero stereo angle with the z direction. Only low voltage readout existed in these gaps, and thus only ϕ angles were measured for intersecting tracks. The gap spacing between high and low voltage wires was 1 cm. Wire spacing in the first four gaps of this type was 2 mm, while the fifth gap had a wire spacing of 4 mm.

The gas used in the cylindrical spark chambers was a mixture of 90% neon and 10% helium bubbled through a -10°C ethyl alcohol bath. The high voltage pulse, triggered by the LASS fast logic, in these chambers was a ~ 4 Kvolt pulse ~ 300 nsec long. The cylindrical gaps were each equipped with a pulsed clearing field of 250 Volts, and a DC clearing

TABLE 2

Cylindrical Spark Chamber Radii,
Efficiencies, and Resolutions

Gap	Radius (cm)	Typical Tracking Efficiency (%)	Spatial Resolution (Sigmas) (cm)
CYL 1 phi z	10.688	91.0	.095 .80
CYL 2 phi	12.708	96.0	.099
CYL 3 phi z	15.748	92.4	.057 .74
CYL 4 phi	17.788	93.3	.169
CYL 5 phi z	20.828	93.0	.061 .71
CYL 6 phi	22.868	23.9	.124
CYL 7 phi z	30.988	85.6	.133 .71
CYL 8 phi	32.012	86.5	.130
CYL 9 phi z	56.388	70.0	.174 1.50
CYL 10 phi	57.412	73.9	.25

field of 40 Volts. During data taking in this experiment a deadtime of 20 msec was imposed between triggered events in order to allow the spectrometer's spark chambers to recover to full efficiency between firings. Shown in table 2 are the typical plane efficiencies, and typical plane resolutions (sigmas) for the cylindrical spark chambers.

The readout system for these chambers was of the capacitor diode type. In this system each wire had an individual discriminator. Each discriminator output was attached directly to an eight bit shift register. When the spark chamber was fired the hit wires set their associated bits in these registers. A controller serially read and coded the data in these shift registers. The coded data was then transferred to the data acquisition system.

A more detailed description of the cylindrical spark chambers is given in reference 8.

F. Capacitative Diode Spark Chambers

Located in the three 6" slots between the solenoid coil assemblies were three full coverage capacitor-diode readout spark chambers. In addition to these three spark chambers, two additional CD readout spark chambers were located in the twist region. All five spark chambers (CD1-5) were identical in geometry, and shared the same readout system.

Each CD spark chambers consisted of two spark chambers gaps. The first gap was formed by a high voltage wire cloth plane giving X readout, and a low voltage wire cloth plane giving Y readout. The second spark chamber gap consisted of two wire cloth planes with readout wires

inclined ± 30 degrees with respect to the vertical. The high voltage plane gave P readout while the low voltage plane gave E readout. The wire cloth mesh used in the construction of these CD chamber gaps had a wire spacing of .907 mm. The gap spacing in each of these spark chamber gaps measured .95 cm. These chambers had an active area of approximately ± 80 cm in the horizontal direction, and ± 80 cm in the vertical direction. Due to high instantaneous beam flux rates in this experiment, and the poor timing resolution of spark chambers, it was necessary to deaden the beam area in each of these five spark chambers. This was done by placing a 21.6 cm diameter circular styrofoam plug in the center of each spark chamber gap.

The gas used in the CD spark chambers was a mixture of 90% neon, 10% helium, and .5% ethyl alcohol. The high voltage pulse, triggered by the LASS fast logic, in these chamber gaps consisted of an ~4 Kvolt pulse 400 nsec in duration. Each spark chamber gap was equipped with a pulsed clearing field of 80 Volts, and a DC clearing field of 20 Volts. The experiment was also run with a deadtime of 20 msec between events to allow the spectrometer's spark chambers to recover to full efficiency between events.

Each of these five CD readout spark chambers shared the same readout system. In these chambers each wire was connected to an individual capacitor diode circuit. When the spark chambers were fired a hit wire then charged its associated capacitor. A controller then serially scanned each capacitor diode circuit in these chambers, coded the hit wire positions, and passed the information on to the data acquisition system.

Shown in table 3 are typical plane efficiencies, and typical plane resolutions (sigmas) for the CD spark chambers during this experiment.

G. Proportional Wire Chambers

The proportional wire chambers were the major track finding and fitting tool in the solenoid region of this spectrometer. Because of high instantaneous flux rates in this experiment, out of time tracks were often seen in the spark chamber systems. Since the proportional devices had much better time resolution than the spark chambers, PWC hits were required on all solenoid tracks used in this analysis. The PWC's also were very efficient chambers with good positional resolution. In the twist and downstream regions the PWC's also played a major role in providing positional, and timing information.

All proportional chambers in LASS shared the same readout system. A typical proportional chamber plane consisted of etched mylar cathodes at high negative voltage positioned on both sides of a wire readout plane at ground voltage. The only exceptions to this typical chamber were the four cathode readout chambers (TA, TB, TC, and JHxy) which will be described later. The proportional wires in these chambers were all 20 μ gold plated tungsten wires with the exception of the John Hopkins' chambers which had 50 μ wires. In the next few subsections a brief geometrical description will be given of each proportional device in the LASS spectrometer.

TABLE 3

Capacitive Diode Spark Chamber
Efficiencies, and Resolutions

Plane	Typical Tracking Efficiency (%)	Typical Resolution (sigma) (cm)
CD 1 X	91.7	.115
Y	96.2	.113
E	94.4	.130
P	72.5	.108
CD 2 X	84.8	.100
Y	92.0	.090
E	90.2	.114
P	88.7	.100
CD 3 X	89.2	.094
Y	94.1	.090
E	92.7	.094
P	79.0	.084
CD 4 X	85.7	.152
Y	90.2	.090
E	61.8	.132
P	49.3	.151
CD 5 X	82.5	.110
Y	95.7	.104
E	92.4	.152
P	84.4	.157

1. Beam Chambers

The beam chamber geometry was discussed in the beam section of this chapter, and will not be repeated here. Both the upstream and downstream PWC's ran at a voltage of ~4.2 KVolts during this experiment. The gas flowed continuously through these chambers consisted of a mixture of 76% argon, 20% isobutane, .25% freon, and 4% methylal.

2. Cylindrical Chamber

The cylindrical PWC consisted of 160 proportional wires arranged cylindrically about the LASS liquid hydrogen target. The chamber had an active area of 98 cm in length, and the radius of the cylindrical chamber measured 5.188 cm. The wires in this cylinder formed a zero stereo angle with the z direction and thus provided azimuthal readout. The wire spacing in this chamber was 2.037 mm, and the wire to cathode gap spacing was 4.71 mm. The cylindrical PWC ran at a voltage of ~ 2.9 KVolts during this experiment, and a mixture of 71% argon, 25% isobutane, and .25% freon formed the proportional gas used in this chamber.

3. Plug Chambers

The five proportional plug chambers (PLUG1-5) in the LASS spectrometer were designed to cover the 8.5" diameter styrofoam plug in each of the five CD readout chambers described previously. In this experiment plug chambers 1-3 were mounted on CD chambers 1-3 respectively. In the

twixt region PLUG4 was positioned directly in front of MS1T, and PLUG5 was mounted directly on CD5. These chambers furnished in-time high resolution measurements of very forward interaction particles.

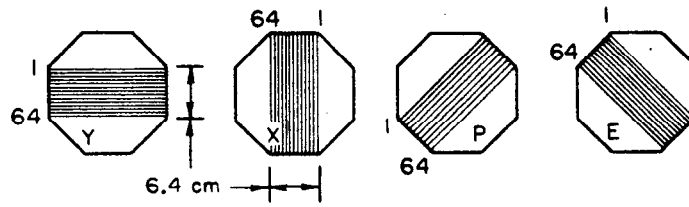
Each plug chamber consisted of three planes with 256 proportional wires in each plane. The wires in these planes were spaced 1.016 mm apart, and the wire to cathode gap spacings measured 4.064 mm. The first two planes in each chamber gave X and Y readout, while the third plane was rotated 35 degrees with respect to the vertical in order to give E readout. The active area of each plane of wires was limited only by the number of wires in one direction, but was limited to ± 14 cm by an etched mylar cathode plane in the other direction (see figure 9). The proportional gas used in these plug chambers was a mixture of 76% argon, 20% isobutane, .25% freon, and 4% methylal. The typical standard operating voltage for the plug chambers was 4.2 KVolts.

4. Full Bore Proportional Chambers

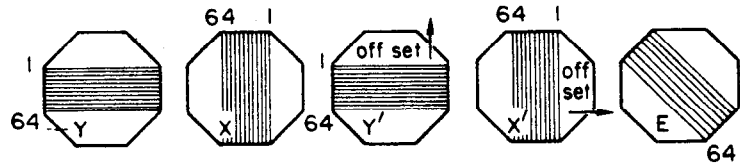
Three full bore proportional chambers (1.5,2.5,3.5) were mounted inside the solenoid magnet, halfway between each 6" solenoid CD chamber gap. Each chamber consisted of three planes with 256 proportional wires in each plane. The wires in these planes were spaced 2.032 mm apart, and the wire to cathode gap spacings measured 4.064 mm. The first two planes in each chamber gave X and Y readout, while the third plane was rotated 45 degrees with respect to the vertical to give E readout. The active area of these proportional chambers formed a nearly perfect octagon (see figure 9). The x and y dimensions of this octagon were

BEAM CHAMBERS
(1mm wire spacing)

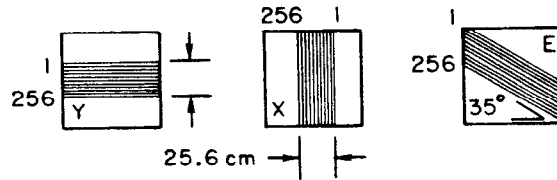
Upbeam Set



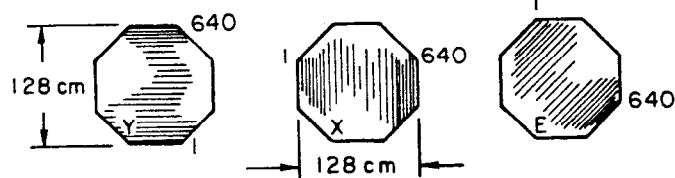
Downbeam Set



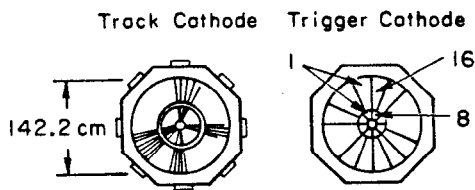
PLUG CHAMBERS
(1mm wire spacing)



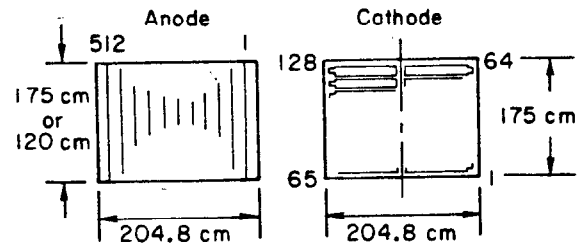
FULL BORE CHAMBERS
(2mm wire spacing)



TRIGGER CHAMBERS



JOHNS HOPKINS HODOSCOPES
(4mm wire spacing)



10-80

All chambers viewed by looking downbeam

3942841

FIG. 9--Proportional Wire Chamber readout planes.

± 64 cm. The proportional gas flowed through these chambers during this experiment was a mixture of 66% argon, 30% isobutane, .25% freon, and 4% methylal. The chambers were typically run at a voltage of ~ 3.0 Kvolts.

5. Trigger Chambers

Three cathode readout proportional chambers (TA, TB, TC) were positioned just upstream of 1.5, 2.5, and 3.5 respectively. Each of these chambers consisted of a single plane of wires, where adjacent wires were spaced 4.064 mm apart. The wire to cathode gap spacing in each chamber was 4.064 mm. These high voltage wires were not read out. Instead of reading out the wires, an etched cathode whose dimensions are shown in figure 9 was read out to give radial and azimuthal coordinates. The coordinates from the trigger chambers were used only for track corroboration in this experiment, and were not used for track fitting.

The proportional gas flowed through these chambers was a mixture of 64% argon, 30% isobutane, and 6% methylal. The chambers were run at a typical voltage of ~ 2.3 Kvolts during the data taking in this experiment.

6. JHxy

The proportional chamber JHxy (built at John Hopkins U.) was located in the twixt region just upstream of PLUG5 and CD5. This chamber had Y coordinate readout on one of the two cathode planes, as well as X readout on the normal proportional wire plane.

The X readout wire plane in this chamber consisted of 512 proportional wires spaced 4.233 mm apart. The wire to cathode gap spacing in this chamber was 6.35 mm. The Y readout cathode in this chamber consisted of two sets of sixty four 2.54 cm x 100 cm fingers etched in the mylar cathode. The first set of these fingers were etched in horizontal rows along the left hand side of the chamber, and the other sixty four were etched in horizontal rows along the right hand side of the chamber. The active area of this chamber measured ± 87.5 cm in the vertical direction, and ± 100 cm in the horizontal direction.

The proportional gas flowed through this chamber during the data taking was a mixture of 80% argon and 20% isobutane. This gas mixture was also flowed through JHup and JHdown which are described in the next subsection. All three chambers (JHxy, JHup, JHdown) typically ran at voltages near 3.7 Kvolts.

7. JHup, JHdown

During this experiment, JHup was located in the twixt region just downstream of the TOF scintillation hodoscope. The JHdown chamber was located in the downstream region just covering the exit of the dipole magnet. Each chamber consisted of a single plane of 512 proportional wires with 4.233 mm wire spacings. This single plane of wires gave X readout, and the wire to cathode gap spacing in these chambers measured 6.35mm. Both JHup and JHdown had an active area in the horizontal direction of ± 100 cm. The JHup chamber had an active area of ± 87.5 cm in the vertical direction, while the JHdown chamber had an active area

of ± 60.0 cm in the vertical direction. These chambers were used during this experiment to supply good timing information, as well as x positions of particles crossing the dipole magnet.

8. PWC Readout

All proportional wire chambers were serviced by the same readout system. Each proportional wire was equipped with an amplifier, a discriminator, and the equivalent of a 32 bit shift register. A proportional pulse on a given wire was amplified, discriminated, and dumped onto the shift register which was continuously strobed by a 40 Mhz clock. A given shift register then carried the past history of the given proportional wire in 25 nsecond slots for the last 800 nanoseconds. When an event took place the strobing of the shift registers was stopped, and a controller serially read, and coded the data in these shift registers. At the coding stage, the controller reduced the number of stored time slots from 32 to 8 for each hit wire. The appropriate time slots for the given trigger were kept so that this reduction caused no loss of information, and a great deal of event storage space was saved. The controller then transferred the coded PWC data to the data acquisition system.

Proportional chamber planes 1.5X and 1.5Y not only served the standard role of track coordinate measurement, but were also incorporated into the main trigger of this experiment. Besides being clocked into shift registers, the discriminator pulses for all wires in the 1.5X and 1.5Y planes were fed into a cluster logic box. This cluster logic box

first combined the signals from adjacent hit wires into a single local logical signal. The resulting signals were then OR'd by this logic box to form a multiplicity signal ($\sum 1.5X > 1$ OR $\sum 1.5Y > 1$). Signals within 1.6 cm of the beam were not included in this OR process. The resulting signal thus indicated whether two or more particles, outside of the beam region, had hit the 1.5 chamber. This logical multiplicity signal was then sent by a fast coaxial cable to the fast logic, where it was used in forming this experiment's main trigger. For a more complete description of this PWC cluster logic system see reference 9.

Typical plane tracking efficiencies, and plane resolutions (sigmas) are given in table 4 for the LASS proportional wire chambers. More detailed information on the LASS proportional chambers can be found in references 10.

H. Magnetostrictive Spark Chambers

1. MS1T and MS2T

Located in the twixt region just downstream of JHup were two large magnetostrictive readout spark chambers; MS1T and MS2T. These two large chambers were both identical in geometry.

Each spark chamber had two spark chamber gaps. The first gap consisted of two wire cloth planes spaced .95 cm apart giving X and Y readout. The second gap consisted of two wire cloth planes with their wires rotated ± 25 degrees with respect to the vertical to give E and P readout. The planes in this second gap were spaced .95 cm apart. The wire

TABLE 4

Proportional Wire Chamber
Efficiencies, and Resolutions

Plane	Typical Tracking Efficiency	Spacial Resolution (Sigma)
BEAM UP X	99.5	.039
Y	99.8	.041
E	98.9	.059
P	99.3	.058
BEAM DWN X	98.7	.059
Y	99.2	.052
X'	99.3	.058
Y'	99.8	.044
E	99.7	.040
CYL PWC	98.2	.068
PLUG 1 X	90.3	.0276
Y	92.2	.0276
E	94.1	.0276
PLUG 2 X	94.6	.0276
Y	93.1	.0276
E	93.0	.0276
PLUG 3 X	95.2	.0276
Y	95.0	.0276
E	92.1	.0276
PLUG 4 X	95.0	.041
Y	86.8	.056
E	92.3	.051
PLUG 5 X	94.6	.036
Y	93.6	.042
E	92.9	.042
1.5 X	95.9	.0552
Y	95.6	.0552
E	95.5	.0552
2.5 X	95.1	.0552
Y	93.7	.0552
E	94.8	.0552
3.5 X	88.8	.0552
Y	87.6	.0552
E	91.0	.0552
TA	98.1	-
TB	97.5	-
TC	90.9	-
JH XY X	98.2	.314
Y	84.2	.259
JH up X	98.2	.800
JH dwn X	92.2	.248

cloth used to make up these wire planes had a wire spacing of $\sim .907$ mm. The active area of these MS twixt chambers measured ± 200 cm in the horizontal direction, and ± 100 cm in the vertical direction. Circular styrofoam plugs 3" in diameter were placed in the center of each gap to deaden the beam region.

The residual solenoid and dipole fields were strong enough, in the twixt region, to alter the magnetization of magnetostrictive wires. To counteract this effect, each magnetostrictive wand was wound with a wire coil. A current of several amps was pulsed through these coils in-time with the beam in order to set up a biasing magnetic field along each MS wire. This allowed normal magnetostrictive readout of these wands.

The gas used in these chambers was a mixture of 90% neon and 10% helium. The high voltage pulse in these chambers, triggered by the LASS fast logic, was a 7-8 Kvolt pulse of approximately 400 nsec duration. These chambers were also equipped with a pulsed 100 Volt clearing field, and a DC clearing field of 50 Volts. The 20 msec deadtime between triggered events proved to be ample time for these chambers to recover to full efficiency between firings.

2. MS1D-MS4D

Track measurement in the downstream region was performed by one PWC (JHdown), and the four MS readout spark chambers (MS1D-MS4D). The four downstream MS chambers were all identical in geometry ¹¹.

Each spark chamber had two spark chamber gaps. The first gap gave X and Y readout, while the second gap gave E and P readout with wires

rotated ± 30 degrees with respect to the vertical. The planes in these gaps were spaced .95 cm apart, and the wire cloth used in constructing these planes had a wire spacing of .907 mm. The active area of these MS downstream chambers measured ± 150 cm in the horizontal direction, and ± 75 cm in the vertical direction. Circular styrofoam plugs 6" in diameter were placed in the center of each gap to deaden the beam region. Each chamber's center position was displaced in the x direction in order to have beam particles travel through the center of these circular plugs.

The gas used in these chambers was a mixture of 90% neon and 10% helium. The high voltage pulse in these chambers, triggered by the LASS fast logic, was a 7-8 Kvolt pulse of approximately 400 nsec duration. These chambers were equipped with a 100 Volt pulsed clearing field, and a 50 Volt DC clearing field. The 20 msec deadtime between triggered events was plenty of time for these chambers to retrain to full efficiency between firings.

The readout system for all MS chambers was the same. Magnetostrictive pulses from the wands were discriminated, and then shaped in zero cross discriminators. These discriminated pulses were then fed into ANNA modules ¹², which digitized and coded these signals. The resulting data was then sent to the data acquisition system.

Show in table 5 are typical plane tracking efficiencies and typical plane resolutions (sigmas) for the MS spark chambers.

TABLE 5

Magnetostrictive Spark Chamber
Efficiencies, and Resolutions

Plane	Typical Tracking Efficiency (%)	Spacial Resolution (sigma) (cm)
MS1T	X	90.4
	Y	91.2
	E	90.8
	P	89.4
MS2T	X	90.8
	Y	91.2
	E	92.4
	P	92.7
MS1D	X	95.6
	Y	97.6
	E	96.5
	P	97.4
MS2D	X	95.6
	Y	95.4
	E	97.7
	P	97.5
MS3D	X	95.7
	Y	97.5
	E	98.0
	P	97.2
MS4D	X	97.1
	Y	98.1
	E	97.2
	P	91.8

I. Scintillation Counters

Located just in front of the LASS eight celled Cerenkov counter, C2, were two large scintillation hodoscopes; HA and HB. The HA and HB hodoscopes are shown schematically in figure 10. The HA hodoscope consisted of an upper and lower row of 8"x33" scintillation paddle counters. Each row contained twenty counters, and in the very center of the array two 4"x33" scintillation counters were placed in order to form a 4"x4" hole in the hodoscope. The HB hodoscope consisted of an upper and lower row with 38 scintillation paddle counters in each row. These counters measured 4"-6"x33", and were arranged as is shown in figure 10. The center counters were once again displaced upward and downward to form a 4"x4" hole in the center of this array. Both the HA and HB hodoscopes center positions were offset in the x direction so that the 11 GeV/c K⁻ beam passed directly through these 4"x4" holes.

The HA and HB hodoscopes were used both for forming secondary triggers, and for time and position corroboration of particles passing through the dipole. For triggering purposes, all HA and HB counter phototube signals were discriminated, and OR'd together to form a fast logic signal. For tracking purposes the signals from the HA and HB discriminators were fed into event latched buffer strobe modules. The data was transferred by a CAMAC system from these modules into the data acquisition system when an event trigger took place.

Covering the 4"x4" hole in the HA and HB hodoscopes was an 9.84 cm radius circular lollipop scintillation counter, LP3. This counter was used in anticoincidence with our main T0 trigger in order to prevent

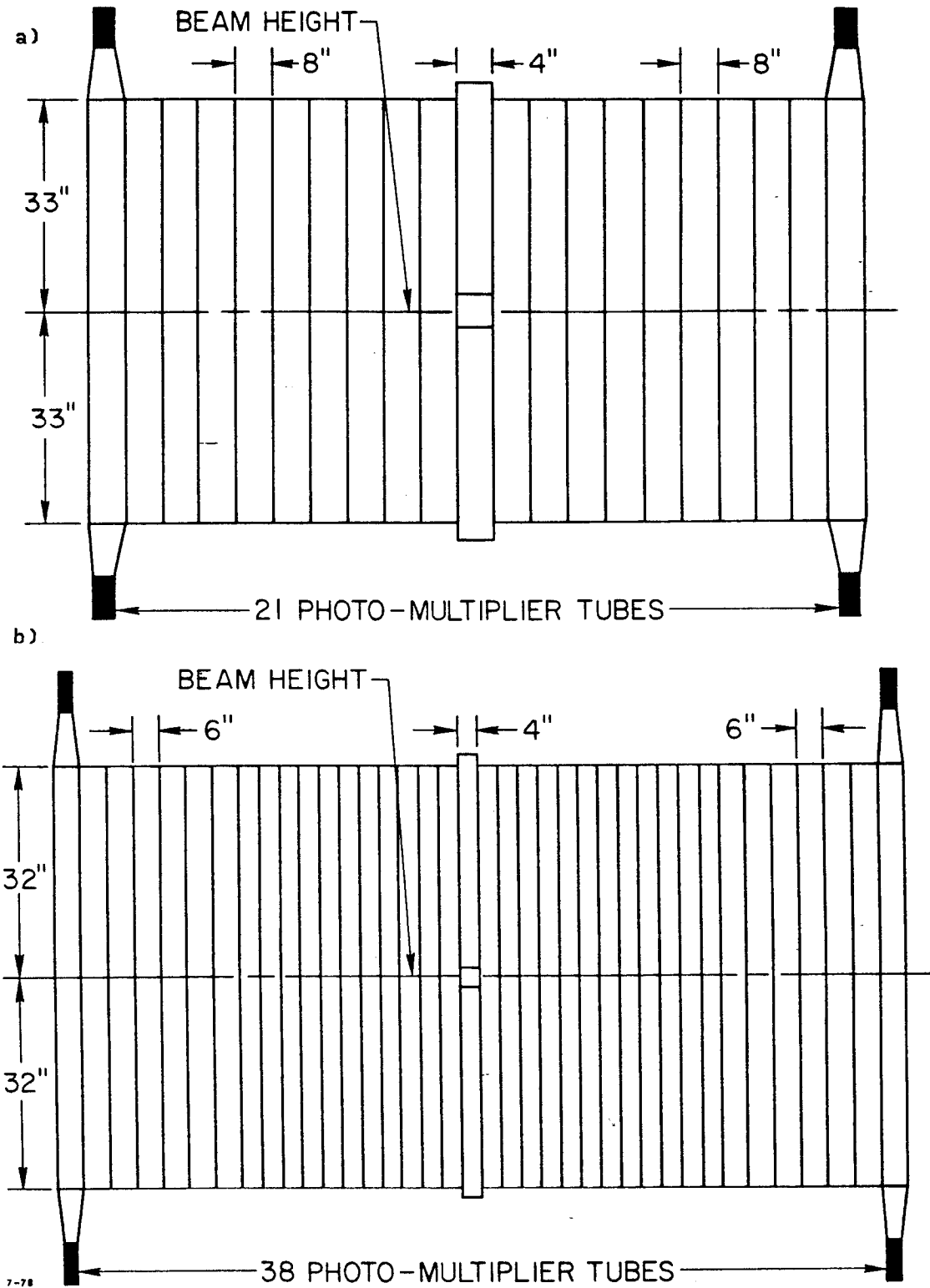


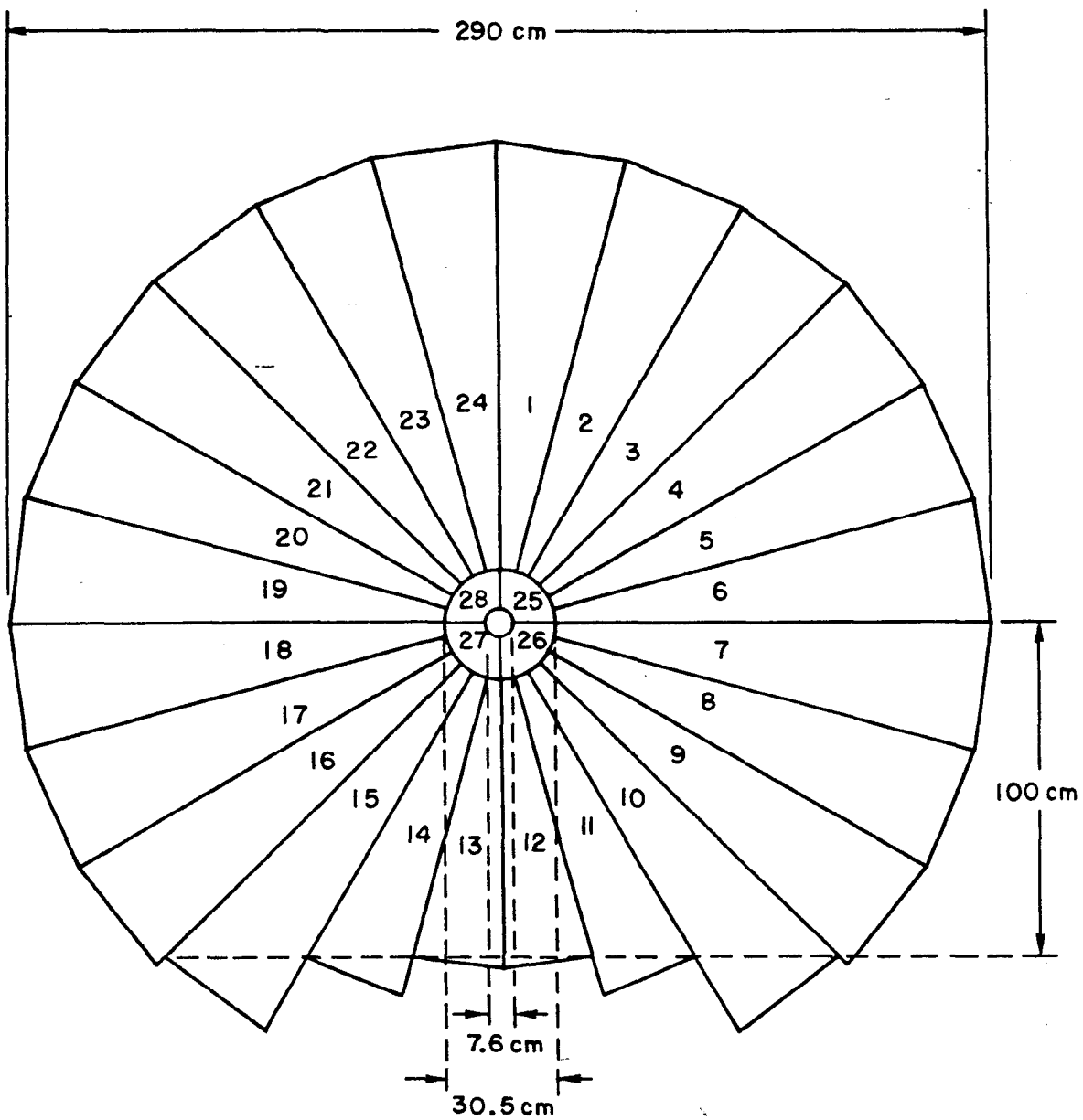
FIG. 10--The HA-HB Scintillation Hodoscope; a) HA and b) HB.

delta rays from triggering the spectrometer. The output from the LP3 phototube was also discriminated, and fed into an event latched buffer strobe module.

J. Particle Identification Systems

Three particle identification systems were present in the LASS spectrometer. These consisted of 1) a 38 celled atmospheric partitioned threshold Cerenkov counter C1¹³, 2) a 24 scintillation counter TOF array¹⁴, and 3) an eight celled nonpartitioned pressurized differential Cerenkov counter C2¹⁵. None of these systems were used for particle identification in the analysis of the $K^-p \rightarrow K^-\pi^+n$ two prong physics presented in this paper. Simple multiplicity, charge conservation, and missing mass cuts sufficed to isolate this two prong channel from almost all background reactions (see Chapter VI section B). The two Cerenkov counters will not be discussed here then. Since the 24 TOF scintillation counters were used, along with the four associated quad scintillation counters, in the main trigger of this experiment, they will be described in this section.

Shown in figure 11 is a diagram of the TOF hodoscope. This scintillation hodoscope was mounted on the downstream face of C1. The external radius of this nearly circular array was 290 cm. The internal radius of the 24 outer TOF counters measured 30.5 cm. Filling in the 30.5 cm hole in this TOF array were four quad scintillation counters. The inner radius of these four counters was 7.6 cm. Due to the relatively large residual magnetic fields at the TOF counters, each



10-80

LOOKING UPBEAM

3942A39

FIG. 11--The Time of Flight (TOF) and Quad Counter Scintillation Hodoscope dimensions. The counters are viewed looking upbeam. Only the scintillation plastic is portrayed.

counter's phototube was equipped with a bucking coil, and magnetic shielding. The bucking coil current was chosen to give the maximum counter efficiency.

Signals from all 28 counters were discriminated, and then logically OR'd in the fast logic. The resulting signal was used in the main trigger. Discriminated pulses were also sent from all 28 counters into event latched buffer strobe units. For particle identification purposes, the signals from the 24 TOF counter were also sent to analog to digital converter (ADC'S) units, and time to digital converter (TDC'S) units. When an event trigger took place the CAMAC system once again transferred the data from the buffer strobe, ADC, and TDC units to the data acquisition system.

Chapter III

TRIGGERING AND DATA COLLECTION

A. Fast Logic and Electronics

1. Beam Logic

The purpose of the beam logic in this experiment was simply to identify, and select incoming beam particles. Shown in figure 12 is a logic diagram of the LASS beam logic. An incoming beam particle was basically defined electronically by a coincidence between the SE scintillation counter, and any one of the four XY scintillation counters. This coincidence was formed by first shaping and discriminating the phototube signals from the four XY counters into 32 nsec long logical pulses. These pulses were then OR'd together to give a logical $\sum XY \geq 1$ output signal. As was mentioned in the beam section, SE defined the beam logic timing. The discriminated pulse from SE was thus made very narrow (~ 8 nsec) by clipping the phototube output signal. The logical SE and $\sum XY \geq 1$ pulses were then AND'd together to define the logical beam particle signal.

Two veto signals were AND'd with this $SE \cdot \sum XY \geq 1$ signal in order to exclude two types of unwanted beam triggers. The $\sum XY \geq 2$ veto effectively discarded beam triggers with two particles passing through separate XY counters within 32 nsec of each other. Two such in-time beam

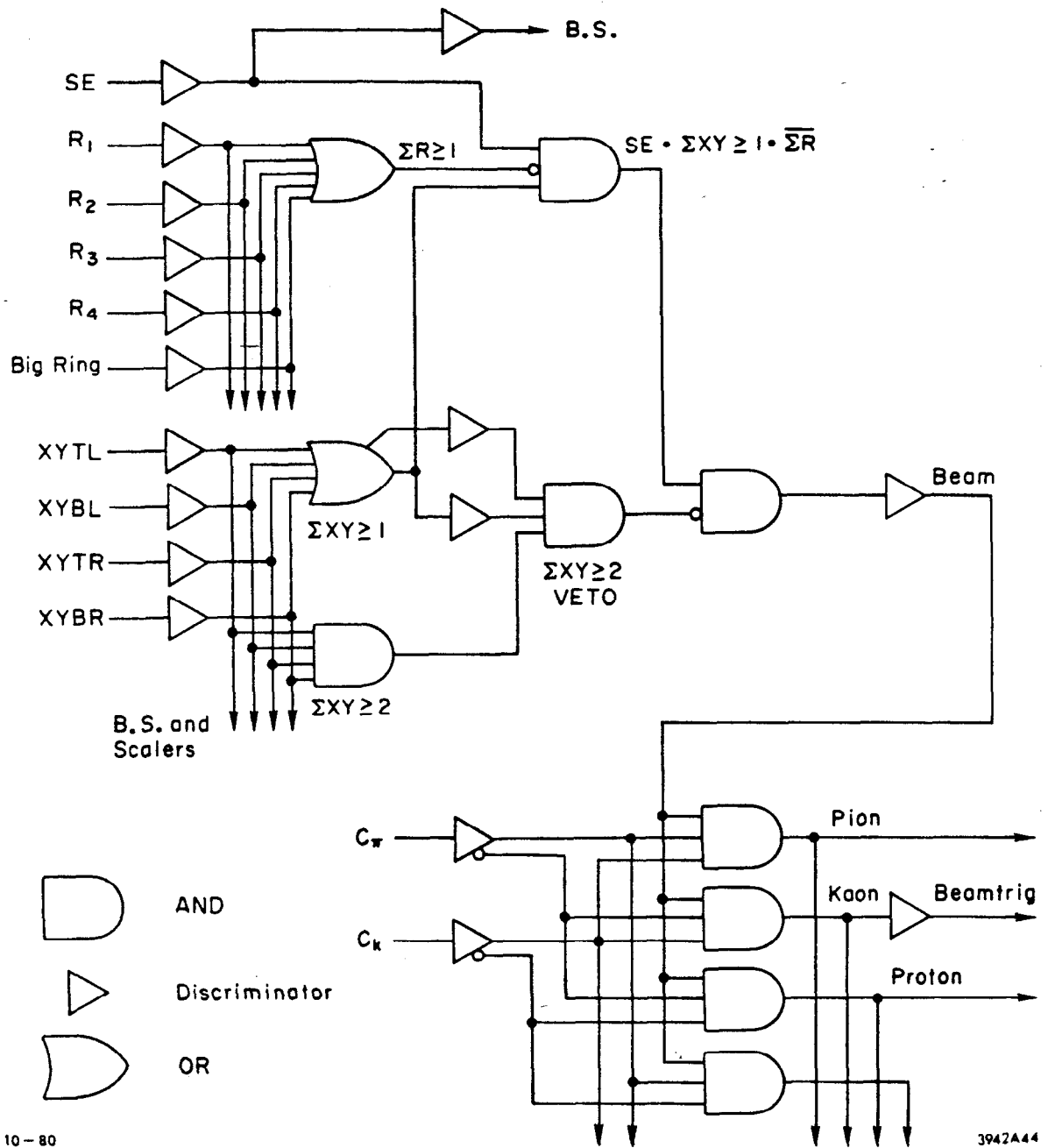


FIG. 12--Beam logic for generating the incident beam kaon (BEAMTRIG) signal.

particles were not separable by the spectrometer hardware, and thus would have led to confusion in event reconstruction. The $\sum R \geq 1$ veto rejected beam particles that had a secondary beam particle pass, through one of the ring counters, within 32 nsec of this beam particle. Such secondary beam particles had a high probability of interacting with the target jacket, and thus had to be rejected. The final logical signal defining a beam particle (BEAM) was defined as $SE \cdot \sum XY \geq 1 \cdot \overline{\sum XY \geq 2} \cdot \overline{\sum R \geq 1}$.

In order to define what kind of particle the particular BEAM signal represented, discriminated 20 nsec pulses from $C\pi$ and CK were used. Logical AND's between the BEAM signal, and these two Cerenkov counter signals thus formed the definition a kaon ($BEAM \cdot CK \cdot \overline{C\pi}$), a pion ($BEAM \cdot CK \cdot C\pi$), and a proton ($BEAM \cdot \overline{CK} \cdot \overline{C\pi}$) in the beam logic. Since this was a K^-p experiment the logical signal BEAMTRIG was defined by the kaon signal, $BEAM \cdot CK \cdot \overline{C\pi}$.

2. Trigger Logic

The trigger logic in this experiment served to select interesting events for the spectrometer to trigger on. Various logical trigger signals were used to study the spectrometer during the setup of this experiment. During the main data taking only four event triggers ($T0, T2, T3, T4$) were employed.

The main trigger ($T0$) in this experiment was designed to trigger on practically the entire K^-p inelastic cross section. This was accomplished by triggering on any K^-p interaction with two or more charged particles downstream of the LASS liquid hydrogen target. Shown in

figure 13 is a logic diagram of the T0 trigger. The first requirement in this T0 trigger was that the beam particle should satisfy the beam logic requirements. The multiplicity requirements, on this trigger, were imposed by requiring one or more interaction particles to pass through the quad-TOF scintillation hodoscope, as well as two or more particles passing outside a 3.2 centimeter square hole in the 1.5 PWC (For a discussion on the cluster logic see Chapt II section 6). The 3.2 centimeter hole requirement greatly suppressed unwanted elastic triggers. The LP3 counter signal was also included in this trigger to veto unwanted triggers caused by delta rays kicked out by non-interacting beam particles. The final T0 trigger was then defined as $BEAMTRIG \cdot (\sum 1.5X \geq 2 \text{ OR } \sum 1.5Y \geq 2) \cdot \sum TOF \geq 1 \cdot \overline{LP3}$.

During this experiment, the three other event trigger types were written to magnetic tape interspersed with the T0 trigger events.

The elastic trigger (T2) in this experiment was defined as $BEAMTRIG \cdot \sum HA \geq 1 \cdot \sum HB \geq 1 \cdot (\sum HA \text{ OR } \sum HB \geq 2) \cdot \sum TOF \geq 1$. This trigger required one, and only one particle to have passed through the HA-HB scintillation hodoscope. Elastic triggers were mainly taken in order to later study track finding in the spectrometer with very simple highly constrained events. The BEAM signal from the beam logic was used as the T3 trigger in this experiment. This trigger provided an unbiased sample of the beam phase space throughout the experiment. This unbiased sample was used primarily in throwing the correct beam phase space in the Monte Carlo, as will be discussed later. The fourth trigger (T4) was defined as $BEAMTRIG \cdot \sum HA \geq 2 \cdot \sum HB \geq 2 \cdot \sum TOF \geq 1$. This trigger was used to select three pion decays of beam kaons. These three body decay tau events were used

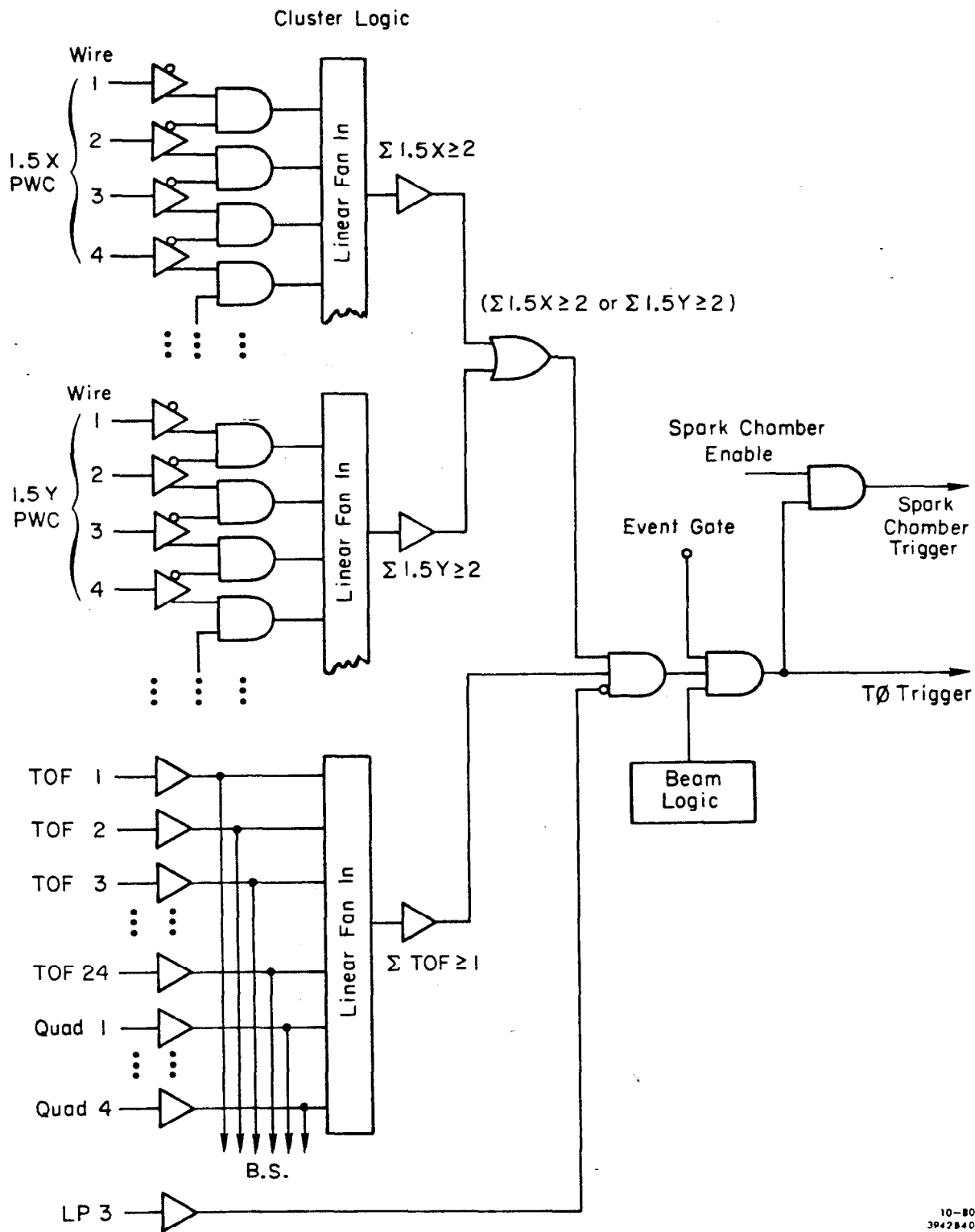


FIG. 13--Trigger logic for the main (T_0) trigger.

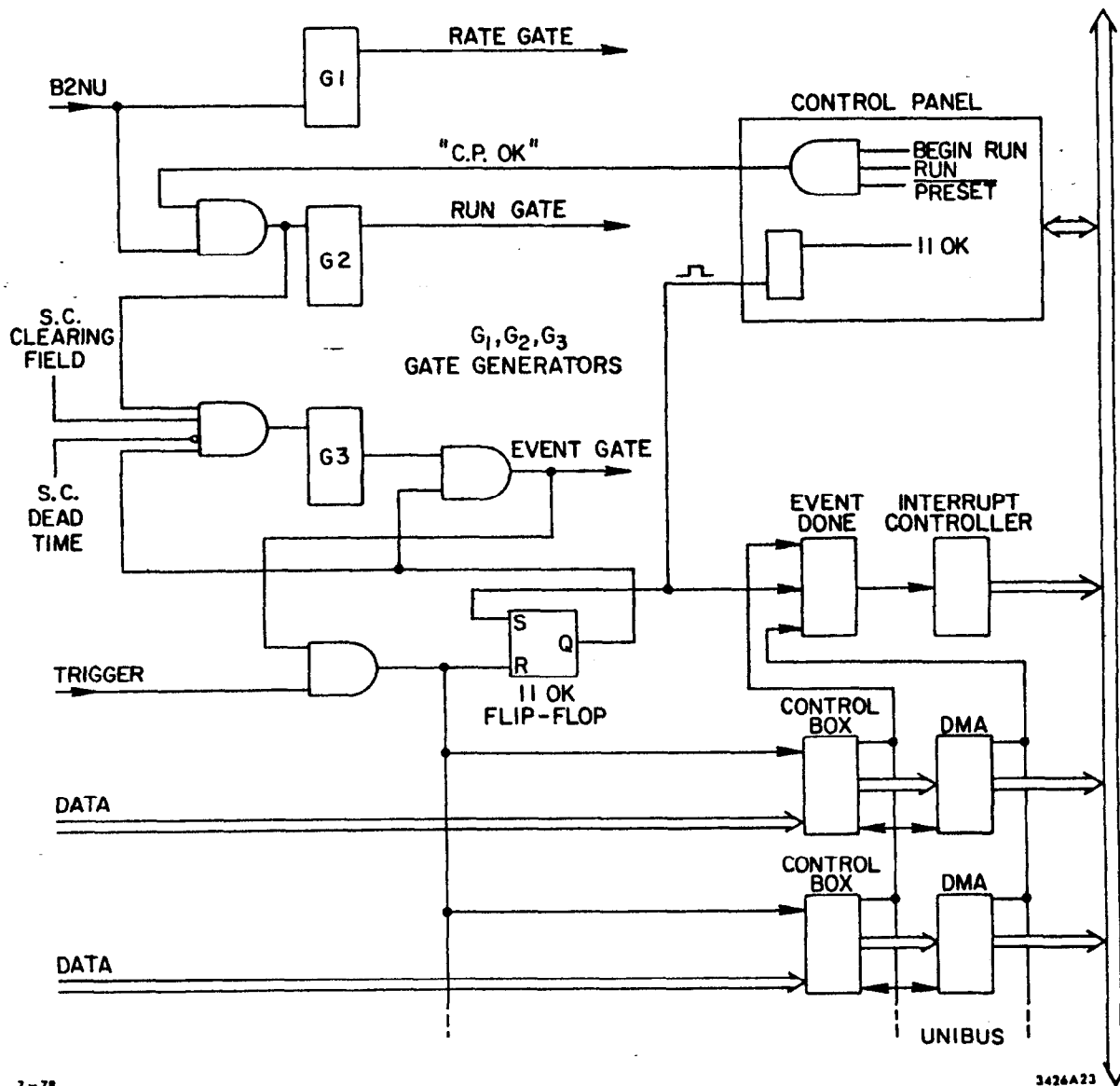
later in the analysis of this data to study the momentum resolution of the dipole, as well as calibrating the P-hodoscope measurement of the beam momentum.

3. Gating Logic

The gating logic in this experiment controlled the triggering of the LASS spectrometer, and initiated the read-in of events into the data acquisition system. These decisions were based on computer readiness as well as on trigger logic signals. Shown in figure 14 is a diagram of the LASS spectrometer's gating logic. Three major logical gates were formed in this experiment; the rate gate, the run gate, and the event gate. Each of these logical signals was created by a separate gate generator. The logical gate from each of these gate generators was initiated by a B2NU signal in coincidence with various logical signal requirements specific to the given gate. This B2NU signal arrived from the main SLAC accelerator exactly 2.5 μ sec before each beam spill.

The rate gate was generated by starting the rate gate generator using just the B2NU signal. The output gate from this gate generator was then stopped after the 1.6 μ sec beam spill. This rate gate was used primarily to control the rate gated scalers which will be discussed later.

The run gate was generated by starting the run gate generator using a coincidence between the main accelerator B2NU signal, and a "CPU OK" signal. This "CPU OK" signal indicated that the data acquisition system was in the run state, and thus in a data taking mode. This signal was



7-78

3426A23

FIG. 14--The gate generating logic.

generated by pushing a series of toggle switches on the main LASS control panel. The gate generator was once again stopped after the 1.6 μ sec beam spill was over. This run gate was primarily used to control the run gated scalers which will be described later.

The most important of the three gating signals was the event gate. Five requirements needed to be met in the gate logic before starting the event gate generator. First a B2NU signal had to be present, as well as a "CPU OK" signal indicating the system was in a run state. The spark chambers pulsed clearing fields had to have turned off since the last event, and a 20 msec spark chamber deadtime had to have passed since the last spark chamber trigger. Lastly the PDP11/20 computer, which served as the first read-in, and buffering device in the data acquisition system, had to be ready to accept an event. When all these requirements were met, the event gate generator was then started. The event generator was then stopped after the 1.6 μ sec beam spill, or when a triggering event took place, whichever came first.

The event gate in coincidence with a logic pulse from the trigger logic served to trigger the spectrometer. This coincidence first gated off the PWC readout system, and \sim 100 nsec later the spark chamber high voltages were applied. This 100 nsec delay was present in order to prevent noise pickup from these spark chambers during PWC read-in. The various control boxes and CAMAC systems for the spectrometer then transferred the data into the PDP11/20 computer by direct memory access (DMA) transfer. When the PDP11/20 completed the read-in cycle an "11-OK" signal was then sent back to the gating logic clearing the way for another event to trigger the spectrometer.

During data taking every T0 trigger in coincidence with an event gate triggered this spectrometer, and thus was written to magnetic tape. The percentage of each type of secondary trigger, in coincidence with an event gate, which triggered the spectrometer was controlled by trigger rate equalizers on each of the secondary triggers. Typically the ratio of events seen in coincidence with an event gate, and the events written to tape for the other three types of triggers was; 1/40 for T2's, 1/1000 for T3's, and 1/5 for T4's. The percentage of each type of trigger written to tape for each type of event trigger for a typical run was; 95.5% T0's, 2.8% T2's, 1.2% T3's and 6.0% T4's. These percentages do not add up to 100% since a given event could satisfy more than one trigger type.

4. Scalers

Three types of scalers were used in this experiment corresponding to the three types of logical gates discussed in the last section. These scalers kept count of relevant signals (SE, BEAM, T0, etc.) which took place during a given logical gate.

The rate gated, and run gated scalers were used to keep track of such absolute quantities as kaon/pulse, SE/pulse, and $\sum XY$ /pulse. These scalers were also used in beam steering and centering. Using a combination of the run gated and event gated scalers, it was also possible to monitor the absolute deadtime during this experiment. This deadtime was caused by a combination of spark chamber deadtime, and buffer backups in the PDP11/20 computer. The rate gated scalers counted scaler quantities

independent of the run state of the data acquisition system, and thus provided a convenient way of observing scalers without altering the run state of the system.

The event gated scalers were the most important scalers in this experiment. These scalers quantities were used in the analysis of this experiment in normalization calculation. The shutoff of the event gate after an event trigger had taken place was kept very tight in order to stop counts in these scalers after this spectrometer trigger. Scalers in this experiment were zeroed at the end of each data run (~ one hour of running, or one tape worth of data).

5. CAMAC

The readout systems of the PWC, MS spark chambers, CD spark chambers, and cylindrical spark chambers were all discussed briefly in the last chapter. The readout of all other hardware was managed by the LASS CAMAC system. All scintillation counter signals, scalers, and digital volt meter readings were thus fed into modules in several CAMAC crates. When an event took place the CAMAC branch controller transferred this data to the PDP11/20 computer. Two separate CAMAC branches were used during this experiment.

The first branch contained modules which needed to be read each event. The modules in these crate consisted of various TDC, ADC, and buffer strobe modules. The only modules in this CAMAC branch used in this analysis were the buffer strobe modules. All relevant discriminated scintillation counter pulses were fed into these buffer strobe

modules. The event gate latched these buffer strobe modules when an event took place, and the data was then read into the PDP11/20 by the CAMAC crate controller.

The second CAMAC branch consisted of modules which were read into the PDP11/20 every 256 events, and then written onto magnet tape. The initiation of this read was carried out by the PDP11/20 computer itself. The modules in these crates consisted of all the run and rate gated scaler modules, as well as digital volt meter (DVM) modules. The DVM modules stored the measured voltage on each of the LASS phototubes for later reference.

As well as being read into the PDP11/20 computer, scaler quantities and DVM readings could be displayed independently on display units in the LASS control room ¹⁶. Relevant scaler quantities were thus monitored throughout the experiment.

B. Data Acquisition System

The main purpose of the LASS data acquisition system was both to store events on high density magnetic tape, and to allow monitoring of the LASS hardware systems during this experiment. The LASS data acquisition system was designed for high data rates (~50 events/sec). When an event trigger had taken place, data was transferred from all the hardware controllers by direct memory access transfer into the LASS PDP11/20 computer ¹⁷. The PDP11/20 then condensed and buffered this data. The buffered data was then transferred to high density magnetic tape using one of two systems. These two data transfer and analysis systems are discussed below.

1. Triplex Computer System

Most of the data stored on tape during this experiment was first transferred from the PDP-11/20 computer to the SLAC triplex computer system. The SLAC triplex computer system consisted of two IBM370/168 computers, and one IBM370/91 computer, all three interconnected. In the transfer process, buffered data was first transferred from the PDP11/20 computer to an IBM SYSTEM7 computer. The SYSTEM7 computer served to reformat the PDP11 data in order to make it compatible with the IBM computers. The reformatted data was then transferred via a 2500 ft coaxial cable from the LASS control room to one of the two IBM370/168 computers. Only the 168 computers could be used for data acquisition. Shown in figure 15 is a schematic of the physical layout of this data acquisition system.

A real-time program called REALTIME controlled the management of these transferred data buffers in the IBM370/168 computer¹⁸. Shown in figure 16 is a schematic diagram of this REALTIME network. Separate tasks within this network were given different priorities. The highest priority of this program was to write each incoming data buffer to high density (6250 BPI) magnetic tape using one of the peripheral SLAC triplex tape drives. The size of the final buffer written to tape for a typical event was approximately 1400 32-bit IBM words long. All other tasks within this program were used to monitor the LASS hardware interactively. The analysis task analysed ~ 5 % of the incoming data events through a sophisticated analysis program. This program was identical to the event reconstruction program which is described in the next chapter.

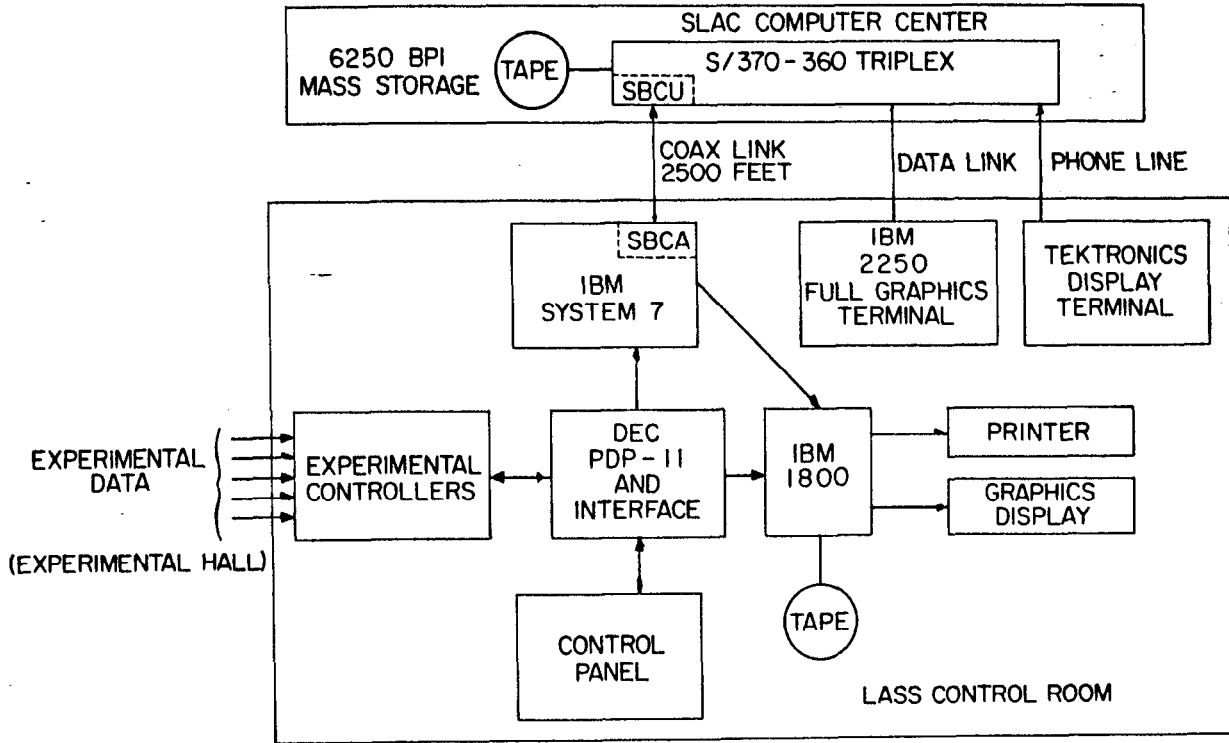


FIG. 15--A schematic of the computers and the data acquisition system.

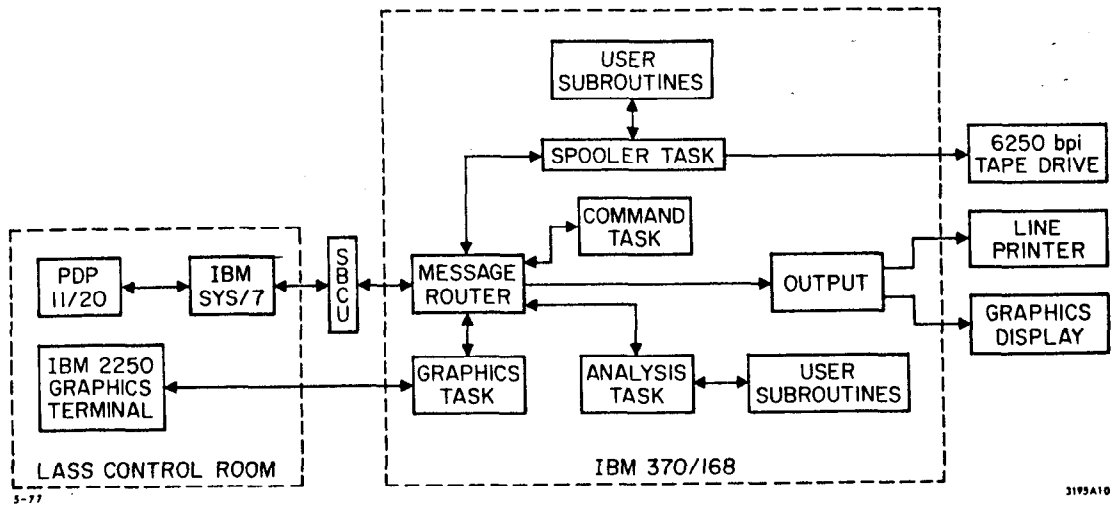


FIG. 16--A schematic of the REALTIME data management network.

This analysis program did track finding, calculated tracking efficiencies, and generally analysed quantities used in monitoring the LASS hardware.

Using the IBM2250 graphics terminal in the LASS control room experimenters could interact with this REALTIME network. Efficiencies, residuals, and wire hits could be displayed for any device in the LASS spectrometer. Histograms and plots of interesting quantities could also be defined and displayed interactively. At the end of each run (approximately 1 tape of data) several hundred lines of efficiencies, and histograms were routed from the IBM370/168 through the IBM1800 computer, and printed out in the line printer in the LASS control room. This output allowed the monitoring of the LASS hardware throughout the data taking.

2. IBM1800

As a backup to the IBM370/168 data acquisition system an IBM1800 computer and two low density (800 BPI) tape drives were located in the LASS control room. These tape drives and the 1800 computers were all controlled by LASS physicists. When using this system buffered events in the PDP11/20 were transferred using DMA to the IBM1800. The 1800 then wrote the event out to tape, and also processed the event through a very simple monitoring program. At the end of several runs (several tapes worth of data) histograms, and relevant numbers were printed out on the line printer. This printout was the sole monitoring information available when data was taken using the 1800 system. The total amount of data stored using the 1800 computer during the data taking in this experiment

amounted to ~ 3 % of the total number of events written to magnetic tape.

Chapter IV

TRACK RECONSTRUCTION AND FITTING

Track reconstruction, and fitting refers to the process of reconstructing event topologies from the raw data events written to magnetic tape. The endpoint of this process was a totally reconstructed event consisting of momentum three vectors for the incident beam particle, a fitted vertex, and the momentum three vectors and charge of each outgoing interaction particle. Track reconstruction and fitting was performed by the LASS FORTRAN track finding and fitting routines¹⁹. These FORTRAN routines are very complex and will only be discussed briefly in the next few subsections. First a discussion of the coordinate and track parameterizations used in this FORTRAN production code will be discussed.

The first step in this LASS production program was the unpacking of the raw data events from magnetic tape, and the transformation of this raw data into physical coordinates in the LASS spectrometer. The coordinate system used, in this process and the all the LASS production routines, was identical to the cartesian coordinate system discussed in the footnote on page 12. The origin of this cartesian coordinate system was chosen arbitrarily to be a point at the upstream face of the solenoid magnet at the exact central axis of the solenoid.

Once these physical coordinates had been calculated, track finding and fitting routines were used to reconstruct event topologies. Track

finding and fitting was done in the three spectrometer regions (beam, solenoid, and dipole) separately.

The beam region was a magnetic field free region to a very good approximation. Thus beam particles were assumed to travel in straight line trajectories from the $\theta\phi$ hodoscope until they interacted in the liquid hydrogen target. Beam particles were parameterized geometrically in this region as:

$$x = x_0 + (z-z_0) dx/dz$$

IV.1

$$y = y_0 + (z-z_0) dy/dz$$

Beam track finding and fitting routines thus determined $x_0, y_0, dx/dz$, and dy/dz at a reference z position z_0 . This information, combined with the P-hodoscopes momentum measurement, gave the three momentum and position of the incident beam particle.

Magnetic fields in both the twixt region and the downstream region were weak enough so that to a very good approximation energetic dipole crossing particles traveled in straight line trajectories in these regions. Thus tracks were fit geometrically to straight lines in the twixt, and the downstream regions. Dipole tracking information in this experiment was used to accurately measure the absolute momentum of dipole crossing tracks. Position and angle measurements of these tracks came from the solenoid fitted tracks linked to these dipole crossing tracks.

The solenoid field, B_z , was highly uniform throughout the tracking region of the solenoid. To a very good approximation charged particles traveled in perfect helices through the solenoid. Solenoid tracks were thus parameterized geometrically in the uniform field region of the solenoid as:

$$\begin{aligned} x &= x_0 + R \cos(\phi_0 + (z-z_0) d\phi/dz) \\ y &= y_0 + R \sin(\phi_0 + (z-z_0) d\phi/dz) \end{aligned} \quad \text{IV.2}$$

Solenoid track finding and fitting routines thus determined x_0 , y_0 , R , $d\phi/dz$, and ϕ_0 for each track at a given reference z position z_0 . The relationship of these quantities to the solenoid track's momentum was quite easily derived to be:

$$\begin{aligned} P_L &= q B_z \left(\frac{d\phi}{dz} \right) & P_T &= q B_z R \end{aligned} \quad \text{IV.3}$$

Where $q = 0.02998 \text{ GeV}/(\text{Kgauss-M})$

The charge of the track could also be determined by the turning direction of its helical trajectory. Thus the three momentum, charge, and position of each fitted solenoid track could be determined from these fit parameters.

A. Unpacking

In reconstructing a particular event, the production job first unpacked each hardware device's raw data which had been stored on

magnetic tape. The raw data was then translated into physical coordinate positions in the spectrometer.

The raw data for the cylindrical spark chambers consisted of the wire numbers of each wire hit in the separate spark chamber planes. Since the cylindrical spark chambers were very noisy it was first necessary to discard hit wire numbers, which were on a hot wire list. In each plane adjacent wires were then clustered together. In the cylinders two clusters surrounding a dead wire were also considered as a single cluster. The centroid of the clusters were then used to calculate the cylindrical coordinate using known wire spacings, and the chamber alignment constants.

The raw data for the CD chambers consisted once again of the wire numbers of each hit wire in the separate spark chamber planes. In each plane adjacent wires were clustered together. Two adjacent clusters with a single nonhit wire in between were also added together to form one big cluster. Using the centroid of these clusters CD coordinates were then calculated using the known wire spacings, and the alignment constants for chamber offsets. Small nonlinear corrections to the coordinate positions were also made at this point to account for nonlinearities in the wire cloth plane wire spacings.

The raw data for the PWC chambers consisted of the wire numbers of each wire hit in separate proportional wire planes, as well as the eight bit time slots discussed in the PWC readout section. At this stage in the processing the eight 25 nsec time slots for all PWC wires hit, except in the beam chambers, had a 100 nsec time mask applied. Wire hits with no bit set within this 100 nsec time mask were rejected. The

beam chambers had a slightly larger time mask of 200 nsec applied. Adjacent wires passing these timing criteria were once again clustered together. Using the centroid of these clusters, PWC coordinates were then calculated from the known wire spacings, and alignment constants for the chamber offsets.

The raw data for the MS chambers consisted of a time measurement for each wire hit in the separate MS spark chamber planes. This time measurement consisted of the time delay in the arrival of the wire hit signal with respect to the arrival of a fixed fiducial along an MS chamber wand. Using the rate of travel of an MS pulse along an MS wire in the wand, as well as alignment constants for chamber offsets and fiducial positions, the MS coordinates were then calculated.

B. Match Points

Match points consisted of combinations of two or more associated X, Y, E, or P coordinates in a single chamber crossing to form a three dimensional point in space. These match points were used in the beam track finding algorithm, as well as both cylindrical and plane solenoid track finding algorithms.

Match points in the cylindrical spark chambers consisted of all possible combinations of left and right slanting wires in the five θ_z readout spark chamber gaps. These combinations lead to θ_z points at fixed radii. The only requirement on these two way match points was that the calculated z crossing of these two wires had to be within the active area of the cylindrical chambers.

The solenoid PWC plane match points were found by first finding all XY match point combinations in a given chamber. The projections of the xy coordinates into the E plane then had to be associated within errors, with E coordinates in order to form three way match points. After storing away these three way match points the production program then stored away all left over two way match points (XY,EY,EX). It was necessary to use two way match points in the solenoid track finding algorithms in order to account for PWC chamber inefficiencies. The beam chamber match points were calculated in the same manner as above but in this case two, three, and four way match points were also possible.

The CD match points were found exactly as the PWC matchpoints. Because of the large number of extra hits in these chambers only three and four way match points were stored away.

C. Beam Track Finding

The first track finding program called in the LASS production code was the beam track finding program. These routines were called first since the beam track finding code was extremely fast, and if no good beam track was found by this code the production of the specific event could be aborted.

Initial trial candidates for beam tracks were formed by calculating all possible combinations of one match point from the upstream beam PWC, and one match point from the downstream beam PWC. Once one of these trial candidates had been calculated coordinate associations with this line were made in the upstream beam PWC, and the downstream beam PWC.

Using these associated wire coordinates, a linear least squares fit was performed yielding a new straight line fit to the trial beam track candidate. The old coordinate associations were then checked once again, and if any points needed to be discarded, the least squares fit process was repeated. This process was repeated until either a track had been found with seven, or more associated coordinates; or else the track had less than seven coordinates in which case a new trial track line was tried.

Once a beam track had been found by this procedure three more requirements were made before its parameters were stored away. The first requirement was that the beam track had to have at least one in-time $\theta\phi$ or XY scintillation counter firing along the projected beam track. The second requirement was that the P-hodoscope could have one and only one momentum bin hit. This P-hodoscope bin was then used to calculate the momentum of the beam particle. The last requirement on the beam track was that it did not share a large number of coordinates with any previously found beam track.

When all these criteria had been met the fitted beam track parameters, beam momenta, and error matrix (from the least squares fit) were stored away for future use. More than one beam particle could be stored away for a given event. In this analysis though, the best corroborated beam track was always used as the beam particle.

D. Dipole Track Finding

The production code's dipole track finding algorithm²⁰ began by finding and fitting straight line tracks in the downstream region. This was done by first calculating various trial track candidates. In forming trial track candidates, sets of three coordinate one dimensional lines were first formed in the X, Y, E, and P coordinate projections. Combinations of these projected lines were then added together, in a similar manner to match point making, to create the final three dimensional trial track candidate lines.

Once one of these trial track candidates had been calculated, coordinate associations with this line were found in the four downstream MS chambers, and the JHdown PWC. If enough coordinates were found a linear least squares fit was then performed using these coordinates. The straight line fit resulting was then used as a trial track candidate, and the process was repeated until two successive iterations yielded the same coordinates, or else the trial track was rejected.

Several requirements were placed on the resulting fitted track before it was accepted as a solid downstream track. First no more than four coordinates could be missing in the final least squares fit. The track also had to have at least two in-time hits out of three possible hits in the good time resolution devices in the downstream (HA, HB, JHdown). Criteria to guard against duplicate tracks were also applied. The procedure outlined above was then repeated until all of the trial track candidates had been exhausted.

Once all downstream tracks had been found one of these tracks was chosen, and extrapolated across the dipole into a particular x coordinate in the twixt region. A modified impulse approximation was used to determine the resulting line through this x coordinate in the twixt region. This twixt line then became a trial track candidate in the twixt region. Just as in the downstream track finding, coordinate associations and least squares fits then were performed iteratively until either the trial track was rejected, or the trial track was accepted. If the trial track was rejected the downstream track was once again extrapolated across the dipole to a new x coordinate, and the process was repeated until either a good twixt join track was found, or all the possible x coordinates in the twixt had been tried.

If a track was accepted various requirements were placed on this track before it was considered a good twixt joined track. The track could be missing no more than eight possible coordinates in the twixt region. Two in-time points were also required out of the three good time resolution devices in the twixt (TOF, JHup, JHxy). Cuts to guard against duplicate tracks were also applied.

Once a good twixt track had been found in this extrapolation process, the actual momentum of the particle which formed this twixt downstream joined pair was computed. An iterative fourth-order Runge Kutta stepping procedure, using a dipole magnet field map, was used to do this final dipole crossing computation. The twixt and downstream tracks were required to link to a high degree of accuracy in this process. The momentum of this joined track pair was thus calculated.

The extrapolation procedure outlined above was continued until all joined twixt and downstream track pairs had been found. It was then necessary to extrapolate each of these joined tracks back into the solenoid. A fourth-order Runge Kutta stepping procedure, with a twixt magnetic field map, was used to extrapolate each track pair through the solenoid fringe field, and into the solenoid tracking region. Using the previously defined helix convention, trial helices were calculated in the solenoid for these extrapolated tracks. Coordinate associations were then made with each trial helix, and a chi-square fit to this helix was performed. New associations to this fitted helix were then made, and the process was repeated until either the joined track had a solid solenoid track joined to it, or no solenoid track was found. Various criteria on the number and type of coordinates on each solenoid track were also required in order to assure a good solenoid track.

In this data analysis, only joined downstream twixt track combinations linked to a solid solenoid track were used. For these tracks particle momenta, solenoid coordinates, and various other useful quantities were stored away.

E. Solenoid Track Finding

The solenoid track finding in this production job was separated into two algorithms; the cylindrical track finding, and the plane track finding. Both algorithms found trial helices using the same basic principle. It is easily shown that a helix projects into a circle on a plane perpendicular to its axis, and for any helix $d\phi/dz$ is a constant.

In calculating trial helices both algorithms first chose three match points in separate solenoid chambers. These three match points then exactly determined the projected circle of a helix. Once this circle had been calculated, the change in ϕ with respect to z was calculated between the first and second match point, and then between the second and third match points. If the resulting change in ϕ with respect to z was found to be constant within tolerances, a helix was calculated and the helix was used as a trial track candidate. If the change in ϕ with respect to z was not found to be constant, then the trial helix was rejected and a new combination of three match points was tried.

In calculating these trial track candidates, the cylindrical track finding routines tried all possible combinations of three chambers from the permutations of the five ϕ - z cylindrical spark chambers, and the CD1 spark chamber. In each combination of three chambers, all combinations of three match points one from each chamber were tested as trial candidates. As well as requiring $d\phi/dz$ to be constant, the cylindrical algorithm required that each trial track candidate have an associated hit in the cylindrical PWC. This assured that the found track would be in-time with the event being reconstructed.

In calculating trial track candidates, the plane track finding routines defined six different sets of three solenoid chambers. In each set all combinations of three match points, one from each given chamber, were tested as trial track candidates. As well as requiring $d\phi/dz$ to be a constant, the planar algorithm made two more requirements on the trial track candidates. The first requirement was that the radius of the trial track candidates helix had to be greater than 2.5 cm. This

requirement saved time by rejecting tracks which would have been so poorly measured as to be useless. The second requirement was that the trial track candidate's helix did not rotate more than 180 degrees between two consecutive solenoid planar chambers.

Once a trial track candidate's helix had been found both algorithms then found associated coordinates in the cylindrical PWC, the cylindrical spark chambers, the CD spark chambers, and the solenoid PWC's. If enough coordinates were found, a helix fit program then used these coordinate to perform a fit. The helix parameters resulting were then used as a trial track candidate and, the coordinate associations and fitting process was repeated. This process continued until either the track was rejected by various criteria, or two successive iterations yielded basically the same coordinates. Duplicate track cuts were also made before this track was defined as a solenoid track.

The helix fitting program, used in this iterative procedure, fit the associated coordinates to a projected circle, and then fit the coordinates separately to obtain $d\phi/dz$. This was done mainly for the reason of speed. Fitting to a projected circle and $d\phi/dz$ separately allows a linearization of the helix fitting program. On the last iteration though a full nonlinear chi-square fit to these associated coordinates was performed.

The process outlined above was repeated until first all the cylindrical tracks had been found, and later all the solenoid plane tracks had been found. Tracks spiraling out of the cylinders, and down through the plane chambers could be found using either algorithm. For the resulting fitted solenoid tracks the helix parameters, solenoid

coordinates, and various other useful quantities were stored away for later use.

It should be noted that match point poisoning was used in the solenoid track finding algorithms. When a particular track was found, match points associated with this track were effectively removed from the match point banks. This removal stopped these match points from being used in calculating a trial helix, but did not stop the coordinates making up this match point from being used as coordinates on tracks found later in the given event. This match point poisoning was essential in speeding up the track finding programs. The match point poisoning also determined the call sequence of the dipole, cylindrical, and plane track finding programs. This call sequence was chosen for maximum processing speed.

F. Vertex Finding

At the end of the track finding and primary fitting of a given event, there existed a single beam track and several solenoid helices found either in the dipole fitting routines or the solenoid fitting routines. It was then necessary to associate this beam track, and the several solenoid helices with a vertex structure defined by the given event's topology. In the $K^-p \rightarrow K^-\pi^+n$ topology of this analysis, only a single primary vertex with two outgoing particles was needed. Thus only this simple vertex topology will be discussed here. In this experiment, vertex association was performed at the end of the production job by a complex multi-topology vertex finding program.

Primary vertices were found by finding a point in space which minimized the sum of the squares of the distances from this point to each track (including the beam). A vertex was then defined, if this sum divided by the number of outgoing interaction tracks was less than 4 cm². The vertex finding program first attempted to form a vertex with all the tracks present in a given event. If the above criteria was not met, all vertex combinations with one track rejected were then tried. This procedure was repeated until a vertex was defined. If more than one set of vertex associations was possible with a given number of outgoing tracks, the best vertex according to the distance sum was chosen. Cuts were then made to assure this vertex was inside the liquid hydrogen target. In the final $K^-p \rightarrow K^-\pi^+n$ event sample, events with a beam track forming a primary vertex with two outgoing tracks were chosen. The two outgoing tracks were also chosen to be charge conserving.

G. Geometrically Constrained Track Fitting

Once the final event topology was chosen, it was possible to refit an entire event constraining the beam particle and the two outgoing solenoid tracks to meet at a common vertex point. This final fitting was performed by a FORTRAN fitting routine called MVFIT. MVFIT was designed to do geometrical as well as kinematically constrained fitting to many complicated event topologies. In this analysis MVFIT was used to geometrically constrain the $K^-p \rightarrow K^-\pi^+n$ two prong events. The input values to MVFIT were the beam fit parameters, the beam fit error matrix, and the solenoid coordinates which were stored for each track. MVFIT

then performed a chi-squared minimization of these coordinates with respect to two helices constrained to the same vertex point. Chamber sigmas were also determined (see section I), and fed into this program. These sigmas were corrected by MVFIT for multiple scattering, and were then used to properly normalize the chi-square sum. The contribution of the beam to this chi-square sum was calculated using the closest approach of the beam particle to this constrained point. The beam contribution to the chi-square was then properly normalized by using the error matrix of the beam track.

As well as outputting the fitted track parameters, MVFIT also output an error matrix for these track parameters, and a fitted vertex position. Elements of the track parameter error matrix were used later in this analysis in calculating the expected momentum resolution for individual tracks. As will be explained in the resolution cut section of chapter V, cuts were made on these expected resolutions in order to get rid of very poorly measured tracks.

The constrained fit results gave the best estimate of each solenoid track's parameters. At this point the three momenta of each interacting particle was calculated by MVFIT. First the incoming beam particle three momentum was corrected for energy loss in the liquid hydrogen target. Next the total momentum was calculated for all solenoid tracks that were not linked to a dipole track. The three momentum of these tracks were then calculated. Finally for the set of dipole tracks linked to a solenoid track, the total track momentum was taken from the previous dipole crossing calculation. Using angles from the new solenoid constrained fit, the three momenta of these dipole tracks were then calculated. The

vertex banks were then filled with the new constrained fit vertex values. As before the charge of the two outgoing particles was determined by the rotation sense of the given particle's helix.

Assuming the event fit was a $K^-p \rightarrow K^-\pi^+n$ event, the positively charged track was defined as the pion and the negatively charged track was defined as a kaon. Using these identifications, energy loss corrections were made to the interaction particle's three momentum to account for energy loss in the liquid hydrogen target and target jacket.

H. Alignment

In the unpacking subsection of this chapter, it was stated that coordinates were calculated using known alignment constants for chamber offsets. This was a gross over simplification of the alignment process, but since spectrometer alignment is not related directly to the track finding and fitting processes, its discussion was left until after these subjects had been presented. Actually chamber alignment was performed before the data was processed through the LASS track finding and fitting production code.

The starting point for the alignment of all devices in the LASS spectrometer was an optical survey done using a transit before this experiment was run. Using these optical constants it was possible to start a self consistent computer tracking and fitting alignment of the spectrometer. The z constants for the spectrometer's devices were taken in this alignment process to be at their optical survey positions. Thus this procedure only modified the x and y chamber shifts given by this survey.

In the first step of the alignment process beam particles (T3) triggers, taken with both the solenoid and the dipole magnets off, were analysed. Beam particles found and fitted in the beam tracking routines were first extrapolated linearly through the six solenoid PWC planes. If 18 associated coordinates (X, Y, and E hits for 6 chambers) were found in the solenoid, a least squares fit was then performed to these 18 coordinates. The resulting line was extrapolated back into the beam chambers where residuals were calculated in the nine beam PWC wire planes, as well as the $\theta\phi$ hodoscope. A plot of the missing XY counter hits was also made in order to align this hodoscope. Residuals were also calculated in the 18 solenoid PWC planes, and extrapolating the least squares fit line into the twixt region residuals were calculated in the four twixt PWC chambers. Using the calculated residuals for hundreds of such events all the PWC chambers in the beam, solenoid, and twixt region had their offset constants shifted. This straight through alignment procedure was then repeated once again. This procedure was repeated until an internally consistent set of alignment constants was obtained for the beam, solenoid, and twixt PWC chambers, as well as the $\theta\phi$ and XY scintillation hodoscopes.

In the second step of this procedure the field off beam particle triggers were once again used. Fitted beam particles were first extrapolated into the solenoid and twixt PWC plug chambers where coordinate associations were found. If all these planes had coordinates, a least squares fit was then performed on these coordinates yielding straight line track parameters. This fitted straight line was then extrapolated into the downstream region. In the downstream region residuals were

then calculated for the four downstream MS spark chambers, as well as the JHdown PWC. Residuals were also calculated in the beam, solenoid, and twixt PWC chambers. Using these residuals for several hundred such events, the alignment constants were once again shifted. This second procedure was repeated until a consistent set of alignment constants was found for these chambers.

The CD spark chambers, and the MS1T and MS2T spark chambers could not be aligned by this procedure since they had styrofoam plugs in the beam region. The MS chambers in the downstream also had plugs in the beam region, but with the dipole off the beam did not travel through these plugs. These CD, MS1T, and MS2T spark chambers were aligned by using field off high angle tracks. The alignment of these chambers was made consistent with the rest of the spectrometer by calculating residuals, and calculating new alignment constant shifts. Using these high angle tracks, the z positions of all chambers in the system were also checked by looking for correlations between track angles and solenoid residuals over several hundred events.

As the last step in the planar chamber and hodoscope alignment, the solenoid and dipole magnetic field on data was used. Particles were tracked and fitted throughout the spectrometer, and residuals were then calculated for several hundred events. Only very small shifts in the planar chamber constants were necessary due to turning on the magnetic fields (E X B effect).

The procedure outlined above aligned every device in the spectrometer, with the exception of the cylindrical chambers. The cylindrical chambers were aligned separately from the plane chambers and hodoscopes.

The cylindrical chamber's external alignment constants consisted of a reference point in space and a set of Euler angles for the PWC cylinder, and a reference point in space and a set of Euler angles for the cylindrical spark chamber package. The internal constants consisted of a ϕ rotation angle about the cylindrical axis for each separate cylindrical wire plane.

Internal constants for the cylinders were determined by first using high angle field off data to calculate and shift constants until a consistent set had been found. This procedure of calculating, shifting, and then recalculating was then repeated using solenoid on data. There were shift differences seen as large as 1.5 mm caused by turning on the solenoid magnetic field. These shifts were a consequence of the well known $E \times B$ effect seen in all spark chambers placed in high magnetic fields.

The cylindrical external alignment constants were determined by using field on high angle tracks. Tracks with a large number of associated solenoid plane coordinates were fitted using only these plane coordinates. Tracks were then extrapolated back into the cylindrical chambers. A chi-square sum of the difference between these extrapolated lines and the chamber wire hits for several hundred events was then formed. This chi-square sum was then minimized with respect to the external cylindrical constants. The results of this minimization were used to fix these cylindrical external alignment constants.

I. Calculation of Plane Sigmas

In each of the chi-square fitting routines mentioned in this chapter, a set of sigmas were needed for the fitted chamber planes in order to normalize these chi-square sums. These sigmas for most chambers in the system were set to first order by merely plotting tracking residuals for these chamber planes for a set of well corroborated tracks, and then calculating sigmas from these residuals. The chamber sigmas calculated in this manner were quite good enough for normal track finding and fitting purposes. The fit error matrices from both the final beam chi-square fit, and the MVFIT two prong vertex constrained fits though were used to simulate track resolutions for making resolution cuts (see chapter V section E). The resulting fit error matrices in both cases were very sensitive to the exact value of these chamber sigmas. Thus the sigmas for the beam chambers, and the solenoid chambers had to be calculated more carefully.

In calculating the sigmas for the beam PWC planes, a set of several hundred beam tracks with coordinates in all nine beam PWC planes were used. Residuals for these tracks were then plotted for each plane separately by leaving out this given plane in a linear chi-square fit, and then calculating the distances from the coordinate to the resulting fit line. The plane sigmas obtained from these residuals were guaranteed to give a properly calibrated beam track error matrix, when they were used to normalize the beam track chi-square.

The calculation of the sigmas for the solenoid chamber planes was done using the standard K_{mn} data sample. Residuals were first plotted

for these $K\pi n$ events in the solenoid by alternately leaving out each given solenoid plane in the full MVFIT vertex constrained two prong fit to these events. The differences between the fitted tracks, and the track coordinates in the left out solenoid plane were then plotted. These residuals were used to calculate sigmas. The calculated sigmas were also checked for sensitivity to cutoff parameters in this calculation, and were found to be insensitive.

Once these solenoid sigmas had been calculated they were used as input to the Monte Carlo job, which calculated fitted tracks in exactly the same manner as the data job (see Monte Carlo section). In performing this part of the study the Monte Carlo was thrown with the best estimate of the $K\pi n$ physics distribution available. Sigmas were then calculated in the Monte Carlo job and compared with the data sigmas. Corrections were then made to the Monte Carlo input sigmas, and new Monte Carlo output sigmas were calculated. This process was repeated until the Monte Carlo output sigmas matched the data sigmas. The final Monte Carlo input sigmas thus gave the best estimate of the solenoid chamber sigmas.

The chamber resolutions presented in chapter II for the solenoid devices were the sigmas calculated in this manner. As a final check of these sigmas, the $K\pi n$ data sample was passed through MVFIT using these solenoid plane sigmas as the input sigmas. A histogram of events as a function of confidence level from this fit was then seen to be quite flat as would be expected. This set of solenoid sigmas then guaranteed a properly calibrated MVFIT track parameter error matrix.

Chapter V

DATA PROCESSING AND SELECTION

In the last chapter, a brief description of the internal workings of the LASS track finding and fitting routines was presented. In this chapter, an overview will be given of how these routines were used to process, and select a final $K^*p \rightarrow K^*\pi^n$ event sample from the ~40 million events written to magnetic tape during this experiment. Kinematical variables used to describe the $K^*p \rightarrow K^*\pi^n$ reaction will be discussed. Finally raw data plots will then be presented and discussed for this final data sample.

A. Data Processing

Shown in figure 17 is a schematic diagram of the data processing chain used in this analysis. In this processing, raw data was first read from tape, and then passed through the LASS production job. This production job called the unpacking, the track finding, the primary fitting, and the vertex finding routines described in the last chapter. Once raw data for a given event had been processed through this production job, fitted track parameters existed for the beam particles and all outgoing charged interaction particles, as well as an associated vertex. These resulting parameters were then written to magnetic tape to form a primary data summary tape (DST).

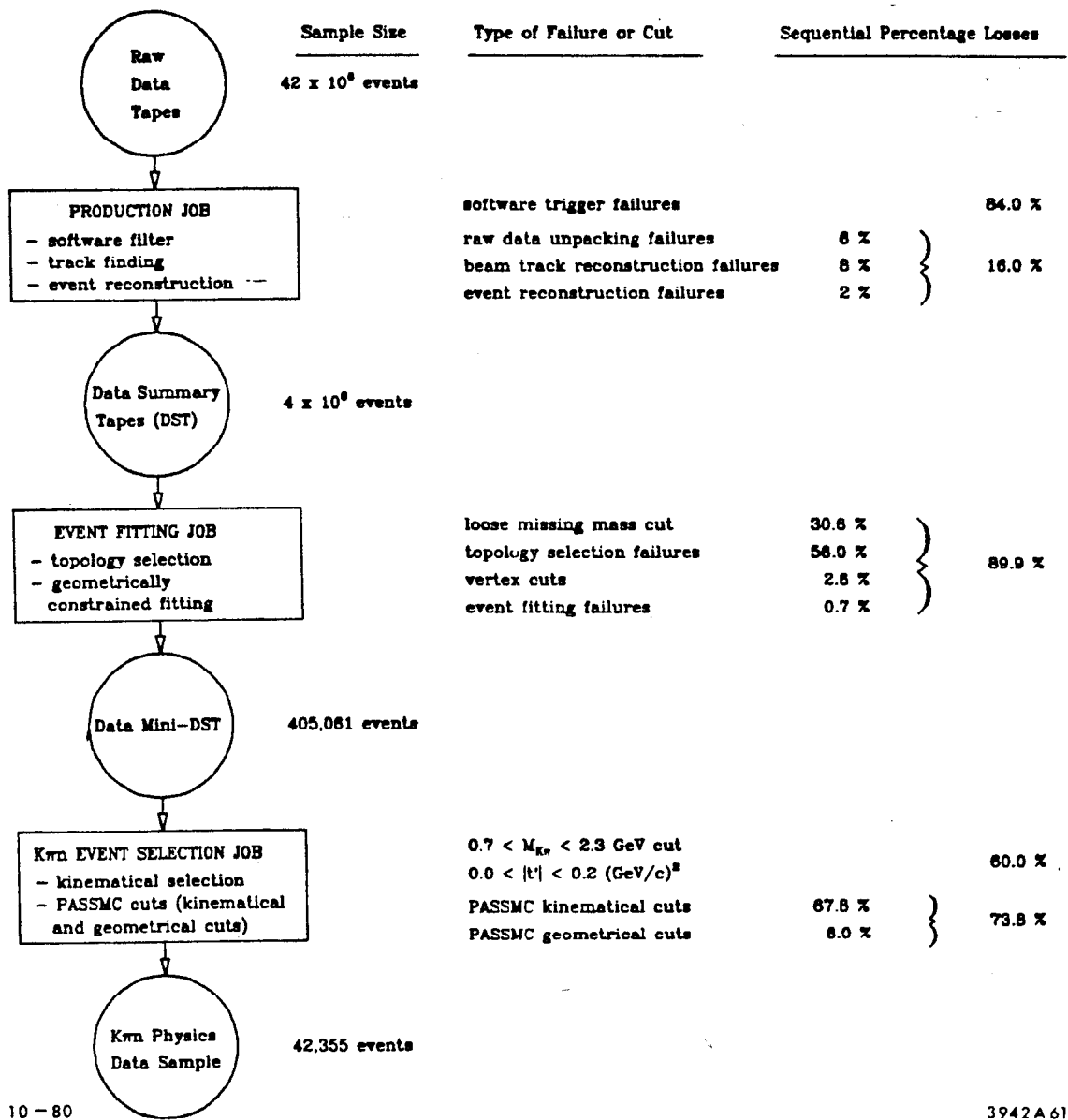


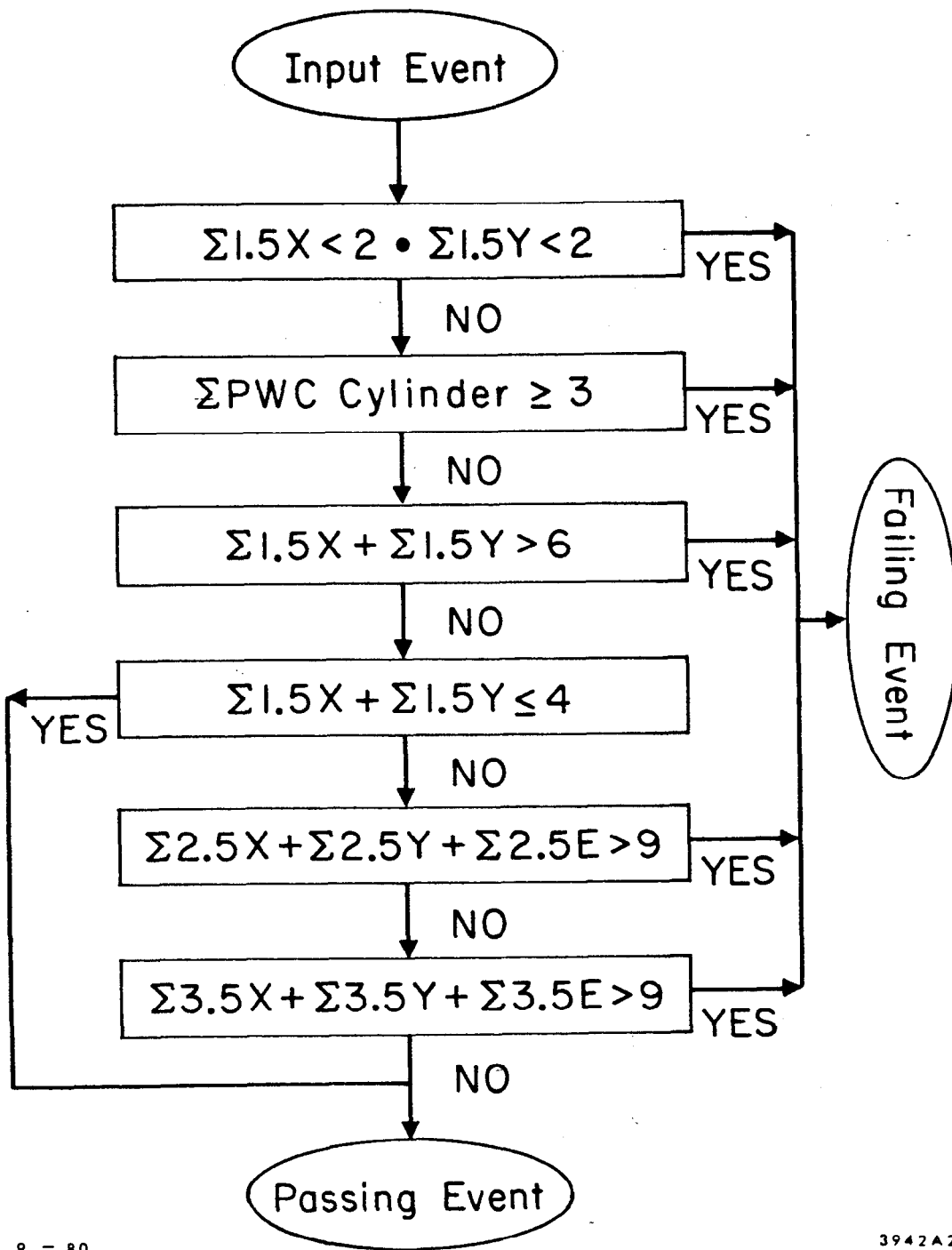
FIG. 17--A schematic diagram of the data processing chain. The sequential percentage of events removed by the major processing cuts are shown on the far right. The number of events left after each stage in the processing are also shown.

In the processing of this data, only raw events tagged as T0 triggers were used. The 40 million raw data events on magnetic tape were subdivided into blocks of events called runs. Each run consisted of approximately one tape's worth of data, and represented about one hours data taking on the LASS spectrometer. There were nearly 1000 good runs taken during this experiment. Each of these separate runs was analysed by the production job, and written to primary DST separately.

The only major data cut imposed by this production job on the raw data was a two prong software filter. As was mentioned previously, the 40 million events written to magnetic tape during this experiment included almost the entire K⁻p inelastic cross section. The processing time involved in fully analysing these events was quite large, and the majority of these events were not two prong events. Thus to speed the analysis of a two prong data sample from these 40 million raw events, a software filter, using raw multiplicities in the solenoid PWC's, was devised.

Shown in figure 18 is a logical diagram of this software filter. In this diagram $\sum 1.5X$ refers to the number of clustered wire coordinates in the 1.5 PWC X readout wire plane. Similarly $\sum \text{PWC CYLINDER}$ refers to the number of clustered wire coordinates in the proportional cylinder for this given event. This software filter selected ~ 15 % of the raw T0 events, and these raw selected events were then processed through the rest of the production code.

A separate study was later made comparing this software filtered processed data sample with several unfiltered fully processed runs. The efficiency of this software filter for selecting two prong events was



9 - 80

3942A26

FIG. 18--A logic diagram of the software filter.

found to be approximately 80 %. The filtered and unfiltered $K^-p \rightarrow K^-\pi^+n$ data samples were also carefully compared in order to check for possible biases imposed by this two prong filtering process. No notable difference between the two data samples was seen.

The production job in this analysis was protected against two general types of program failures, which made events impossible to analyse. These failures were first noted by the production job, and then the associated events were discarded.

The first general type of failures were the unpacking failures (KFAILS). If the production job was unable to unpack a given event for any reason, processing of the given event was then terminated. Unpacking failures were generally due to some hardware failure in a given device's read-in system during the experimental data taking. For instance, an MS chamber was missing a fiducial spark, or a given device's data was garbled. Protection was also made here for possible overflow of software storage banks used to store the raw data during processing.

The second general type of failures were the processing failures (IFAILS). If the production job was unable to analyse an event for any reason processing of the given event was terminated. These failures were generally due to an attempt to overflow some storage bank in the production code. A typical error of this type was the program finding more tracks than it was able to store away (15 tracks was the set maximum).

After the beam track finding and fitting routines were called approximately 8 % of the events passing the software filter requirements were found to have no reconstructable beam track. The events with no

reconstructable beam tracks were also discarded at this point in the data processing. Shown in figure 17 are the percentages of events processed by the production job which were rejected at each point in the production job.

At the end of the production job's processing of a given run, scaler information, and production failure information was written to the primary DST. This information was necessary for calculating the reaction cross section for this experiment. Along with the scaler information and the failure information, a production job monitor record was also written to both the DST and to hardcopy paper output. This production monitor record consisted of 804 important numbers such as chamber efficiencies, average number of tracks/event, and chamber residuals for the given run. These 804 numbers were primarily used to monitor the output of the production job. These production monitor records were also used in conjunction with the logbooks written during the data taking to discard bad runs. Bad runs were runs which had some hardware problem during this hours worth of data collection which adversely effected track finding. Such runs were discarded outright. These bad runs amounted to only a small fraction of the runs processed through the production code in this experiment.

After all the ~1000 raw data tapes had been processed through the production job, approximately 50 high density magnetic tapes of primary DST data were left. These primary DST tapes carried all the information necessary for event normalization; as well as event topologies, primary fit quantities, geometrical quantities, and solenoid coordinates for each processed event. At this stage in the data processing, no attempt

had been made to select out the $K^-p \rightarrow K^-\pi^+n$ event topology except for the rough two prong cut imposed by the software trigger.

The next step in the data processing chain was event topology selection and geometrical fitting. Both of these chores were done by the fit job (see diagram 17). The fit job first read events from the primary DST. Rough kinematical cuts were then made to extract the $K^-p \rightarrow K^-\pi^+n$ two prong data sample. The first requirement made on these tracks was that they had to have a primary vertex consisting of a beam track and exactly two charged outgoing tracks. Charge conservation was also required on these two outgoing charged tracks.

After these rough kinematical cuts had been made, MVFIT was called to perform geometrically constrained fitting on these two prong charge conserving events (see chapter IV section G for a description of MVFIT). For a small percentage of events passed to MVFIT, the chi-square minimization process in MVFIT did not converge. These events were discarded. After MVFIT processing a confidence level cut was also imposed on the constrained event fits. Events with MVFIT confidence levels of less than .001 were also discarded.

Using the resulting fit parameter from MVFIT, a vertex cut was then imposed. The fitted vertex was required to be inside the liquid hydrogen target. The z coordinate was required to be in the range 18.8 cm to 107.6 cm, and the xy position of this vertex was required to be inside a radius of 2.3 cm. Using the MVFIT three momenta of the interaction particles, a cut was also made on the missing mass opposite the two charged particles, assuming that the negative particle was a kaon and the positive particle was a pion. This missing mass squared was required to be in the range from -0.5 GeV^2 to 2.5 GeV^2 .

After the processing of a given event through the fit job, all events passing the fit job cuts were written out to a mini-DST tape. The record written to this mini-DST for each event was very small consisting of less than 60 32-bit IBM words. This 60 word record contained the kinematical variables, beam track three momentum, the two outgoing particle's three momentum, and various geometrical quantities needed to define the final event sample. After all the primary DST data was analysed through the fit job and events had been rejected, ~450,00 events had been written to this mini-DST.

This single mini-DST tape was used as the input tape to all the data analysis routines used in this $K\pi n$ analysis. Before processing these events through each analysis job, a final set of event cuts were made in a routine called PASSMC. This subroutine made all the final kinematical and geometrical cuts which were necessary to define the final $K^-p \rightarrow K^-\pi^+n$ data sample. Before fully describing these PASSMC data cuts, it is first necessary to discuss the kinematical variables used to describe this $K^-p \rightarrow K^-\pi^+n$ final state.

B. Kinematical Variables

At the end of the fit job there existed geometrically constrained charge conserving two prong events. It was then necessary to isolate the $K^-p \rightarrow K^-\pi^+n$ events in this data sample from all other competing two prong reactions. This was done by identifying the two outgoing charged particles in a given event with a particular reaction hypothesis ($K^-p \rightarrow K^-p$, $K^-p \rightarrow K^-\pi^+X^0$, etc.). For this particular hypothesis the MVFIT

three momenta of the beam and the two outgoing charged particles could be used to calculate standard kinematical variables. For instance if the reaction $K^-p \rightarrow K^-\pi^+X^0$ was assumed, the negatively charged particle in a given event was identified as a kaon, and the positively charged particle as a pion. The missing mass squared opposite the $K^-\pi^+$ system was then calculated using standard four vector products as:

$$MM^2 = M_{X^0}^2 = (P_{\text{beam}} + P_{\text{target}} - P_{K^-} - P_{\pi^+})^2 \quad \text{V.1}$$

Cuts were then made on these kinematical variables to isolate the $K^-p \rightarrow K^-\pi^+n$ final state (see the next section).

Once the $K^-\pi^+n$ final state data sample was selected it was necessary to define kinematical variables to fully describe this data in the following analysis. Six variables were needed to fully determine this two prong reaction. In the following analysis, the six variables chosen to specify this reaction were:

- s - the center of mass energy squared of the K^- beam particle plus the p target particle
- ϕ_{lab} - the laboratory ϕ angle of the missing neutron with respect to the laboratory cartesian coordinates
- $M(K\pi)$ - the invariant mass of the outgoing $K^-\pi^+$ system
- $t'=t-t_{min}$ - where t is the 4-momentum transfer squared between the K^- beam particle and the outgoing $K^-\pi^+$ system, and t_{min} is the minimum kinematically allowed value for $|t|$
- $\cos\theta_j, \phi_j$ - where $\cos\theta_j$ and ϕ_j are the Jackson angles defined in the center of mass of the $K^-\pi^+$ system ²¹ (see figure 19)

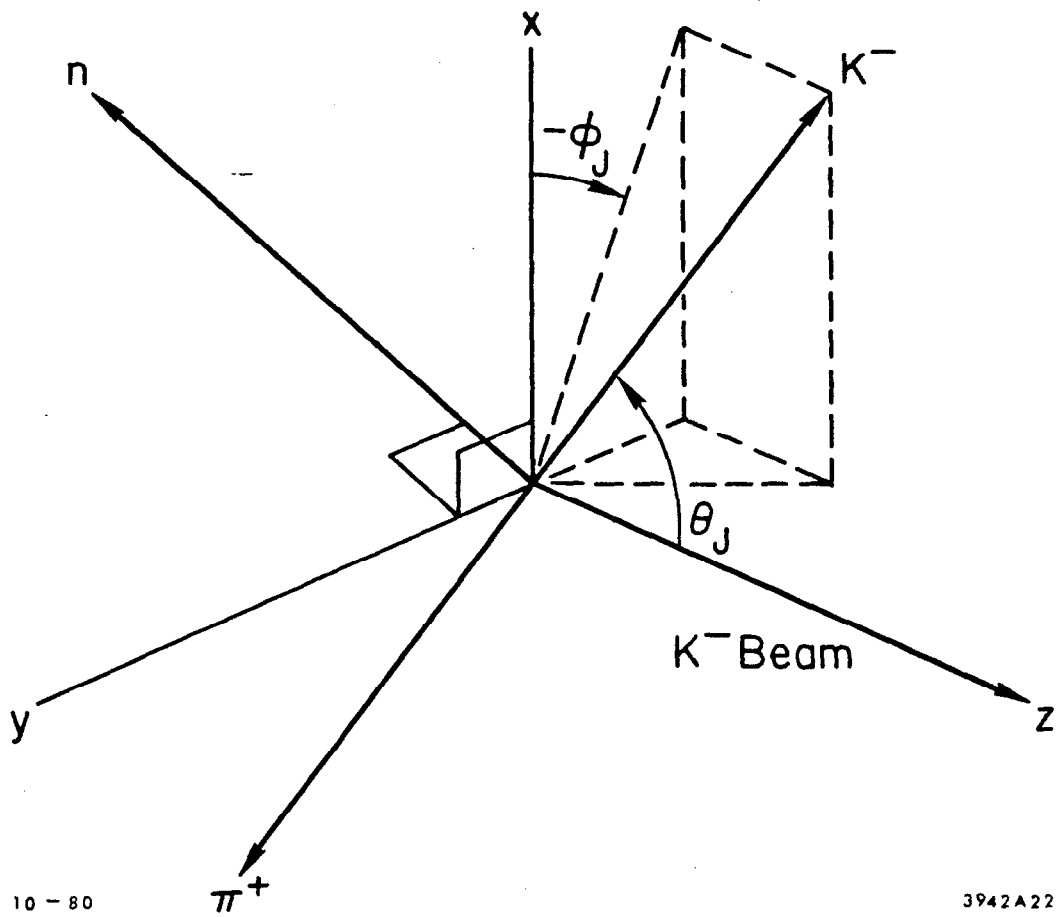


FIG. 19--A diagram showing the definition of the t-channel helicity or Jackson angles, θ_j and ϕ_j , in the outgoing $K^-\pi^+$ center of mass.

Since this experiment was run at a nearly fixed incident beam momentum, s to a good approximation was a constant. Without a polarized target, the physics was also independent of ϕ_{lab} . Thus there were four interesting variable left. These four variables will be used to describe this $K^-p \rightarrow K^-\pi^+n$ data in the following analysis.

These kinematical variables were all calculated in the standard manner, with the exception of t , using the MVFIT geometrical constrained and energy loss corrected three momenta. For instance using these three momenta and the $K^-\pi^+$ particle associations, momentum four vectors could be calculated for the outgoing K^- and π^+ particles, and the invariant $K^-\pi^+$ mass computed using the standard four vector product:

$$M_{K\pi}^2 = (P_{K^-} + P_{\pi^+})^2 \quad V.2$$

Once the final $K^-p \rightarrow K^-\pi^+n$ data sample was chosen it would have been possible to add one kinematical constraint to this final data sample, since the missing mass opposite the outgoing K^- and π^+ was known. Imposing this kinematical constraint, in MVFIT fitting, did not change any of the four interesting variables, for given events, noticeably with the exception of t . Thus kinematically constrained fitting was not performed on the final data sample. A nonstandard calculation of t was used though, which imposed this constraint explicitly. The result of this t calculation versus a full blow kinematically constrained fit agreed to a few tenths of a percent. The resolution on t calculated in this manner was far better than the resolution in t calculated by the conventional four momenta product calculation.

C. Selection of the Final $K\pi n$ Event Sample

As was mentioned previously, the single mini-DST tape formed the input data to all physics analysis programs used in the following data analysis. A routine, PASSMC, was called in each analysis program to reject bad events before any data analysis was performed. The PASSMC data cuts could be classified into three basic types; kinematic cuts, trigger cuts, and geometrical cuts.

The main purpose of PASSMC was to define a final $K^-p \rightarrow K^-\pi^+n$ data sample. A secondary purpose of this routine was to define clean kinematical, geometrical, and trigger cuts on the data sample to make possible the Monte Carlo acceptance correction calculations which will be discussed later. By imposing PASSMC cuts on both the Monte Carlo events as well as on the mini-DST data events, identical final cuts were assured on both event samples.

The primary kinematical cuts imposed in PASSMC were a missing mass cut, and an elastic cut. The missing mass cut required the missing mass squared opposite the two outgoing charged tracks, assuming a $K^-p \rightarrow K^-\pi^+n$ reaction hypothesis, to lie in the range 0.2 GeV^2 to 1.1 GeV^2 for each event. This cut served to select the neutron recoil $K^-\pi^+n$ final state from other possible charge conserving two prong reactions. The elastic cut served to remove the major source of background in the resulting sample. Elastic events in this program were defined by the requirements that; 1) the outgoing K^- particle had to have a momentum greater than $8 \text{ GeV}/c$, 2) the missing mass squared opposite the outgoing K^- particle had to be in the range -2.0 GeV^2 to 5.0 GeV^2 , and 3) the missing mass

squared opposite the two charged outgoing tracks, assuming an elastic hypothesis, had to be in the range -0.2 GeV^2 to 0.2 GeV^2 . Events satisfying these conditions were rejected. This cut also removed most of the diffractively produced $K^-p \rightarrow K^-\pi^0p$ events. Background $K^-p \rightarrow \bar{K}^0X^0 \rightarrow \pi^+\pi^-X^0$ events were also cut from this data sample in PASSMC by removing events with a two prong invariant mass, assuming this \bar{K}^0 decay hypothesis, in the range $.482 \text{ GeV}$ to $.513 \text{ GeV}$.

Trigger cuts were imposed in PASSMC to put more stringent requirements on the definition of an event trigger. First the trigger hole in the PWC 1.5 trigger requirement was increased from 3.2 cm to 3.6 cm . A cluster cut was also imposed on these associated points in PWC 1.5 x and PWC 1.5 y planes such that if the K^- and π^+ coordinates were closer than $.3 \text{ cm}$ in a given plane, they were treated as a single hit in forming this trigger requirement. Events were then required to have associated coordinates on the K^- and π^+ tracks which satisfied the main T0 trigger.

The last set of cuts imposed on the mini-DST data sample by PASSMC was a set of geometrical cuts. These cuts were performed separately on each of the two outgoing tracks. The first cuts made on these tracks were cuts on their expected momentum resolution calculated using the MVFIT error matrix. These resolution cuts will be described in greater detail at the end of this chapter.

Next geometrical cuts were made on those tracks found in the dipole track finding routines. The downstream line of each of these tracks was extrapolated to the downstream face of the dipole magnet, the MS4D spark chamber, and the HA-HB scintillation hodoscope. Aperture cuts were then made at each of these three devices. Events with a dipole track outside

of any of these aperatures were rejected. Events were also rejected if a dipole track extrapolated into the LP3 veto scintilation counter.

The last set of geometrical cuts was made on events found using the cylindrical and plane track finding routines. Cuts were first imposed which rejected solenoid tracks with helical radii smaller than a given minimum. A cut was also made imposing a minimum forward θ angle on any solenoid found track. Lastly a cut was made imposing a minimum longitudinal momentum on these solenoid tracks. This last cut effectively discarded events with helices containing multiple turns between consecutive solenoid plane chambers.

Shown in table 6 is a list of the PASSMC cuts imposed on this data, with the percentage of mini-DST events rejected by each of these cuts. As well as the PASSMC cuts, the final data was also restricted to a $|t'|$ region less than $.2 \text{ GeV}^2$. This restriction served to isolate the pion exchange portion of this reaction as will be described later. Mini-DST events not rejected by this set of standard cuts then formed the standard $K^-p \rightarrow K^-\pi^+n$ data sample used in the rest of this analysis. With all these cuts imposed, this standard $K^-p \rightarrow K^-\pi^+n$ data sample consisted of 42,355 events in the $K\pi$ invariant mass range from 0.7 GeV to 2.3 GeV.

D. Raw $K\pi n$ Data Distributions

To conclude this chapter a few raw data plots will be shown. The data sample used in producing these plots consisted of the standard $K\pi n$ event sample discussed in the last section. In figure 20 is shown an invariant $K\pi$ mass histogram of this standard event sample. The most

TABLE 6

PASSMC Cuts

Cut Type	Typical Percentage of Data Lost
Kinematic Cuts -	
1) Elastic Cut	25.1 %
2) MM^2 Cut	41.8 %
3) K^0 Cut8 %
Trigger Cuts and Target Cuts -	
1) PWC 1.5 active area cut6 %
2) More Stringent T0 trigger	1.7 %
3) Target Cuts	1.0 %
Geometrical Cuts (Dipole Tracks) -	
1) Dipole Aperature Cut2 %
2) MS4D Active Area Cut3 %
3) HA-HB Active Area Cut	<.1 %
4) LP3 Veto Requirement	<.1 %
Geometrical Cuts (Solenoid Tracks) -	
1) $ \theta < .03$ radians	<.1 %
2) Helical Radii < 3.0 cm	<.1 %
3) $P < (.035 P + .030 \text{ GeV})$3 %
4) $P < .350 \text{ GeV}/c$	<.1 %
5) $\sigma_P < .500 \text{ GeV}/c$	2.0 %
6) $\sigma_P/P < .100$	<.1 %

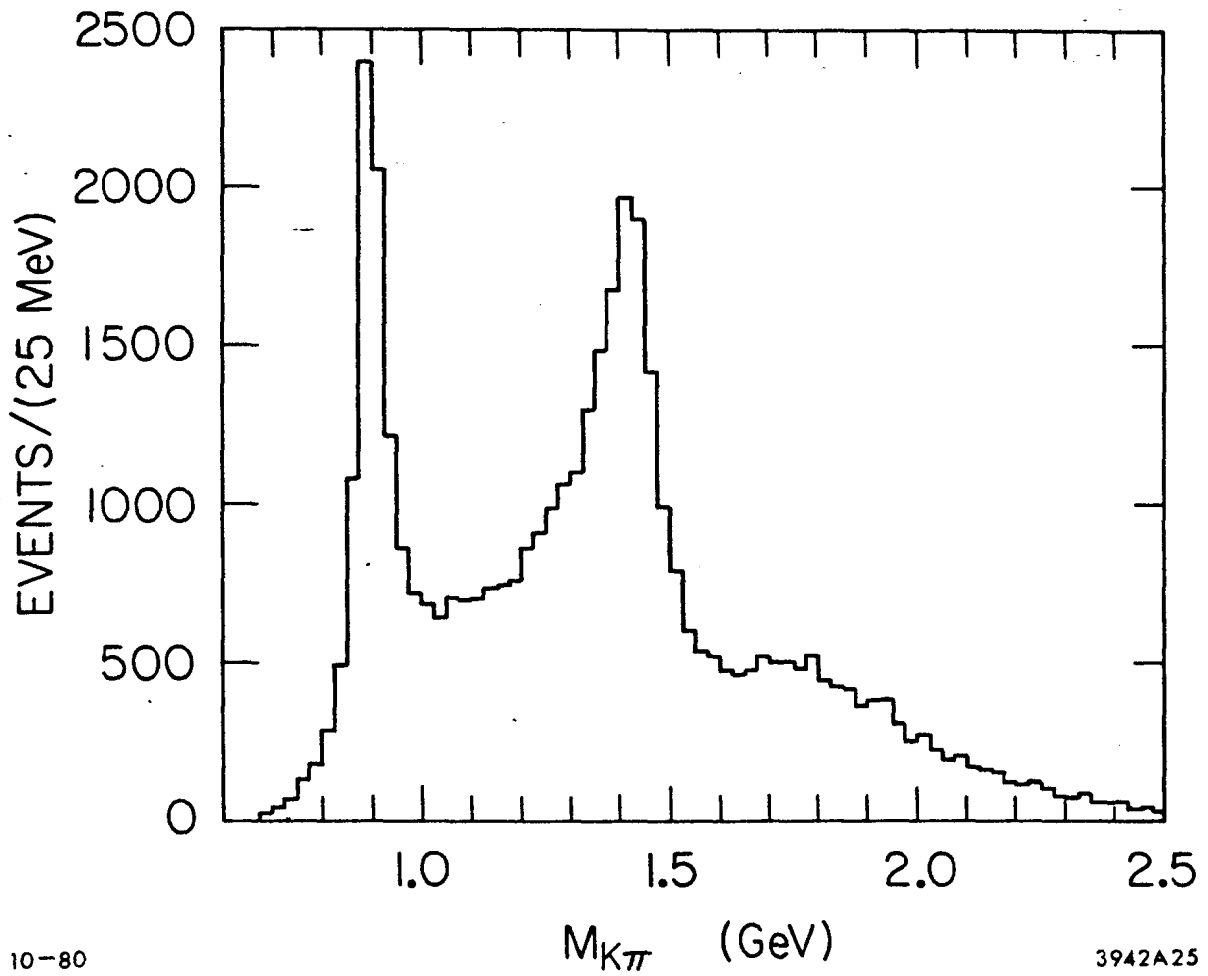
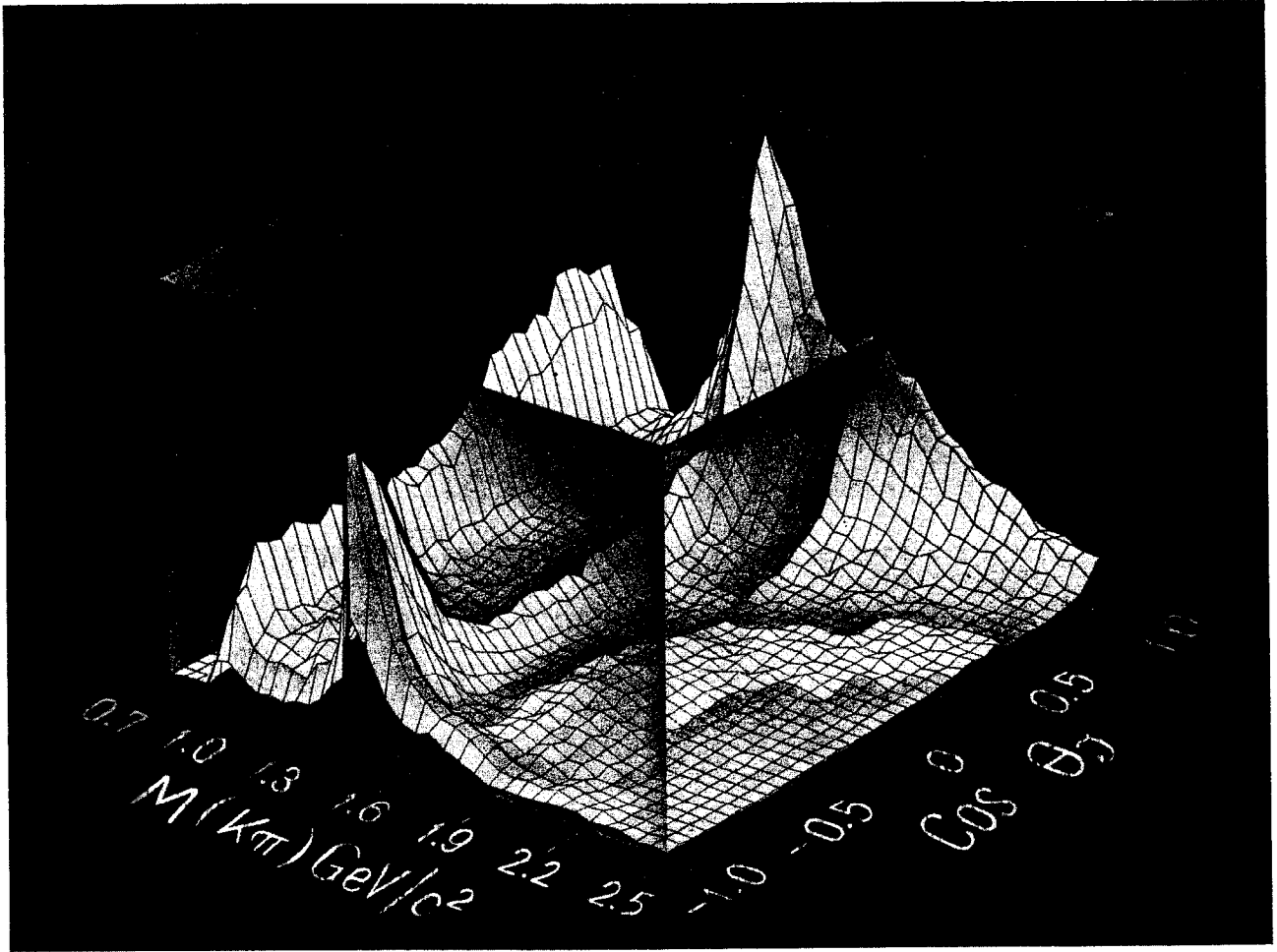


FIG. 20--A histogram of the $K^-\pi^+$ invariant mass for the standard $K^-p \rightarrow K^-\pi^+n$ data sample.

striking features in this histogram are the two sharp peaks corresponding to the $K^*(895)$ and the $K^*(1430)$ resonances. There is also some hint of structure in the mass region around 1.8 GeV, but besides this hint, there is little evidence for any other resonances besides the two well known leading K^* resonances.

A great deal more structure is revealed when another dimension is added to this $K\pi$ invariant mass plot. Shown in figure 21 is a projected three dimensional plot of the $K\pi$ invariant mass versus $\cos\theta_j$. The height of this surface gives the number of events per bin arbitrarily scaled. The data sample used to produce this raw data plot consisted of the standard data sample with looser missing mass and t' cuts imposed ($0.0 \text{ GeV}^2 < M^2 < 2.0 \text{ GeV}^2$, $|t'| < 1.0 \text{ GeV}^2$). The $K^*(895)$ is once again clearly visible as a ragged wall in the low mass region of this plot, and at slightly higher mass sharp peaks in the forward and backward $\cos\theta_j$ regions are indicative of the $K^*(1430)$ resonance.

Besides the two well known leading resonances interesting high mass structure can also be seen in this plot. One of the most prominent structures in this high mass region is the steep forward peaking ridge in the very forward $\cos\theta_j$ region extending from the $K^*(1430)$ resonances up to very high $K\pi$ mass. This ridge becomes steeper as one increases in mass, and is indicative of $K^-\pi^+$ diffractive scattering. The fall off of this ridge at high mass is due to the limited acceptance of this experiment's trigger (see chapter VII section B.9). The forward ridge in this plot has a broad peak at a $K\pi$ invariant mass near 1.70 GeV. This peak combined with a broad bump at an invariant $K\pi$ mass of 1.80 GeV and a $\cos\theta_j$ of around -0.5 could be considered to be indicative of the $K^*(1780)$



10-80

3942A62

FIG. 21--A projected three dimensional plot of $\cos\theta_j$ vs the $K^-\pi^+$ invariant mass. The vertical scale represents the number of events per bin. There are approximately 1000 events in the highest bin on this plot.

resonance. At higher masses there also seems to be a great deal of structure in both the forward $\cos\theta_j$ region from 0.0 to 0.7, and also in the very backward $\cos\theta_j$ region. In any case it is clear that there is a great deal more structure in this data than a simple $K\pi$ invariant mass histogram would indicate.

A slightly different way of viewing this data is shown in figure 22. These eight $K\pi$ invariant mass histograms consist of data from different consecutive $\cos\theta_j$ bands each with a width of .25. The data sample used to make this plot consisted of the standard $K\pi$ data sample with the normal missing mass and t' cuts applied ($0.2 \text{ GeV}^2 < M^2 < 1.1 \text{ GeV}^2, |t'| < 0.2 \text{ GeV}^2$). The change of apparent mass and width of the resonance structures is dramatic in the different $\cos\theta_j$ slices. In particular the $K^*(1430)$ peaks at $\sim 1.430 \text{ GeV}$ in the forward and backward $\cos\theta_j$ direction, but peaks substantially lower near $\cos\theta_j$ equal to zero. This effect will be shown later to be due to S wave and P wave interference. Interference effects are so strong near the $K^*(1780)$ resonance region that here the mass and width of this invariant $K\pi$ mass bump varies rapidly with even small changes in $\cos\theta_j$.

It is clear that in order to understand the angular structure of this data a more sophisticated analysis must be performed. The following chapters will present a more sophisticated analysis of this $K\pi$ data.

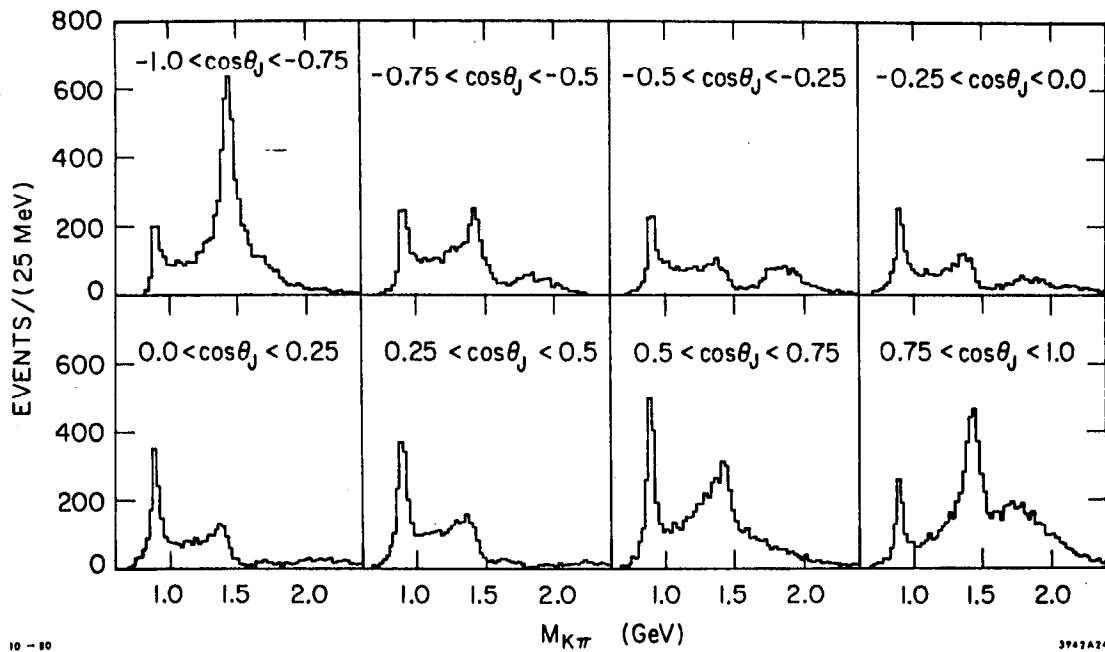


FIG. 22--Eight $K^-\pi^+$ invariant mass histograms in consecutive $\cos\theta_j$ slices for the standard $K^-p \rightarrow K^-\pi^+n$ data sample.

E. Track Resolution Cuts

In the following analysis a good understanding of the spectrometer resolution was required for several purposes; 1) to understand and correct for resolution dependent cuts on the $K\pi\pi$ data sample, 2) to correct final resonance widths for resolution smearing in mass, and 3) to remove and correct for $K\pi\pi$ events with poorly measured tracks. For the first two purposes the spectrometer resolution was calculated using the Monte Carlo as will be described in chapter VII section B. For the last purpose resolution cuts were performed on both the $K\pi\pi$ data sample, and the Monte Carlo event sample, as will be described in this section.

In the final event sample, there were certain types of tracks found in the solenoid track finding and fitting routines which had extremely poor momentum resolution. An example of such a track would be a high momentum forward K^- particle with very little transverse momentum, which decayed before reaching the dipole. Such tracks traveled in nearly straight line trajectories, and the absolute momentum of these tracks were thus very poorly measured. For such tracks the momentum measurement was often so poor that the associated event added no useable information to this analysis. The Monte Carlo simulation of such events would also have depended on the extremely fine details of the chamber resolutions. Thus in this analysis events containing these poorly measured tracks were cut both from the Monte Carlo event sample, and the data event sample.

To remove these tracks, the MVFIT output correlated error matrix described earlier was used. This error matrix contained the correlated

errors ($\langle x_0 x_0 \rangle, \langle x_0 y_0 \rangle, \langle x_0 R \rangle$, etc) of the track parameters ($x_0, y_0, R, d\phi/dz, \phi_0$) for each of the two tracks fitted in this vertex constrained fit. Propagation of error formulas were then used to derive the momentum error on each solenoid track in terms of the associated track parameter's correlated errors. The resolution error on a given track in terms of its track parameter's correlated errors was given by:

$$\langle dP dP \rangle = \frac{q^2 B_z^2}{\{ 1 + R^2 \left(\frac{d\phi}{dz} \right)^2 \}} \left\{ R^2 \left(\frac{d\phi}{dz} \right)^2 \langle dR dR \rangle - 2 R \frac{\langle dR d \left(\frac{d\phi}{dz} \right) \rangle}{\left(\frac{d\phi}{dz} \right)} - \frac{1 \langle d \left(\frac{d\phi}{dz} \right) d \left(\frac{d\phi}{dz} \right) \rangle}{\left(\frac{d\phi}{dz} \right)^2} \right\} \quad \text{V.3}$$

$$\sigma_p = \sqrt{\langle dP dP \rangle}$$

Where $q = 0.02998 \text{ GeV}/(\text{Kgauss-M})$

Monte Carlo and data events were then rejected in the subroutine PASSMC (see chapter V section C) if the given event had a solenoid track with a σ_p greater than 500 MeV, or a σ_p/P greater than 10 %.

Chapter VI

MOMENTUM CALIBRATION, BACKGROUNDS, AND NORMALIZATION

A. Momentum Calibration

In order to assure proper experimental mass values for the $K\pi$ resonances fit in this analysis, it was necessary to check the calibration of the three momentum measuring systems in the LASS spectrometer; 1) the beam, 2) the solenoid, and 3) the dipole. For the solenoid and the dipole magnets this calibration factor was defined by respective magnetic field constants. In the beam hodoscope this momentum constant was defined by bin constants for the eleven P-hodoscope momentum bins.

The first step in this process of momentum calibration was to check the dipole and solenoid magnetic field constants, which had been measured previously using magnetic probes. These constants were checked by performing fits to inclusive $K^0 \rightarrow \pi^+\pi^-$ events. In this study the $\pi^+\pi^-$ invariant mass squared of these K^0 decay events were fit to a Gaussian term plus a simple polynomial background. Two separate fits were performed. The first used events where both decay products had been measured in the solenoid. This fit then tested the solenoid magnetic field constant. The second fit made use of events where both decay products had been measured in the dipole. This fit then tested the dipole magnetic field constant. The two fits yielded the following values for the

fitted K^0 mass:

2-solenoid tracks 496.7 ± 2.0 MeV

2-dipole tracks 497.1 ± 1.0 MeV

where the errors are conservative estimates of the systematic errors present in the fits. The fits were shown to be insensitive to the exact form of the polynomial background used. These fits are seen to agree quite well with the accepted value of 497.7 ± 1 MeV for the K^0 mass³.

Once we were fairly confident about the dipole and solenoid measured magnetic field constants, the P-hodoscope was then calibrated with respect to the dipole magnetic field. Tau decays of beam kaons (T4 triggered events), with all three decay products measured in the dipole, were used in this process. For each tau decay event, the three momentum of the three decay products were added, and the resulting momentum was corrected for energy loss in the spectrometer. The dependence of these corrected momenta versus the eleven P-hodoscope momentum bins was then fit yielding the bin constants for each P-hodoscope bin.

A final check on the momentum calibration of the beam, the solenoid, and the dipole was provided by a fit to the $K^-p \rightarrow K^- \pi^+ X^0$ missing mass squared spectrum shown in figure 23. In performing this fit, the missing mass shape used to fit this missing mass squared spectrum was generated using Monte Carlo events. The exact procedure used to perform this fit will be discussed in detail in chapter VII section B.7.

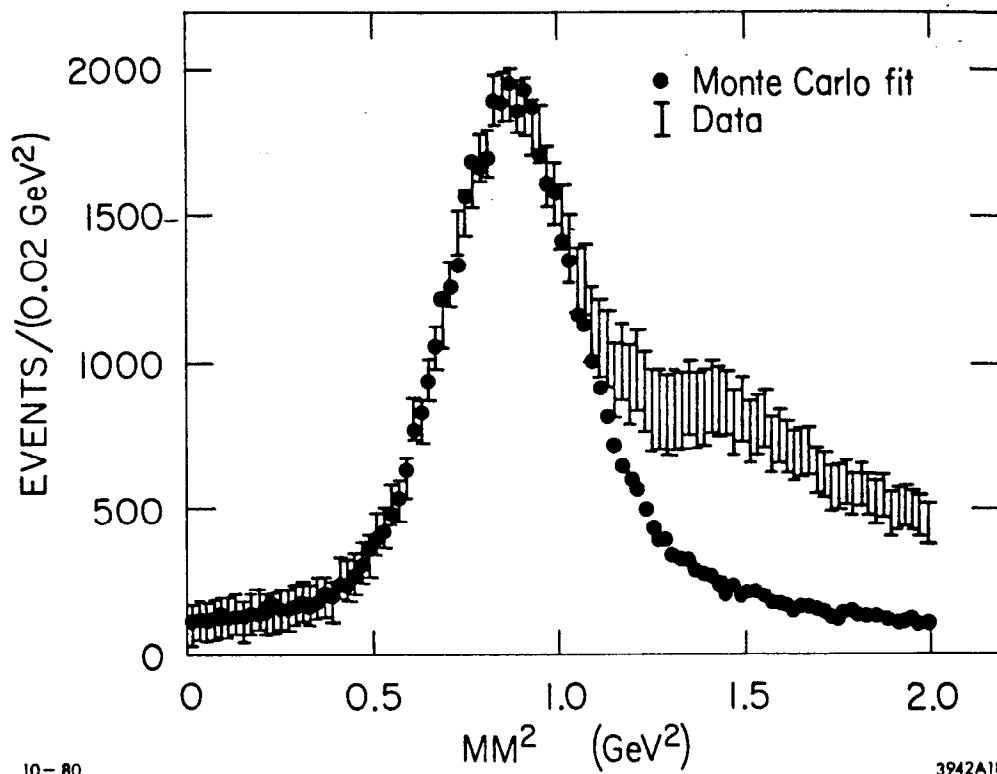


FIG. 23--A missing mass squared plot with a Monte Carlo fit superimposed. The symbol • represents the fitted Monte Carlo missing mass squared plus a linear background term. The data is represented by the error bars. The error bars represent the statistical errors on the Monte Carlo spectrum and the statistical errors on the data added in quadrature.

The results of this fit gave a value for the neutron mass of:

$$945.4 \pm 3.0 \text{ MeV}$$

where the error on this quantity is statistical in nature only. This fit value is thought to be quite consistent with the accepted value of 940 MeV for the neutron mass within systematic fitting errors.

B. Backgrounds

As was mentioned in the last chapter, various kinematical cuts were used to isolate the $K^-\pi^+$ final sample from other possible charge conserving two prong reactions. Due to resolution smearing and misidentifications, a small number of background events invariably passed these kinematical cuts. Shown in figure 24 is a plot of the missing mass squared opposite the $K^-\pi^+$ using the standard $K^-\pi^+n$ data sample with a very loose missing mass cut imposed. In this plot it is seen that the missing mass structure is quite different above and below the mass of the neutron. It is thus easiest to discuss possible background reactions which contribute in the low missing mass region, and the high missing mass region separately.

Various reactions could possibly contribute to background events in the low missing mass region ($K^-p \rightarrow K^-p$, $K^-p \rightarrow \pi^+\pi^-n$, $K^-p \rightarrow \bar{K}^0\pi^-p$, $K^-p \rightarrow K^-\pi^0p$). The largest source of possible background events in this low missing mass region was the elastic events. As was mentioned in the last chapter the elastic events, as well as the charge exchange \bar{K}^0 decay

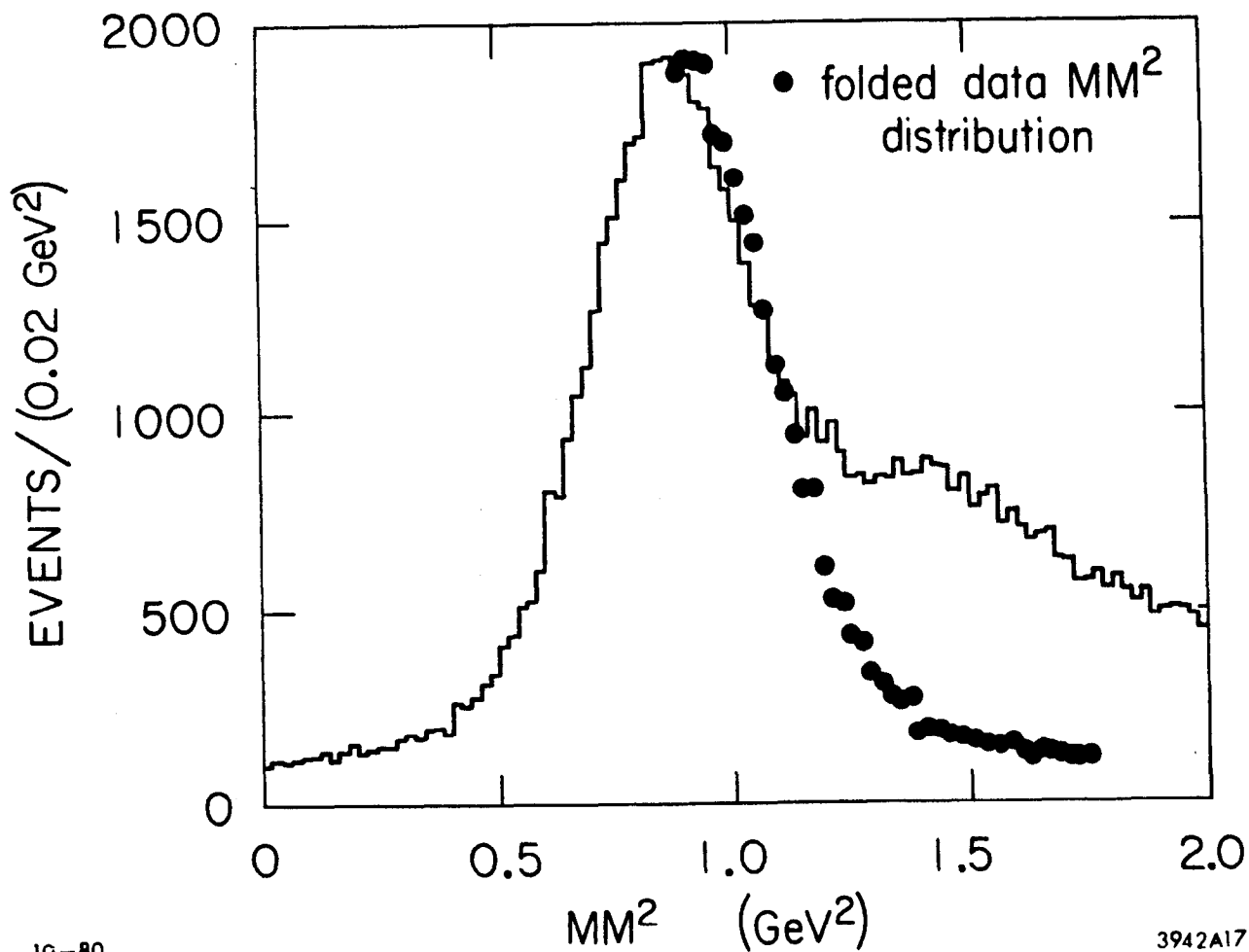


FIG. 24--The missing mass squared spectrum with a folded missing mass squared spectrum superimposed. The symbol ● represents the lower portion of this missing mass squared spectrum folded about the neutron mass squared.

events, were removed explicitly by the PASSMC cuts. A Monte Carlo study was used to show that the elastic cut also effectively removed all $K^-p \rightarrow K^-\pi^0p$ background events. The only other possible source of background in this low missing mass region came from the reaction $K^-p \rightarrow \bar{K}^0\pi^-p$. Simple kinematical arguments suffice to show that almost none of these events would feed into the small t' region in which this data was selected. Thus in this low missing mass region there were extremely few background events.

In the high missing mass region, a large number of reactions could possibly contribute to background events ($K^-p \rightarrow K^-\pi^+\Delta^0$, $K^-p \rightarrow \Lambda^0K^-K^+$, $K^-p \rightarrow \Lambda^0\pi^-\pi^+$, $K^-p \rightarrow \bar{K}^0\pi^-\pi^+n$, $K^-p \rightarrow K^-\pi^0\pi^0n$, etc.). The standard missing mass cut ($0.2 \text{ GeV}^2 < MM^2 < 1.1 \text{ GeV}^2$) imposed on this data removed most of these background events. These background events were also suppressed by the fact that all events containing nonneutral decays of excited baryons were rejected in the event topology selection. Tight vertex requirements also served to suppress \bar{K}^0 and lambda decays as backgrounds in the final $K\pi n$ data sample. We have used two separate methods in order to estimate the amount of background present from these high missing mass background events in our final $K\pi n$ data sample.

The first method is demonstrated in figure 24. Using the fact that there was very little background in the low missing mass region, and that resolution smearing was very nearly symmetric in the missing mass squared, the low missing mass spectrum was folded over the upper missing mass spectrum at the neutron mass squared. Making the standard missing mass cut ($0.2 \text{ GeV}^2 < MM^2 < 1.1 \text{ GeV}^2$), and subtracting the folded spectrum from the actual data spectrum, the results were consistent with no background within statistical errors.

In the second method the leading edge of this missing mass squared spectrum was fit to a Monte Carlo missing mass squared spectrum plus a constant background (for a description of the fit see chapter VII section B.7). The results of this fit predicted a contamination of eight percent background events in the final $K^-\pi^+$ data sample. This estimate is very conservative since most of the background implied by the fit was in the constant background. This linear background was more likely due to a slight misunderstanding of the resolution in the Monte Carlo simulation of $K^-\pi^+$ events, than due to actual background events.

C. Normalization

In order to calculate cross sections from the observed number of events in this experiment, it was necessary to correct the measured number of incident kaons and the observed number of $K\pi$ events for beam losses and event losses. Losses which depended on the specific geometry of a given event were corrected for in this analysis using the LASS Monte Carlo as will be discussed in the following chapter. Shown in table 7 is a list of these losses taken into account by the Monte Carlo. The $K\pi$ data fits shown in the following chapters were explicitly corrected for these acceptance losses. Besides these Monte Carlo corrected losses, two other types of geometry independent losses had to be corrected for in order to calculate cross sections for this data; 1) run dependent losses, and 2) run independent losses. Shown in table 7 is a list of these correction factors, and an estimate of the systematic errors inherent in each correction. To calculate the run dependent

TABLE 7
Normalization Corrections

Correction Type	Correction Value	Systematic Error Estimate
MONTE CARLO		
1) Geometry		
2) Trigger		
3) Tracking Efficiency		
4) Secondary Absorption		
5) Secondary Decay		
6) Resolution Cuts		
7) Kinematical Cuts		
Run Dependent Factors		
1) Target Density	.07082 gm/cm ³	±.0028 gm/cm ³
2) Beam Deadtime/Doubles	1.025	±.013
3) Trigger Deadtime	1.010	±.005
4) Program Failures		
- KFAIL Errors .08 %		
- IFAIL Errors .06 %	.84	±.10
- Beam Reconstruction Failures .02 %		
Run Independent Factors		
1) K ⁻ Decay in Beam	1.028	±.003
2) K ⁻ Absorption in Beam	1.044	±.005
3) Vertex Cut	1.016	±.010
4) MT Target Subtraction	1.00	±.01
5) Software Filter Inefficiency	1.18	±.06

TOTAL EXPOSURE 1004 events/μb
Systematic Error Estimate ±12.5 % (added in quadrature)
±24.5 % (added linearly)

factors, this experimental normalization was calculated and added on a run to run basis. The target density for each run, as was discussed earlier, was measured on a run to run basis using a platinum resistor located at the front of the liquid hydrogen target. The other run dependent factors were calculated using the output monitor and scaler information from the production job. The correction values shown in figure 7 have been averaged in this manner over approximately 1000 runs.

The systematic error estimate for this normalization has been calculated in two ways. In the first method the systematic error estimates of each of the correction factors have been added in quadrature. This addition assumes that the systematic errors were uncorrelated, which is not a well justified assumption. The second method of calculating the total systematic error was to add the individual systematic errors. This method assumes the opposite extreme that all the systematic errors were totally correlated. The actual systematic error is probably somewhere in between these two extremes. In the rest of this thesis the systematic error quoted will be the error calculated by adding these errors in quadrature.

Taking into account all the correction factors listed in table 7, one acceptance corrected event in the following chapters corresponds to:

$$0.00100 \pm 0.00012 \text{ microbarns/(acceptance corrected event)}$$

Figure 25 shows the total cross section calculated in this experiment ** for the reaction $K^-p \rightarrow K^-\pi^+n$ versus other experimental measurements of this total cross section at different incident beam momenta ²². The

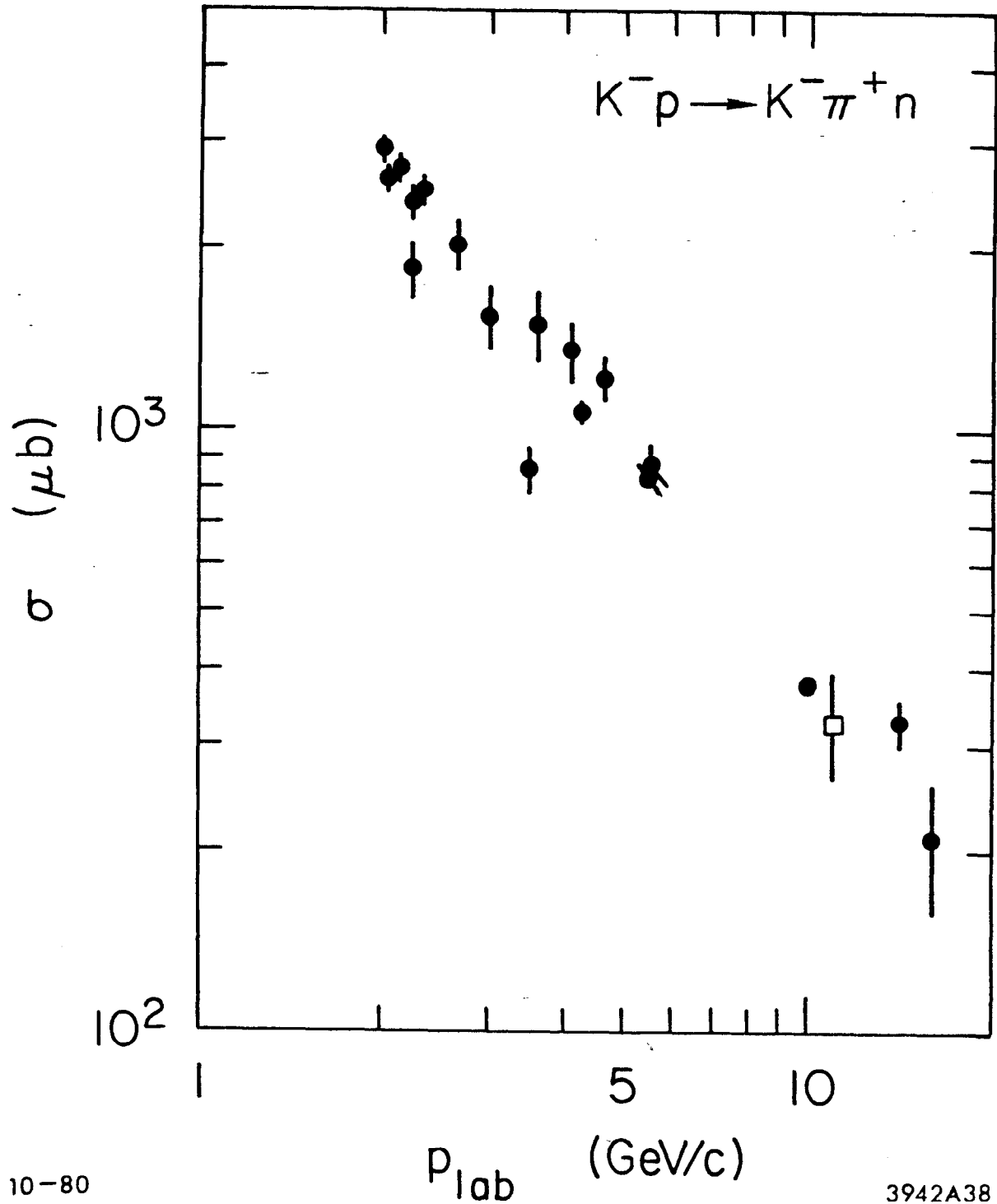


FIG. 25--A sample of total exclusive cross section measurements for the reaction $K^- p \rightarrow K^- \pi^+ n$ versus K^- beam momentum. The cross section measured in this experiment is represented by the symbol \square

total $K^-p \rightarrow K^-\pi^+n$ cross section calculated in this experiment is seen to agree quite well with these other experimental cross sections.

** Since we have performed acceptance corrections to our data only in the region $|t'| < 0.2 \text{ GeV}^2$ and $0.80 \text{ GeV} < M(K\pi) < 2.3 \text{ GeV}$, when calculating the total cross section it was necessary to correct for the number of events outside of this range. In t' we have assumed an $e^{-\theta^2 t}$ distribution and thus corrected our data using t' integrals. In mass we have performed this correction using the average value of the percentage of events seen in the given mass range from a 10 GeV and 16 GeV experiment;

M. Grassler et al., Nucl. Phys. B125, 189 (1977)
and also a 14.3 GeV experiment;

M. Spiro et al., Nucl. Phys. B125, 162 (1977).

Chapter VII

ANGULAR MOMENTS ANALYSIS

The central aim in this thesis was to extract the K^* resonance structure from our standard $K^-p \rightarrow K^-\pi^+n$ raw data sample. As was shown using the raw $K\pi$ invariant mass plots, this extraction entailed the understanding of the angular dependence of the $K\pi n$ data, as well as the invariant mass structure of this data. The selected $K\pi n$ data sample presented in these $K\pi$ invariant mass plots was also biased by the various acceptance losses present in the LASS spectrometer. It was thus also necessary to correct this observed raw $K\pi$ data for acceptance losses before the K^* resonance structure could be fully understood.

The observed distribution function of the raw $K\pi n$ data sample, P , was related to the $K\pi n$ physics distribution, I , by an acceptance function A :

$$P(M_{K\pi}, t', \cos \theta_j, \phi_j) = A(M_{K\pi}, t', \cos \theta_j, \phi_j) I(M_{K\pi}, t', \cos \theta_j, \phi_j) \quad \text{VII.1}$$

The kinematical dependence of each of these three functions is fully described by the four kinematical variables; $M(K\pi)$, t' , $\cos\theta_j$, and ϕ_j .

In this chapter, a parameterization is first presented for the physics distribution I . The two methods used to fit this parameterization to the raw data are then presented. A discussion is then given on the

general structure of the Monte Carlo program used to calculate the acceptance function A. The method used to calculate this acceptance function is then discussed. Lastly, acceptance corrected fits to this $K^-p \rightarrow K^-\pi^+n$ data will be presented.

A. Angular Moments Fitting Methods

In this analysis, the $K\pi n$ physics distribution function, I, was parameterized by expanding this function in spherical harmonics. Thus:

$$I(\Omega, \mathbf{x}) = \sum_{l m}^{\infty \infty} (4\pi)^{-1/2} t_{lm}(\mathbf{x}) Y_{lm}(\Omega)$$

$$\mathbf{x} = M_{K\pi}, t'$$

$$\Omega = \cos \theta_J, \phi_J$$
VII.2

where the $t_{lm}(\mathbf{x})$ terms are here defined as the acceptance corrected angular moments. This parameterization summed to all orders in l and m is quite general, but several restrictions were made on the above sum in this analysis.

First parity conservation is known to rule out the presence of the imaginary parts of any spherical harmonics in the above sum²³. Applying this restriction to the spherical harmonic sum yielded:

$$I(\Omega, \mathbf{x}) = \sum_{l m \geq 0}^{\infty \infty} (4\pi)^{-1/2} t_{lm}(\mathbf{x}) (2 - \delta_{m0}) \text{Re}(Y_{lm}(\Omega))$$
VII.3

where δ_{m0} is a Kronecker delta, and the sum over m is restricted to only positive values of m .

The assumption was also made in this analysis that all values of l were less than some l_{\max} in the above sum. Likewise all values of m were limited to less than some m_{\max} . Only terms with m equal to zero would have been present if the $K^-p \rightarrow K^-\pi^+n$ reaction had been mediated solely by pion exchange. This was approximately true at small t' ($|t'| < 0.2 \text{ GeV}^2$), and in the later fit process it was shown experimentally that very few m terms were needed to describe this $K\pi n$ data. The restriction on l came from the observation that at low $K\pi$ invariant mass no high spin objects resonate in the outgoing $K\pi$ system. The physics under these circumstances should be representable by a finite number of l terms. This was indeed found to be the case in later experimental data fitting to the angular moments, $t_{lm}(x)$.

Fits to this spherical harmonic sum using the standard $K\pi n$ data sample were performed in small $M(K\pi)$ and t' bins. Integrating $I(\Omega, x)$, $t_{lm}(x)$, and $P(\Omega, x)$ over a given small bin, the following functions could be defined within this bin:

$$\begin{aligned}
 I(\Omega) &= \int_{\Delta m}^{\Delta m} I(\Omega, x) dx \\
 P(\Omega) &= \int_{\Delta m}^{\Delta m} P(\Omega, x) dx \\
 t_{lm} &= \int_{\Delta m}^{\Delta m} t_{lm}(x) dx
 \end{aligned}
 \tag{VII.4}$$

where the integral over dx refers to the integral over this small $M(K\pi)$ and t' bin. With these definitions, and the l and m restrictions from the previous paragraph, the spherical harmonic sum became:

$$I(\Omega) = \sum_{l=0}^{l_{\max}} \sum_{m=0}^{m_{\max}} (4\pi)^{-1/2} t_{lm} (2 - \delta_{m0}) \text{Re}(Y_{lm}(\Omega)) \quad \text{VII.5}$$

Within this given $M(K\pi)$ and t' bin an acceptance function was then defined by the equation:

$$P(\Omega) = A(\Omega) I(\Omega) \quad \text{VII.6}$$

The fitting of the physics distribution, I , then reduced to fitting the constant t_{lm} 's, using equations VII.5 and VII.6, to the standard $K\pi$ data sample within these small $M(K\pi)$ and t' bins.

Theoretically given an extremely large sample of $K\pi$ events, the data could have been sliced into an extremely fine $M(K\pi)$ and t' grid, and the t_{lm} 's would then have been fit in these small bins. Due to the finite statistics of this experiment though, fits to the raw $K\pi$ data were performed in two different ways depending on the physics that needed to be extracted. To extract the mass dependence of these angular moments, t_{lm} , a single t' bin was chosen ($|t'| < 0.2 \text{ GeV}^2$), and the $K\pi$ invariant mass was binned in multiple small mass bins (typically 40 MeV wide). To extract the t' dependence of these moments, the opposite approach was taken. The raw $K\pi$ data was first binned into large mass bins (typically 120 MeV wide), and these mass bins were sliced into small t' bins (typically .02 GeV^2 wide) in the other dimension. The

t_{1m} 's in both cases were then fit as constants within these given mass and t' bins, and the desired dependence of these angular moments was then plotted.

In this analysis, two separate methods were used to fit the acceptance corrected angular moments, within these small $M(K\pi)$ and t' bins, to the raw $K\pi\pi$ data; 1) the maximum likelihood method, and 2) the moments method. Both methods were shown to give the same corrected angular moments for this data within errors. These methods will be described in the next two subsections.

1. Moments Fitting Method

The first method used to fit the acceptance corrected angular moments, t_{1m} , to the raw $K\pi\pi$ data in a given small mass and t' bin was the moments method. In order to discuss this fitting method it is first necessary to manipulate a few equations. By substituting equation VII.5 into equation VII.6, multiplying by $(2-\delta_{m0})\text{Re}(Y_{1,m}(\Omega))$, and integrating the result over 4π in the Jackson angles, equation VII.6 becomes:

$$\sum_{l_{\max} m_{\max}}^{l_{\max} m_{\max}} (4\pi)^{-1/2} (2 - \delta_{m0}) (2 - \delta_{m'0}) \int \text{Re}(Y_{1m}(\Omega)) \text{Re}(Y_{l'm'}(\Omega)) A(\Omega) d\Omega$$

VII.7

$$t_{1m} = \int P(\Omega) (2 - \delta_{m0}) \text{Re}(Y_{1m}(\Omega)) d\Omega$$

Defining the matrices:

$$A_{lm'l'm'} = \int (4\pi)^{-1/2} (2 - \delta_{m'0}) (2 - \delta_{m'0}) \operatorname{Re}(Y_{lm}(\Omega)) \operatorname{Re}(Y_{l'm'}(\Omega)) A(\Omega) d\Omega \quad \text{VII.8}$$

$$M_{l'm'} \equiv \int P(\Omega) (2 - \delta_{m'0}) \operatorname{Re}(Y_{l'm'}(\Omega)) d\Omega \quad \text{VII.9}$$

Equation VII.7 then reduces to the simple form:

$$\sum_{l \geq 0}^{l_{\max}} \sum_{m \geq 0}^{m_{\max}} A_{lm'l'm'} t_{lm} = M_{l'm'} \quad \text{VII.10}$$

This simple equation forms the basis of the moments fitting method.

In practice the integral $A_{lm'l'm'}$ were calculated using Monte Carlo events, as will be discussed in section C of this chapter. The $M_{lm'l'm'}$ integrals were calculated by using the raw data sample passed through final $K\pi\pi$ data cuts:

$$M_{l'm'} \cong \sum_{i=1}^N (2 - \delta_{m'0}) \operatorname{Re}(Y_{l'm'}(\Omega_i)) \quad \text{VII.11}$$

where the sum was over the N $K\pi\pi$ data events in the given small $M(K\pi)$ and t' bin.

With the $A_{1m1,m}$, and $M_{1,m}$ matrices determined, equation VII.10 consisted of N equations in M unknowns. A solution for the t_{1m} 's was possible as long as the number of equations was greater than or equal to the number of unknowns.

Once the t_{1m} 's had been calculated using equation VII.10 it was necessary to calculate the statistical error on these angular moments. The correlated statistical error, $D_{1m1,m}$, on the matrix M_{1m} was given by the expression:

$$D_{1m1,m} \cong \sum_{i=1}^N (2-\delta_{m'0}) \operatorname{Re}(Y_{1m}(\Omega_i)) (2-\delta_{m0}) \operatorname{Re}(Y_{1m}(\Omega_i)) \quad \text{VII.12}$$

The error matrix $D_{1m1,m}$ could then be transformed to give the error matrix E for the t_{1m} 's. In matrix notation:

$$E = A^{-1} D (A^{-1})^{\dagger} \quad \text{VII.13}$$

Since the matrices A and D were easily calculated, the t_{1m} error matrix was thus determined.

In practice the solutions to the determined set of equations VII.10 in this analysis were calculated using a modified version of a FORTRAN program developed by G.W.Brandenburg²⁴. The raw $K\pi n$ data sample from the mini-DST, in a given small $M(K\pi)$ and t' bin, was first passed through the final data cuts in the routine PASSMC in this program. Passing events were then used to calculate the M_{1m} matrix. The

acceptance matrix $A_{l_m l, m}$, which had been calculated using Monte Carlo events, was then read into the program. Using matrix inversion techniques the determined set of equations VII.10 was then solved. In performing this calculation, an exactly determined set of equations was always used since no extra information could be gained by overdetermining this system of equations ²⁵. Equations VII.12 and VII.13 were then used to calculate the error on these resulting angular moments. The moments fitting method thus calculated the t_{l_m} 's, and the t_{l_m} error matrix for each given mass and t' bin.

The moments fitting method was mainly used in this analysis as a secondary check on the angular moment fits produced using the maximum likelihood fitting procedure (see chapter VII section F). The final angular moments fits performed in this analysis used the maximum likelihood fitting method.

2. Maximum Likelihood Fitting Method

The second method used in this analysis to fit the acceptance corrected angular moments, t_{l_m} , to the raw $K\pi\pi$ data within a given small $M(K\pi)$ and t' bin, was provided by the maximum likelihood method. Once again it is necessary to manipulate a few equations before discussing this procedure. Defining the expected number of $K\pi\pi$ events in a given small $M(K\pi)$ and t' bin by:

$$F = \int A(\Omega) I(\Omega) d\Omega$$

VII.14

The likelihood distribution function for the N $K\pi\pi$ data events in this bin is given by the expression:

$$L = \left[\prod_{i=1}^N \frac{P(\Omega_i)}{F} \right] \frac{F^N}{N!} e^{-F} \quad \text{VII.15}$$

where the term within the brackets is merely the normalized probability of the given event distribution, and the term outside of the brackets is the Poissonian probability for the overall normalization of $I(\Omega)$.

Now the acceptance function $A(\Omega)$ can be expanded in spherical harmonics as:

$$A(\Omega) = \sum_{l=0}^{\infty} \sum_{m \geq 0}^{\infty} \sqrt{4\pi} a_{lm} \operatorname{Re}(Y_{lm}(\Omega)) + \sqrt{4\pi} s_{lm} \operatorname{Im}(Y_{lm}(\Omega)) \quad \text{VII.16}$$

Performing some algebra and making use of the orthogonality properties of spherical harmonics, the following loglikelihood function results:

$$w = \log(L) = \sum_{i=1}^N \log \left(\sum_{l=0}^{l_{\max}} \sum_{m \geq 0}^{m_{\max}} t_{lm} (2 - \delta_{m0}) \operatorname{Re}(Y_{lm}(\Omega_i)) \right) - \sum_{l=0}^{l_{\max}} \sum_{m \geq 0}^{m_{\max}} t_{lm} a_{lm} \quad \text{VII.17}$$

Where the sum is over the N $K\pi\pi$ data events within the given $M(K\pi)$ and t' bin. This function forms the basis of the maximum likelihood fitting method. The most probable value of the t_{lm} terms was found by maximizing this loglikelihood function. The a_{lm} 's were calculated by Monte

Carlo techniques, as will be described in section C of this chapter. Note that the imaginary acceptance moments, s_{lm} , did not have to be known, and the real acceptance moments, a_{lm} , needed to be known to order l_{max} and m_{max} , in order to calculate this loglikelihood function.

Now finally the error matrix E for the t_{lm} 's was given in matrix notation by:

$$E = D^{-1} C (D^{-1})^{\dagger} \quad \text{VII.18}$$

where:

$$D_{lm'l'm'} = \frac{\partial w}{\partial t_{lm} \partial t_{l'm'}} \quad \text{VII.19}$$

and:

$$C_{lm'l'm'} \cong \sum_{i=1}^N \frac{(2-\delta_{m'0}) \operatorname{Re}(Y_{lm}(\Omega_i)) (2-\delta_{m0}) \operatorname{Re}(Y_{l'm'}(\Omega_i))}{\left\{ \sum_{\substack{l''m'' \geq 0 \\ l''m'' \leq l_{max} m_{max}}} t_{l''m''} (2-\delta_{m''0}) \operatorname{Re}(Y_{l''m''}(\Omega_i)) \right\}^2} \quad \text{VII.20}$$

The maximization of the loglikelihood function in practice was performed by one of two programs. The first program was a modified version of a maximum likelihood fitting program developed by G.W.Brandenburg ²⁶. This program was built around a FORTRAN minimizing program called OPTIME ²⁷. The other minimizing program used to perform these loglikelihood minimizations was written specifically for this analysis using

the FORTRAN minimizing package MINUIT ²⁸. Both programs read the raw $K\pi n$ data sample from the mini-DST, for a given small $M(K\pi)$ and t' bin. Final data cuts were then imposed by calling the routine PASSMC described earlier. The acceptance moments, a_{1m} , which had been calculated using Monte Carlo events, were then read into this program. Using these acceptance moments and the passing data events, the loglikelihood function was calculated. This resulting loglikelihood function was then minimized as a function of the t_{1m} 's. The MINUIT minimization package had the advantage that it could handle non-parabolic errors, but it ran much slower than the OPTIME package. Both programs gave identical t_{1m} 's, and the estimated errors were also shown to be parabolic using the MINUIT maximum likelihood fitting program. Thus the OPTIME package was used to perform all the final angular moments fits in this analysis. The t_{1m} 's and the t_{1m} error matrix for a given $M(K\pi)$ and t' bin were thus calculated.

B. Monte Carlo

1. Overview

In order to calculate the acceptance integrals $a_{1m1,m}$, and a_{1m} , used in the acceptance corrected angular moments fits, a Monte Carlo program was used to mimic the LASS spectrometer acceptance. The general idea behind the LASS Monte Carlo was to generate $K^-\pi \rightarrow K^-\pi^+n$ events, and then track these events through the LASS spectrometer simulating all sources of event losses in this $K\pi n$ analysis. This program calculated

losses in the LASS spectrometer, and the track finding, track fitting, and event selection routines due to:

- 1) geometrical losses
- 2) trigger inefficiencies
- 3) secondary absorption
- 4) secondary decay
- 5) track reconstruction efficiency
- 6) resolution cuts
- 7) kinematical cuts
- 8) PASSMC cuts

A set of Monte Carlo events was then written to magnetic tape with each event tagged as passing or failing the event loss cuts in this Monte Carlo.

The LASS Monte Carlo consisted of multiple complex FORTRAN subroutines. These subroutines performed basically four functions in this Monte Carlo; 1) event generation, 2) geometrical tracking, 3) event reconstruction simulation, and 4) track resolution simulation. Each of these basic sections of the LASS Monte Carlo will be discussed briefly in the next few subsections. For a more complete description of these Monte Carlo routines see reference 29. At the end of this Monte Carlo section checks on the Monte Carlo's ability to simulate the experimental acceptance in this analysis will be presented. Finally the results from Monte Carlo event processing will be used to generally discuss the experimental acceptance and the spectrometer resolution for this analysis.

2. Event Generation

The LASS Monte Carlo event generating routines were written in order to produce a $K^-p \rightarrow K^-\pi^+n$ event sample with a distribution as close to the actual physics distribution as possible. The first step in event generation for a particular Monte Carlo event was the creation of a beam particle, and an interaction vertex. Kinematical parameters of a beam kaon in these Monte Carlo routines were set by reading the fitted position and three momentum, of a processed special (T2) beam trigger, from magnetic tape. A randomized proper mix of these processed data beam tracks had been stored on magnetic tape, so that an unbiased Monte Carlo beam phase space matching the beam phase space of our selected $K\pi n$ data sample was assured. Once a Monte Carlo beam particle had been calculated, this beam particle was then extrapolated into the LASS liquid hydrogen target, where an interaction vertex was calculated using a random generating function. This random generating function was defined to throw a random z value within the target such that for multiple throws an absorption corrected z distribution was seen within the target.

Once the beam particle and vertex had been created for this given Monte Carlo event, it was necessary to define the $K\pi n$ final state particles produced at this vertex. In producing this final state, the laboratory angle of the recoil neutron about the incident beam direction was calculated randomly. This left the four kinematical variables; $M(K\pi)$, t' , $\cos\theta_j$, and ϕ_j to be calculated for this event. Monte Carlo events in this analysis were always generated in the small $M(K\pi)$ and t' bins in which a given angular moments fit was to be run in. The invariant mass

of the $K^-\pi^+$ Monte Carlo event was then generated randomly within the given $M(K\pi)$ and t' bin. The t' distribution for this event was produced within this $M(K\pi)$ and t' bin, using a random generating function. Various nonflat distributions in t' were thrown during this analysis. These will be described in more detail in chapter VII section D. Finally the Jackson angles of the outgoing K^- and π^+ particles were generated using another random generating function, which was defined to throw an angular distribution described by the latest acceptance corrected angular moments fit in the given $M(K\pi)$ and t' bin. It should be noted that t' , $M(K\pi)$ and the Jackson angles were all generated independently of each other, which was a very good approximation to the physics within each given $M(K\pi)$ and t' bin.

Once the four kinematical variable had been generated for this event, the four momenta of the outgoing K^- and π^+ particles were calculated from these variables. Since the recoil neutron was undetectable in the LASS spectrometer, this particle was ignored in the rest of the Monte Carlo processing. The generated four momenta of the K^- and π^+ particles were then energy lossed to correct for energy losses in the liquid hydrogen target and target jackets. Thus at the end of the Monte Carlo event generation routines, a Monte Carlo event had been defined.

3. Geometrical Tracking

The next job of the LASS Monte Carlo was to define geometrical trajectories of the K^- and π^+ Monte Carlo interaction particles in the spectrometer. Particle tracking in the solenoid magnet consisted of

calculating track helices using each particles four momentum. These helices were then extrapolated to the downstream end of the solenoid where a fourth-order Runge Kutta stepping procedure, with a magnetic field map, was used to track the particles across the solenoid fringe field and into the twist region. Tracking in the twist region was done assuming straight line trajectories, and once again a fourth-order Runge Kutta stepping procedure, with a dipole magnetic field map, was finally used to track Monte Carlo particles across the dipole and into the downstream region. In the downstream region tracks were once again extrapolated as straight lines.

Both tracks in each event were checked for collisions with the physical boundaries of the spectrometer (solenoid walls, dipole walls, chamber apertures, etc.) during this tracking procedure. The geometrical tracking of the given particle was stopped if its track intersected any one of these solid physical boundaries (total absorption was assumed). Two random mechanisms could also stop the geometrical tracking of a particle in this Monte Carlo; 1) particle absorption, and 2) particle decay.

Particle absorption was taken into account in this Monte Carlo by first dividing the spectrometer into four sections; 1) the cylindrical chambers, 2) the solenoid plane chambers, 3) the C1 Cherenkov counter, and 4) the dipole chambers. An absorption probability was calculated for each of these sections according to the amount of material a particle would pass through in traversing these sections. As a particle was tracked past each of these positions, a random number was thrown; and this random number, combined with the absorption probability, defined

whether the geometrical tracking of this particle was stopped at this position or not.

Absorption of interaction particles in the liquid hydrogen target, or target jackets was treated slightly differently. The probability of each particle being absorbed in the target, and target jackets was first calculated separately. The product of these absorption probabilities for each charged interaction track then gave a target absorption probability for the entire event, w_i . This w_i was then stored for each event.

To account for particle decays, a decay length (important only for K^- interaction particles) was generated for the K^- and π^+ outgoing particle tracks. This decay length was calculated using a random number, and the known lifetime of each particle. If the decay position of a given particle was reached, the geometrical tracking of this particle was once again stopped. This was a slightly naive way to treat decays since secondary charged particles do emerge from particle decays, but this procedure gave a first order correction for the data track reconstruction code's ability to treat charged particle decays.

Two other small effects were ignored in the geometrical tracking of the K^- and π^+ particles through the spectrometer in this Monte Carlo; 1) energy losses outside of the target, and 2) multiple scattering both inside of the target, and outside of the target. The addition of either of these effects would have greatly complicated the Monte Carlo track finding routines, and both effects were shown to be quite small.

As a Monte Carlo particle was tracked past each device in the spectrometer, information was stored away giving whether the given particle

had passed through each chamber's active area or not. Solenoid coordinates in intersected solenoid devices were also stored away for later use. Thus a bank of "possible" chambers hits was formed for each track.

4. Event Reconstruction

The purpose of the Monte Carlo event reconstruction routines was to simulate event reconstruction and geometrical losses in the LASS data track finding routines. The first step in this process was to mimic the device inefficiencies for each chamber and counter in the LASS spectrometer. Using the experimental chamber efficiencies and throwing random numbers, a set of "actual" chamber hits was calculated from the "possible" chamber hit banks for each track. The chamber efficiencies used in this calculation were tracking efficiencies for each device taken from the production monitor output, averaged over all data runs (see chapter V section A). The "actual" hit banks along with geometrical information for each track gave enough information to reliably simulate the track finding cuts in the three data track finding algorithms (see chapter III). In this simulation process, a Monte Carlo track was flagged as being findable in either the dipole track finding algorithm, the plane track finding algorithm, or the cylindrical track finding algorithm; or else the track was flagged as being unreconstructable. If either track in a given event was flagged as unreconstructable, an event failure flag was set, and this event was written out to magnetic tape.

All geometrical, absorption, and decay losses of events in the spectrometer were correctly accounted for by these event reconstruction

program cuts. For instance, a particle in the Monte Carlo which was calculated to decay half way down the solenoid magnet would not have enough solenoid intersections in its "actual" chamber hit banks to be flagged as reconstructable in any of these three track finding routines. Consequently this event would have failed to pass the Monte Carlo.

Once an event had passed these event reconstruction cuts, trigger cuts were then imposed on these Monte Carlo events. These trigger cuts consisted of the main (T0) trigger requirement discussed previously. The Monte Carlo imposed these trigger requirements by using the "actual" chamber hit banks. For an event failing this trigger, the event failure flag was once again set and this event was written out to magnetic tape.

5. Track Resolution

After a Monte Carlo event had passed through the Monte Carlo event reconstruction routines, it had been classified as having triggered the spectrometer, and both outgoing tracks had been classified as findable in one of the three data track finding algorithms. The next job of this Monte Carlo program was the simulation of the spectrometer's track resolutions for the Monte Carlo beam particle, and the two outgoing interaction particles.

A major reason to require accurate Monte Carlo track resolutions was to simulate the resolution dependent cuts imposed on the $K\pi n$ data sample by the routine PASSMC. The most obvious of these resolution dependent cuts in PASSMC was the missing mass cut ($0.2 \text{ GeV}^2 < MM^2 < 1.1 \text{ GeV}^2$) used to isolate the $K^-p \rightarrow K^-\pi^+n$ reaction from other possible two

prong events. In this spectrometer the missing mass resolution was a strong function of the four kinematical variables; $\cos\theta_j$, ϕ_j , $M(K\pi)$, and t' . This missing mass cut then acted like an acceptance cut, since it cut away different amounts of real $K\pi n$ data in different kinematical regions. Thus the Monte Carlo had to accurately simulate this missing mass resolution as a function of the four kinematical variables in order to correct for this acceptance loss.

The basic idea behind the Monte Carlo track resolution simulation was to properly offset the Monte Carlo "physics" tracks generated by the Monte Carlo event generating routines, and thereby create a set of "measured" tracks. This track resolution simulation was performed separately on the beam particle and the two outgoing interaction particles.

First, a resolution smeared ("measured") beam track was calculated from the Monte Carlo ("physics") beam track for a given event. When the throwing routines generated this "physics" beam particle the fitted position, angle, and beam track error matrix were read from a magnetic tape of processed special (T2) beam triggers, as was mentioned previously. Using elements from this beam track error matrix and a random number generator, angular and positional offsets were calculated to properly shift the "measured" beam track parameters from the "physics" beam track parameters. The absolute momentum of this "measured" beam track was calculated by shifting the "physics" beam track's momentum using a random Gaussian generator. The width of the Gaussian was chosen to take into account measurement errors in the P-hodoscope as well as small random drifts in the beamline magnets during this experiment. This procedure then yielded a properly smeared ("measured") beam track.

Once the resolution smeared beam track had been calculated in the Monte Carlo, the next job of the Monte Carlo routines was to calculate properly smeared ("measured") outgoing K^- and π^+ track parameters. In the data all track parameters were measured in the solenoid with the exception of the absolute momentum on tracks found in the dipole track finding algorithm. It is convenient to discuss the Monte Carlo simulation of dipole momentum resolution, before discussing the simulation of resolution for solenoid measured track parameters.

A study of tau decay triggers and K_p elastics taken during this experiment showed that the dipole measured momentum distribution, for fixed momentum dipole tracks, was consistent with a Gaussian distribution. The width of this Gaussian for tracks with a momentum, P , was fit in this study to a simple polynomial form yielding:

$$\sigma_p = 6.53 \times 10^{-4} P^2 + 1.15 \times 10^{-3} P$$

where P is the momentum of the dipole track in GeV/c

For the Monte Carlo tracks flagged as found in the dipole track finding algorithm, the absolute momentum of the "measured" track was calculated by adding a random Gaussian offset of the above form to the absolute momentum of the associated "physics" track.

Resolution on track parameters measured in the solenoid could not be simulated as simply as either the dipole momentum resolution, or the beam track parameter resolutions. Resolutions on solenoid measured track parameters depended strongly on the number and type of solenoid

coordinates on a given track, as well as the given particles trajectory through the solenoid. Simulation of the resolution on track parameters in the solenoid was further complicated by the fact that a geometrically constrained fit had been performed on our data to improve this resolution (see chapter IV section G). A more complex method, mimicking the data analysis' geometrically constrained fit, was thus used in this Monte Carlo simulation.

As was mentioned previously solenoid coordinates as well as "actual" chamber hit banks for both outgoing interaction particles were stored away during Monte Carlo geometrical tracking. Using experimentally derived chamber errors (see chapter IV section I) and a random Gaussian generator, a new set of resolution smeared solenoid track coordinates for each track was formed. Just as in the data event fitting, these resolution smeared solenoid track coordinates, as well as the "fitted" beam parameters and beam error matrix, formed the input to the subroutine MVFIT. The routine MVFIT then performed geometrically constrained fitting to the Monte Carlo events in a manner identical to the procedure outlined in chapter IV section G. The only exception to this statement is the fact that the chamber errors were not corrected for multiple scattering, since the Monte Carlo program did not simulate multiple scattering. The MVFIT error handling in both the Monte Carlo and the data were also the same. A certain number of Monte Carlo events also failed to converge in MVFIT, and this small percentage of events were immediately flagged as bad and written to magnetic tape. A cut was also made on the MVFIT fit confidence level in order to simulate the confidence level cut made on the data. The output of MVFIT then yielded

"measured" three momentum for the Monte Carlo K^- and π^+ particles along with a resolution smeared vertex and an MVFIT error matrix.

In the data processing, the output MVFIT error matrix was used to define resolution cuts on the data tracks to remove poorly measured tracks from the $K\pi n$ data sample. These cuts were simulated in the Monte Carlo in exactly the same manner. The Monte Carlo output MVFIT error matrix was used to calculate a momentum resolution error on each Monte Carlo track. Identical cuts were made on this momentum resolution error as were made on the data sample (see chapter V section E).

Thus the Monte Carlo track resolution routines yielded "measured" quantities for a given event's beam particle, vertex, and two outgoing interaction particles. A set of cuts on these quantities (or quantities derived from these quantities) thus simulated an identical set of cuts performed on the data.

6. Monte Carlo Output

At the end of the Monte Carlo processing of a given event, a record consisting of less than 60 32-bit IBM words was written out to magnetic tape. This 60 word record consisted of "measured" kinematical variables, "measured" beam track three momentum, the "measured" three momenta of the two outgoing particles, and various geometrical quantities needed to define the final Monte Carlo event. This Monte Carlo output record was chosen to be almost identical in form to the data mini-DST record mentioned in chapter V section A. The only difference between these two output records were two words added to the Monte Carlo record; the

first word flagging whether a Monte Carlo event was rejected in the Monte Carlo or not, and the second being the target absorption weight, w_i . The data and Monte Carlo output records were chosen to be nearly identical so that the set of final cuts imposed by the routine PASSMC on the data events could also be imposed on the Monte Carlo events. As was mentioned before the PASSMC cuts were imposed on the data events read from the mini-DST before these events were analysed. In a similar fashion the same PASSMC cuts were imposed on the Monte Carlo events before these events were used in any acceptance calculation.

7. Monte Carlo Checks

Various checks were made, in this analysis, to assure that the Monte Carlo accurately simulated the event losses, and the spectrometer resolution. Some of these checks are discussed separately in section F of this chapter. Two more checks of the Monte Carlo simulation will be discussed here.

Once the final angular moments and t' fits to the standard $K\pi\pi$ data sample had been performed, a set of Monte Carlo events were generated with these fit distributions. The number of events thrown in each bin was taken to be proportional to the acceptance corrected number of data events in these bins. The resulting Monte Carlo event sample was then passed through the final event selection cuts (PASSMC cuts), and the passing events were histogrammed. These histograms were then compared with histograms of the standard $K\pi\pi$ data sample. No significant deviation of the Monte Carlo distributions from the data distributions was

seen. In particular the ratio's of cylinder found, plane found, and dipole found tracks was seen to agree to a few percent between the two samples.

As a check on the Monte Carlo simulation of the track resolution, the $K^-p \rightarrow K^-\pi^+\chi^0$ missing mass squared spectrum of the final $K\pi n$ data sample was fit. In performing this fit, the Monte Carlo event sample discussed in the last paragraph was used to generate a Monte Carlo resolution smeared missing mass squared spectrum. This Monte Carlo spectrum plus a linear background was then fit to the data missing mass squared spectrum. In performing this fit the free parameters in the Monte Carlo resolution spectrum consisted of a normalization parameter, an offset parameter, and a linear scale parameter. The fit was performed in the missing mass squared region from 0.2 GeV^2 to 0.90 GeV^2 .

Shown in figure 23 is this missing mass squared fit. The error bars shown on the data points represent statistical errors in both the data and the Monte Carlo event samples added in quadrature. The chi-square of this fit was 33 for 36 degrees of freedom. The linear scale factor had a final fit value of 1.10. Thus the Monte Carlo resolution was 10 % better than that of the real data. The flat background in this fit had a height about 4 % as high as that of the neutron peak. This background probably indicated a slight misunderstanding of the poorly measured solenoid tracks in the Monte Carlo. This discrepancy was small enough to cause no observable problem in the calculation of the spectrometer acceptance.

8. Spectrometer Resolution

As was shown in the last subsection, the LASS Monte Carlo describes the data missing mass squared spectrum quite well. The LASS Monte Carlo then could be used to investigate the spectrometer resolution in our four kinematical variables; $M(K\pi)$, t' , $\cos\theta_j$, and ϕ_j . Unfortunately since the spectrometer resolution is a very complicated non-Gaussian function of these four kinematical variables, no obvious means exists to display this resolution systematically. Using Monte Carlo events then, a rough estimate of our resolution in the four kinematical variables over many different kinematical regions yielded:

Variable	Resolution
$M(K\pi)$	4 MeV - 15 MeV
t'002 GeV ² - .006 GeV ²
$\cos\theta_j$003 - .015
ϕ_j03 radians - .05 radians

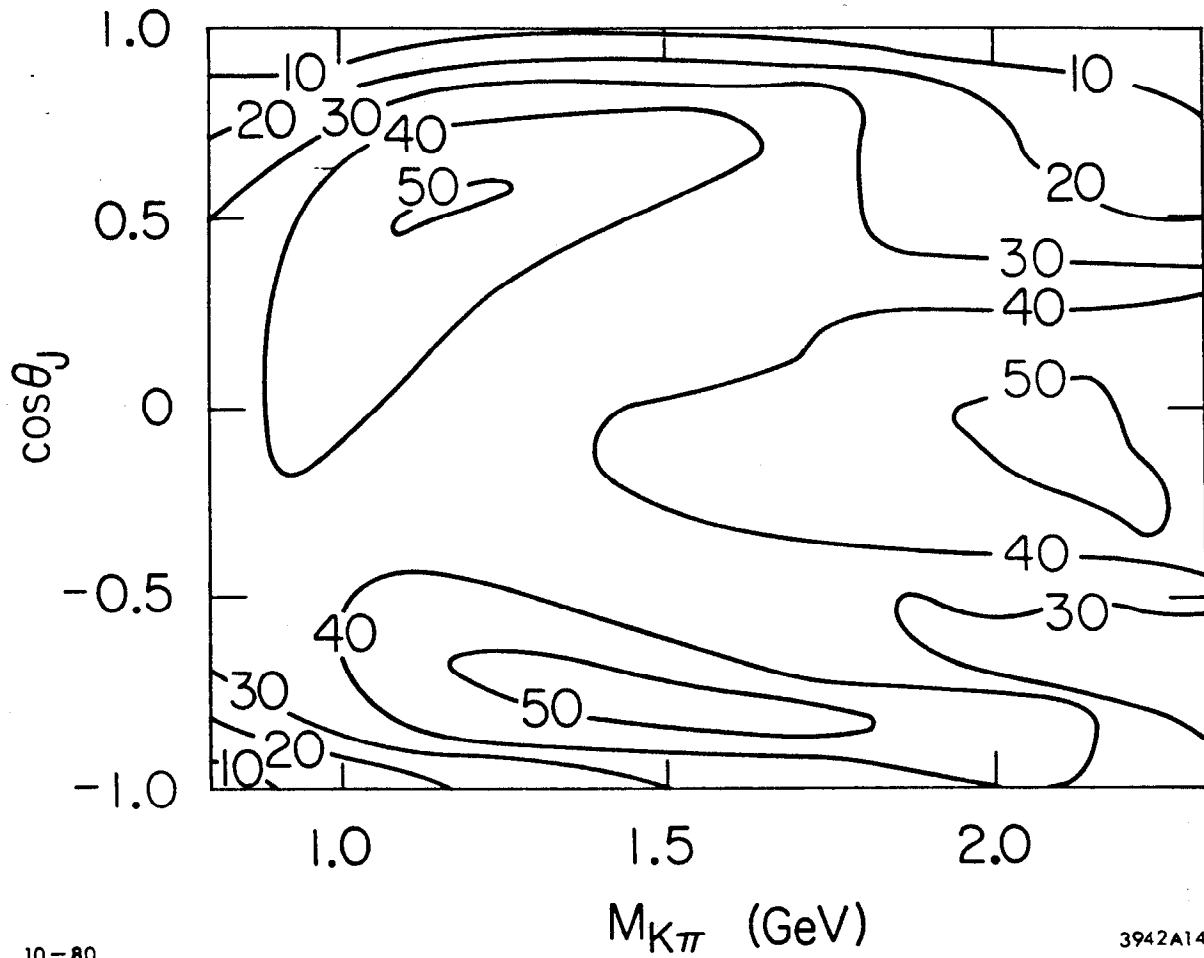
When correcting resonance widths in this paper for resolution smearing in mass, Monte Carlo events were generated in the region of this resonance with a distribution as close to the actual physics distribution as possible. Histograms of the difference between $M(K\pi)$ "physics" and $M(K\pi)$ "measured" from these Monte Carlo events were then used to estimate the $M(K\pi)$ resolution in the region of this resonance.

9. Spectrometer Acceptance

To end this section it seems appropriate to show a graph of the Monte Carlo generated acceptance function, $A(\Omega)$. Shown in figure 26 is a contour plot of this acceptance plotted as a function of $\cos\theta_j$ and $M(K\pi)$. This plot was generated using the final set of Monte Carlo events discussed in section D of this chapter. Monte Carlo events used in generating this function were first passed through the final $K\pi n$ data sample cuts (PASSMC), and were also restricted to the $|t'|$ region less than $.2 \text{ GeV}^2$.

Trigger cuts and resolution cuts (mainly the missing mass cut) played the most important role in limiting the acceptance in this analysis. One of the most prominent features in figure 26 is the drop in acceptance in the forward and backward $\cos\theta_j$ region at low $K\pi$ invariant mass. This effect was due to the fact that at low mass in the forward (backward) $\cos\theta_j$ region the K^- (π^+) was so far forward in the laboratory frame that it quite often passed through the hole in the 1.5 PWC cluster logic. Since the 1.5 PWC cluster logic signal was necessary to trigger the spectrometer, such events were not seen. This effect lessened at higher mass due to larger $K\pi$ center of mass energies, and thus greater $K\pi$ laboratory angles.

At a mass of $\sim 1.8 \text{ GeV}$ and above, in the forward $\cos\theta_j$ region, figure 26 once again shows a marked drop in the acceptance. In this case the laboratory angle of the π^+ was large enough so that this particle missed the active area of the 1.5 PWC completely, and thus did not trigger the spectrometer. This effect also came into play in the backward



10-80

3942A14

FIG. 26--A Monte Carlo generated acceptance contour plot in the variables $M(K\pi)$ and $\cos\theta_j$. The numbers on the contour lines represent the percentage of passing events in the given kinematical region.

$\cos\theta_j$ region at slightly higher mass. At the very highest mass, events were also lost in the central $\cos\theta_j$ region. Here the K^- and π^+ particles were produced with such large laboratory angles that both particles missed the TOF hodoscope, also required in this T0 trigger.

The only other obvious structure in this plot is the two valley structure in the central $\cos\theta_j$ region at intermediate masses. This effect was caused the removal of events from this central region by resolution cuts.

In summary, the spectrometer acceptance is seen to be nonzero in nearly all regions of $M(K\pi)$ and $\cos\theta_j$, and is large and uniform in all but the extreme forward and backward $\cos\theta_j$ regions. The acceptance is also seen to be smoothly varying, and thus was easily corrected for in the fitting of this final data sample.

C. Calculation of the Acceptance Moments

In order to perform the acceptance corrected angular moments fits to the $K\pi\pi$ data, the moments and maximum likelihood fitting methods each required the calculation of various acceptance function integrals. In the moments fitting method these integrals were of the form:

$$A_{l_1 m_1 l_2 m_2} = \int (4\pi)^{-1/2} (2 - \delta_{m_1 0}) (2 - \delta_{m_2 0}) \operatorname{Re}(Y_{l_1 m_1}(\Omega)) \operatorname{Re}(Y_{l_2 m_2}(\Omega)) \quad \text{VII.21}$$

$$A(\Omega) d\Omega$$

within a small $M(K\pi)$ and t' bin

In the maximum likelihood fitting method these acceptance integrals were of the form:

$$a_{lm} = (4\pi)^{-1/2} \int A(\Omega) (2-\delta_{m0}) \operatorname{Re}(Y_{lm}(\Omega)) d\Omega \quad \text{VII.22}$$

within a small $M(K\pi)$ and t' bin

Where the integral form for the a_{lm} 's has been calculated by merely using the orthogonality of the spherical harmonics. The a_{lm} 's are here defined as angular acceptance moments.

The first step in calculating the acceptance integrals for a given $M(K\pi)$ and t' bin was to generate a large number of Monte Carlo events within this bin. In this analysis the number of Monte Carlo events thrown in a given mass and t' bin was chosen to be at least ten times the number of acceptance corrected data events within this same bin. In a later study it was checked for several bins that the t_{lm} fit values did not change appreciably when more Monte Carlo events were thrown. Thus the statistical errors in the data dominated over the statistical errors from the calculation of these acceptance moments.

Within this given $M(K\pi)$ and t' bin, the Monte Carlo events were generated flat in mass, nonflat in t' , and according to a spherical harmonic sum of the fitted angular moments in the Jackson angles. The event generating function, $I_{mc}(\Omega)$, integrated over $M(K\pi)$ and t' within the given bin, could then be represented by the properly normalized sum

of these angular moments:

$$I_{mc}(\Omega) = N_{th} \sum_{l \geq 0}^{l_{max}} \sum_{m \geq 0}^{m_{max}} (4\pi)^{1/2} \begin{cases} t_{lm} \\ t_{00} \end{cases} (2 - \delta_{m0}) \operatorname{Re}(Y_{lm}(\Omega)) \quad \text{VII.23}$$

where N_{th} represents the number of Monte Carlo events thrown, and the t_{lm} 's were the angular moments which were used to throw this Monte Carlo within the given $M(K\pi)$ and t' bin.

Equation VII.6 gives the relationship between the acceptance function A , the observed distribution P , and the physics distribution I for our data within a given $M(K\pi)$ and t' bin. Using the Monte Carlo analogs to these data expressions, the Monte Carlo acceptance function was defined by the expression:

$$A_{mc}(\Omega) = \frac{P_{mc}(\Omega)}{I_{mc}(\Omega)} \quad \text{VII.24}$$

where $I_{mc}(\Omega)$ was given by equation VII.23, and $P_{mc}(\Omega)$ was the Monte Carlo observed resolution smeared angular distribution of the passing events thrown in the given $M(K\pi)$ and t' bin. Once again the final data selection cuts in PASSMC have been imposed on these Monte Carlo events. By defining the Monte Carlo acceptance in the above form, resolution smearing in mass and t' has been ignored. Since the final acceptance is a slowly varying function of mass and t' this approximation was well justified. Since the distribution, $P_{mc}(\Omega)$, was resolution smeared in angle, and $I_{mc}(\Omega)$ was not, the acceptance function defined by equation

VII.24 served to correct the $K\pi\pi$ data for resolution smearing in the Jackson angles, as well as for acceptance losses.

With the definition of equation VII.24, equations VII.21-VII.24 can be combined to give Monte Carlo approximations to the two acceptance integral expressions in equations VII.21 and VII.22. In this analysis then, the acceptance integral for the moments fitting method was calculated as

$$A_{lm'l'm'} \approx \sum_{i=1}^{N_{\text{pass}}} \frac{4\pi w_i (2-\delta_{m0}) \text{Re}(Y_{lm}(\Omega_i)) (2-\delta_{m'0}) \text{Re}(Y_{l'm'}(\Omega_i))}{I_{mc}(\Omega_i)} \quad \text{VII.25}$$

The acceptance integral for the maximum likelihood fitting method was calculated as

$$a_{lm} \approx \sum_{i=1}^{N_{\text{pass}}} \frac{\sqrt{4\pi} w_i (2-\delta_{m0}) \text{Re}(Y_{lm}(\Omega_i))}{I_{mc}(\Omega_i)} \quad \text{VII.26}$$

where the sums are over the N_{pass} passing Monte Carlo events, and the w_i are the target absorption probabilities for these events (see Monte Carlo section). The function $I_{mc}(\Omega)$ is given by equation VII.23, and Ω_i is the resolution smeared Jackson angles for the i th Monte Carlo event.

If $I_{mc}(\Omega)$ was ever zero where passing Monte Carlo events were present, then the acceptance integral calculations above would have become indeterminant. In order to keep this from happening fifteen percent of the Monte Carlo events were always thrown flat in the Jackson angles. It was shown later experimentally that the final angular moments fits were not changed within errors by throwing five percent flat versus fifteen percent flat.

D. Angular Moments Fits

In this chapter the moments and maximum likelihood fitting methods, used to fit the acceptance corrected angular moments to the standard $K\pi\pi$ data sample, were presented. To end this chapter these final angular moments will be presented as a function of mass, but first a brief discussion of the data cuts and the iterative procedure used to obtain these final fits will be discussed.

The standard $K\pi\pi$ data sample graphed at the end of chapter V formed the input data sample to the final angular moments fits. For these final fits, the data once again was restricted to the $|t'|$ region less than $.2 \text{ GeV}^2$. This restriction served to emphasize the pion exchange portion of this reaction. In mass, the data sample was divided into 40 MeV bins below 1.800 GeV, and 80 MeV mass bins above this mass. The angular moments fits were performed, and the Monte Carlo events were also generated in these same bins.

These final angular moments fits were performed in the mass region from 0.80 GeV to 2.30 GeV. At masses below .800 GeV the spectrometer acceptance was so low that there were not enough events to support a fit. Above 2.3 GeV in mass it was impossible to obtain convergence of the moments fits in this analysis due to near singularities in the fit correlation matrices. In performing these final fits, the maximum likelihood procedure was used.

The calculation of the acceptance moments, a_{1m} , discussed in the last chapter clearly depended on how the Monte Carlo events were thrown. The best approximation to the acceptance moments was obtained when the

Monte Carlo was thrown with a distribution as close to the acceptance corrected data distribution as possible. This fact necessitated performing the final maximum likelihood fits to the acceptance corrected angular moments iteratively.

In the first iteration, within a given $M(K\pi)$ and t' bin, Monte Carlo events were generated flat in mass, and flat in the Jackson angular variables. The t' distribution of these Monte Carlo events was thrown with a simple exponential fit to experimental data from a previous $K\pi n$ data analysis performed by this group, SLAC experiment E-75 ***. This exponential fit described the data quite well. Acceptance moments were then calculated, and maximum likelihood fits to the standard $K\pi n$ data sample were performed yielding a set of angular moments, t_{1m} , for each separate mass bin.

In the second iteration, the Monte Carlo events were once again thrown flat in mass, and with the exponential dependence in t' described in the last paragraph. In angle the Monte Carlo was thrown according to the spherical harmonic sum of the t_{1m} 's from the previous angular moments fits in each bin. Once again acceptance moments were calculated, and a maximum likelihood fit performed yielding a new set of angular moments.

In the third and final iteration, the Monte Carlo events were thrown flat in mass. The Monte Carlo t' distribution was thrown according to partial wave fits to the t' dependence of the standard $K\pi n$ data

*** These simple exponential fits were performed on the $|t'|$ data from G.W. Brandenburg et al., XVIII International Conference on High Energy Physics (1976), A1-119

sample. This t' dependence is described at the end of section B in chapter VIII. Lastly the Monte Carlo was thrown in angle with the t_{1m} fits from the previous iteration. Acceptance moments were once again calculated, and maximum likelihood fits were performed yielding final values for the angular moments, as well as acceptance moments in each separate mass bin. The angular moments were then compared to those of the second iteration and found to be identical within errors. It was therefore assumed that this iterative procedure had converged.

Shown in figure 27 is a comparison of the final angular moments fit (a) to the data (error bars) as a function of $\cos\theta_j$ in four typical mass bins. The error bars on the data are statistical in nature only. These fit points were calculated, acceptance corrected, and added in a 16×16 $\cos\theta_j - \phi_j$ grid. Within errors the maximum likelihood fits are seen to describe the data quite well in these four different mass regions. These plots along with similar plots in ϕ_j were used to check the quality of all angular moment fits performed in this analysis.

1. Final Angular Moments Presentation

The set of final angular acceptance moments, a_{1m} , used to derive the final set of angular moments in this analysis are shown in figures 28-30. The mass binning used to generate these acceptance moments corresponds to 40 MeV bins below 1.8 GeV, and 80 MeV overlapping bins above 1.8 GeV. The bin to bin fluctuations in these acceptance moments was caused by the statistical uncertainties in the calculation of these acceptance moments. The general structure of these moments is seen to

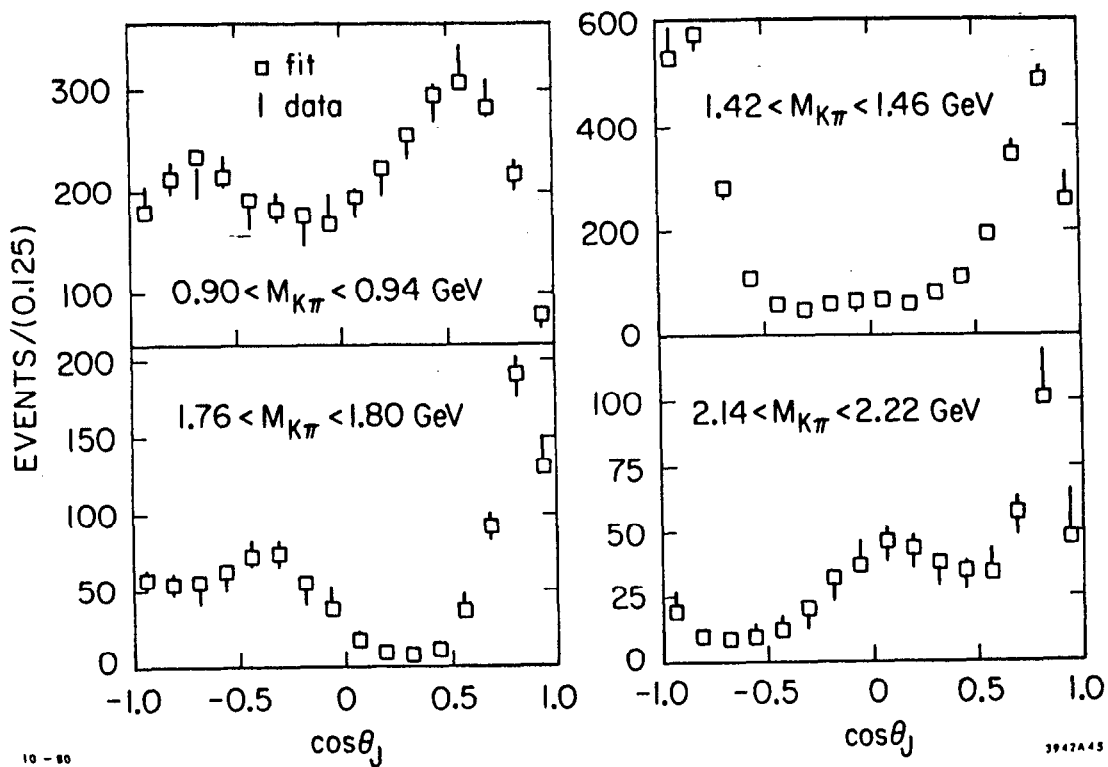


FIG. 27--A comparison of the final angular momentum fits (\square) to the data (error bars) as a function of $\cos\theta_j$ in four typical mass bins.

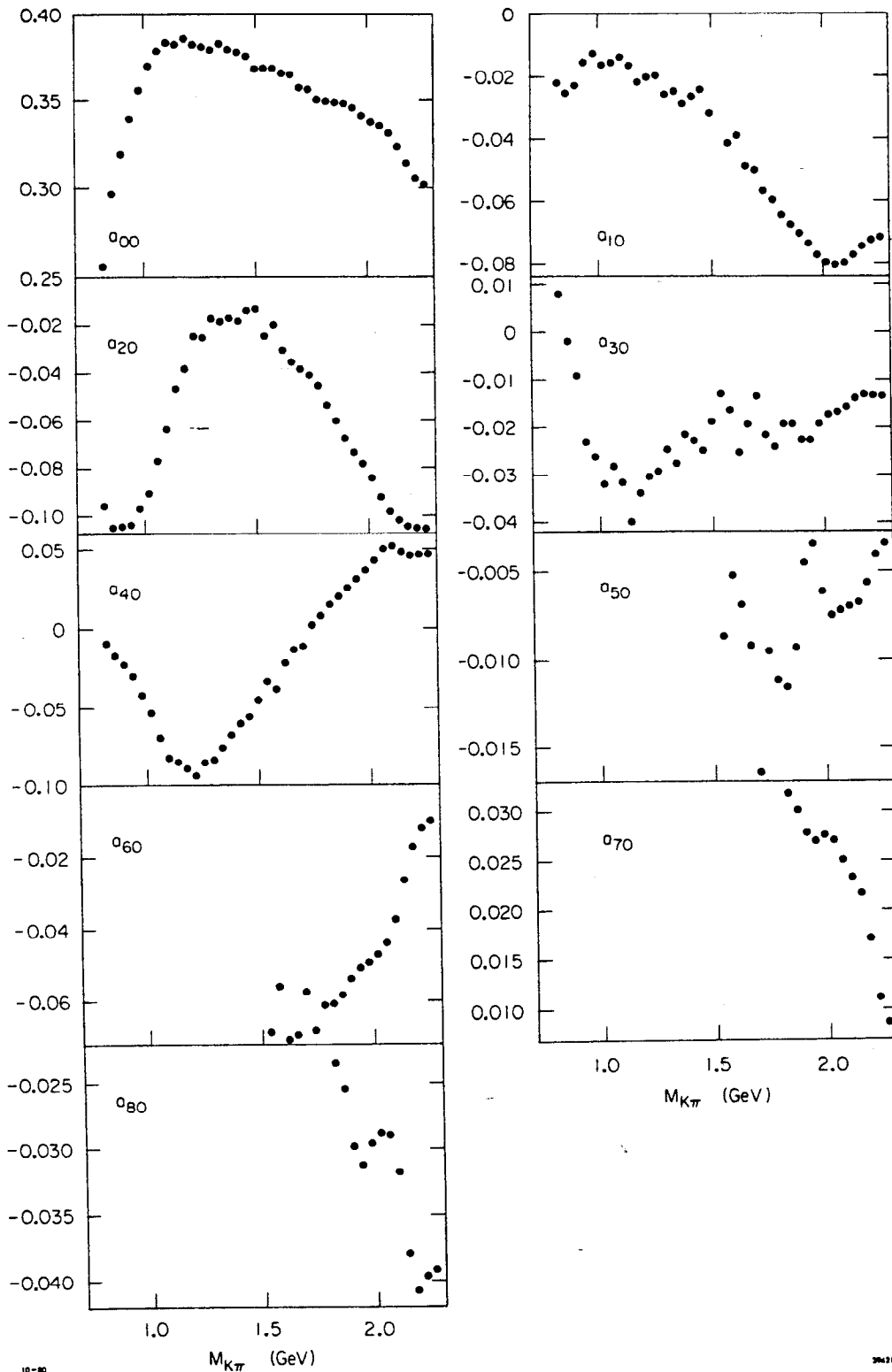


FIG. 28--The final $m=0$ acceptance moments as a function of mass. These moments were calculated in the t' region, $|t'| < 0.2 \text{ GeV}^2$, and in 40 Mev mass bins below 1.8 GeV and 80 Mev overlapping mass bins above this mass.

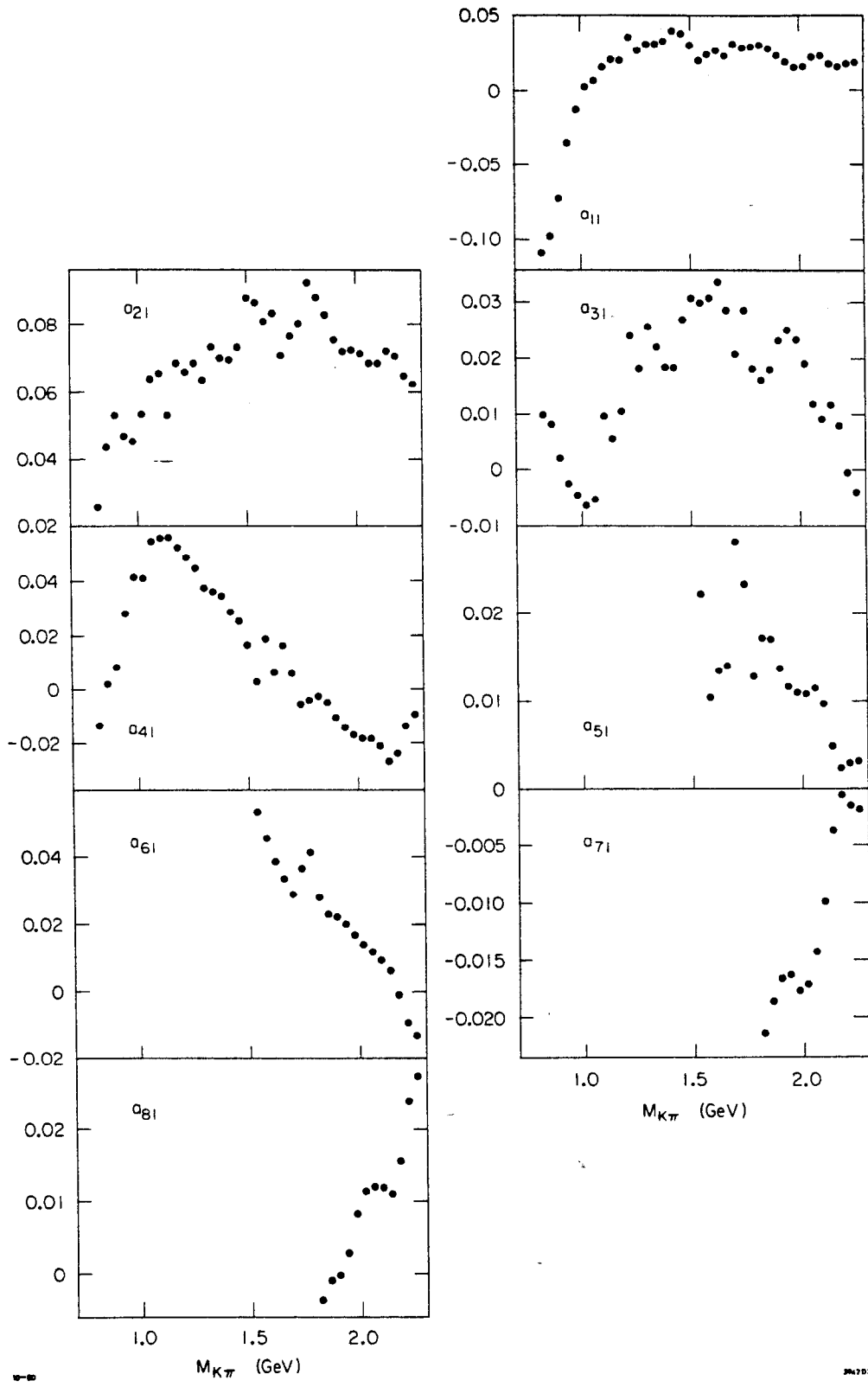


FIG. 29--The final $m=1$ acceptance moments as a function of mass. These moments were calculated in the t' region, $|t'| < 0.2 \text{ GeV}^2$, and in 40 Mev mass bins below 1.8 GeV and 80 Mev overlapping mass bins above this mass.

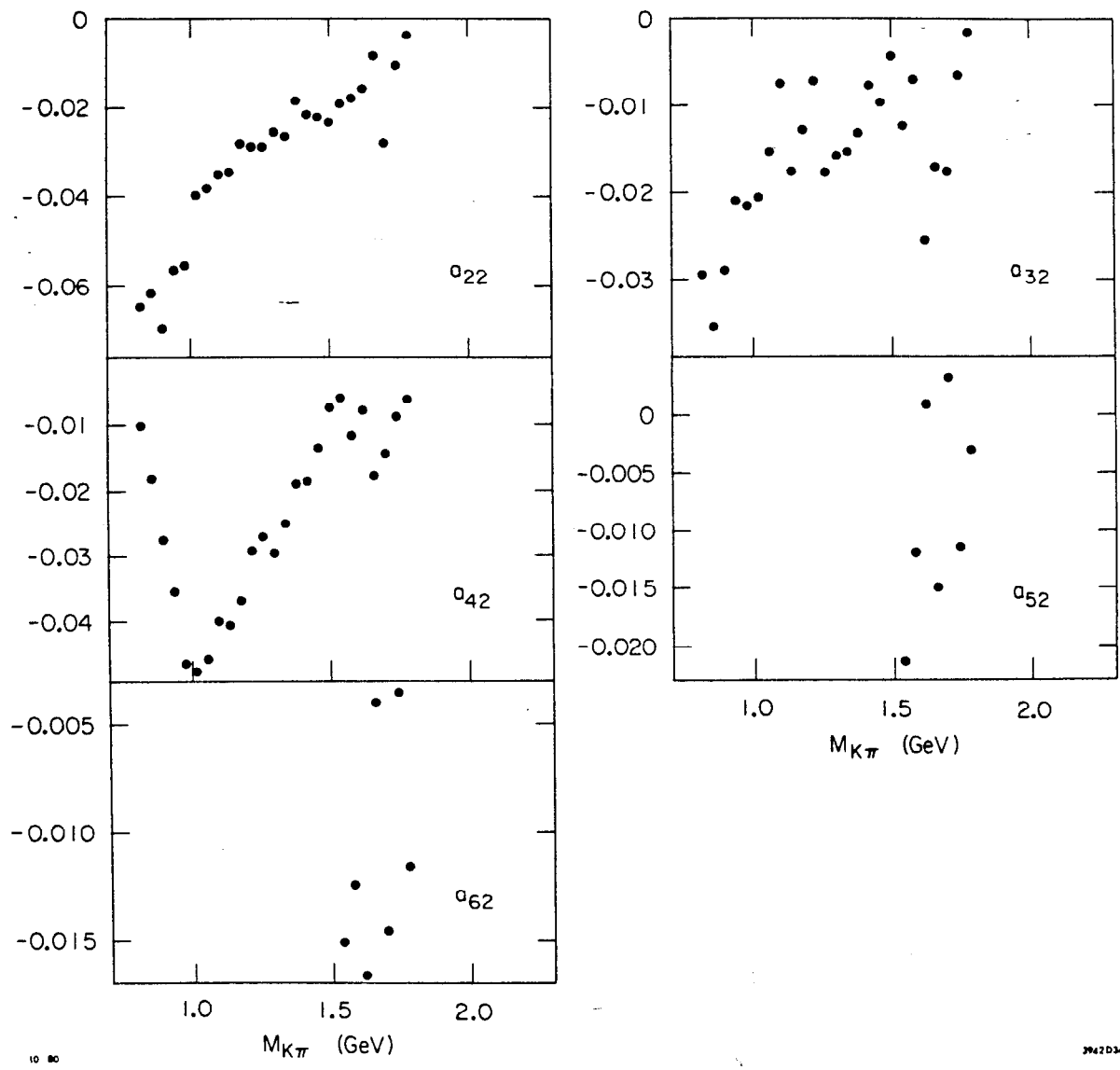


FIG. 30--The final $m=2$ acceptance moments as a function of mass. These moments were calculated in the t' region, $|t'| < 0.2 \text{ GeV}^2$, and in 40 Mev mass bins below 1.8 GeV and 80 Mev overlapping mass bins above this mass.

be quite smooth, and no sharp structures are present which would cause problems in this analysis. The a_{00} acceptance moments represents the spectrometer's integrated acceptance as a function of mass. This integrated acceptance ranges from 25% to 39%. The falloff of this integrated acceptance at low and high mass was described earlier (see chapter VII section B.9).

Shown in figures 31-33 and listed in table 8 are the final angular moments fit in this analysis. Once again the mass binning corresponds to 40 MeV bins below 1.8 GeV, and 80 MeV overlapping bins above this mass. The error bars shown in the plot and listed in the table represent statistical errors only. The t_{1m} 's have been multiplied by a factor of $1/\Delta M(K\pi)\Delta t'$, in order to correct for bin size in the t_{1m} normalization.

These fits were obtained using the smallest number of l and m moments required to fit the data in each mass region. When higher order m terms were added the resulting added terms were seen to be consistent with zero within errors. If higher order l terms were added in these fits, the resulting added terms were also seen to be negligible. In the final moments fits these additional l and m terms were not included, since the addition of these higher order terms increased the error bars on the moments substantially. This increase was due to strong correlations between moments caused by the nonuniform acceptance in this experiment.

The first feature to notice in these angular moments is the rapid decrease in the size of the angular moments as m increases from $m=0$ to $m=1$, and finally to $m=2$. Above 1.800 GeV in fact the $m=2$ moments were

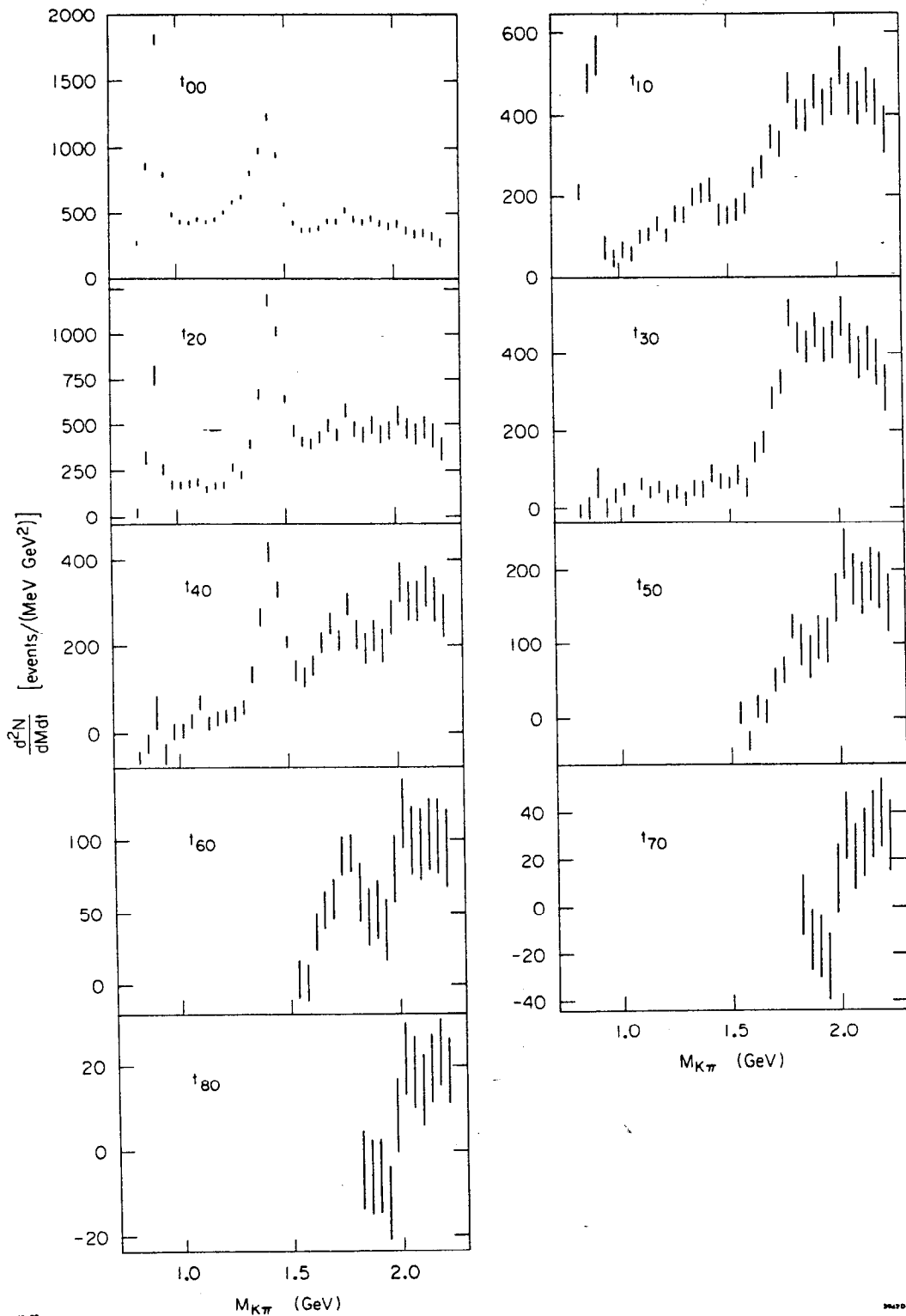


FIG. 31--The final $m=0$ acceptance corrected angular moments as a function of mass. These moments were calculated in 40 MeV mass bins below 1.8 GeV, and 80 MeV mass bins above this mass. The data used in performing these fits was also selected from the small t' region, $|t'| < 0.2 \text{ GeV}^2$. The moments presented have been divided by the mass bin width and the t' bin width.

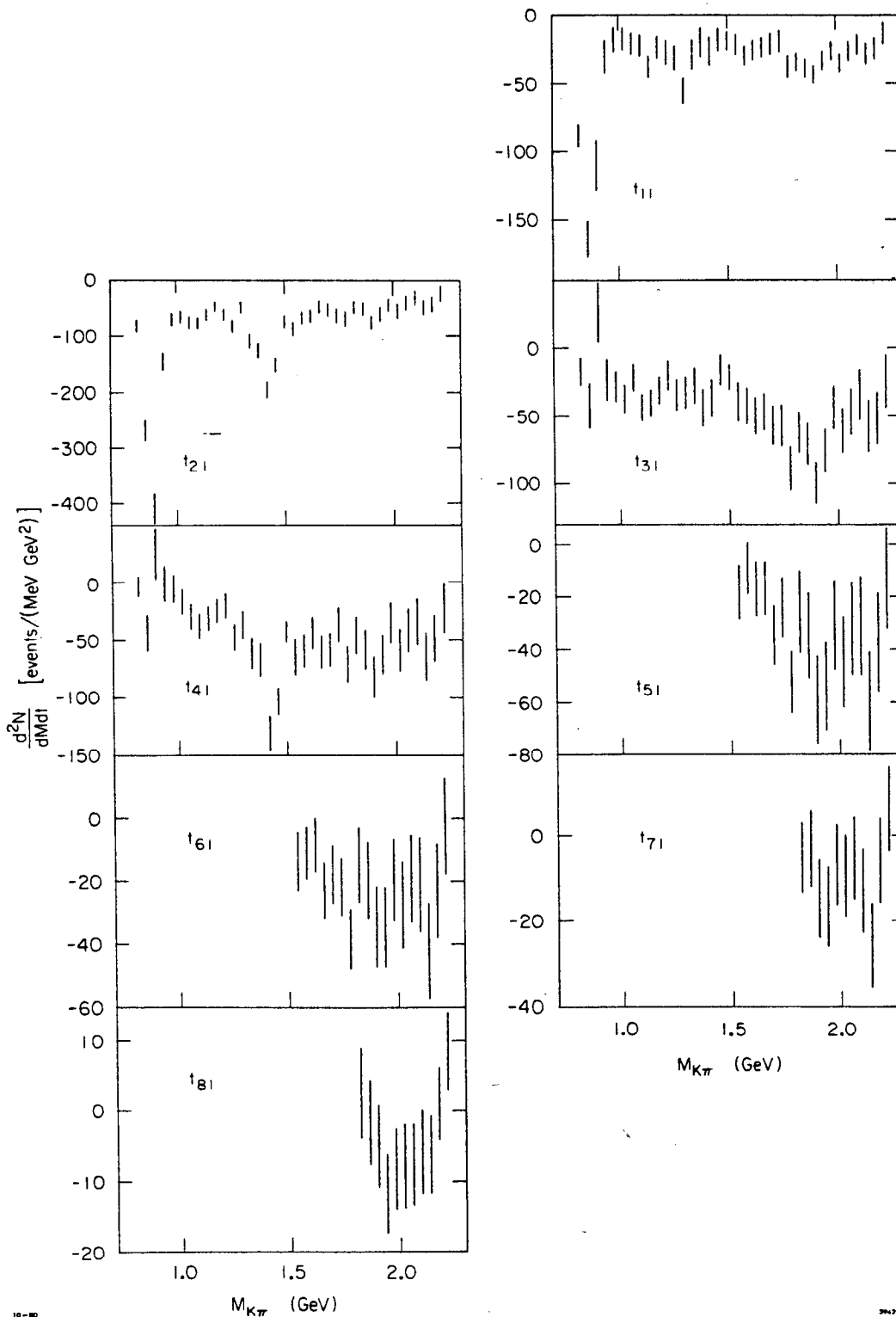


FIG. 32--The final $m=1$ acceptance corrected angular moments as a function of mass. These moments were calculated in 40 MeV mass bins below 1.8 GeV, and 80 MeV mass bins above this mass. The data used in performing these fits was also selected from the small t' region, $|t'| < 0.2 \text{ GeV}^2$. The moments presented have been divided by the mass bin width and the t' bin width.

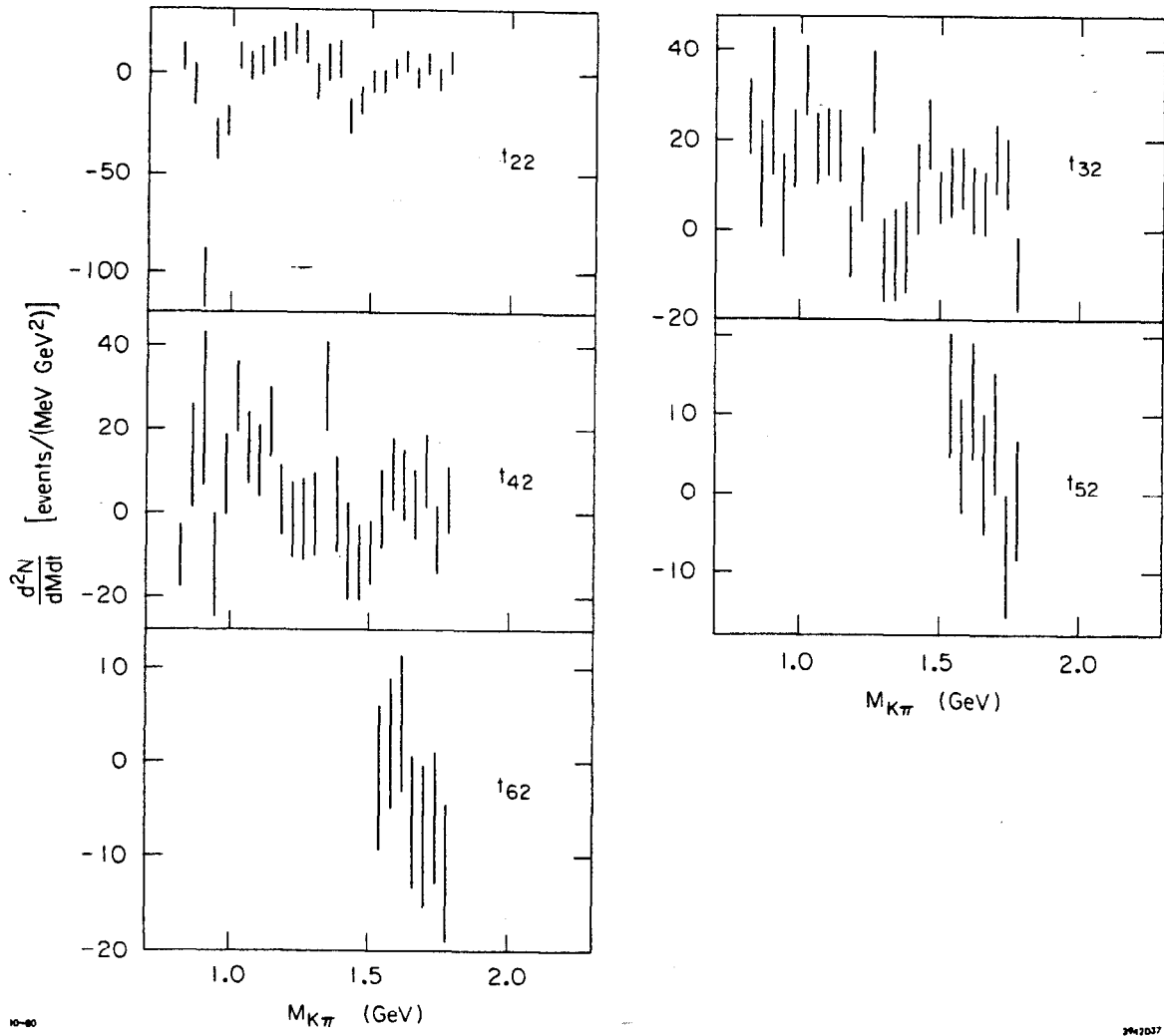


FIG. 33--The final $m=2$ acceptance corrected angular moments as a function of mass. These moments were calculated in 40 MeV mass bins below 1.8 GeV, and 80 MeV mass bins above this mass. The data used in performing these fits was also selected from the small t' region, $|t'| < 0.2 \text{ GeV}^2$. The moments presented have been divided by the mass bin width and the t' bin width.

TABLE 8

Final $K^+p \rightarrow K^-\pi^+n$ Acceptance Corrected
Angular Moments as a Function of Mass

(Both the moments and the errors on these moments are listed. All quantities are measured in events/(GeV²MeV).)

$M(KW)$	t_{00}	t_{10}	t_{11}	t_{20}	t_{21}	t_{22}	t_{30}	t_{31}	t_{32}	t_{40}	t_{41}	t_{42}	t_{50}	t_{51}	t_{52}	t_{60}	t_{61}	t_{62}
0.82	272.1 15.9	212.7 20.6	-87.9 8.8	22.0 23.2	-82.9 11.2	8.6 7.2	-7.1 17.9	-17.1 10.4	25.1 8.4	-56.3 16.6	-3.7 8.6	-10.1 7.6	--	--	--	--	--	--
0.86	862.3 27.5	490.1 37.0	-164.2 13.7	326.4 38.5	-269.3 19.5	-5.6 10.5	0.5 28.5	-42.2 16.8	12.3 12.0	-24.4 24.0	-44.1 15.7	13.6 12.4	--	--	--	--	--	--
0.90	1808.8 38.1	544.7 50.3	-110.5 18.7	776.7 54.7	-410.4 26.4	-103.1 14.7	65.5 39.1	26.4 22.1	28.6 16.5	44.3 37.3	24.8 22.2	25.2 18.3	--	--	--	--	--	--
0.94	797.8 23.1	74.1 29.7	-30.1 12.0	260.6 32.4	-146.9 16.5	-32.9 10.1	2.2 24.3	-23.3 14.5	5.4 11.5	-47.1 24.4	-1.3 15.3	-12.3 12.4	--	--	--	--	--	--
0.98	494.7 17.4	46.2 21.8	-18.1 9.0	174.2 23.8	-72.1 12.4	-23.7 7.8	32.1 18.0	-28.1 11.1	18.1 8.7	3.6 18.2	-5.9 11.7	9.2 9.6	--	--	--	--	--	--
1.02	435.3 16.3	66.3 20.3	-17.4 8.2	173.1 22.1	-66.6 11.3	8.7 7.0	48.5 16.7	-36.9 10.4	33.2 7.9	5.3 16.6	-17.3 11.0	28.0 8.6	--	--	--	--	--	--
1.06	427.4 16.0	57.6 19.1	-20.9 8.0	179.3 22.0	-76.9 10.9	3.8 6.9	-7.8 16.0	-21.8 9.9	18.0 7.7	25.8 16.4	-29.7 10.8	15.7 8.5	--	--	--	--	--	--
1.10	455.0 15.9	101.0 18.7	-22.2 7.9	188.4 21.1	-78.2 10.3	6.2 7.3	61.1 16.0	-43.5 10.1	19.6 7.5	67.8 16.0	-38.3 10.8	12.7 8.5	--	--	--	--	--	--
1.14	436.7 14.9	106.4 17.6	-37.9 8.1	149.9 19.4	-63.5 10.0	10.9 7.4	40.8 15.7	-40.4 9.9	18.6 7.9	19.7 15.3	-31.6 10.3	21.6 8.4	--	--	--	--	--	--
1.18	455.7 15.2	133.2 18.2	-23.4 8.3	167.5 20.3	-47.8 10.1	13.6 7.5	54.0 16.4	-31.0 10.2	-2.8 8.0	30.1 16.0	-25.3 10.4	3.3 8.3	--	--	--	--	--	--
1.22	508.4 15.5	103.7 18.2	-27.1 8.0	172.3 20.3	-63.7 10.5	17.5 8.1	29.2 16.6	-20.3 10.8	10.2 8.4	37.2 16.5	-20.8 10.9	-1.2 8.9	--	--	--	--	--	--
1.26	585.8 16.8	157.6 20.3	-31.1 9.2	269.8 22.7	-83.5 11.5	13.4 8.4	41.5 18.0	-34.4 11.4	30.6 9.1	41.9 17.5	-48.1 11.6	-1.2 9.6	--	--	--	--	--	--
1.30	624.2 16.9	154.8 20.0	-55.2 9.6	227.4 22.2	-48.7 11.3	-3.6 8.9	23.4 16.8	-32.7 11.7	-6.7 9.4	56.0 17.9	-37.4 11.8	-0.0 9.9	--	--	--	--	--	--
1.34	807.3 19.3	198.8 23.2	-29.0 10.7	398.1 26.2	-109.4 13.2	6.1 9.7	50.9 20.9	-27.7 13.1	-5.4 10.2	131.1 20.4	-62.0 13.6	30.4 10.8	--	--	--	--	--	--
1.38	976.9 21.1	208.7 26.3	-19.9 10.8	672.5 29.7	-127.5 13.9	7.5 9.6	47.1 22.4	-44.0 13.9	-3.7 10.3	264.0 22.3	-67.6 14.5	2.2 11.3	--	--	--	--	--	--
1.42	1231.3 23.8	216.5 30.7	-26.5 10.4	1189.1 35.0	-196.5 15.3	-20.9 9.0	88.9 24.1	-37.1 13.8	9.2 10.2	416.0 23.8	-132.0 15.2	-9.0 11.6	--	--	--	--	--	--
1.46	943.3 20.7	154.5 27.2	-18.4 8.6	1018.0 30.3	-153.6 13.5	-13.1 6.9	68.4 19.9	-15.9 11.3	21.5 7.8	326.9 19.8	-104.0 12.2	-11.8 9.2	--	--	--	--	--	--
1.50	568.6 16.3	153.8 21.8	-19.1 6.8	645.0 23.7	-74.8 10.8	-3.6 5.3	64.7 14.7	-21.5 9.1	7.5 5.9	205.3 15.4	-43.9 9.3	-9.2 7.5	--	--	--	--	--	--
1.54	428.0 19.3	167.1 27.8	-21.9 7.6	469.1 31.2	-86.3 12.7	-3.5 5.4	85.1 26.6	-39.7 14.5	10.7 7.8	139.2 25.1	-65.5 15.6	1.3 9.3	6.0 14.8	-18.3 10.1	12.5 7.9	3.6 13.6	-13.8 9.5	-1.7 7.6
1.58	373.6 17.3	181.0 25.2	-29.6 7.1	410.2 28.0	-69.1 11.9	3.0 4.8	51.8 23.7	-42.4 13.6	11.5 6.9	124.1 22.1	-60.0 14.4	9.2 8.6	-31.1 13.5	-9.1 9.8	4.8 7.3	0.8 12.6	-11.2 8.4	2.0 7.0
1.62	376.0 18.7	245.6 26.9	-25.7 7.4	398.2 30.0	-65.9 12.1	6.6 5.1	143.6 26.4	-50.1 13.7	6.8 7.4	151.2 23.7	-44.9 14.1	6.9 8.4	14.4 14.7	-17.1 10.4	11.8 7.5	36.6 13.3	-8.7 8.7	4.1 7.3
1.66	389.5 19.8	272.3 28.6	-23.9 7.3	433.3 32.5	-48.9 12.2	-1.6 5.1	171.1 27.6	-46.9 13.9	5.9 7.3	204.1 25.0	-60.9 14.5	2.4 8.3	7.9 15.8	-16.7 10.2	2.6 7.7	51.2 13.2	-22.9 9.1	-6.4 7.0
1.70	443.4 21.3	347.4 31.1	-21.4 7.8	496.1 34.6	-54.3 12.7	5.2 5.4	283.2 30.0	-56.9 14.6	15.8 7.6	246.8 26.3	-59.3 14.7	10.1 8.6	50.2 16.7	-34.5 11.3	7.7 7.7	58.8 14.3	-17.9 9.4	-7.9 7.5
1.74	439.1 22.0	328.3 31.6	-19.3 8.1	446.5 34.9	-64.9 13.1	-2.4 5.5	326.9 31.3	-57.3 15.4	12.5 7.8	207.4 26.0	-38.1 15.1	-6.0 8.1	63.6 17.3	-24.1 11.2	-7.9 7.9	88.3 13.9	-21.9 9.4	-5.9 7.1
1.78	524.2 25.1	464.9 36.3	-37.9 8.5	581.3 39.6	-70.1 13.9	5.8 5.7	504.0 34.7	-88.8 16.4	-10.0 8.2	291.8 26.9	-71.6 15.3	3.3 8.0	122.6 17.0	-52.5 11.8	-0.9 7.5	89.9 13.6	-38.6 9.5	-11.8 7.2

TABLE 8 (cont.)

M(Kw)	t ₀₀	t ₁₀	t ₂₁	t ₂₀	t ₂₁	t ₂₀	t ₂₁	t ₀₀	t ₁₀	t ₂₀	t ₂₁	t ₀₀	t ₁₀	t ₂₀	t ₂₁	t ₀₀	t ₁₀
1.82	457.2 23.7	399.8 37.5	-34.2 6.7	478.3 42.2	-49.4 11.0	440.1 40.6	-62.0 15.0	221.9 35.9	-47.3 16.6	97.8 28.4	-25.7 15.6	63.3 20.5	-15.0 12.0	0.2 12.8	-5.4 8.4	-4.7 9.4	2.6 6.4
1.86	434.6 24.3	396.1 38.6	-38.8 6.9	446.9 43.4	-52.4 12.2	416.1 41.6	-70.6 15.4	187.3 36.5	-59.6 17.1	81.3 28.8	-34.7 16.2	46.2 20.2	-19.8 12.3	-14.4 13.1	-3.2 8.9	-6.3 9.0	-1.6 6.1
1.90	463.1 25.8	455.6 41.0	-43.6 6.9	497.9 45.8	-77.1 12.6	460.6 43.7	-99.3 15.9	217.0 37.8	-83.5 17.7	107.7 29.7	-59.3 16.8	51.2 20.2	-34.8 12.8	-17.3 13.4	-14.7 9.3	-6.1 8.7	-5.0 5.9
1.94	428.3 26.7	418.3 42.5	-33.4 7.0	450.8 47.6	-62.4 12.7	421.3 45.5	-75.7 16.1	195.9 39.6	-63.8 17.8	103.4 31.1	-53.9 16.9	37.7 21.5	-34.7 12.8	-25.8 14.2	-16.8 9.4	-12.4 8.9	-11.7 5.6
1.98	404.8 27.6	442.6 43.9	-26.1 6.8	468.8 49.8	-45.1 12.6	433.7 47.9	-43.7 16.0	258.7 42.1	-36.6 17.8	161.3 33.2	-30.8 16.9	79.4 23.3	-19.8 13.3	11.8 14.6	-7.1 9.5	8.1 8.8	-8.2 5.8
2.02	422.7 30.2	517.9 48.0	-35.0 7.0	550.7 54.3	-56.4 13.1	496.3 51.9	-60.9 16.8	341.0 45.1	-59.6 18.5	219.8 35.0	-44.7 17.4	117.0 24.3	-27.7 14.0	33.9 14.5	-9.4 9.7	21.4 8.6	-7.8 6.1
2.06	371.5 30.8	448.7 49.0	-26.7 7.2	479.3 55.5	-41.6 13.6	423.7 52.8	-47.0 17.3	298.3 45.5	-42.9 19.0	185.8 34.9	-32.8 17.7	98.3 24.1	-19.5 14.1	20.7 14.1	-5.4 14.1	18.2 8.5	-7.6 5.9
2.10	343.9 32.0	427.1 50.9	-21.7 7.4	448.6 57.5	-33.2 14.0	386.9 54.7	-34.8 18.4	297.4 47.0	-35.9 20.3	173.9 35.8	-31.0 18.7	95.7 25.0	-21.3 15.1	26.7 14.5	-13.0 9.9	13.9 8.4	-5.8 6.0
2.14	352.2 34.2	459.5 54.4	-28.0 7.7	481.3 60.9	-49.8 14.6	410.8 57.5	-57.5 19.3	330.8 48.9	-65.7 21.0	193.0 36.8	-59.6 19.1	102.9 25.6	-42.4 15.3	34.5 14.3	-26.0 9.9	19.0 8.0	-6.2 5.6
2.18	324.7 35.1	429.7 55.9	-24.4 7.7	439.6 62.9	-44.3 14.6	375.0 59.6	-51.7 18.9	301.3 50.8	-50.1 20.5	184.2 38.6	-37.2 18.7	101.5 26.3	-23.2 15.0	39.6 14.6	-5.9 10.0	22.9 8.0	1.1 5.2
2.22	277.4 35.9	363.4 57.5	-13.4 7.9	366.6 64.7	-24.9 14.8	307.8 61.4	-24.6 19.5	261.6 52.3	-24.2 21.0	154.6 39.4	-12.8 19.2	93.2 27.1	-2.5 15.5	29.6 15.2	6.3 9.9	18.3 7.7	8.5 5.6

found to be negligible. The dominance of the $m=0$ moments is a reflection of the dominance of single pion exchange in this reaction in the small $|t'|$ region from which this fitted data was selected. Had the reaction been mediated solely by pion exchange, only $m=0$ moments would have been present. Since single pion exchange is the dominant process in this reaction, the resonance structures can be discussed by considering the mass dependence of the $m=0$ moments only.

The first feature to notice in these $m=0$ moments is the sharp spike at .890 GeV in the t_{00} and t_{20} moments. This spike is indicative of the $J^P=1^-$ $K^*(895)$ resonance. The t_{40} moment in the region of the $K^*(895)$ is seen to be quite flat, and shows no structure. This brings up a quite general statement that can be made about resonances in angular moments plots. In the even ($m=0$) angular moments, a resonance of spin j appears as bumps in the even angular moments up to the moment t_{2j0} , and in no higher moments (see chapter VIII section A). Therefore since a bump is seen in the t_{00} and t_{20} moments, and not in the t_{40} moment, the $K^*(895)$ can be assigned a spin of one from this data. Parity conservation allows only natural spin parity resonance states to be seen in this reaction so the $K^*(895)$ is assigned a negative parity. The strong interference pattern in the t_{10} moment in this .890 GeV region is also indicative of this resonance.

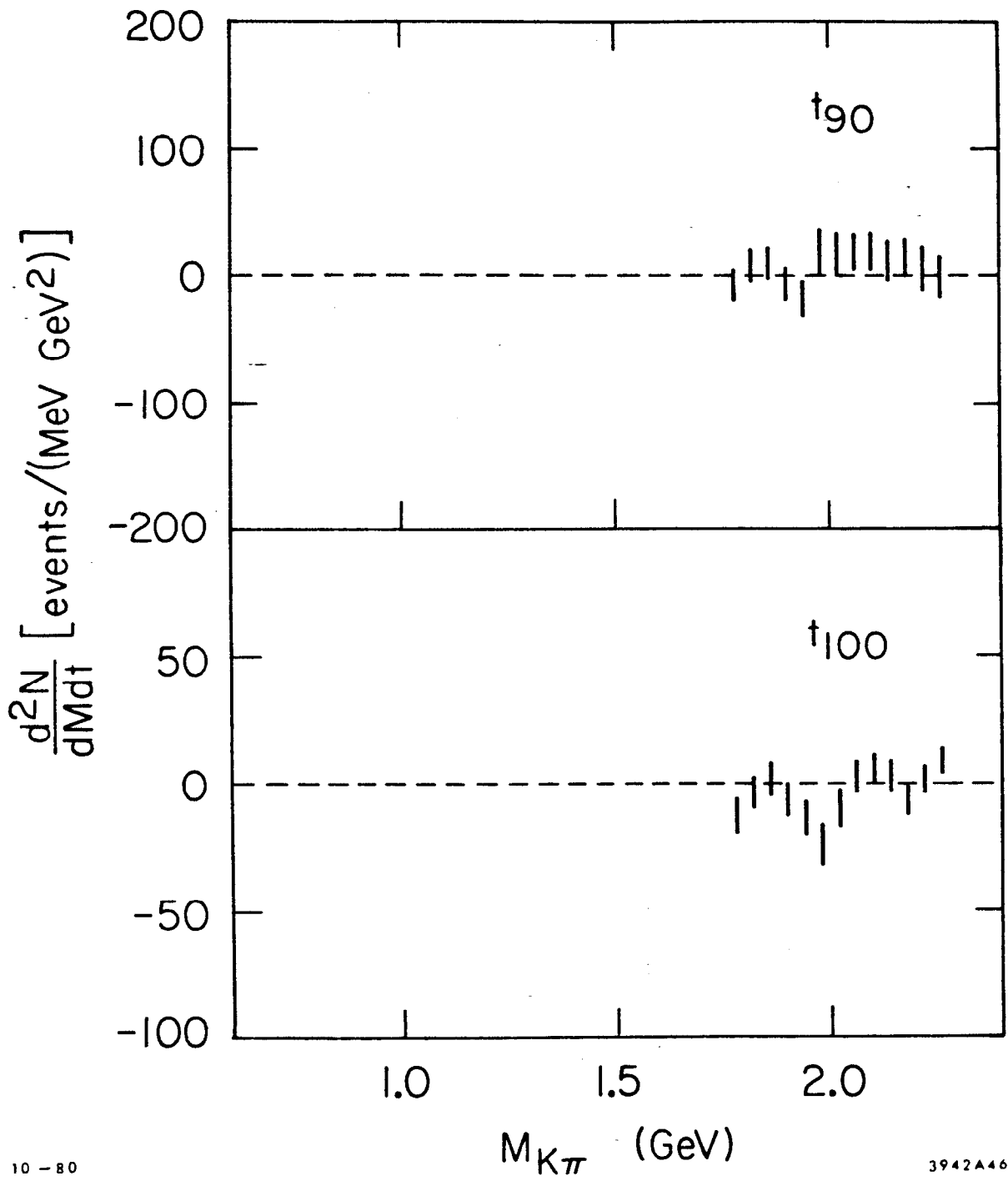
The $J^P=2^+$ $K^*(1430)$ is seen in these moments as a bump at 1.430 GeV in the t_{00} , t_{20} , and t_{40} angular moments. Fits were also run with the $l=5$ and $l=6$ terms added, and these moments were seen to be extremely small. The t_{10} moment is also seen to vary rapidly in this region. Thus this well known 2^+ resonance is seen in these angular moments, and its spin is verified.

At higher mass definite peaks in the t_{40} and t_{60} angular moments at a mass around 1.78 GeV are indicative of the $J^P=3^-$ $K^*(1780)$. Fits were also run in this region including the $l=7$ and $l=8$ angular moments. These added moments were seen to be negligible.

Lastly at even higher mass there are clear peaks in the t_{60} and t_{80} angular moments in the mass region around 2.07 GeV. A rapid variation in the t_{70} moment in the region around 1.95 GeV is also seen. This structure is most easily interpreted in terms of a 4^+ K^* resonance in the region of 2.07 GeV. The rapid variation in the t_{70} moment being caused by an interference between the F and G wave tails of the $K^*(1780)$ and the $K^*(2080)$. Shown in figure 34 are the t_{90} and the t_{100} moments from separate angular moments fits which included these moments. These moments are seen to be consistent with zero within the statistical errors. As well as confirming the $K^*(2080)$ is a spin 4^+ object, this result also implies there are no spin five resonances, within the statistics of this experiment, up to a mass of 2.3 GeV.

Thus in these angular moments, four leading K^* resonances are easily visible, and the spin of these resonances is clearly determined. The three lowest mass leading K^* states (the 1^- $K^*(895)$, the 2^+ $K^*(1430)$, and the 3^- $K^*(1780)$) have been clearly seen in previous $K^-p \rightarrow K^-\pi^+n$ experiments, and the properties of these resonances are now rather well understood³. Evidence for the spin 4^+ $K^*(2080)$, before this analysis, was very sparse³⁰.

There is obviously far more structure in these angular moments than just these four leading K^* resonances would indicate. Clearly a more sophisticated analysis was needed in order to fully understand these



10 - 80

3942A46

FIG. 34--The t_{90} and t_{100} angular moments from angular moments fits run with $l_{max}=10$ and $m_{max}=2$ (80 MeV mass bins, $|t'| < 0.2$ GeV²).

moments. A partial wave analysis then was performed on these angular moments. This partial wave analysis is the subject of the next chapter. To conclude this chapter, quantitative fits which yielding resonance parameters for these four leading K^* resonances will be discussed.

E. Fits to the Leading K^* Resonances using the Angular Moments

In this section simple fits to the acceptance corrected angular moments will be presented yielding resonance parameters for the four leading K^* resonances: 1) $J^P=1^- K^*(895)$, 2) $2^+ K^*(1430)$, 3) $3^- K^*(1780)$, and 4) $4^+ K^*(2080)$. It is easily seen, in the angular moments presented in the last section, that the leading K^* resonances contribute to the highest l -order angular moment not consistent with zero within their respective mass regions. In terms of the simple exchange model of the next chapter this implies that the leading K^* resonances make up the highest spin nonzero partial wave necessary to describe this data in their given mass regions. Using this fact it is easily proven using this exchange model that in the mass region of a leading spin j K^* resonance, the t_{2j0} angular moment is proportional (ignoring the production parameters' slow variations as functions of mass) to the square of the $K^-\pi^+$ elastic scattering partial waves times $M(K\pi)^2/q$.

$$t_{2j0}^{th} \propto \frac{M_{K\pi}^2}{q} |a_j|^2$$

VII.27

Thus assuming the j wave turn-on is dominated by resonance production, the t_{2j_0} angular moment can be fit to a simple Breit-Wigner resonance form yielding the resonance parameters of this spin j leading K^* resonance.

Chi-square fits using a simple Breit-Wigner resonance form with a Blatt-Weisskopf barrier factor ³¹ have been performed on the leading edge of the resonance peaks in these t_{2j_0} angular moments. Table 9 gives the form of the Breit-Wigner used in these fits. Shown in figure 35 and in table 10 are the four chi-square fits to these t_{2j_0} angular moments. Where the factor R is not shown in table 10 this factor was fixed to a value of 1 fm. The resonance widths presented in table 10 have been corrected for binning effects, as well as smearing caused by the finite mass resolution of the LASS spectrometer. The systematic errors in this table represent conservative estimates of the systematic effects present in the measurement of these resonance parameters. Where the systematic errors are not shown, statistical errors are believed to dominate over systematic effects. These fits will be compared to world averages in chapter VIII section D.

In fitting the spin 4^+ K^* resonance to the leading edge of the t_{80} angular moment, not all the information available in the angular moments has been used. Another approach was to perform a simple energy dependent amplitude analysis using the angular moments; t_{60} , t_{70} , and t_{80} presented in the last section. This approach suffers from lack of knowledge of possible underlying states as well as the detailed behavior of the tail of the $K^*(1780)$, but the added statistics make this fit well worth while.

TABLE 9

Breit-Wigner Resonance Parameterization
with a Blatt-Weisskopf Barrier Factor^μ

$$\frac{a_L}{\sqrt{2L+1}} = \frac{\epsilon M_R \Gamma}{(M_R^2 - M_{K\pi}^2) - i M_R \Gamma}$$

$$\Gamma = \left(\frac{q}{q_R}\right)^{2L+1} \Gamma_R \frac{D_L(q_R R)}{D_L(q R)}$$

where

$$D_0(x) = 1$$

$$D_1(x) = 1 + x^2$$

$$D_2(x) = 9 + 3x^2 + x^4$$

$$D_3(x) = 225 + 45x^2 + 6x^4 + x^6$$

$$D_4(x) = 11025 + 1575x^2 + 135x^4 + 10x^6 + x^8$$

^μ J.W. Blatt and V.F. Weisskopf, 'Theoretical Nuclear Physics' (Wiley, N.Y., 1952), p361, p409-410

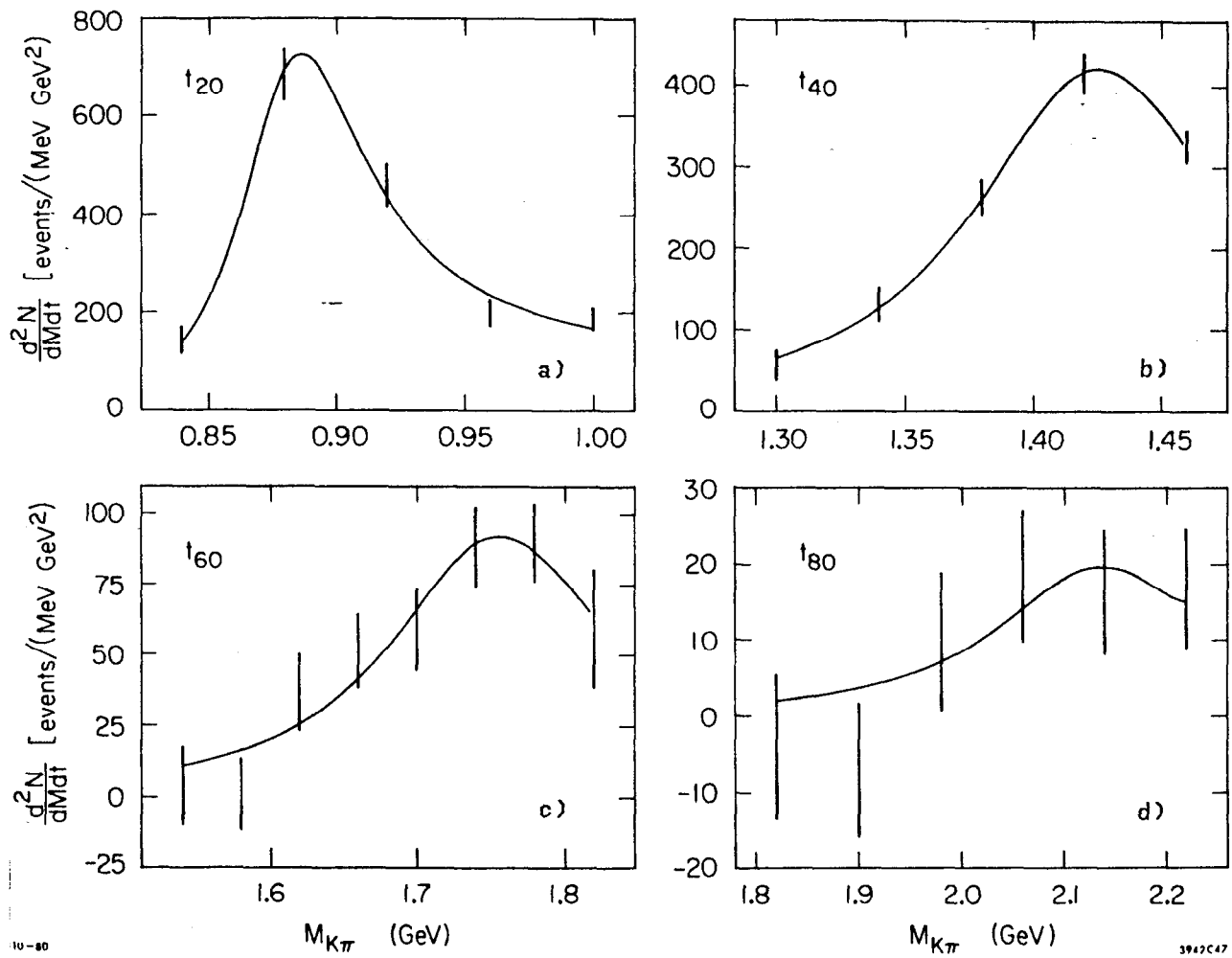


FIG. 35--Leading resonance fits to the t_{2j_0} moments; a) the $K^*(895)$ fit, b) the $K^*(1430)$ fit, c) the $K^*(1780)$ fit, and d) the $K^*(2080)$ fit.

TABLE 10

Resonance Parameters from Breit-Wigner Fits to the Angular Moments

(a) Spin 1 Fit to the t_{20} Moment

Parameter	Fit Value	Statistical Error	Systematic Error
Mass	887.0	± 3.3	± 2.0 MeV
Width	58.8	± 7.1	MeV
R	0.0	± 4.0	GeV ⁻²
$\chi^2/\text{DOF}^{\text{B}}$	2.9/1		

(b) Spin 2 Fit to the t_{40} Moment

Parameter	Fit Value	Statistical Error	Systematic Error
Mass	1426	± 3	± 4 MeV
Width	118	± 13	MeV
χ^2/DOF	0.32/2		

(c) Spin 3 Fit to the t_{60} Moment

Parameter	Fit Value	Statistical Error	Systematic Error
Mass	1756	+ 17 - 13	± 20 MeV
Width	185	+ 53 - 38	MeV
χ^2/DOF	3.4/5		

(d) Spin 4 Fit to the t_{80} Moment

Parameter	Fit Value	Statistical Error	Systematic Error
Mass	2140	+ 140 - 60	± 30 MeV
Width	250	+ 300 - 130	MeV
χ^2/DOF	2.5/3		

^B Chi-square per Degree of Freedom

The simple exchange model of the next chapter (see chapter VIII section A) can be used to derive a relationship between the angular moments t_{60} , t_{70} , and t_{80} ; and the $K^-\pi^+$ elastic scattering partial waves, a_L . Assuming 1) only helicity zero amplitudes contribute (one particle exchange model), 2) the production parameter b is a slowly varying function of mass, and 3) the G wave is the highest spin nonzero partial wave in the given mass region; the following relationships were derived:

$$t_{80}^{\text{th}} = \frac{100}{33\sqrt{13}} |F|^2 + \frac{20}{11\sqrt{13}} |G|^2 + \frac{30\sqrt{5}}{11\sqrt{13}} \text{Re}(D G^*)$$

$$t_{70}^{\text{th}} = \frac{70\sqrt{35}}{143\sqrt{3}} \text{Re}(F G^*)$$

VII.28

$$t_{80}^{\text{th}} = \frac{490}{143\sqrt{17}} |G|^2$$

$$D \propto \frac{M_{K\pi}}{\sqrt{q}} a_D \quad F \propto \frac{M_{K\pi}}{\sqrt{q}} a_F \quad G \propto \frac{M_{K\pi}}{\sqrt{q}} a_G$$

The theoretical angular moments were then parameterized, and fit to the experimental angular moments presented in this chapter.

In performing these fits the D, F, and G wave backgrounds were parameterized as simple polynomials in $M(K\pi)$. The F and G wave resonances were parameterized by the simple Briet-Wigner forms of table 9. The exact parameterizations used in these fits is given in table 11. As input to this fit the mass and width of the $3^- K^*(1780)$ were fixed according to the t_{60} angular moment fit listed in table 10.

TABLE 11

Parameterization for the D, F, and G Waves for the Energy Dependent Fit to the t_{60} , t_{70} , and t_{80} Angular Moments.

$$D = \frac{M_{K\pi}}{\sqrt{q}} e^{i\phi_1} (A_1 + B_1 M_{K\pi})$$

$$F = \frac{M_{K\pi}}{\sqrt{q}} \left\{ e^{i\phi_2} (A_2 + B_2 M_{K\pi} + C_2 M_{K\pi}^2) + N_2 BW(M_{K\pi}, M_F, \Gamma_F) \right\}$$

$$G = \begin{cases} \frac{M_{K\pi}}{\sqrt{q}} N_3 BW(M_{K\pi}, M_G, \Gamma_G) & M_{K\pi} \leq 1.98 \text{ GeV} \\ \frac{M_{K\pi}}{\sqrt{q}} \left\{ B_3 (M_{K\pi} - 1.98 \text{ GeV}) + N_3 BW(M_{K\pi}, M_G, \Gamma_G) \right\} & M_{K\pi} > 1.98 \text{ GeV} \end{cases}$$

where $BW(M_{K\pi}, M, \Gamma) = \frac{M\Gamma}{(M^2 - M_{K\pi}^2) - i M\Gamma}$

and Γ is given by TABLE 9

free parameters: $\phi_1, A_1, B_1, \phi_2, A_2, B_2, C_2, N_2, B_3, N_3, M_G, \Gamma_G$

fixed parameters: M_F, Γ_F

The results of a fully correlated chi-square fit to this simple model are shown in figure 36 and table 12. The systematic error presented in table 12 represent conservative estimates of possible systematic effects. The significance of the spin 4^+ state in this model is 4.6 standard deviations. Results from a fit to this model using angular moments run with a slightly looser missing mass cut give nearly identical results with slightly smaller statistical errors. Results from these looser missing mass angular moments fits are presented in reference 32.

F. Checks on the Angular Moments Fits

One of the best checks of the Monte Carlo simulation of the LASS spectrometer acceptance was provided by rerunning the angular moments fits, shown in this chapter, varying the final $K\pi\pi$ data sample cuts (PASSMC cuts) which were imposed on both the data events and the Monte Carlo events. Accurate Monte Carlo simulation implied that no difference should be seen between varied cut and standard cut fitted moments. Conversely if the data and Monte Carlo event samples differed radically, variations in the fitted moments would be evident between the varied cut and the standard cut fitted moments. A great number of such checks were run varying the target cuts, the elastic cuts, the missing mass cut, the resolution cuts, the trigger cuts, and the geometrical aperture cuts in PASSMC. It would be impossible due to space limitations to show all of the comparisons here. Instead a representative sample will be shown.

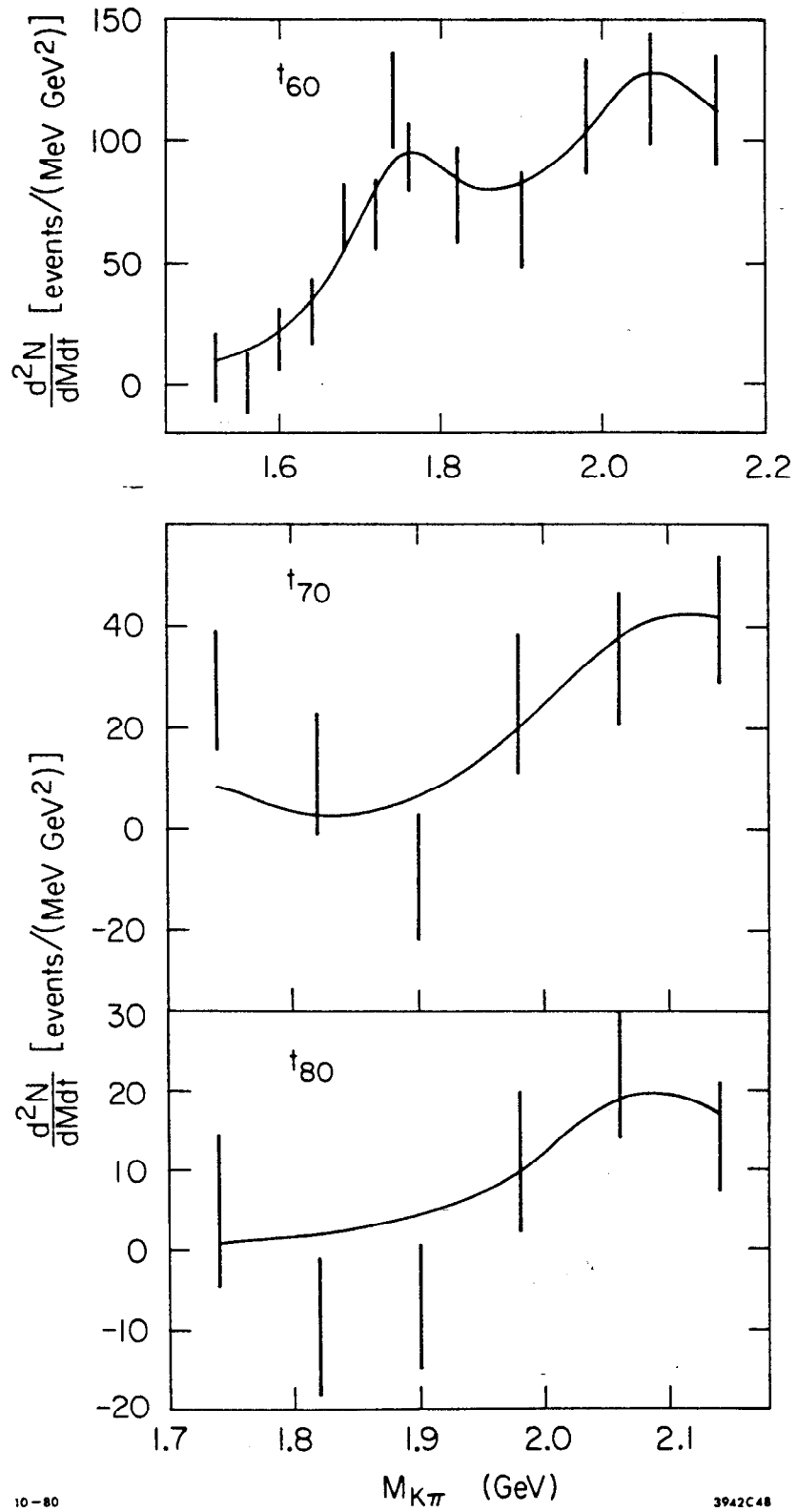


FIG. 36--The energy dependent fit the the t_{60} , t_{70} , and t_{80} angular moments (see text for a description of this fit).

TABLE 12

Resonance Parameters from the Energy Dependent
Fit to the t_{60} , t_{70} , and t_{80} Angular Moments

Parameter	Fit Value	Statistical Error	Systematic Error
Mass	2075	+ 40 - 30	± 30 MeV
Width	240	+ 400 - 80	MeV
$\chi^2/\text{DOF}^{\text{B}}$	15.7/13		

^B Chi-square per Degrees of Freedom

Shown in figures 37 b) - 39 b) are comparisons of fits run varying the missing mass cut to the standard angular moments fits in three typical mass bins. In this missing mass comparison, the standard missing mass cut fits ($0.2 \text{ GeV}^2 < MM^2 < 1.1 \text{ GeV}^2$) are compared to tighter missing mass cut fits ($0.4 \text{ GeV}^2 < MM^2 < 1.0 \text{ GeV}^2$). The tight and standard missing mass cut fits are seen to agree quite well in the three different mass regions within errors. As well as showing that the Monte Carlo simulates the missing mass resolution quite well, this result implies the final angular moments are not sensitive to possible background events. As was shown in the background discussion of chapter VI, a tighter missing mass cut would drastically reduce the signal to background ratio in the final $K\pi\pi$ data sample. These angular moments fits are thus shown to be insensitive to these background events.

Shown in figures 37 a) - 39 a) are comparisons of fits run with tighter aperture cuts, to the standard angular moments fits in the same three mass bins. In these tight aperture cut fits, all PASSMC aperture cuts were decreased radically. The tight and standard aperture cut fits are seen to agree quite well within errors in all three different mass regions.

As well as checking the moments for stability to changes in the final data cuts, the final angular moments fits were also checked for sensitivity to the bin to bin fluctuations in the acceptance moments. This was done by two methods. In the first method the acceptance moments were smoothed using simple polynomial fits to the acceptance moments as a function of mass. Angular moments fits were then run using these smoothed acceptance moments and compared to the standard angular

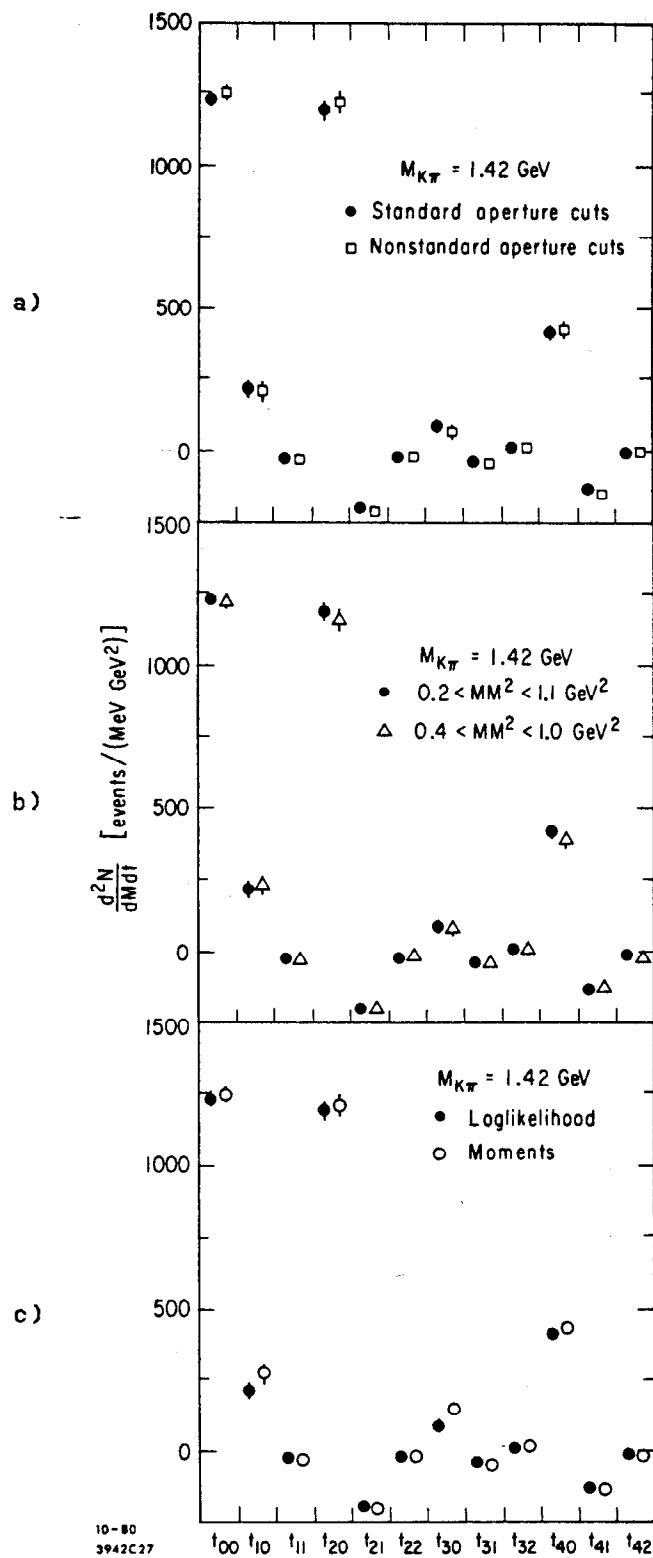


FIG. 37--Angular Moments Comparisons in the mass bin $1.40 \text{ GeV} < M(K\pi) < 1.44 \text{ GeV}$;
 a) tight aperture cut vs standard aperture cut
 b) tight missing mass cut vs standard missing mass cut
 c) maximum likelihood fit vs moments method fit

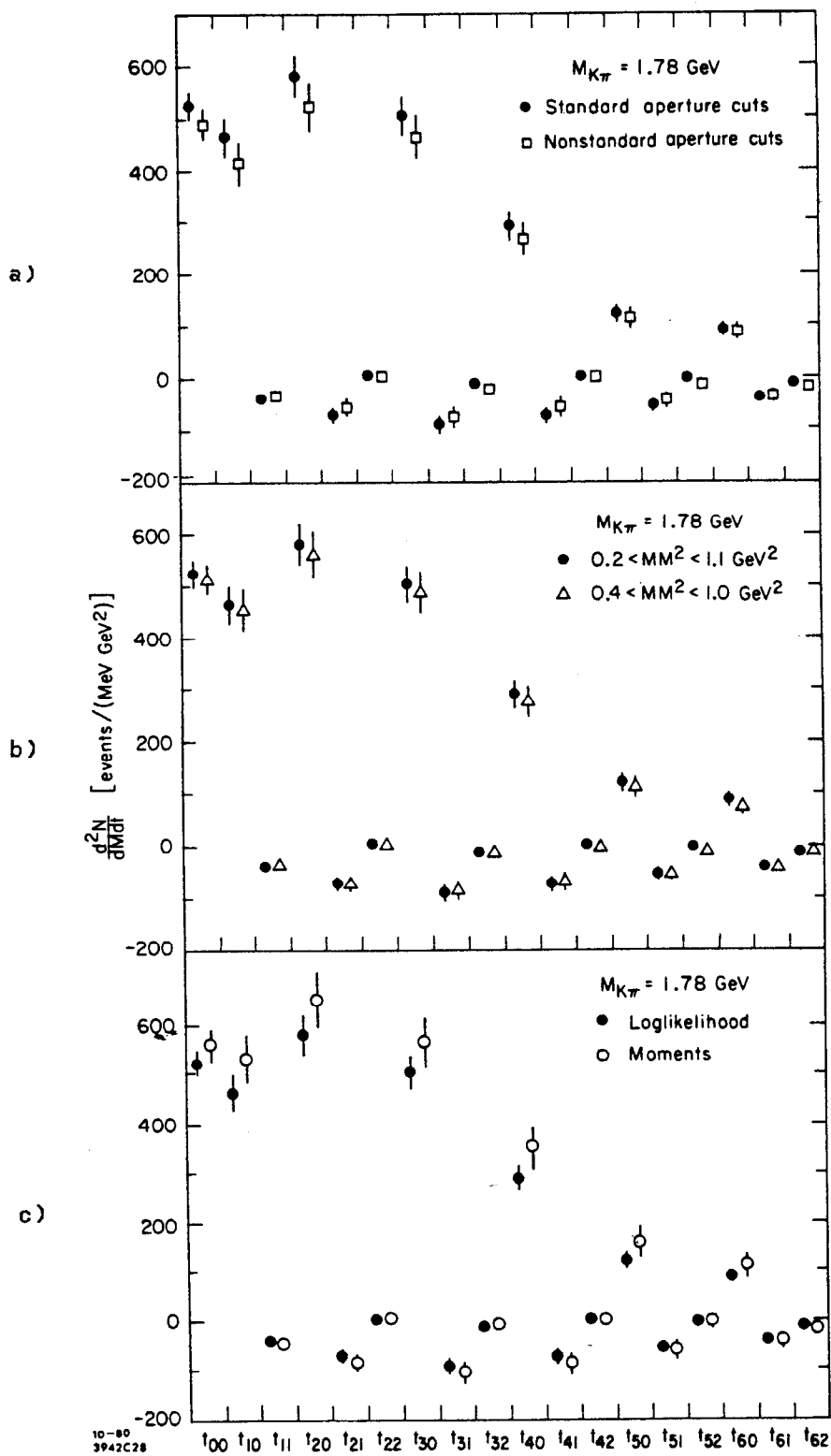


FIG. 38--Angular Moments Comparisons in the mass bin $1.76 \text{ GeV} < M(K\pi) < 1.80 \text{ GeV}$;
 a) tight aperture cut vs standard aperture cut
 b) tight missing mass cut vs standard missing mass cut
 c) maximum likelihood fit vs moments method fit

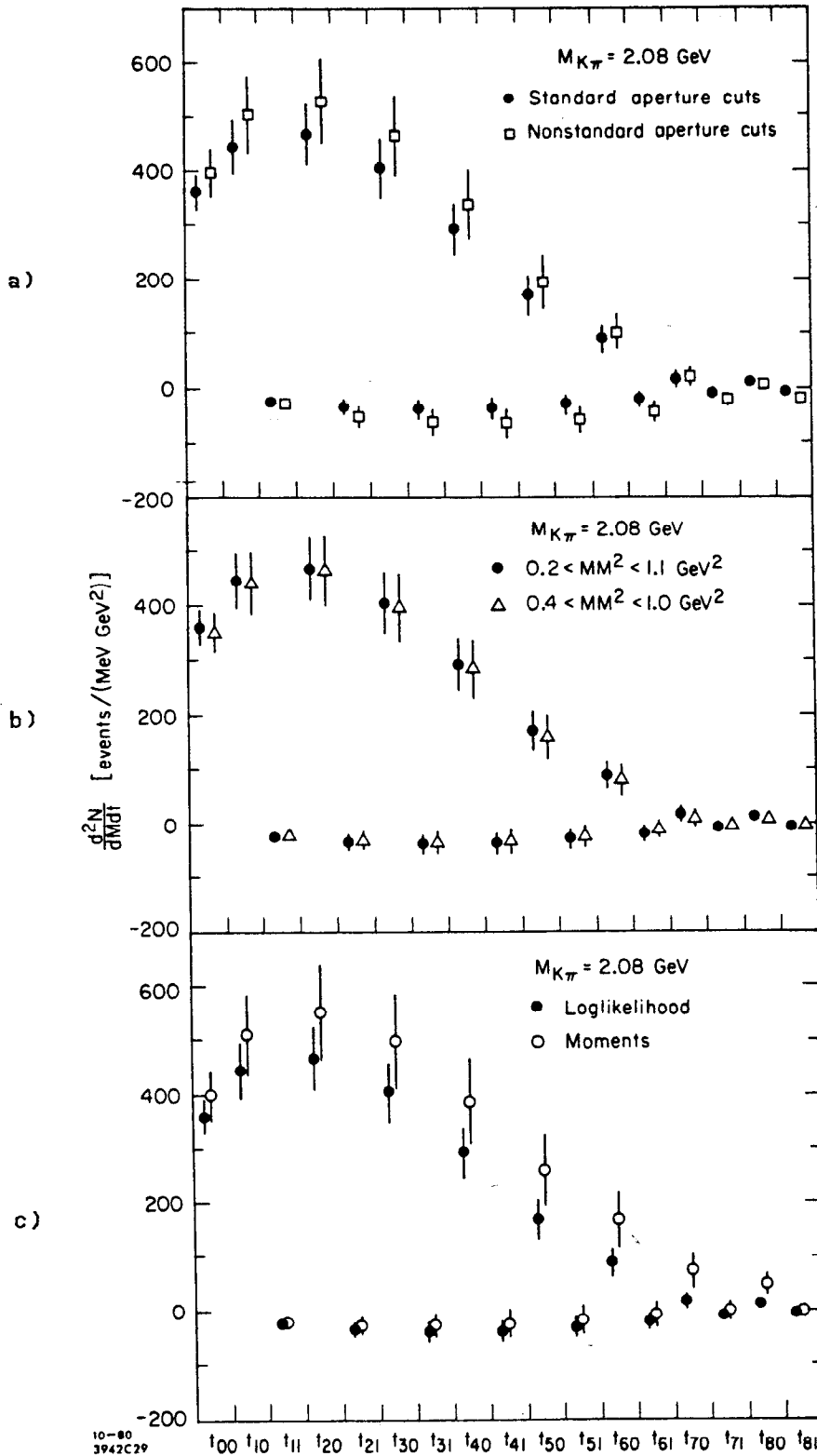


FIG. 39--Angular Moments Comparisons in the mass bin $2.04 \text{ GeV} < M(K\pi) < 2.12 \text{ GeV}$;
 a) tight aperture cut vs standard aperture cut
 b) tight missing mass cut vs standard missing mass cut
 c) maximum likelihood fit vs moments method fit

moments fits. In the second method acceptance moments were offset 40 MeV to an adjacent mass bin. Fits were then run using these offset acceptance moments and comparisons were made with the standard angular moments fits. Both methods showed the final angular moments fits to be quite insensitive to rapid bin to bin variations of the acceptance moments.

Shown in figures 37 c) - 39 c) is a comparison of angular moments fits run using the moments fitting method, to fits run using the maximum likelihood fitting method in these three typical mass bins. The maximum likelihood and moments methods are seen to agree very well within errors in the 1.42 GeV and 1.78 GeV mass bins. At the highest mass though, there are variations on the order of a standard deviation or more in some of the moments. This variation is due to the fact that the maximum likelihood and the moments method are quite different estimators of the angular moments. Since the maximum likelihood method is the best estimator of the true angular moments³³, the maximum likelihood fitting method was used to perform the final angular moments fits in this analysis.

Chapter VIII

ENERGY INDEPENDENT PARTIAL WAVE ANALYSIS

The acceptance corrected angular moments presented in the last chapter quite clearly displayed the four leading K^* resonances. Under careful inspection, these angular moments show far more structure than simply the leading resonances would indicate. In order to understand the intricate structure hidden in the angular moments, it was necessary to perform an energy independent partial wave analysis on these moments. This was done following the method and model of Estabrooks et al. ⁴.

A. Discussion of the Exchange Model

As was mentioned earlier, the reaction $K^-p \rightarrow K^-\pi^+n$ is dominated by pion exchange in the small t' region from which the standard $K\pi n$ data sample was selected ($|t'| < 0.2 \text{ GeV}^2$). The purpose of this energy independent partial wave analysis was to extract the physical $K^-\pi^+$ elastic scattering partial wave amplitudes from these $K\pi n$ angular moments. Conceptually, this procedure entailed first isolating the pion exchange contribution to this $K^-p \rightarrow K^-\pi^+n$ reaction from other possible exchange mechanisms. Once this pion exchange portion had been isolated, an extrapolation to the pion pole ($t=\mu^2$) then yielded the real $K^-\pi^+$ elastic scattering amplitudes. The third step in this conceptual procedure was to perform a straight forward partial wave analysis on these $K^-\pi^+$

elastic scattering amplitudes resulting in $K^-\pi^+$ elastic scattering partial waves as a function of mass.

In practice these $K^-\pi^+$ elastic scattering partial waves were extracted by fitting a simple exchange model parameterization to the $K\pi n$ angular moments. In this analysis the $K^-p \rightarrow K^-\pi^+n$ production reaction was parameterized by the small t' limit of the simple Regge exchange model of reference 34. The small t' limit of this exchange model was also used in a previous $K\pi$ partial wave analysis performed by this group ⁴, and similar exchange models have been used for years in various $\pi\pi$ partial wave analysis ³⁵.

In this simple exchange model at a given $K\pi$ invariant mass the t' dependence of the helicity amplitudes ****, $L_{\lambda\pm}$, with angular momentum L , and t -channel helicity λ were parameterized by:

$$L_0(M_{K\pi}, t') = g_L(M_{K\pi}, t') \frac{\sqrt{-t}}{\mu^2 - t} \quad \text{VIII.1}$$

$$L_{1-}(M_{K\pi}, t') = (2)^{-1/2} g_L(M_{K\pi}, t') \sqrt{L(L+1)} \gamma_c(M_{K\pi}) \quad \text{VIII.2}$$

$$L_{1+}(M_{K\pi}, t') = (2)^{-1/2} g_L(M_{K\pi}, t') \sqrt{L(L+1)} \{ \gamma_c(M_{K\pi}) - 2i \gamma_a(M_{K\pi}) |t'| \} \quad \text{VIII.3}$$

**** For simplicity the nucleon helicity labels have been suppressed. See P. Estrabrooks et al., Nucl. Phys. B79, 301 (1974) for a discussion of this simplification.

$$L_{\lambda^*}(M_{K\pi}, t') = 0 \quad \lambda \geq 2$$

VIII.4

where in the high energy limit these helicity amplitudes corresponded to natural (+), and unnatural (-) parity exchange. In this model absorptive corrections were taken into account by a nonevasive cut term (the γ_c term), and higher order exchange mechanisms were taken into account by a strongly exchange degenerate ρ - A_2 Regge exchange term (the γ_a term).

The relationship of g_L to the $K^-\pi^+$ elastic scattering partial wave amplitudes, a_L , was given by:

$$g_L(M_{K\pi}, t') = \eta \frac{M_{K\pi}}{\sqrt{q}} a_L(M_{K\pi}) e^{b(M_{K\pi}) \{t - \mu^2\}}$$

VIII.5

Since the a_L are $K^-\pi^+$ elastic scattering partial wave amplitudes, these amplitudes can be decomposed into an isospin 1/2 part and an isospin 3/2 part summed with the appropriate Clebsch-Gordon coefficients:

$$a_L(M_{K\pi}) = a_L^{1/2}(M_{K\pi}) + a_L^{3/2}(M_{K\pi})/2$$

VIII.6

where a factor of $\sqrt{2}$ has been absorbed into the definition of the normalization constant, η . Only the sum of the two isotopic spin contributions, a_L , was measurable in this analysis (see section E).

The $K^-\pi^+$ elastic scattering partial wave, a_L , can be written in terms of a magnitude and phase. Below $K^-\pi^+$ scattering inelastic

threshold, elastic unitarity could be imposed on both the I=1/2 and the I=3/2 partial wave amplitude yielding:

$$a_L(M_{K\pi}) = \sqrt{2L+1} \sin(\delta_L^{1/2}(M_{K\pi})) e^{i \delta_L^{1/2}(M_{K\pi})}$$

VIII.7

$$+ \frac{\sqrt{2L+1}}{2} \sin(\delta_L^{3/2}(M_{K\pi})) e^{i \delta_L^{3/2}(M_{K\pi})}$$

In imposing elastic unitarity in this analysis we have calculated δ_L^k using the parameterization from the previous $K\pi$ partial wave analysis by Estabrooks et al. *****. Above $K\pi$ scattering inelastic threshold, a more general parameterization of these amplitudes in terms of a magnitude and phase was used:

$$a_L(M_{K\pi}) = |a_L(M_{K\pi})| e^{i \phi_L(M_{K\pi})}$$

VIII.8

At this point it is convenient to derive the relationship of the helicity amplitudes, $L_{\lambda\pm}$, presented in this chapter to the $K\pi n$ angular

***** To correct for the isospin 3/2 portion of these $K^-\pi^+$ partial waves we have used the results from P. Estabrook et al., Nucl. Phys. B133, 499 (1978) that below 1.6 GeV in mass the isospin 3/2 P and D partial waves are consistent with zero ($\delta_p^{3/2} = \delta_D^{3/2} = 0$), and that the isospin 3/2 S wave phase shift, $\delta_s^{3/2}$, is described by an effective range form:

$$\cot(\delta_s^{3/2}) = - \frac{1}{q} \left\{ \frac{1}{a} + r q^2 \right\}$$

with

$$a = -1.03 \pm 0.10 \text{ GeV}^{-1}$$

$$r = -0.94 \pm 0.50 \text{ GeV}^{-1}$$

moments discussed in the last chapter. In deriving this relationship it is necessary to define a change of basis in the definition of the helicity amplitudes. The normal helicity amplitude, H_{λ}^L , are defined in terms of the natural (+) and unnatural (-) parity exchange helicity amplitudes by the expressions:

$$\left. \begin{aligned} H_{\lambda}^L &= \frac{1}{\sqrt{2}} [L_{\lambda^+} + L_{\lambda^-}] \\ H_{-\lambda}^L &= \frac{(-1)^{\lambda}}{\sqrt{2}} [L_{\lambda^+} - L_{\lambda^-}] \end{aligned} \right\} \lambda \geq 0 \quad \text{VIII.9}$$

$$H_0^L = L_0 \quad \lambda = 0$$

Using these helicity amplitudes the unnormalized density matrix for the $K^-p \rightarrow K^-\pi^+n$ reaction was defined by the expression:

$$\rho_{\lambda'\lambda}^{LL}(M_{K\pi}, t') = H_{\lambda}^L(M_{K\pi}, t') H_{\lambda'}^{L*}(M_{K\pi}, t') \quad \text{VIII.10}$$

The physics distribution was related to these density matrix elements by the expression:

$$I(\Omega, X) = \sum_{L'L} \rho_{0'0}^{L'L}(X) Y_{L'0}(\Omega) Y_{L0}^*(\Omega) \quad \text{VIII.11}$$

$$\Omega = \cos(\theta), \phi, \quad X = M_{K\pi}, t'$$

Using the above expressions, the relationship of the density matrix elements to the angular moments, t_{lm} , defined in the last chapter, was

calculated ³⁶ to be:

$$t_{lm}^{th}(M_{K\pi}, t') = \sum_{\substack{L L' \\ \lambda \lambda'}} (-1)^{m+\lambda} [(2l+1)(2L+1)(2L'+1)]^{1/2} \begin{vmatrix} 1 & L & L' \\ m & \lambda & \lambda' \end{vmatrix}$$

VIII.12

$$\begin{vmatrix} 1 & L & L' \\ 0 & 0 & 0 \end{vmatrix} \text{Re}(\rho_{\lambda\lambda}^{LL}(M_{K\pi}, t'))$$

where the symbols in brackets are the Wigner three-J symbols. For a list of the coefficients for the above expression see reference 37. It should be noted in passing that the properties of the three-J symbols combined with this equation give the result that a resonance of spin J contributes to the even (m=0) angular moments to order 2J as was stated in the last chapter.

In performing the energy independent partial wave analysis, the $t_{lm}^{th}(M_{K\pi}, t')$ as given by equations VIII.1-VIII.12 were fit to the acceptance corrected angular moments, t_{lm} . Due to the finite statistics of this experiment this partial wave analysis was performed in two steps. In the first step of this partial wave analysis (PWA), the t' dependence of this exchange model was fit to the t' dependence of the experimental angular moments in large mass bins. These fits yielded the production parameters γ_a , γ_c , and b which were slowly varying functions of mass. In the second step of this partial wave analysis, these production parameter fits were used to integrate this exchange model over multiple small mass bins and a single large t' bin. This integrated exchange model was then fit to the angular moments in each of these bins. This second step

yielded the $K^-\pi^+$ elastic scattering waves, a_L , as a function of mass. A description is given of each of these steps in the next two sections of this chapter.

B. Multiple t' Bin Partial Wave Analysis

In this section the method used to fit the t' dependence of this exchange model to the t' dependence of the $K\pi\pi$ experimental angular moments will be discussed. In order to fit this t' dependence, the single t' bin multiple mass bin angular moments of the previous chapter could not be used. New acceptance corrected angular moments were thus fit to the standard $K\pi\pi$ data sample in large mass bins and multiple small t' bins for this purpose.

The method used in generating these angular moments, as well as the final data cuts imposed, were identical to the maximum likelihood procedure discussed in the previous chapter. Various checks of the stability of these moments to data cut changes were also performed, and these angular moments proved to be insensitive to these cut changes.

Shown in table 13 are the number of events fitted, in each t' interval of a typical large mass bin, in order to produce these angular moments as a function of t' . It is seen that even near the $K^*(895)$ resonance, where our cross section is the largest, we still had limited statistics with which to perform these fits. Above 1.2 GeV, 120 MeV mass bins had to be used in order to fit these moments. In figure 40 the Monte Carlo generated acceptance moments used to perform these fits are plotted as a function of t' in this same large mass bin, and in

TABLE 13

The Number of Events Fitted in Each t' Bin for the
Multiple t' Bin PWA in the Mass Bin $.920 \text{ GeV} < M(K\pi) < .960 \text{ GeV}$

$ t' $ Bin (GeV^2)	Number of Events in $ t' $ Bin
0.00-0.02	367
0.02-0.04	311
0.04-0.06	255
0.06-0.08	185
0.08-0.12	309
0.12-0.20	404

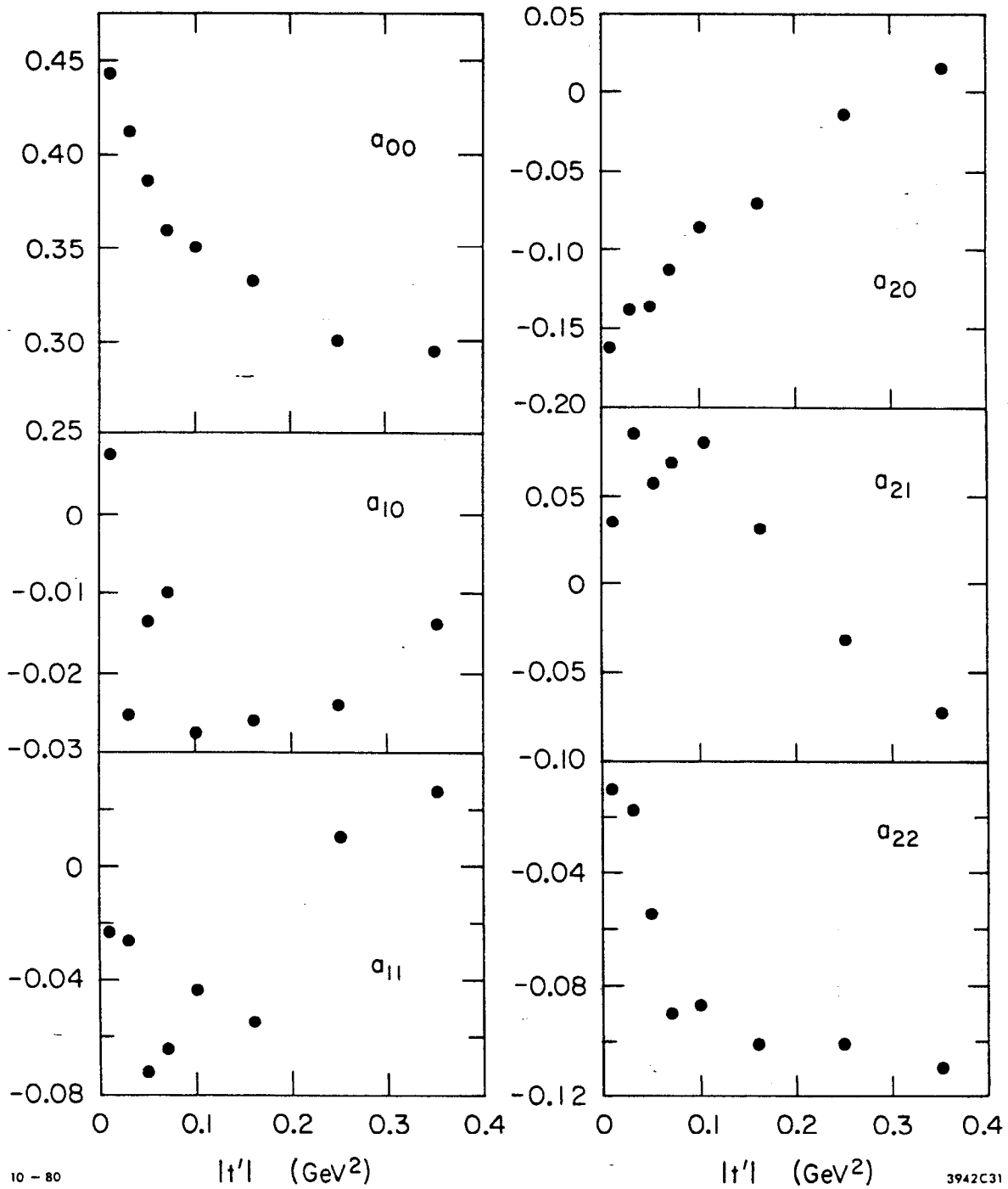
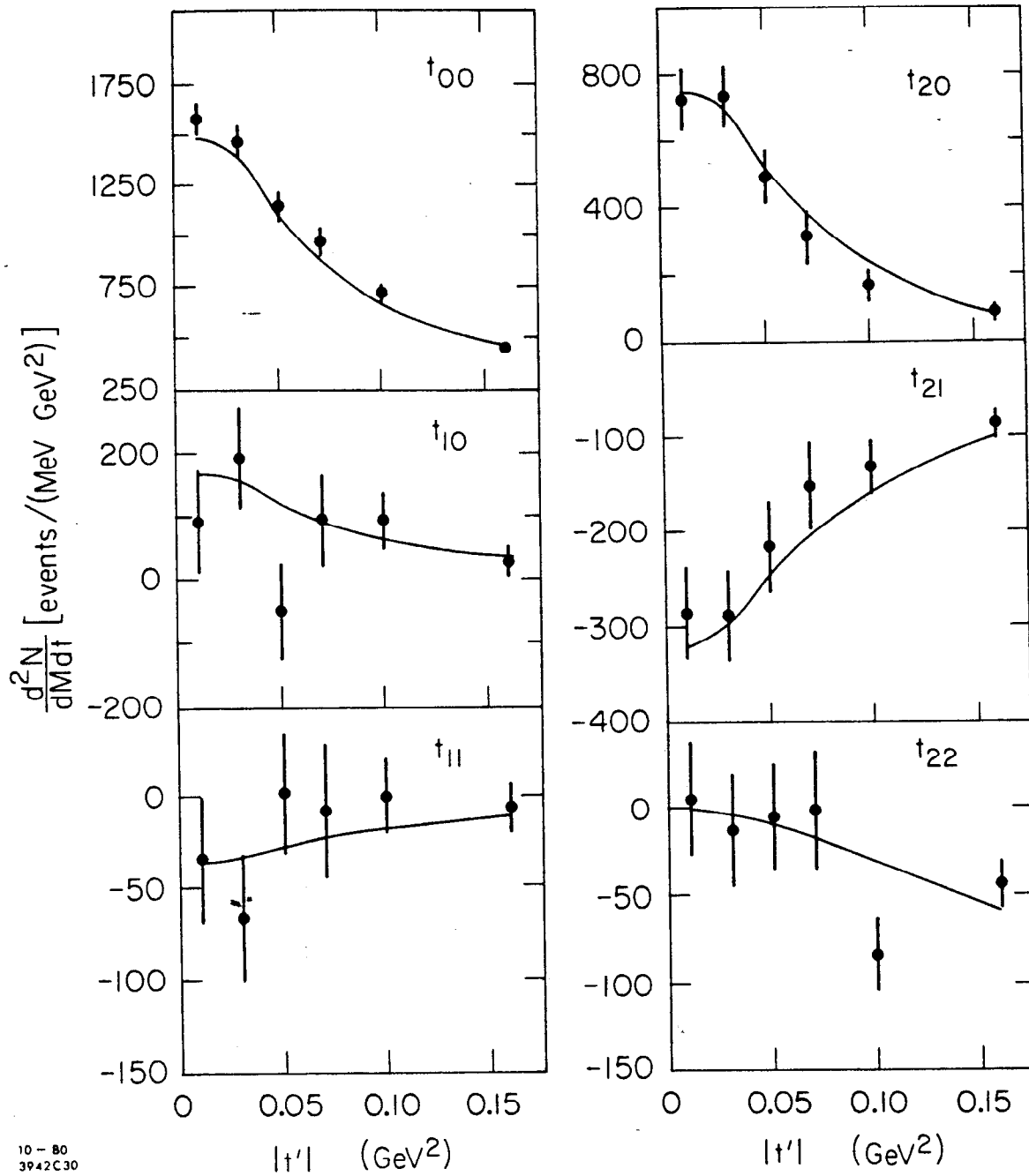


FIG. 40--The angular acceptance moments as a function of t' in the mass bin $0.90 \text{ GeV} < M(K\pi) < 0.94 \text{ GeV}$.



10 - 80
3942C30

FIG. 41--The acceptance corrected angular moments as a function of t' in the mass bin $0.90 \text{ GeV} < M(K\pi) < 0.94 \text{ GeV}$. The moments have been divided by the mass bin width and the t' bin width. The curves drawn through these moments represent the simple exchange model fit to these moments described in the text.

figure 41 the final angular moments in this same mass bin are plotted. The error bars drawn through these angular moments represent statistical errors only. An explanation will be given later of the smooth curves drawn through the angular moments in figure 41.

In each large mass bin the exchange model parameters were fit to the t' dependence of these angular moments by minimizing the chi-square:

$$\chi^2 = \sum_{i=1}^N \sum_{l, m \geq 0}^{l_{\max} m_{\max}} \frac{(t_{lm}^{\text{th}}(M_{K\pi}, t'_i) \Delta M_{K\pi} \Delta t'_i - t_{lm i})^2}{\sigma_{t_{lm i}}^2} \quad \text{VIII.13}$$

where the sum over i is a sum over the N t' bins in this given large mass bin; and $\Delta M_{K\pi}$ and $\Delta t'$ are the width of this i th bin in mass and t' respectively. Lastly the $t_{lm i}$'s are the experimental $K\pi\pi$ angular moments in the i th t' bin, and the $\sigma_{t_{lm i}}$ are the diagonal error matrix elements of the $t_{lm i}$ from the maximum likelihood angular moments fits. The $t_{lm}^{\text{th}}(M_{K\pi}, t')$ were given by equations VIII.1-VIII.2. This parameterization was found to be nearly constant in mass and t' within each given bin, so that in the fitting process the $t_{lm}^{\text{th}}(M_{K\pi}, t')$ were calculated evaluating $M(K\pi)$ and t' at the center of each mass and t' bin.

In performing this chi-squared minimization in each bin, the parameters which were minimized were the production parameters γ_a , γ_c , and b ; and also the partial wave magnitudes and phases ($|a_L|$, ϕ_L or $\delta_L^{1/2}$ when elastic unitarity was imposed). The mass dependences of the magnitudes and phases determined by this procedure were not very interesting since they were averaged over large mass bins. (Since the magnitudes and phases obtained in these minimizations were not studied in detail, the

discrete ambiguities (see section C.2) could be ignored. Any one of these ambiguous solutions would yield the same fit values for the production parameters.)

There was one more quantity which had to be determined in order to minimize the chi-square in equation VIII.13, and that was the overall normalization constant η . Since η was an energy independent parameter it had to be treated separately from the other parameters. This normalization constant was set in this analysis by requiring elasticity of the $K^*(895)$ resonance. Since in this region elastic unitarity was imposed on both the S wave and the P wave the partial wave fits in this region were highly constrained. Thus in determining η two methods were used. The first method is illustrated in table 14. In these five mass bins, adjacent to the $K^*(895)$ resonance, multiple minimizations of equation VIII.13 were performed varying the value of η for each set of fits. The value of η was fixed at the minimum of the sum of the chi-squares of these five bins. In the second method, chi-square fits to the $K^*(895)$ were run fitting a Briet-Wigner spin one resonance with a Blatt-Weiskopf barrier factor (see table 9) to the unitary P wave phase, $\delta_p^{1/2}$, resulting from the PWA fits in each of these same five bins. η was given a different value for each separate fit. The value for η was chosen in this second method where the chi-square of these Briet-Wigner fits was a minimum. These procedures produced values for η of 9.25 and 9.5 respectively. These were later found to be quite consistent with the normalization constant determined in the single t' bin PWA described in the next section of this chapter. In the final PWA fits, which determined the production parameters, the normalization constant was set to

TABLE 14

Chi-square per 31 Degree of Freedom for the Multiple t'
Bin Partial Wave Fits as a Function of Mass Bin and η

η \ Mass (GeV)	.86	.90	.94	.98	1.06	1.18	Chi-square Sum for 6 Bins
8.0	59.41	193.84	57.40	52.23	54.65	76.70	494.23
8.5	59.45	123.11	47.96	45.91	44.69	63.11	384.23
9.0	59.47	74.08	39.26	42.51	47.91	66.73	329.96
9.5	59.48	46.06	31.81	42.25	63.97	87.11	330.68
10.0	59.48	35.16	26.06	45.16	91.69	123.20	380.75

(minimum Chi-Square Sum $\eta=9.2$)

9.25 using the results from the more accurate determination of η from the single t' bin multiple mass bin PWA results.

The minimization of equation VIII.13 in these large mass bins was performed using a program developed by P. Estabrooks³⁸. This program made use of the FORTRAN minimization package MINUIT²⁸. In performing these multiple t' bin partial wave fits several assumptions were made:

- 1) The fits were run on the minimum number of angular moments needed to describe the data.
- 2) For $K\pi$ invariant masses less than 1.3 GeV, elastic unitarity was imposed on the P and D waves (Notation- S, P, D, F, and G correspond to $L = 0, 1, 2, 3,$ and 4 $K^-\pi^+$ elastic scattering partial waves respectively).
- 3) When elastic unitarity was imposed, the 13 GeV/c SLAC experiment's $I=3/2$ parameterization was used (see footnote p.183).

After the final fits had been performed, imposing the above assumptions, a few checks on the stability of these production parameter fits to cut changes were made. As a first check of the stability of these fits to cut changes, the t' fitting region was varied from the standard value of $|t'|$ less than .2 GeV² to $|t'|$ less than .3 GeV². No change, within errors, was seen in the production parameters due to this cut change. Several different assumptions were also made as to which waves had elastic unitarity imposed on them below a $K\pi$ invariant mass of 1.3 GeV, and the production parameter fits also proved to be insensitive to these assumptions.

The smooth curves drawn through the $K\pi\pi$ angular moments in figure 41 are the exchange model fit to the t' dependence of these angular moments in this typical mass bin. The t' dependence of this acceptance

corrected data was clearly quite well fit by this simple exchange model. This was quite generally the case in all mass bins. In this analysis the fit quality of the chi-square minimization of equation VIII.13 in each mass was monitored both by looking at a distributions similar to figure 41, and by monitoring the chi-square value for these fits.

Figure 42 and table 15 shows the final fits to the production parameters, γ_a , γ_c , and b , as a function of $K\pi$ invariant mass. These fits were run in 40 MeV mass bins below 1.2 GeV, and above 1.2 GeV 120 MeV mass bins were used. The error bars drawn through the fit values represent statistical errors only. Simple polynomial fits to the mass dependence of these parameter are also drawn through each production parameter plot. These simple polynomial fits were used in the second step of this partial wave analysis. The results of step two were quite insensitive to the exact form of these polynomial fits as will be mentioned later. The results of these fits were also found to agree quite well with the results from similar fits discussed in reference 4.

It should also be noted that these fits were used to check the sensitivity of the acceptance moment calculations to the exact t' distribution thrown in the Monte Carlo (see chapter VII section D). The multiple- t' bin partial wave fits represented the best estimate of the physics distribution's t' dependence. In the last iteration the Monte Carlo was thus thrown with a t' distribution from the PWA fits shown in this section. The latest angular moment fits, tlm 's, were used to throw the Monte Carlo in the Jackson angles, and the $K\pi$ mass was thrown flat within each small mass bin. Calculating new acceptance moments, and redoing all the angular moment maximum likelihood fits, the results were

TABLE 15

Production Parameter Fit Values

Mass (GeV)	b (GeV ⁻²)	γ_c	γ_a (GeV ⁻²)
0.82	3.25 ±0.34	-1.66 ±0.13	4.24 ±1.21
0.86	2.76 ±0.21	-1.36 ±0.06	5.54 ±0.47
0.90	2.09 ±0.12	-1.17 ±0.05	6.11 ±0.32
0.94	2.58 ±0.26	-1.04 ±0.08	5.40 ±0.56
0.98	2.51 ±0.33	-1.02 ±0.12	6.17 ±0.79
1.06	2.06 ±0.20	-1.17 ±0.10	0.00 ±3.91
1.18	2.16 ±0.15	-1.02 ±0.08	0.00 ±2.02
1.30	1.90 ±0.12	-0.81 ±0.05	0.00 ±0.79
1.42	2.43 ±0.10	-0.42 ±0.02	2.14 ±0.21
1.54	1.18 ±0.15	-0.49 ±0.03	0.00 ±0.37
1.66	2.10 ±0.15	-0.46 ±0.02	0.00 ±0.26
1.78	1.74 ±0.15	-0.32 ±0.02	0.00 ±0.88
1.90	1.90 ±0.16	-0.34 ±0.02	0.00 ±0.30
2.08	1.77 ±0.06	-0.27 ±0.01	0.00 ±0.21

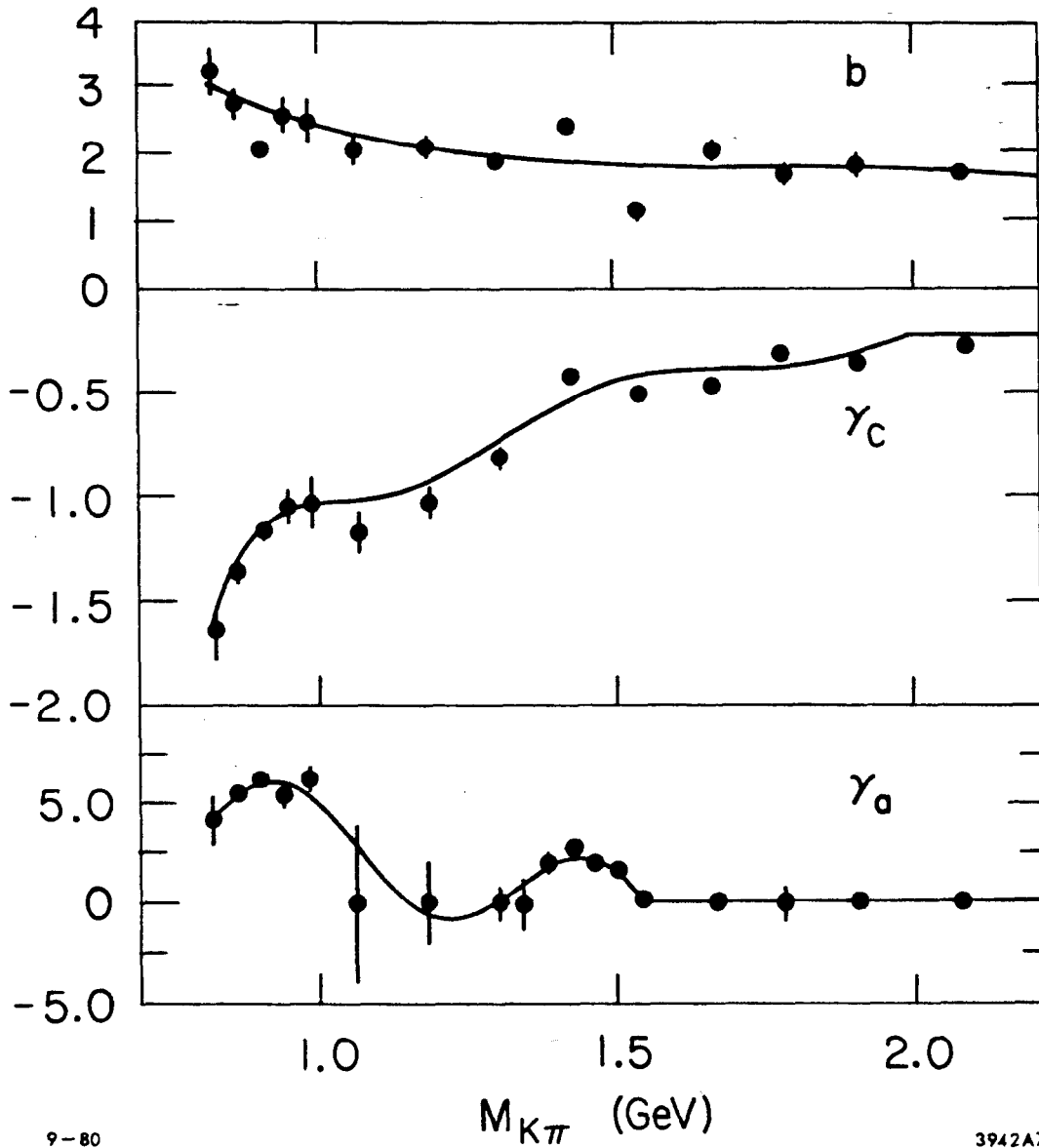


FIG. 42--The production parameters γ_a , γ_c , and b as a function of mass. The smooth curves drawn through these data points represent simple polynomial fits to the mass dependence of these parameters. These fits were used in the second step of this PWA to specify the t' dependence of the simple exchange model.

seen to agree with the results from more primitive Monte Carlo throwing.

C. Integrated t' Partial Wave Analysis

1. Fitting Method

The multiple t' bin large mass bin partial wave fits discussed in the last section yielded simple polynomial fits describing the slowly varying mass dependence of the three production parameters; γ_a , γ_c , and b . These simple polynomial fits completely determined the t' dependence of our simple exchange model. The second step in this partial wave analysis was to use this t' dependence to integrate the exchange parameterization over a single large t' bin ($|t'| < 0.2 \text{ GeV}^2$), and then to perform partial wave fits, fitting this integrated parameterization to experimental angular moments, t_{1m} , in each bin for multiple small mass bins (typically 40 MeV wide). These partial wave fits then yielded the $K^-\pi^+$ elastic scattering partial waves as a function of mass, which was the desired endpoint of this partial wave analysis. This section will describe the extraction of these $K^-\pi^+$ elastic scattering partial waves.

The angular moments, which formed the input to this multiple mass bin PWA, were fit in an identical fashion to the angular moments presented in the last chapter with one additional cut imposed. In investigating resonance structures in the $K\pi$ system in the reaction $K^-p \rightarrow K^-\pi^+n$, the removal of data from regions where the π^+ and n form narrow resonance structures is appropriate. It is not clear how one should deal with wide N^* resonance states though. In the simple exchange

parameterization of this chapter no attempt has been made to describe these N^* reflections. At low $K^-\pi^+$ mass we have thus cut out these possible N^* reflections by removing all Monte Carlo and data events with a $n\pi$ invariant mass below 1.8 GeV before performing the angular moments fits. This cut was made in the $K\pi$ invariant mass region from .80 GeV to 1.6 GeV. For $K\pi$ invariant masses above 1.6 GeV the spectrometer acceptance allowed no events with an $n\pi$ invariant mass less than 1.4 GeV to be seen. Imposing a stricter $n\pi$ cut than this at high mass would also have seriously limited our statistics. At high mass there was also little evidence for narrow N^* reflections in this data. Thus no $n\pi$ invariant mass cut was made in fitting the angular moments above 1.6 GeV.

The switch over region between making this $n\pi$ cut, and not making this $n\pi$ cut has been studied extensively. Figure 43 shows $K^-\pi^+$ elastic scattering partial waves extracted, in this region, from angular moments fit with and without the $n\pi$ cut imposed. It is seen that in this region the $n\pi$ cut makes no difference to the final partial wave magnitudes and phases extracted.

With this new set of angular moments in multiple small mass bins and a single large t' bin, our exchange parameterization could then be fit to these angular moments. The first step in this fitting procedure was to integrate the theoretical angular moments, $t_{1m}^{+h}(M_{K\pi}, t')$, over each given $M(K\pi)$ and t' bin. In performing these integrals the production parameter polynomial fits described in the last section were used. Since they were nearly independent of $M_{K\pi}$ within these small bins, this

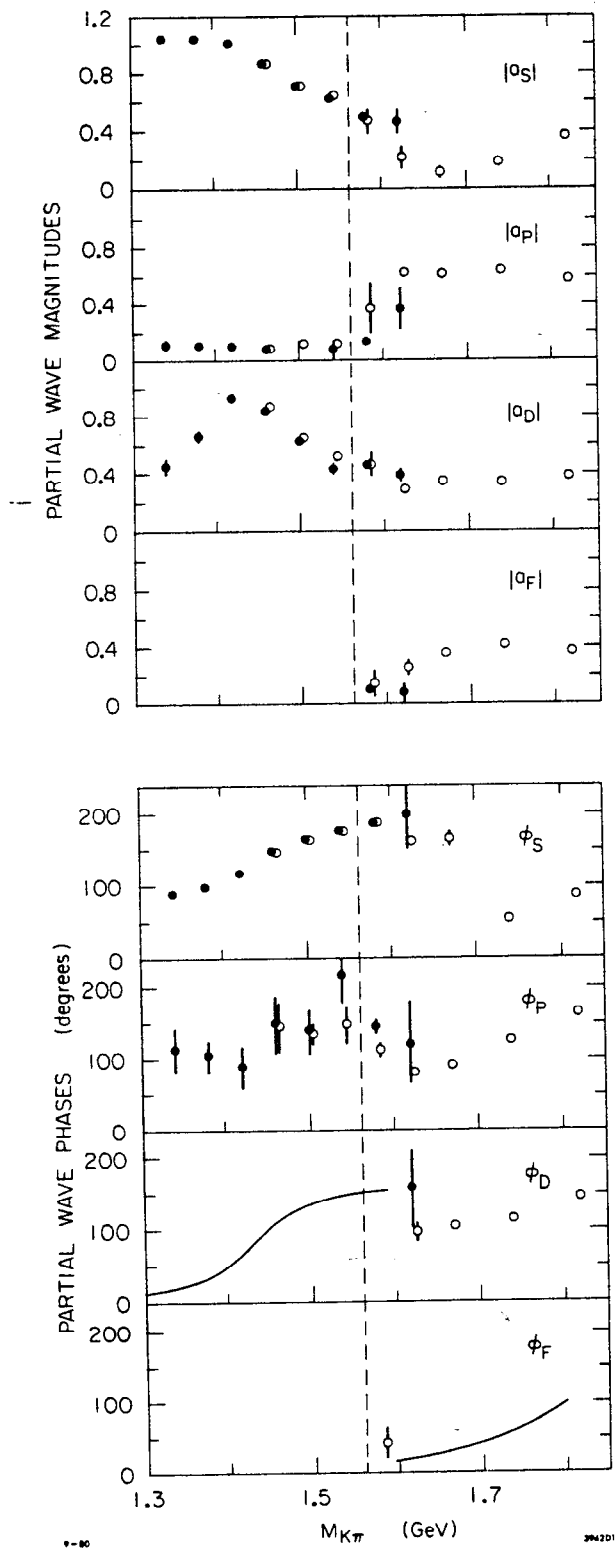


FIG. 43--The $K\pi^+$ elastic scattering partial waves in the 1.40 GeV- 1.60 GeV mass region with (\bullet) and without (\circ) a cut of $M(n\pi) > 1.8$ GeV imposed on the data. The overall phase has been fixed to the Briet-Wigner curves drawn on these plots.

integral was given by the expression:

$$t_{lm}^{th} = \int_{-0.2 \text{ GeV}^2}^{0.0 \text{ GeV}^2} t_{lm}^{th}(M_{K\pi}, t') dt' \quad \Delta M_{K\pi} \quad \text{VIII.14}$$

where $\Delta M_{K\pi}$ is the width of the given mass bin, $M_{K\pi}$ is the mass at the center of this bin, and $t_{lm}^{th}(M_{K\pi}, t')$ is given by equations VIII.1-VIII.12.

In the next step in this integrated t' bin PWA, these integrated angular moments were then fit to these experimental angular moments within the given multiple mass bins. These fits were performed in each given bin by minimizing the chi-square:

$$\chi^2 = \sum_{\substack{l_{\max} \\ l_m \geq 0 \\ l_{m'} \geq 0}}^{m_{\max}} \frac{(t_{lm}^{th} - t_{lm}) (t_{l'm'}^{th} - t_{l'm'})}{E_{lml'm'}^{-1}} \quad \text{VIII.15}$$

where the $t_{l'm'}$'s are the experimental angular moments, and the t_{lm}^{th} are the integrated theoretical angular moments given given by equation VIII.14. The matrix E is the covariance matrix from the maximum likelihood fits which produced the $t_{l'm'}$'s. It was necessary to use the fully correlated error matrix in these fits since the t_{lm} fits were highly correlated for masses above 1.5 GeV.

In performing this chi-square minimization in each bin, the parameters which were minimized were the partial wave magnitudes and phases ($|a_L|$, ϕ_L ; or $\delta_L^{1/2}$ when elastic unitarity was imposed). The only other parameter which needed to be specified in order to perform these fits was the energy independent normalization parameter η . This

normalization constant was determined in this step of the PWA in exactly the same manner as it was determined in the multiple t' bin PWA (see the previous section). The resulting normalization constant, η , from this procedure was a more accurate determination of the normalization than the calculated in the multiple t' bin PWA since smaller mass bins and more mass bins were used in this determination.

The chi-square minimization of equation VIII.15 with respect to the $K^-\pi^+$ elastic scattering partial waves was performed using a program developed by P. Estabrooks³⁸. This program made use of the FORTRAN minimization package MINUIT. The subroutine MINOS in this MINUIT²⁸ package was used to investigate nonparabolic errors. In performing these final minimizations in each mass bin the fit quality was monitored by observing the final chi-square value for each fit. As a check on the sensitivity of these fits to the exact polynomial form used for the production parameter fits, various other polynomial fits to the production parameters were tried. The resulting fits were quite insensitive to the exact to the exact polynomial mass parameterization used.

In performing the final integrated t' partial wave fits several assumptions were made:

- 1) The fits were run using the minimum number of angular moments needed to describe the data.
- 2) Elastic unitarity was imposed on the S wave for masses less than 1.24 GeV, and on the P wave for mass less than 1.12 GeV.
- 3) When elastic unitarity was imposed, the 13 GeV/c SLAC experiment's $I=3/2$ parameterization was used (see footnote p.183)

Before showing the final $K^- \pi^+$ elastic scattering partial waves fit using this procedure, it is first necessary to discuss ambiguities in this PWA.

2. Ambiguities and Solution Classification

The minimization of the chi-squared sum in equation VIII.15 does not have a unique solution. Two different types of ambiguities arise mathematically in this minimization process: 1) continuous ambiguities, and 2) discrete ambiguities.

The continuous ambiguities arose from the fact that it is impossible to see any change in a physics distribution when each of the helicity amplitudes, $L_{\lambda\pm}$, is multiplied by a constant complex phase factor $e^{i\phi}$. Since only the square of these amplitudes is observable this fact is easily proven. There was thus one overall phase which could not be determined in these partial wave fits. In this analysis for fitting and graphing purposes, this phase was fixed by setting the phase of one of the partial waves (see the next section).

The discrete ambiguities can best be explained by examining the dominant pion exchange portion of the helicity amplitudes. If only pion exchange were present in this reaction, only helicity zero amplitudes would be nonzero in our exchange model. In this case equation VIII.11 can be written:

$$I(\Omega, X) = \sum_{\substack{LL \\ \lambda\lambda}} \rho_{\lambda\lambda}^{LL}(X) Y_{L\lambda}(\Omega) Y_{L\lambda}^*(\Omega)$$

VIII.16

$$\Omega = \cos(\theta_1), \phi_1 \quad X = M_{K\pi} t'$$

Some algebraic manipulations of this expression with equations VIII.1-VIII.12 leads to the one particle exchange model for this reaction:

$$I(\Omega, X) = \eta^2 \frac{M_{K\pi}^2}{q} \frac{-t}{(\mu^2 - t)^2} e^{2b(M_{K\pi})(t - \mu^2)}$$

VIII.17

$$\left| \sum_{L=0}^{L_{\max}} (2L+1) a_L(M_{K\pi}) P_L(\cos(\theta_j)) \right|^2$$

Note that various factors of $\sqrt{4\pi}$ have been absorbed into the definition of η . Now the expression in brackets:

$$\sum_{L=0}^{L_{\max}} (2L+1) a_L P_L(z) \quad z = \cos(\theta_j) \quad \text{VIII.18}$$

is just a complex polynomial of order L_{\max} in z . This polynomial can thus be factored into its L_{\max} roots, z_i :

$$\sum_{L=0}^{L_{\max}} (2L+1) a_L P_L(z) = C \prod_{i=1}^{L_{\max}} (z - z_i) \quad \text{VIII.19}$$

where the z_i 's are the Barrelet zero's³⁹. In this one particle exchange model, only the square of this expression is observable, and thus if a given root, z_i , is replaced by its complex conjugate z_i^* , the observed distribution remains the same. Taking all permutations of complex conjugated roots this procedure yields $2^{L_{\max}}$ ambiguous solutions. The addition of the helicity one amplitudes into these equations does

not change this ambiguity argument since these terms make only small contributions to this reaction in comparison to the dominant pion exchange terms. Thus the minimization of the chi-square in equation VIII.15 yielded $2^{L_{max}}$ discrete ambiguous solutions.

In practice within a given $M(K\pi)$ and t' bin, these ambiguous solutions were found by first minimizing equation VIII.15, and obtaining one of these solutions. Once this solution had been found the program calculated the Barrelet zeros for this particular solution. The program then formed all $2^{L_{max}}$ possible polynomial combinations of these Barrelet zeros. Using these polynomials the program then calculated the partial wave magnitudes and phases from these polynomials by solving equation VIII.19. The calculated partial wave magnitudes and phases for each ambiguous solution were then used as starting values in the chi-square minimization of equation VIII.15. The results of these chi-square minimizations yielded the $2^{L_{max}}$ ambiguous solutions desired. It was necessary to re-minimize equation VIII.15 since when helicity one amplitudes are added the relationship described in equation VIII.19 were only approximately correct.

In order to investigate the resonance structures present in the final $K^-\pi^+$ partial waves, the mass dependence of these waves needed to be studied. With $2^{L_{max}}$ ambiguous solutions in each mass bin, a prohibitive number of combinations existed for plotting these solutions as a function of mass. Thus these ambiguous solutions had to be classified and associated as a function of mass.

The Barrelet zeros provided a convenient method of classifying the $2^{L_{max}}$ solutions within each mass bin. Solutions in this analysis were

classified by the sign of the imaginary part of each Barrelet zero for the partial wave fit within each mass bin. Figure 44 shows the Barrelet zeros calculated in this partial wave analysis as a function of mass (The Barrelet zero's plotted have been chosen so that $\text{Im}(z_i)$ is continuous as a function of mass). The Barrelet zero's plotted are seen to be smoothly varying functions of mass. A smoothness argument was thus used to associate solutions in adjacent mass bins. By applying smoothness associations in this analysis the assumption has been made that bin to bin variations were not present in these Barrelet zeros. Thus if there were rapid bin to bin variations in the final $K^-\pi^+$ elastic scattering partial waves, these variations would not have been seen in this analysis.

In making these mass associations we have imposed the condition that new partial wave amplitudes had to rise from zero in a counter clockwise direction on a resonance loop in an Argand diagram. This condition is basically the Wigner condition ⁴⁰. In terms of Barrelet zeros this implied that when, increasing in mass, a new partial wave was added, the associated Barrelet zero had to turn on with a negative imaginary part. Thus:

$\text{Im}(z_1) < 0$ below the first P wave resonance
 $\text{Im}(z_2) < 0$ below the first D wave resonance
 $\text{Im}(z_3) < 0$ below the first F wave resonance
 $\text{Im}(z_4) < 0$ below the first G wave resonance

The above condition along with the imposition of elastic unitarity below 1.30 GeV established a unique solution below this mass. Furthermore increasing in mass and making bin to bin associations, an ambiguous solution could be added only when one of the $\text{Im}(z_i)$ approached very close

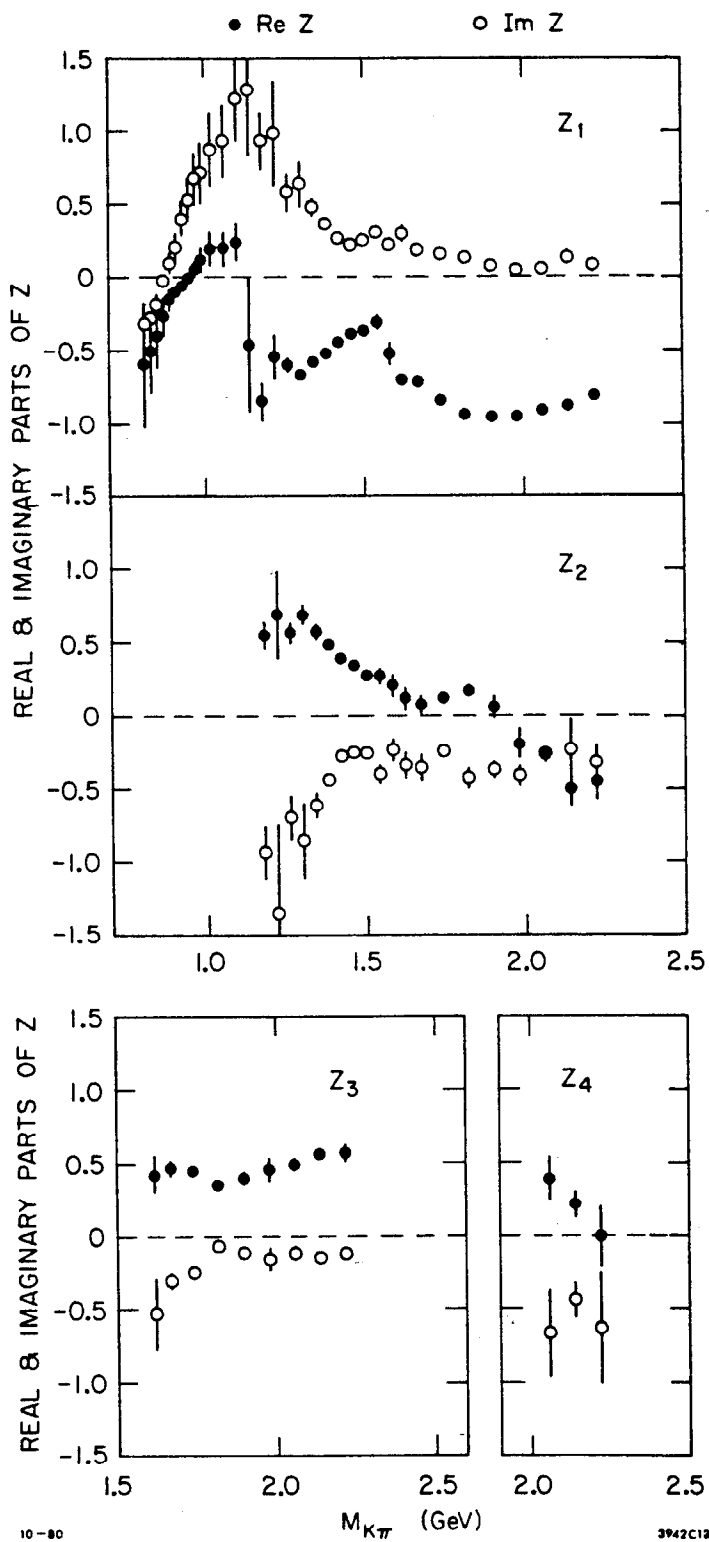


FIG. 44--The Barrelet zeros as a function of mass (see text for a description).

to zero within errors. The problem of classifying ambiguous solutions thus reduced to determining when the imaginary part of a given Barrelet zero was within a few standard deviations of zero.

In figure 44, error bars are drawn through the Barrelet zeros. These error bars are statistical in nature only. These errors were generated by first finding a given partial wave solution. The fully correlated error matrix from this partial wave solution was then used in conjunction with a Gaussian random number generator to offset this partial wave solution's magnitudes and phases. Using these smeared magnitudes and phases, a set of Barrelet zeros was then calculated. By repeating this process one thousand times for each partial wave fit, the errors on the associated Barrelet zeros were calculated. It should be noted that smearing the fitted magnitudes and phases in a correlated Gaussian manner was not well justified in certain mass bins. In these bins larger Gaussian errors were thrown to check for possible crossings of these Barrelet zeros. We have defined a Barrelet zero cross when the imaginary part of a given Barrelet zero is within three standard deviations of zero.

As was mentioned before, imposing elastic unitarity on the partial wave fits established a unique solution below 1.3 GeV. The first possible Barrelet zero cross can be seen in figure 44 to be in the $\text{Im}(z_3)$ in the region around 1.86 GeV. The next possible change of sign of the imaginary part of a Barrelet zero can be seen to be in the $\text{Im}(z_1)$ around 2.02 GeV. Therefore defining these two Barrelet zero crossing points, a single unique solution was found in this analysis below 1.86 GeV. From 1.86 GeV to 2.02 GeV two ambiguous solutions were found in this

analysis, and above 2.02 GeV four ambiguous solutions existed. It should be noted that in the region of 1.9 GeV, $\text{Im}(z_1)$ stays very close to zero. Since in this region from 1.9 GeV to 2.1 GeV, $\text{Im}(z_1)$ is very nearly zero, the ambiguous solutions that would have been added by flipping the sign of $\text{Im}(z_1)$ would have been very nearly identical. Thus no information would have been added to this analysis by allowing more than one $\text{Im}(z_1)$ crossings in this region.

Shown in table 16 are the Barrelet zero classifications of the four ambiguous solutions seen in this analysis. The next section of this chapter will give a qualitative description of these four partial wave solutions, found by minimizing equation VIII.15 in multiple mass bins and then classifying the resulting solutions as a function of mass.

3. Final $K^-\pi^+$ Elastic Scattering Partial Waves

Shown in figures 45-49 and tables 17-18 are the final $K^-\pi^+$ elastic scattering partial wave magnitudes and phases fit in this analysis. As was discussed in the last section four ambiguous solutions (solutions A-D) were obtained. All four solutions are identical below 1.86 GeV. From 1.86 GeV to 2.06 GeV only two distinct solutions can be seen, and above 2.06 GeV all four solutions are distinct. Shown in table 19 are the number of angular moments used to fit these partial waves in each mass region. These fits were run, with a 0.0 to 0.2 $\text{GeV}^2 |t'|$ cut, in 40 MeV mass bins below 1.72 GeV, and 80 MeV mass bins above this mass. It should be noted that table 18 presents overlapping solutions run in 80 MeV bins every 40 MeV above 1.72 GeV. The error bars in these

TABLE 16

The Barrelet Zero Solution Classifications

solution \ Mass (GeV)	1.30 - 1.86			1.86 - 2.02				2.02 - 2.30			
	z ₁	z ₂	z ₃	z ₁	z ₂	z ₃	z ₄	z ₁	z ₂	z ₃	z ₄
A	+	-	-	+	-	+	-	-	-	+	-
B	+	-	-	+	-	-	-	-	-	-	-
C	+	-	-	+	-	+	-	+	-	+	-
D	+	-	-	+	-	-	-	+	-	-	-

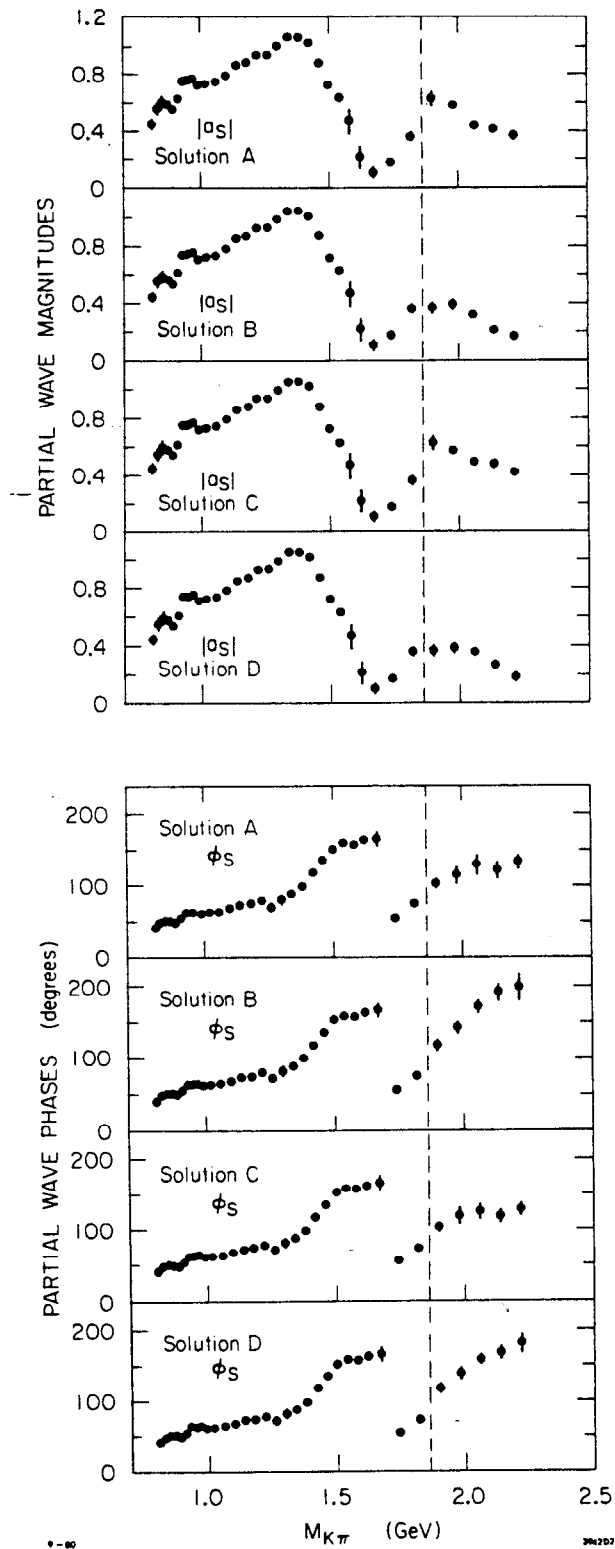


FIG. 45--The four ambiguous $K^-\pi^+$ elastic scattering S wave magnitudes and phases.

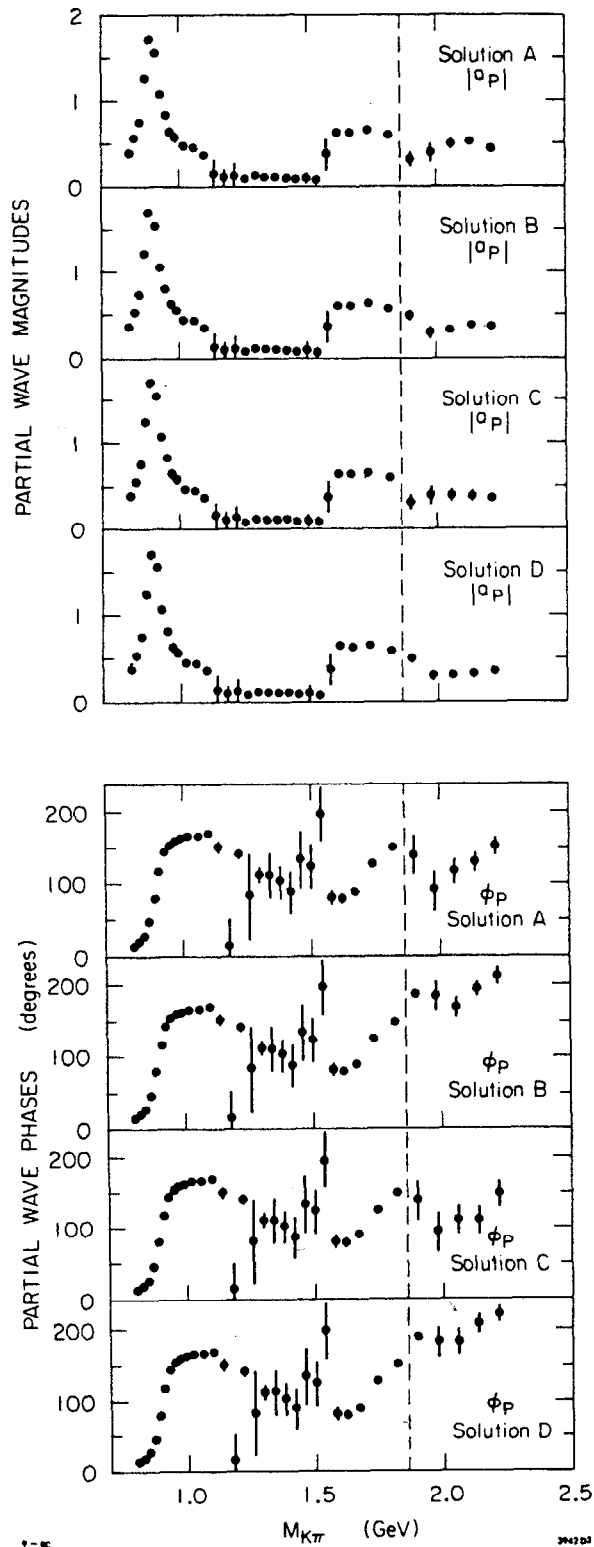


FIG. 46--The four ambiguous $K^-\pi^+$ elastic scattering P wave magnitudes and phases.

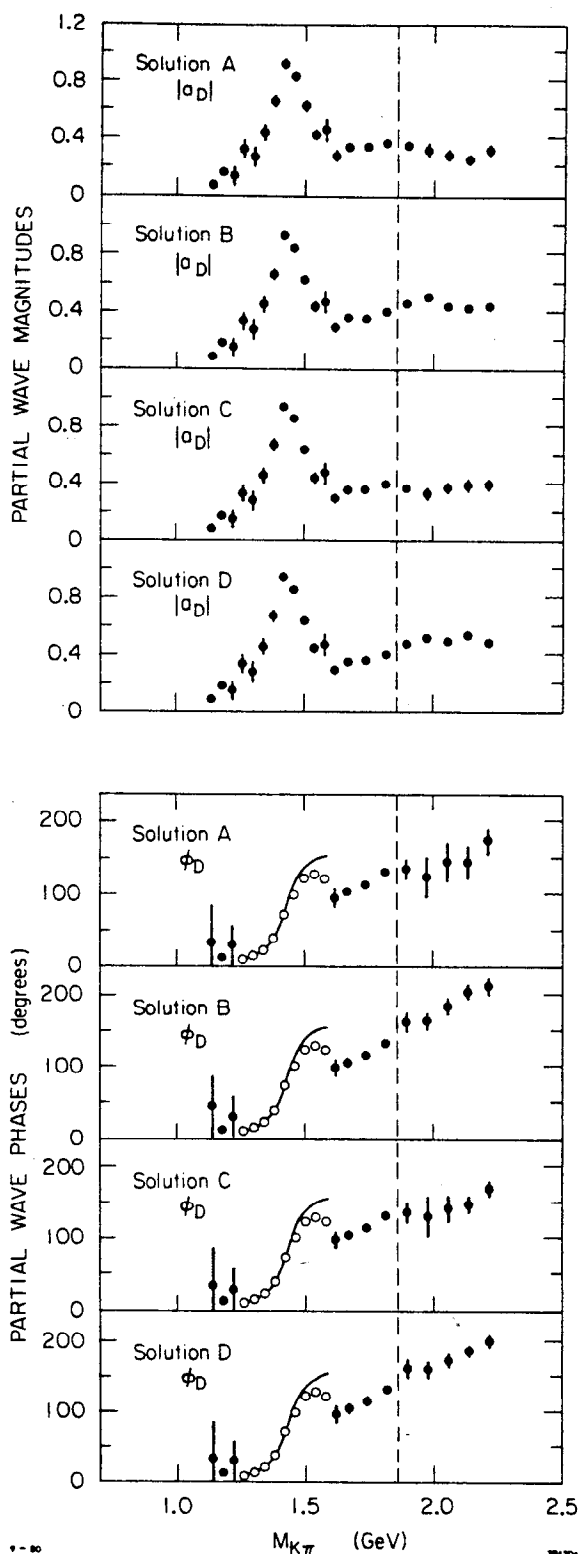


FIG. 47--The four ambiguous $K^-\pi^+$ elastic scattering D wave magnitudes and phases. The smooth curve drawn on the phase plots represents the D wave phase predicted by the $K^*(1430)$ Breit-Wigner resonance fit in table 20. The overall phase in this region was fixed to the phase represented by the symbol o.

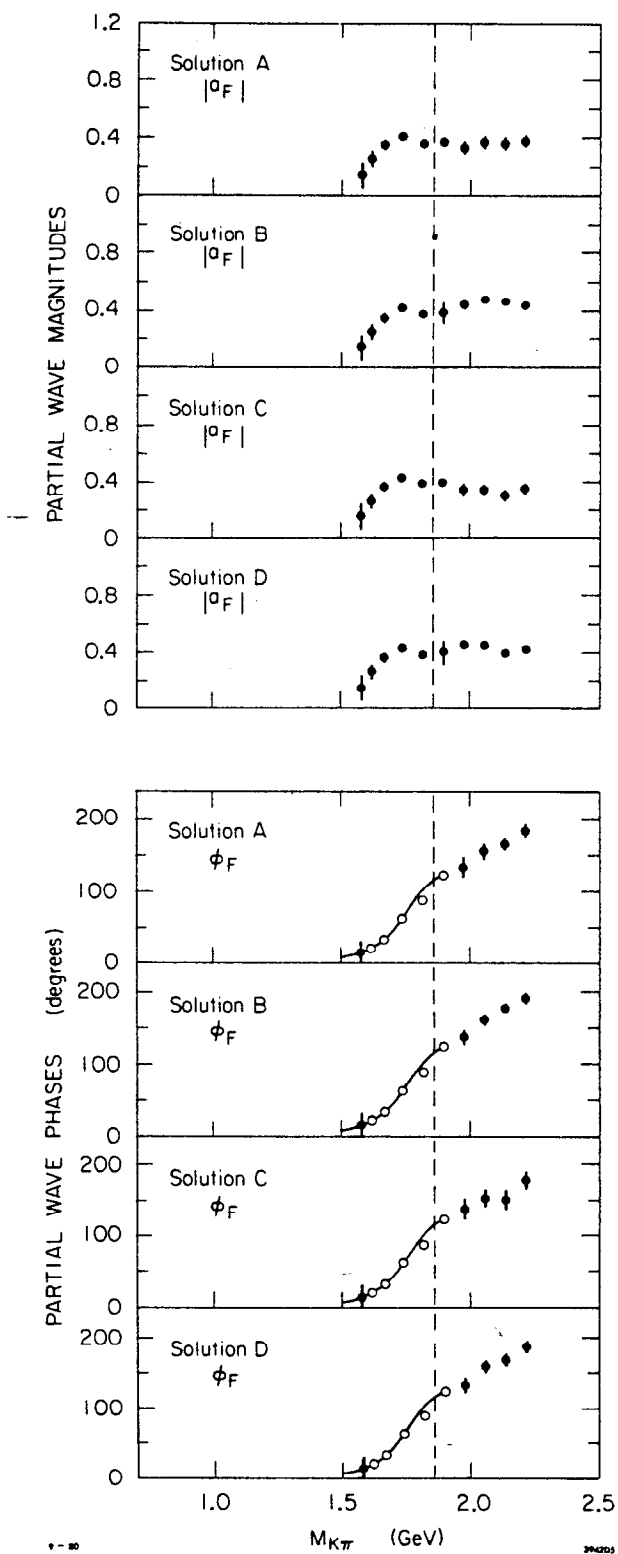


FIG. 48--The four ambiguous $K^-\pi^+$ elastic scattering F wave magnitudes and phases. The smooth curve drawn on the phase plots represents the F wave phase predicted by the $K^*(1780)$ Breit-Wigner resonance fit in table 20. The overall phase in this region was fixed to the phase represented by the symbol o.

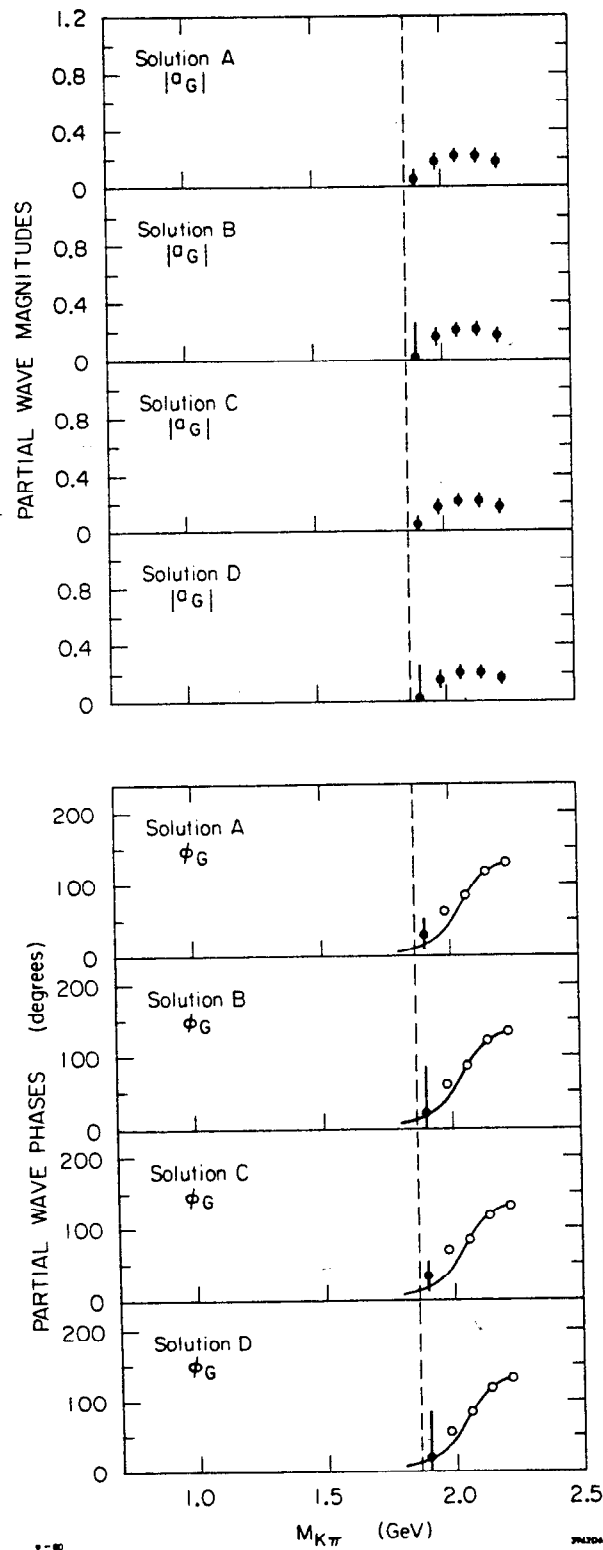


FIG. 49--The four ambiguous $K^-\pi^+$ elastic scattering G wave magnitudes and phases. The smooth curve drawn on the phase plots represents the G wave phase predicted by the $K^*(2080)$ Breit-Wigner resonance fit in table 20. The overall phase in this region was fixed to the phase represented by the symbol \circ .

TABLE 17

Partial Wave Phases for the
S and P Waves in the Elastic Region

(all phases are in degrees)

M(K π) (GeV)	I=1/2 S-Wave	I=3/2 S-Wave	I=1/2 P-Wave	I=3/2 P-Wave
0.81	31.1 \pm 2.8	-12.8	12.6 \pm 1.4	0.0
0.83	37.7 \pm 3.8	-13.6	18.2 \pm 1.6	0.0
0.85	40.8 \pm 4.4	-14.3	25.7 \pm 1.6	0.0
0.87	39.9 \pm 2.5	-15.1	45.6 \pm 1.1	0.0
0.89	37.1 \pm 2.0	-15.8	79.5 \pm 3.4	0.0
0.91	42.3 \pm 2.7	-16.4	116.9 \pm 2.1	0.0
0.93	51.3 \pm 2.8	-17.1	142.3 \pm 1.4	0.0
0.95	51.6 \pm 3.1	-17.7	151.9 \pm 1.5	0.0
0.97	52.4 \pm 3.3	-18.3	158.2 \pm 1.7	0.0
0.99	49.0 \pm 3.0	-18.9	160.8 \pm 1.7	0.0
1.02	49.2 \pm 1.9	-19.8	164.6 \pm 1.3	0.0
1.06	50.1 \pm 1.7	-20.9	165.2 \pm 1.3	0.0
1.10	53.4 \pm 1.7	-21.9	168.0 \pm 1.6	0.0
1.14	59.0 \pm 3.5	-22.8		
1.18	60.1 \pm 1.2	-23.7		
1.22	64.5 \pm 2.0	-24.5		

TABLE 18

**K π Elastic Scattering Partial Wave
Magnitude and Phases in the Inelastic Region
(all phases are in degrees)**

M(K π)	ϕ_{rot}	S Magnitude	S Phase	P Magnitude	P Phase	D Magnitude	D Phase	F Magnitude	F Phase	G Magnitude	G Phase
1.14	0	0.85 \pm 0.02	72 \pm 4	0.13 \pm 0.17	151 \pm 8	0.08 \pm 0.02	33 \pm 53				
1.18	0	0.87 \pm 0.01	73 \pm 1	0.10 \pm 0.09	13 \pm 38	0.17 \pm 0.03	13 \pm 5				
1.22	0	0.92 \pm 0.01	78 \pm 2	0.11 \pm 0.09	141 \pm 7	0.14 \pm 0.07	30 \pm 28				
1.26	0	0.93 \pm 0.03	72 \pm 6	0.08 \pm 0.03	82 \pm 59	0.33 \pm 0.06	10				
1.30	0	0.99 \pm 0.02	82 \pm 7	0.12 \pm 0.02	112 \pm 10	0.27 \pm 0.07	15				
1.34	0	1.05 \pm 0.02	88 \pm 3	0.11 \pm 0.04	111 \pm 31	0.45 \pm 0.05	23				
1.38	0	1.05 \pm 0.03	98 \pm 2	0.10 \pm 0.02	102 \pm 22	0.67 \pm 0.04	39				
1.42	0	1.02 \pm 0.03	117 \pm 1	0.10 \pm 0.02	87 \pm 29	0.93 \pm 0.03	72				
1.46	-14	0.87 \pm 0.03	148 \pm 1	0.08 \pm 0.02	147 \pm 40	0.85 \pm 0.03	114				
1.50	-14	0.71 \pm 0.02	165 \pm 2	0.10 \pm 0.03	136 \pm 30	0.63 \pm 0.03	137				
1.54	-19	0.62 \pm 0.02	177 \pm 4	0.08 \pm 0.05	215 \pm 38	0.44 \pm 0.04	148				
1.58	-31	0.46 \pm 0.09	188 \pm 5	0.37 \pm 0.18	112 \pm 9	0.46 \pm 0.08	153	0.14 \pm 0.09	42 \pm 21		
1.62	0	0.21 \pm 0.08	163 \pm 6	0.63 \pm 0.03	80 \pm 6	0.29 \pm 0.04	97 \pm 12	0.25 \pm 0.05	21		
1.66	0	0.15 \pm 0.04	172 \pm 5	0.62 \pm 0.02	87 \pm 3	0.34 \pm 0.02	102 \pm 6	0.32 \pm 0.03	30		
1.70	0	0.04 \pm 0.02	94 \pm 47	0.65 \pm 0.01	103 \pm 2	0.33 \pm 0.01	105 \pm 6	0.38 \pm 0.03	44		
1.74	0	0.18 \pm 0.03	55 \pm 5	0.64 \pm 0.02	126 \pm 2	0.34 \pm 0.01	114 \pm 5	0.41 \pm 0.02	63		
1.78	0	0.31 \pm 0.03	70 \pm 3	0.61 \pm 0.02	145 \pm 3	0.36 \pm 0.01	129 \pm 4	0.41 \pm 0.02	85		
1.82	-14	0.36 \pm 0.03	87 \pm 3	0.58 \pm 0.02	163 \pm 3	0.38 \pm 0.02	145 \pm 4	0.37 \pm 0.03	103		

* ϕ_{rot} is the overall phase rotation which has been added to the phases in this table to obtain the plots shown in figures 45-49.

TABLE 18 (cont.)

(a) SOLUTION A

M(Kw)	ϕ_{rot}	S Magnitude	S Phase	P Magnitude	P Phase	D Magnitude	D Phase	F Magnitude	F Phase	G Magnitude	G Phase
1.86	0	0.59 ± 0.03	94 ± 3	0.38 ± 0.04	145 ± 8	0.31 ± 0.03	134 ± 8	0.37 ± 0.02	116		
1.90	0	0.62 ± 0.05	104 ± 7	0.31 ± 0.08	139 ± 27	0.36 ± 0.03	135 ± 13	0.38 ± 0.02	124	0.04 ± 0.07	32 ± 22
1.94	0	0.62 ± 0.03	112 ± 8	0.27 ± 0.04	114 ± 35	0.35 ± 0.05	136 ± 13	0.36 ± 0.02	129	0.10 ± 0.08	33 ± 26
1.98	26	0.57 ± 0.02	89 ± 12	0.39 ± 0.10	64 ± 26	0.32 ± 0.05	99 ± 28	0.33 ± 0.05	109 ± 14	0.17 ± 0.06	38
2.02	26	0.44 ± 0.02	97 ± 13	0.52 ± 0.05	77 ± 14	0.29 ± 0.03	103 ± 25	0.37 ± 0.04	122 ± 9	0.23 ± 0.04	59
2.06	0	0.42 ± 0.02	130 ± 14	0.49 ± 0.05	116 ± 16	0.29 ± 0.04	146 ± 27	0.37 ± 0.04	156 ± 10	0.21 ± 0.05	84
2.10	0	0.41 ± 0.02	127 ± 14	0.50 ± 0.03	123 ± 14	0.25 ± 0.03	146 ± 29	0.37 ± 0.04	162 ± 9	0.19 ± 0.05	105
2.14	0	0.40 ± 0.02	123 ± 12	0.50 ± 0.02	129 ± 12	0.26 ± 0.03	144 ± 23	0.36 ± 0.04	166 ± 8	0.21 ± 0.05	119
2.18	0	0.39 ± 0.02	131 ± 11	0.47 ± 0.02	138 ± 12	0.29 ± 0.04	159 ± 18	0.35 ± 0.04	177 ± 8	0.21 ± 0.05	127
2.22	0	0.37 ± 0.03	134 ± 10	0.42 ± 0.02	151 ± 12	0.32 ± 0.04	174 ± 16	0.38 ± 0.04	184 ± 9	0.17 ± 0.05	132
2.26	0	0.36 ± 0.03	137 ± 9	0.41 ± 0.02	160 ± 10	0.30 ± 0.04	182 ± 13	0.34 ± 0.04	188 ± 8	0.17 ± 0.04	135

(b) SOLUTION B

M(Kw)	ϕ_{rot}	S Magnitude	S Phase	P Magnitude	P Phase	D Magnitude	D Phase	F Magnitude	F Phase	G Magnitude	G Phase
1.86	0	0.33 ± 0.03	107 ± 3	0.55 ± 0.02	179 ± 3	0.42 ± 0.02	159 ± 4	0.37 ± 0.02	116		
1.90	0	0.37 ± 0.04	118 ± 7	0.50 ± 0.05	188 ± 6	0.45 ± 0.02	162 ± 14	0.38 ± 0.08	124	0.02 ± 0.24	21 ± 64
1.94	0	0.37 ± 0.09	130 ± 6	0.43 ± 0.14	196 ± 9	0.47 ± 0.02	166 ± 8	0.39 ± 0.06	129	0.06 ± 0.08	17 ± 42
1.98	21	0.39 ± 0.03	122 ± 9	0.30 ± 0.06	164 ± 21	0.49 ± 0.02	142 ± 12	0.44 ± 0.03	116 ± 10	0.16 ± 0.06	38
2.02	11	0.35 ± 0.02	142 ± 7	0.34 ± 0.02	138 ± 11	0.45 ± 0.02	154 ± 9	0.50 ± 0.02	129 ± 6	0.22 ± 0.05	59
2.06	0	0.31 ± 0.02	171 ± 10	0.34 ± 0.02	169 ± 14	0.43 ± 0.02	185 ± 12	0.48 ± 0.02	161 ± 7	0.21 ± 0.05	84
2.10	0	0.26 ± 0.02	187 ± 10	0.36 ± 0.02	187 ± 12	0.43 ± 0.03	201 ± 11	0.48 ± 0.03	170 ± 7	0.19 ± 0.05	105
2.14	0	0.21 ± 0.02	191 ± 12	0.39 ± 0.02	195 ± 9	0.42 ± 0.02	205 ± 10	0.47 ± 0.02	177 ± 6	0.21 ± 0.05	119
2.18	0	0.20 ± 0.02	199 ± 14	0.38 ± 0.02	204 ± 11	0.43 ± 0.02	210 ± 11	0.45 ± 0.02	187 ± 6	0.21 ± 0.05	127
2.22	0	0.17 ± 0.03	198 ± 19	0.37 ± 0.02	213 ± 12	0.43 ± 0.02	212 ± 12	0.44 ± 0.03	191 ± 8	0.17 ± 0.05	132
2.26	0	0.14 ± 0.03	194 ± 21	0.37 ± 0.02	214 ± 12	0.41 ± 0.02	216 ± 13	0.40 ± 0.03	195 ± 8	0.17 ± 0.05	135

TABLE 18 (cont.)

(c) SOLUTION C

M(Kw)	ϕ_{rot}	S Magnitude	S Phase	P Magnitude	P Phase	D Magnitude	D Phase	F Magnitude	F Phase	G Magnitude	G Phase
1.86	0	0.59 ± 0.03	94 ± 3	0.36 ± 0.04	145 ± 8	0.31 ± 0.03	134 ± 8	0.37 ± 0.02	116		
1.90	0	0.62 ± 0.05	104 ± 7	0.31 ± 0.08	139 ± 27	0.36 ± 0.03	135 ± 13	0.38 ± 0.02	124	0.04 ± 0.07	32 ± 22
1.94	0	0.62 ± 0.03	112 ± 8	0.27 ± 0.04	114 ± 35	0.35 ± 0.05	136 ± 13	0.36 ± 0.02	129	0.10 ± 0.08	33 ± 26
1.98	31	0.57 ± 0.02	89 ± 12	0.39 ± 0.10	64 ± 26	0.32 ± 0.05	99 ± 28	0.33 ± 0.05	109 ± 14	0.17 ± 0.06	38
2.02	32	0.50 ± 0.03	93 ± 11	0.45 ± 0.07	70 ± 17	0.36 ± 0.03	102 ± 19	0.34 ± 0.04	119 ± 11	0.23 ± 0.04	59
2.06	0	0.49 ± 0.02	126 ± 11	0.39 ± 0.07	110 ± 20	0.37 ± 0.04	141 ± 19	0.33 ± 0.04	154 ± 12	0.21 ± 0.04	84
2.10	0	0.51 ± 0.02	120 ± 10	0.37 ± 0.06	110 ± 21	0.38 ± 0.04	141 ± 14	0.31 ± 0.04	154 ± 12	0.19 ± 0.05	105
2.14	0	0.48 ± 0.03	119 ± 9	0.38 ± 0.06	110 ± 19	0.38 ± 0.04	146 ± 12	0.29 ± 0.04	152 ± 13	0.21 ± 0.05	119
2.18	0	0.45 ± 0.02	129 ± 9	0.38 ± 0.05	125 ± 17	0.38 ± 0.04	159 ± 12	0.30 ± 0.04	168 ± 12	0.21 ± 0.05	127
2.22	0	0.42 ± 0.03	129 ± 9	0.35 ± 0.02	147 ± 18	0.39 ± 0.04	168 ± 11	0.34 ± 0.04	179 ± 12	0.17 ± 0.05	132
2.26	0	0.40 ± 0.03	132 ± 11	0.33 ± 0.03	151 ± 23	0.40 ± 0.05	175 ± 12	0.28 ± 0.04	179 ± 16	0.17 ± 0.05	135

(d) SOLUTION D

M(Kw)	ϕ_{rot}	S Magnitude	S Phase	P Magnitude	P Phase	D Magnitude	D Phase	F Magnitude	F Phase	G Magnitude	G Phase
1.86	0	0.33 ± 0.03	107 ± 3	0.55 ± 0.02	179 ± 3	0.42 ± 0.02	159 ± 4	0.37 ± 0.02	116		
1.90	0	0.37 ± 0.04	118 ± 7	0.50 ± 0.05	188 ± 6	0.45 ± 0.02	162 ± 14	0.38 ± 0.08	124	0.02 ± 0.24	21 ± 64
1.94	0	0.37 ± 0.09	130 ± 6	0.43 ± 0.14	196 ± 9	0.47 ± 0.02	166 ± 8	0.39 ± 0.06	129	0.06 ± 0.08	17 ± 42
1.98	17	0.39 ± 0.03	122 ± 9	0.30 ± 0.06	164 ± 21	0.49 ± 0.02	142 ± 12	0.44 ± 0.03	116 ± 10	0.16 ± 0.06	38
2.02	17	0.38 ± 0.02	131 ± 6	0.29 ± 0.02	149 ± 16	0.49 ± 0.02	144 ± 8	0.46 ± 0.02	127 ± 7	0.22 ± 0.05	59
2.06	0	0.35 ± 0.02	158 ± 8	0.29 ± 0.02	181 ± 18	0.48 ± 0.02	173 ± 9	0.44 ± 0.02	160 ± 8	0.21 ± 0.05	84
2.10	0	0.30 ± 0.04	162 ± 10	0.33 ± 0.05	204 ± 14	0.50 ± 0.03	181 ± 9	0.41 ± 0.02	165 ± 9	0.19 ± 0.05	105
2.14	0	0.27 ± 0.03	168 ± 9	0.32 ± 0.04	206 ± 13	0.53 ± 0.03	186 ± 7	0.38 ± 0.03	169 ± 9	0.21 ± 0.05	119
2.18	0	0.25 ± 0.03	182 ± 10	0.32 ± 0.03	213 ± 14	0.51 ± 0.03	196 ± 8	0.39 ± 0.03	182 ± 8	0.21 ± 0.05	127
2.22	0	0.19 ± 0.04	181 ± 13	0.36 ± 0.04	220 ± 10	0.47 ± 0.03	205 ± 9	0.40 ± 0.03	188 ± 9	0.17 ± 0.04	132
2.26	0	0.18 ± 0.05	177 ± 14	0.34 ± 0.05	219 ± 14	0.48 ± 0.04	201 ± 11	0.34 ± 0.04	189 ± 12	0.17 ± 0.05	135

TABLE 19

Number of Partial Waves Used and Angular Moments
Fitted in the Integrated t' Bin PWA

mass region (GeV)	partial waves included in fit	maximum angular moment fit to	
		lmax	mmax
0.80 - 1.12	S,P	2	2
1.12 - 1.56	S,P,D	4	2
1.56 - 1.88	S,P,D,F	6	1
1.88 - 2.28	S,P,D,F,G	8	1

partial wave plots, as well as the error bars listed in tables 17-18, are statistical in nature only. The errors on parameters were found to be quite parabolic in most fits. In certain mass bins though, positive and negative error estimates on a given parameter were substantially different. In these cases, the average of these positive and negative error estimates are shown.

In performing these fits, elastic unitarity was imposed on the S wave below 1.24 GeV, and on the P wave below 1.14 GeV. In order to impose elastic unitarity on these waves, it was necessary to specify the isospin 3/2 portion of the $K^-\pi^+$ elastic scattering waves, a_L . Shown in table 17 are the isospin 3/2 phase shifts taken from the $K\pi$ PWA of Estabrooks et al. (see footnote p.183) in order to perform these fits. Also shown in this table are the isospin 1/2 S wave and the isospin 1/2 P wave phase shifts fit in this analysis in this elastic region. Below 1.24 GeV the imposition of elastic unitarity on the S wave fixed the overall phase in this region absolutely so that the phase ambiguities discussed in the last section did not exist.

Above 1.24 GeV elastic unitarity was no longer imposed on the S wave, and thus the phase ambiguity discussed in the last section did exist. Since only the relative phases of the partial waves could be observed, it was necessary to fix one of the partial wave phases. In performing these fits in the mass region from 1.24 GeV to 1.60 GeV the D wave was held constant. In the mass region from 1.60 GeV to 1.88 GeV the F wave was held constant, and lastly in the mass region above 1.88 GeV the G wave was held constant. For presentation purposes these constant phases were set close to the phase predicted by the leading

resonance in a given mass region. Thus in the region where the D wave phase was held constant, this D wave phase was fixed to a simple Breit-Wigner fit to the $K^*(1430)$. In the region where the F wave phase was held constant, this F wave phase was fixed to a simple Breit-Wigner fit to the $K^*(1780)$, and finally in the region where the G wave phase was held fixed, the G wave phase was fixed to a simple Breit-Wigner fit to the $K^*(2080)$. The resonance parameters used to calculate these Breit-Wigner phases are shown in table 20. Table 18 gives these $K^-\pi^+$ elastic scattering partial waves with the fixed phases set to these Breit-Wigner forms in each region.

The lines drawn in the plots of the D, F, and G wave phases in figures 45-49 also represent these fixed Breit-Wigner phases. In these plots though, the overall phase was chosen by requiring approximate Breit-Wigner behavior, but small shifts of these fixed phases away from the Breit-Wigner values were allowed to assure continuity of the phases. These rotations were small, and are shown in the left hand column of table 18. In figures 45-49 the overall phase was fixed to points near or on the Breit-Wigner curves. These phase fixing points on these plots are represented by the symbol o. It should be emphasized again that only the relative phases between different partial waves in a particular fit could be observed in this PWA. However, it is believed that any reasonable choice of overall phase will lead to the same physics interpretations that are made in the next few subsections.

TABLE 20

Resonance Parameters from Breit-Wigner
Fits to the Partial Wave Amplitudes

(a) Spin 1 Fit to the P Wave Phase

Parameter	Fit Value	Statistical Error	Systematic Error
Mass	894.6	± 0.8	± 2.0 MeV
Width	49.8	± 1.2	MeV
R	7.8	± 3.2	GeV ⁻²
$\chi^2/\text{DOF}^{\text{B}}$	3.9/7		

(b) Spin 2 Fit to the D Wave Magnitude

Parameter	Fit Value	Statistical Error	Systematic Error
Mass	1428	± 3	± 4 MeV
Width	98	± 8	MeV
Elasticity	0.43	± 0.01	
χ^2/DOF	3.8/4		

(c) Spin 3 Fit to the F Wave Magnitude

Parameter	Fit Value	Statistical Error	Systematic Error
Mass	1753	+ 25 - 18	± 20 MeV
Width	300	+170 - 80	MeV
Elasticity	0.16	± 0.01	
χ^2/DOF	0.06/1		

(d) Spin 4 Fit to the G Wave Magnitude

Parameter	Fit Value	Statistical Error	Systematic Error
Mass	2070	+ 100 - 40	± 30 MeV
Width	240	+ 500 - 100	MeV
Elasticity	0.07	± 0.01	
χ^2/DOF	0.86/2		

^B Chi-square per Degrees of Freedom

a) S Wave Solutions

Shown in figure 45 are the four sets of $K^-\pi^+$ elastic scattering S wave magnitudes and phases from each of the four ambiguous solutions extracted in this analysis. All four solutions are seen to be identical below the first Barrelet zero cross represented in these plots by the dotted line. At low mass, the S wave magnitude and phase is seen to rise slowly in the 0.8 GeV to 1.3 GeV mass region. At a mass near 1.4 GeV there is then a sharp peak in the S wave magnitude and a rapid S wave phase variation. This behavior is indicative of a $J^P=0^+$ resonance at a mass of approximately 1.4 GeV. Looking at higher masses the S wave magnitude is seen to be extremely small in the 1.7 GeV mass region. The S wave phase also has a discontinuous jump here. This phase discontinuity is easily explained. In terms of a resonance loop in an Argand diagram this merely means the S wave has gone once around this loop and is passing through or near zero.

At even higher mass in figure 45, the four S wave solutions are seen to be quite similar in overall behavior even though the four solutions are seen not to agree in fine details. All four S wave solutions have a magnitude peak combined with a rapid phase variation in the mass region around 1.9 GeV. This behavior is indicative of a second 0^+ resonance in this 1.9 GeV mass region.

A slightly different way of presenting this data is shown in the Argand diagrams of figures 50-53. This plot represents the partial wave amplitudes plotted in the complex plane. Here the partial wave solutions of figures 45-49 with the same identical phase fixing conventions

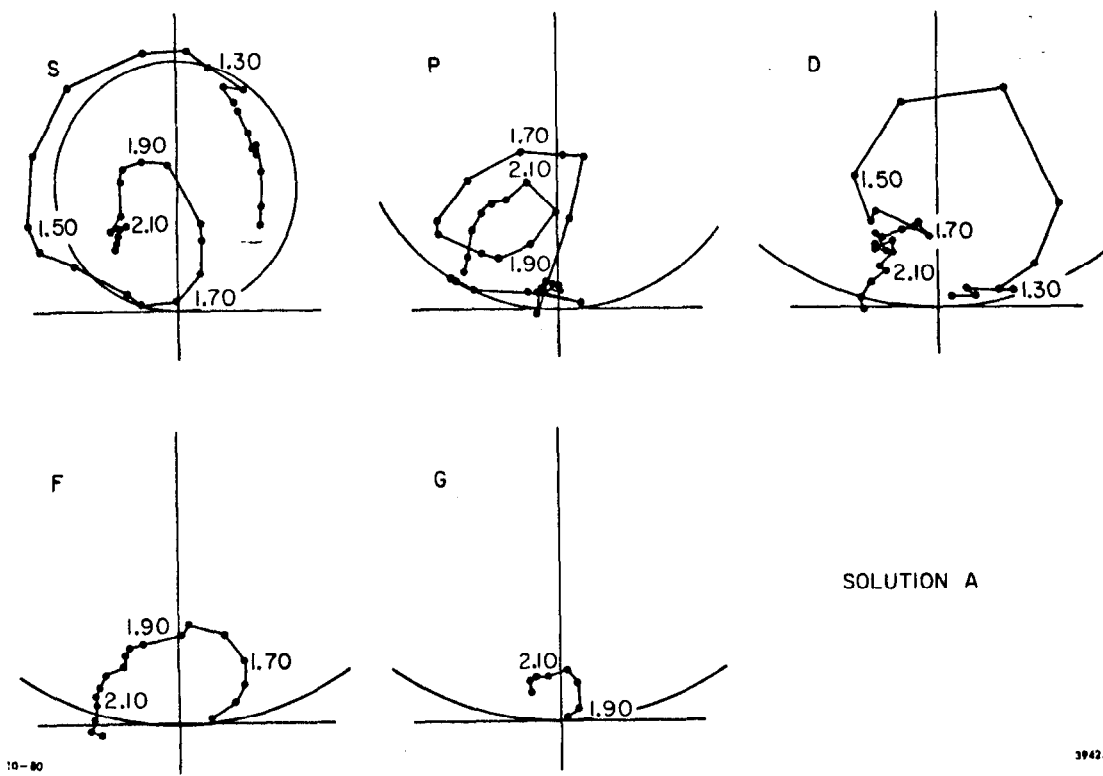


FIG. 50--Argand diagrams for the $K^-\pi^+$ elastic scattering partial waves of solution A. The phase has been fixed as in figures 45-49. The points plotted represent fits run in 40 MeV bins below 1.8 GeV and fits run in overlapping 80 MeV bins above this mass.

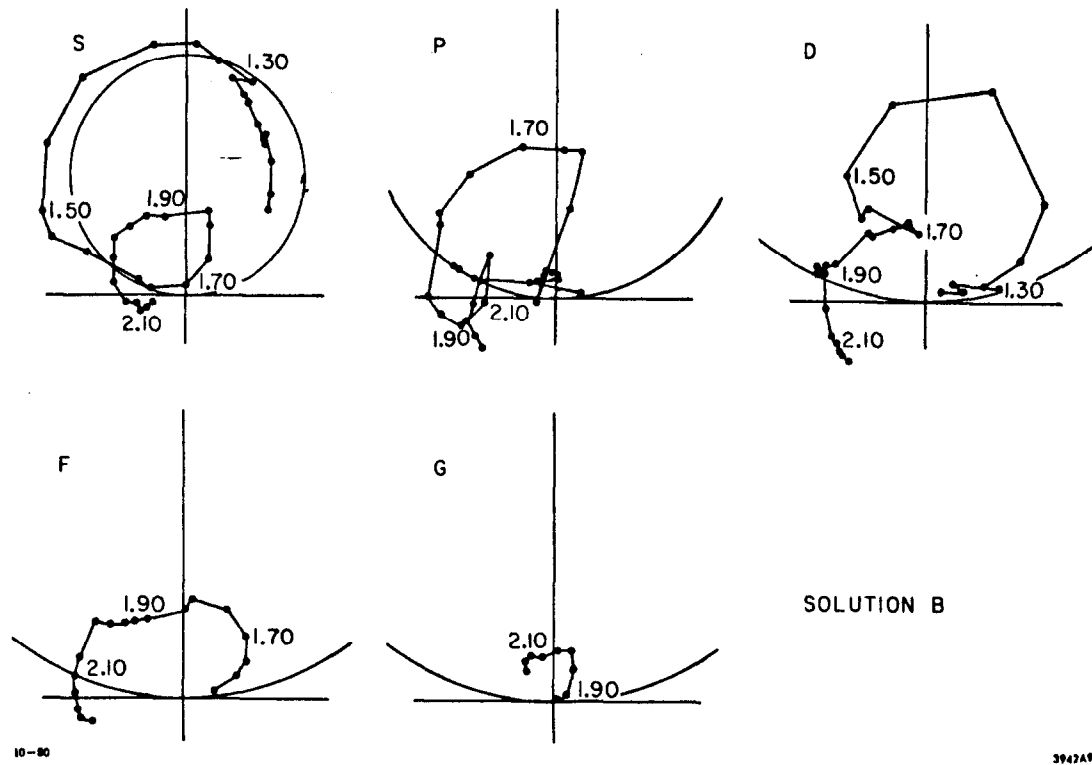


FIG. 51--Argand diagrams for the $K^-\pi^+$ elastic scattering partial waves of solution B. The phase has been fixed as in figures 45-49. The points plotted represent fits run in 40 MeV bins below 1.8 GeV and fits run in overlapping 80 MeV bins above this mass.

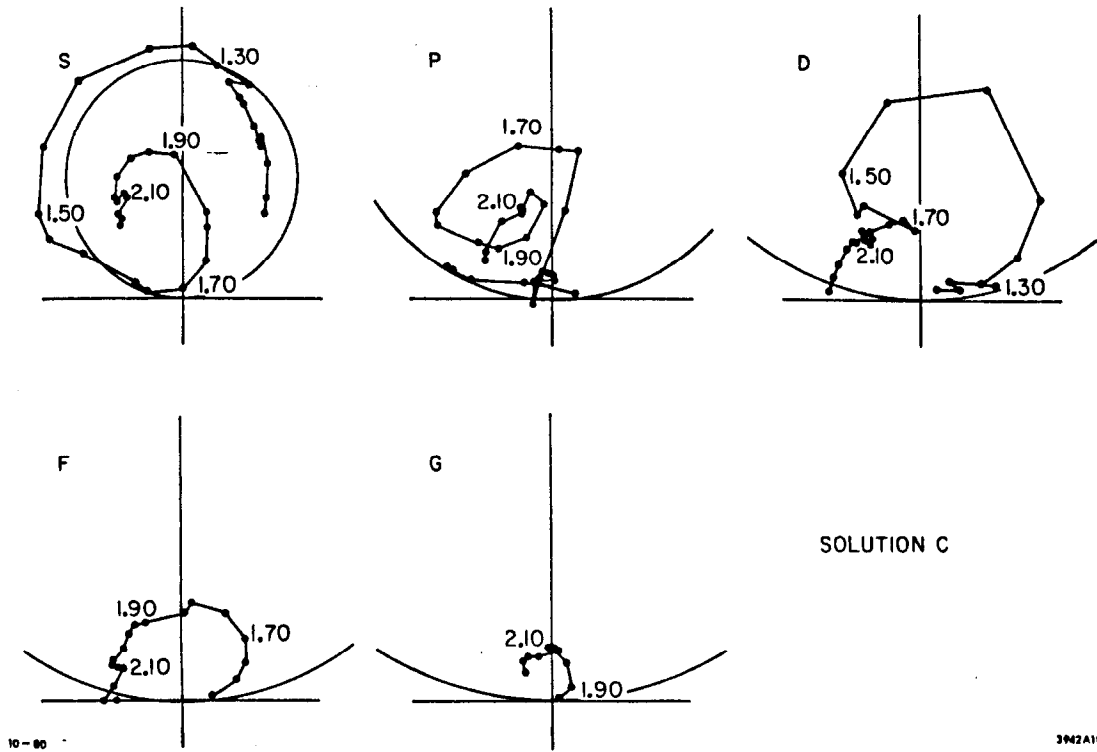


FIG. 52--Argand diagrams for the $K\pi^+$ elastic scattering partial waves of solution C. The phase has been fixed as in figures 45-49. The points plotted represent fits run in 40 MeV bins below 1.8 GeV and fits run in overlapping 80 MeV bins above this mass.

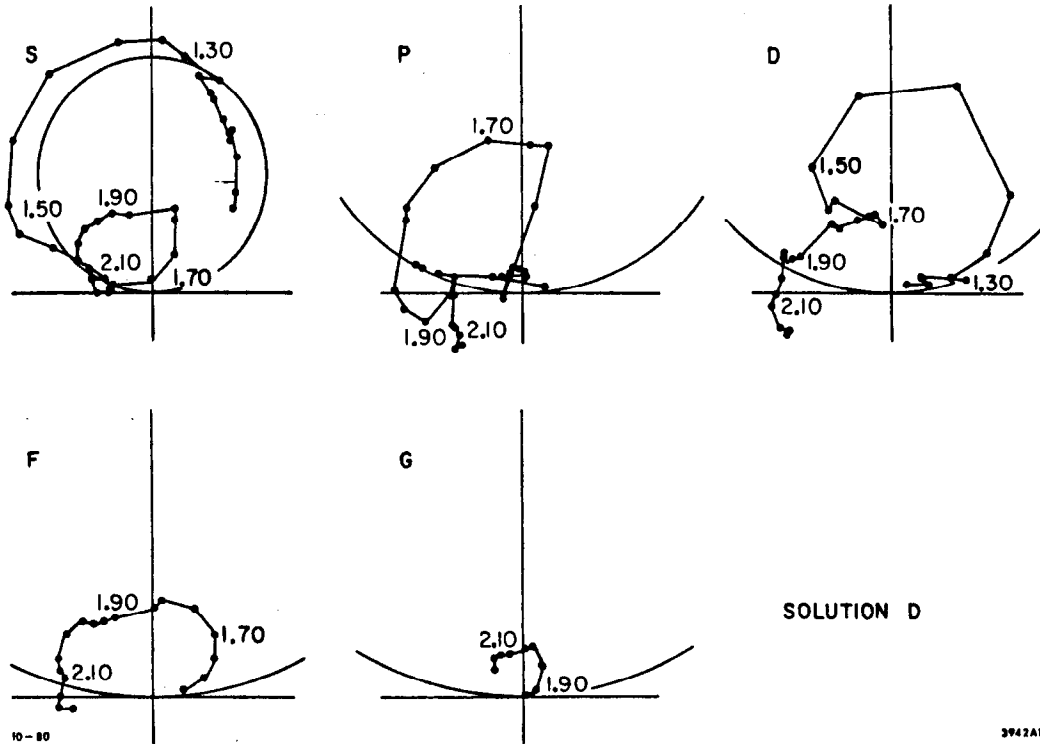


FIG. 53--Argand diagrams for the $K^-\pi^+$ elastic scattering partial waves of solution D. The phase has been fixed as in figures 45-49. The points plotted represent fits run in 40 MeV bins below 1.8 GeV and fits run in overlapping 80 MeV bins above this mass.

have been plotted. Above 1.76 GeV though, solutions fit in 80 MeV bins overlapped every 40 MeV are shown. The circles drawn in these plots represent the unitary circles. These unitary circles have a diameter of $\sqrt{2L+1}$. In all four solutions the S wave is seen to move outside of this unitary circle. This is due to the fact that the partial waves plotted are sums of an isospin 1/2 part and an isospin 3/2 part. Only the separate isospin partial waves are required to stay within the unitary circle. Figure 54 demonstrates this point by using the isospin 3/2 parameterization of the 13 GeV SLAC experiment E-75 to isolate the isospin 1/2 part of the S wave in this analysis (see footnote p.183). The correction has been made up to a mass of 1.6 GeV. Above this mass there is little information available on the isospin 3/2 waves. Higher isospin decomposition of the $K^-\pi^+$ elastic scattering partial waves will have to wait until the $K^+\pi^+$ data currently being analysed by this group is fully processed (see chapter VIII section E). In figure 54, the isospin 1/2 S wave is seen to remain within the unitary circle with only small deviations of the S wave out of this circle consistent with the statistical errors inherent in these partial wave fits. Taking this fact into account we return to the Argand diagrams of figures 50-53.

Figures 50-53 clearly show the circular motion of the S wave amplitudes in the Argand diagrams. It is a well known fact that backgrounds tend to rotate the peak of a resonance away from the 90 degree point on a resonance loop in an Argand plot⁴¹. In these Argand plots, it is seen that the most rapid variation of the S wave in the resonance loop of the first $J^P=0^+$ resonance is in the region of 1.42 GeV. This position of rapid phase variation should be associated with the 0^+ resonance

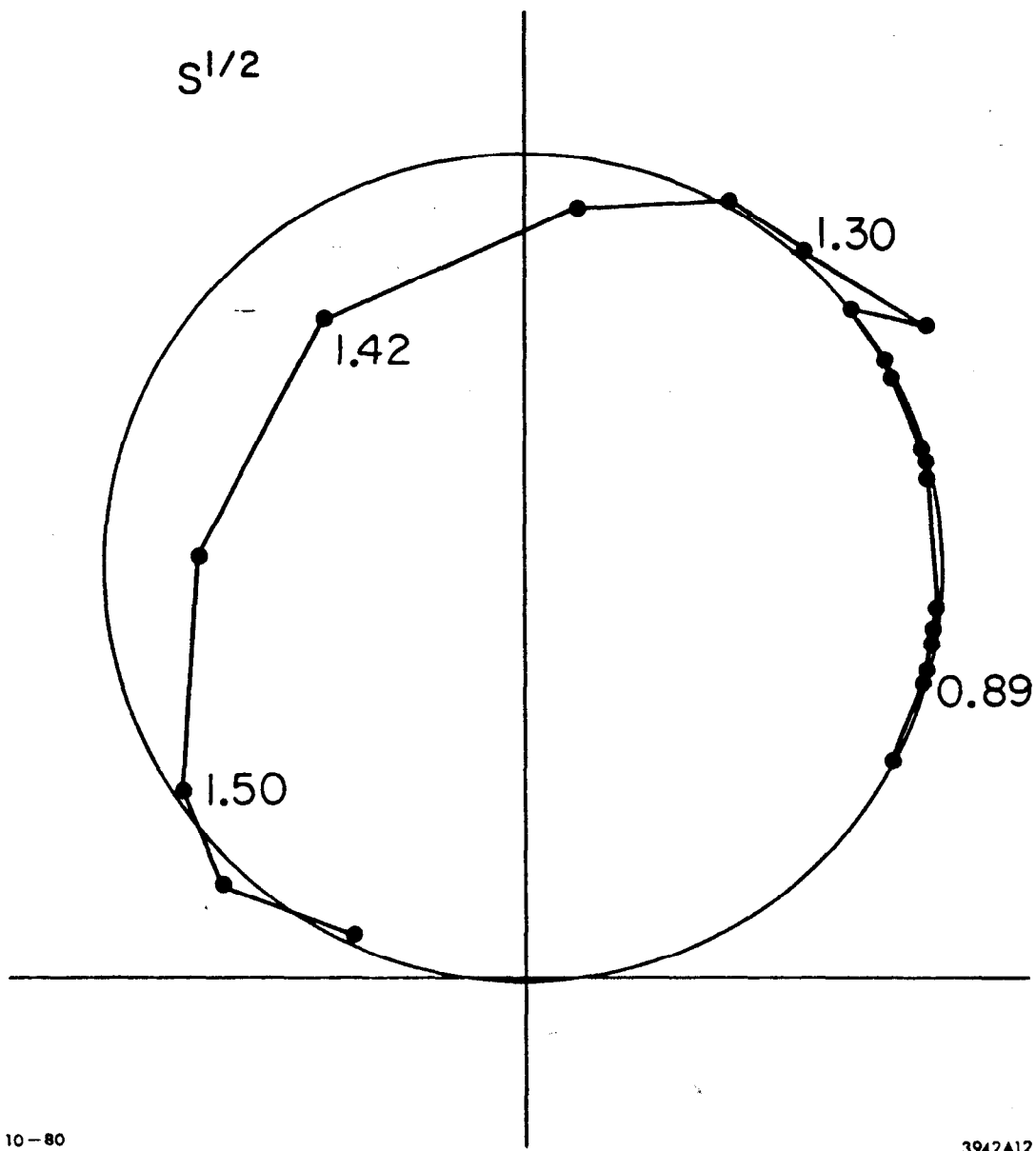


FIG. 54--An Argand diagram of the isospin $1/2 K^- \pi^+$ elastic scattering S wave. To isolate this isospin $1/2$ portion, an isospin $3/2$ parameterization from a previous PWA performed by this group was used (see footnote p.183).

mass, and not the 90 degree point. Although this point of rapid phase variation depends on the choice of overall phase it is thought that any reasonable choice of overall phase will lead to approximately the same resonance mass.

A second loop in the S wave Argand diagrams of figures 50-53 is clearly seen in all four solutions. This second loop is associated with the second 0^+ resonance in the 1.9 GeV region. In this mass region it is clear the estimation of resonance parameters of this second 0^+ resonance depends on the assumptions made about backgrounds in both the isospin $1/2$ and the isospin $3/2$ waves, and also the choice of overall phase. This caution extends to the estimation of resonance parameters for all higher underlying resonances seen in this analysis.

b) P Wave Solutions

Shown in figure 46 and in figures 50-53 are the four ambiguous sets of $K^-\pi^+$ elastic scattering P wave magnitudes and phases extracted in this analysis. In figure 46, the $1^- K^*(895)$ is seen as a sharp magnitude peak combined with a rapid 180 degree phase shift in the 0.895 GeV mass region. This leading resonance displays a classic Breit-Wigner resonance behavior. Increasing in mass, in the region from 1.2 GeV to 1.5 GeV, the P wave magnitude is seen in figure 46 to be extremely small. The errors on the P wave phase are also seen to be extremely large in this region. This is an example of the fact that when a partial wave magnitude becomes very small, the associated partial wave phase becomes nearly indeterminate.

The next prominent structure in figure 46 is a broad peak combined with a rapid phase variation in the 1.7 GeV mass region. In figures 50-53, this is seen as a circular loop in all four P wave Argand diagrams. This behavior is evidence for a $J^P=1^-$ resonance state (or states) in this mass region.

At the highest mass interesting structure is seen in solutions A and C of this partial wave analysis. Both solutions show a broad peak combined with a phase variation in the 2.1 GeV mass region. In the Argand diagrams this structure is seen as a second circular loop in the P wave Argand diagrams of solutions A and C. The behavior is suggestive of possible high mass 1^- resonance states, although only two of the four ambiguous solutions display this behavior.

c) D Wave Solutions

Shown in figure 47 and in figures 50-53 are the four ambiguous sets of $K^-\pi^+$ elastic scattering D wave magnitudes and phases extracted in this analysis. The most obvious structure in figure 47 is the $J^P=2^+$ $K^*(1430)$ seen as a magnitude peak in the 1.43 GeV mass region. As was mentioned previously, in this mass region the overall phase was set by fixing the D wave phase. In the Argand diagrams the $K^*(1430)$ is seen as the first circular loop in the D wave Argand plots.

At high mass in figure 47, all four ambiguous D wave solutions show little clear evidence of resonance structure. However in the Argand diagrams of all four solutions, an intriguing cusp is seen in the 1.7 GeV mass region. Thus interesting resonance structure may still lie hidden in this high mass region.

d) F Wave Solutions

Shown in figure 48 and in figures 50-53 are the four ambiguous F wave $K^-\pi^+$ elastic scattering partial wave solutions extracted in this analysis. The most striking feature in figure 48 is the $J^P=3^- K^*(1780)$ resonance seen as a rising amplitude with a fairly broad magnitude peak in the 1.75 GeV mass region. In this mass region the overall phase has been fixed by fixing the F wave phase. In the Argand plots, this $K^*(1780)$ is seen as a circular loop in the F wave Argand diagrams. In all four ambiguous solutions, the F wave amplitude is seen to remain large in the high mass region, but no other resonance structure in this high mass region is obvious.

e) G Wave Solutions

Lastly shown in figure 49 and in figures 50-53 are the four ambiguous G wave $K^-\pi^+$ elastic scattering partial wave solutions extracted in this analysis. In figure 49, all four solutions show a rather broad magnitude bump in the 2.1 GeV mass region. In this mass region the overall phase has been fixed by fixing this G wave phase. In the Argand plots, a circular loop is seen in all four ambiguous G wave Argand diagrams. This behavior in the 2.1 GeV mass region is indicative of the

$J^P=4^+$ $K^*(2080)$ discussed in the angular moments section.

D. Leading K^* Resonance Fits using the Partial Waves

In this section simple fits to the $K^-\pi^+$ elastic scattering partial waves will be presented yielding resonance parameters for the four leading K^* resonances: 1) $J^P=1^-$ $K^*(895)$, 2) 2^+ $K^*(1430)$, 3) 3^- $K^*(1780)$, and 4) 4^+ $K^*(2080)$. In performing these fits a simple Breit-Wigner resonance form with a Blatt-Weisskopf barrier factor was used³¹. Table 9 give the form of this Breit-Wigner.

In performing this fit to the $K^*(895)$, the $\delta_p^{1/2}$ of table 17 was fit to this simple Breit-Wigner form. It was assumed in performing this fit that no P wave isospin 1/2 background was present in the mass region around this resonance. Figure 55 and table 20 show the results of this chi-square fit.

In performing the fits to the other three leading K^* resonances the corresponding $K^-\pi^+$ partial wave magnitudes of table 18 were fit to simple Briet-Wigner forms (see table 9). In performing these fits it was also assumed that the turn on of a given partial wave was dominated by resonance production of the leading K^* resonance associated with that partial wave, and that the isospin 3/2 portion of the associated partial wave was negligible in the region of these leading K^* resonances. Shown in figure 55 and in table 20 are the results of these four chi-square fits (Note the G wave solutions are so similar that all four solutions gave the same resonance parameters). The resonance widths given in table 20 for these Briet-Wigner fits to the $K^-\pi^+$ elastic scattering

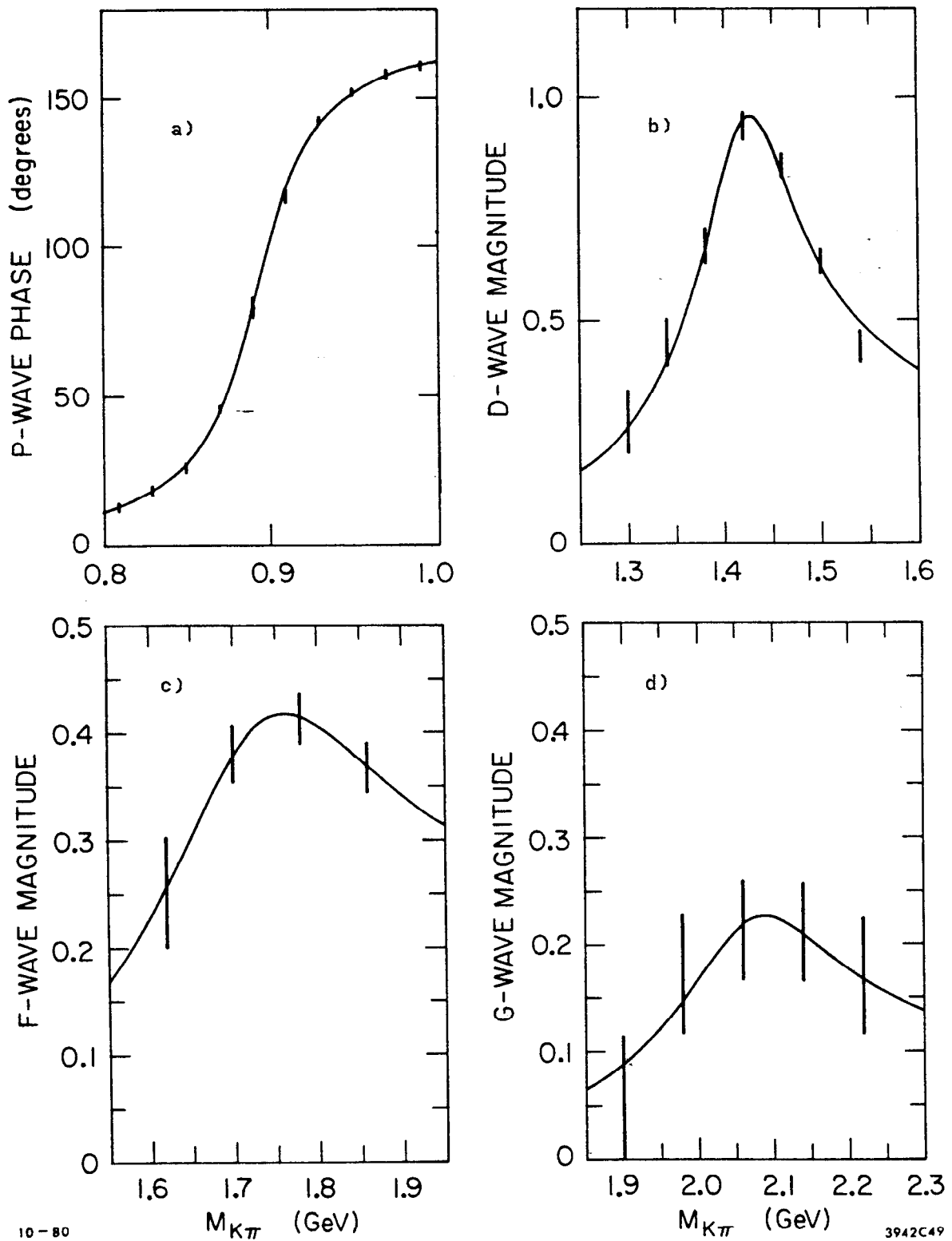


FIG. 55--Partial wave Breit-Wigner fits to the leading K^* resonances (for details see the text);
 a) the $K^*(895)$ fit
 b) the $K^*(1430)$ fit
 c) the $K^*(1780)$ fit
 d) the $K^*(2080)$ fit

partial waves have been corrected for binning effects as well as for the finite mass resolution of this spectrometer. Where a value of R is not shown in this table, R was fixed to a value of 1 fm in performing these fits. The systematic errors listed in this table represent conservative estimates of the systematic effects present in the measurement of these resonance parameters. Where systematic errors are not shown, statistical errors are believed to dominate over systematic effects.

Table 21 compares: 1) resonance parameters from the Breit-Wigner fits to the angular moments presented in the last chapter, 2) resonance parameters from the Breit-Wigner fits to the partial waves presented in this section, and 3) resonance parameters from the Particle Data Group's table values³. Both the angular moments fits, and the partial wave fits are seen to agree well within errors with these table values for the three leading K^* resonances with the minor exception of the Breit-Wigner fit to the t_{20} angular moments. The fact that this fit yielded such a small resonance mass is probably due to the fact that the assumption that the production parameters; γ_a , γ_c , and b did not vary rapidly in the region of the $K^*(895)$ was not well justified (see chapter VII section E)). No comparisons are given with the spin 4^+ leading K^* resonance seen in this analysis since no published parameters exist for this resonance.

E. Future Isotopic Spin Decomposition of the Partial Waves

In this chapter a partial wave analysis of $K^-p \rightarrow K^-\pi^+n$ data yielding the $K^-\pi^+$ elastic scattering partial wave amplitudes has been

TABLE 21

Resonance Parameters from Breit-Wigner Fits to the Partial Wave Analysis Results, from Breit-Wigner Fits to the Moments and the Particle Data Groups Table Values;
 (a) Spin 1 , (b) Spin 2 , (c) Spin 3 , (d) Spin 4

Parameter	Breit-Wigner Fit to P-Wave Phase			Breit-Wigner Fit to t_{20} Moment			PDG Table Value ^y
	Fit Result	Stat. Error	Syst. Error	Fit Result	Stat. Error	Syst. Error	Table Value ^y
Mass	894.6	± 0.8	± 2.0 MeV	887.0	± 3.3	± 2.0 MeV	896.1 ± 0.3 MeV
Width	49.8	± 1.2	MeV	58.8	± 7.1	MeV	52.2 ± 0.5 MeV
R	7.8	± 3.2		0.0	± 4.0		
χ^2/DOF^{β}	3.9/7			2.9/1			

Parameter	Breit-Wigner Fit to D-Wave Magnitude			Breit-Wigner Fit to t_{40} Moment			PDG Table Value ^y
	Fit Result	Stat. Error	Syst. Error	Fit Result	Stat. Error	Syst. Error	Table Value ^y
Mass	1428	± 3	± 4 MeV	1426	± 3	± 4 MeV	1434 ± 5 MeV
Width	98	± 8	MeV	118	± 13	MeV	100 ± 10 MeV
Elasticity	0.43	± 0.01		--	--		0.49 ± 0.02
χ^2/DOF	3.8/4			0.32/2			

Parameter	Breit-Wigner Fit to F-Wave Magnitude			Breit-Wigner Fit to t_{60} Moment			PDG Table Value ^y
	Fit Result	Stat. Error	Syst. Error	Fit Result	Stat. Error	Syst. Error	Table Value ^y
Mass	1753	+ 25 - 18	± 20 MeV	1756	+ 17 - 13	± 20 MeV	1785 ± 6 MeV
Width	300	+ 170 - 80	MeV	185	+ 53 - 36	MeV	126 ± 20 MeV
Elasticity	0.16	+ 0.01		--	--		0.19 ± 0.05
χ^2/DOF	0.06/1			3.4/5			

Parameter	Breit-Wigner Fit to G-Wave Magnitude			Breit-Wigner Fit to t_{80} Moment			Special Spin 4 Breit-Wigner Fit to t_{60} , t_{70} , t_{80} Moments		
	Fit Result	Stat. Error	Syst. Error	Fit Result	Stat. Error	Syst. Error	Fit Result	Stat. Error	Syst. Error
Mass	2070	+ 100 - 40	± 30 MeV	2140	+ 140 - 60	± 30 MeV	2075	+ 40 - 30	± 30 MeV
Width	240	+ 500 - 100	MeV	250	+ 300 - 130	MeV	240	+ 400 - 80	MeV
Elasticity	0.07	± 0.01		--	--		--	--	
χ^2/DOF	0.86/2			2.5/3			15.7/13		

β Chi-square per Degrees of Freedom
^y Reference (3)

presented. Assuming invariance under SU(3) transformations ⁴² these measured $K^-\pi^+$ elastic scattering partial waves can be related to other $K\pi$ scattering partial waves through isotopic spin decomposition:

$$a_L(K^-\pi^+ \rightarrow K^-\pi^+) = \frac{2}{3} (a_L^{1/2} + \frac{1}{2}a_L^{3/2}) \quad \text{VIII.20}$$

$$a_L(K^+\pi^+ \rightarrow K^+\pi^+) = a_L^{3/2} \quad \text{VIII.21}$$

$$a_L(K^-\pi^+ \rightarrow \bar{K}^0\pi^0) = \frac{\sqrt{2}}{3} (-a_L^{1/2} + a_L^{3/2}) \quad \text{VIII.22}$$

where the $a_L^{1/2}$ and the $a_L^{3/2}$ partial waves are independent of the $K\pi$ scattering reaction. In this experiment besides taking K^-p triggers, approximately five percent of our triggers were taken with an incident K^+ beam. This data consisted of ~50 consecutive tapes of data. The analysis of this K^+p data is ongoing and within a few months a partial wave analysis similar to the PWA presented in this chapter, will be performed on the reaction $K^+p \rightarrow K^+\pi^+n$. The measured partial waves from this analysis, $a_L(K^+\pi^+ \rightarrow K^+\pi^+)$, will determine the isospin 3/2 partial waves, and thus will allow the isolation of the resonant, $a_L^{3/2}$, scattering partial wave part from the $K^-\pi^+$ elastic scattering partial waves presented in this chapter.

F. Resolution of the Barrelet Zero Ambiguities

As was discussed in the ambiguity section of this chapter, the four ambiguous partial wave solutions predict identical differential cross sections for the reaction $K^-p \rightarrow K^-\pi^+n$. The simplest means of discarding

solutions in previous analysis has been to discard solutions which badly violate elastic unitarity. Without the isospin decomposition discussed in the last section though it is impossible to discard any solution on these grounds in this present analysis. Since all four solutions do stay fairly well inside the unitary circle in the Argand diagrams, it is doubted whether this method will prove useful in discarding solutions even when this decomposition is made, and no other means exists for ruling out any of the solutions from a physics point of view. One experimental method of resolving these ambiguities, which might prove more useful, is afforded by equation VIII.22 above. Using the $a_{L^{\frac{1}{2}}}^{\frac{1}{2}}$ and the $a_{L^{\frac{3}{2}}}^{\frac{3}{2}}$ partial wave amplitudes extracted in the joint $K^-p \rightarrow K^-\pi^+n$ and $K^+p \rightarrow K^+\pi^-n$ PWA described in the previous section, and the exchange model presented in this chapter; equation VIII.22 can be used to predict angular moments for the reaction $K^-p \rightarrow \bar{K}^0\pi^0n$. Since this isospin spin sum is quite different from equation VIII.20, the four ambiguous solutions predict different sets of angular moments. By comparing these angular moments with experimental $K^-p \rightarrow \bar{K}^0\pi^0n$ angular moments the ambiguity in theory could be resolved. It is extremely hard to perform an experiment to measure $K^-p \rightarrow \bar{K}^0\pi^0n$ angular distributions though, since one would have to measure either the outgoing n or the outgoing π^0 (either of which is extremely hard). Even if this experiment is performed, the four ambiguous solutions presented in this PWA are so similar that very large statistics would be needed in order to resolve these ambiguities.

One other means exists for resolving these Barrelet ambiguities. Given a much larger statistics $K^-p \rightarrow K^-\pi^+n$ PWA, it is possible that where a given Barrelet zero was very close to zero within errors in this

analysis, the same Barrelet zero may be well separated from zero in a higher statistics PWA. Since in this case no Barrelet zero cross would be present, the particular ambiguity seen in this analysis would be resolved. If the Barrelet zero is still found to be consistent with zero, this ambiguity would remain.

Chapter IX

SUMMARY AND CONCLUSIONS

A. Summary of the Results

A great number of interesting results have been presented in the angular moments analysis, and the energy independent partial wave analysis discussed in the last two chapters. This section will describe the new physics extant in these results.

Both the angular moments analysis and the partial wave analysis discussed in this paper showed clear evidence for the three well known leading natural spin-parity strange meson states: 1) the $J^P=1^- K^*(895)$, 2) the $2^+ K^*(1430)$, and 3) the $3^- K^*(1780)$. As well as confirming the spins and parities of these resonances, fits were discussed which yielded resonance parameters for these three leading states (see table 21). These states have been rather extensively studied in the past (see reference 3) and most properties of these states are now rather well understood. Two salient points stand out in our study of these resonances though.

Past amplitude analysis ⁴ ⁴³ have found the mass of the $K^*(1430)$ to be closer to 1.430 GeV than the value of 1.420 GeV traditionally found when fitting the invariant mass spectrum. This is attributed to the fact that invariant mass fits do not correctly account for the strong S wave background which peaks and then drops rapidly in the 1.400 GeV mass

region (see figure 45). This analysis confirms the S wave peak and rapid drop in this 1.400 GeV region, and the fitted resonance mass was quite consistent with the mass values obtained in the previous partial wave analysis.

Although it is a well established resonance, there has been a great deal of variation in resonance parameters published for the $3^- K^*(1780)$. In particular the values quoted for the width of this resonance have ranged from 90 MeV to over 300 MeV. This analysis sheds some light on why these resonance parameters for this state have been so difficult to measure. In figure 48 the $K^-\pi^+$ F wave magnitude is seen to rise sharply in the mass region from 1.6 GeV to 1.75 GeV. Above this mass the F wave magnitude in all four solutions remains very large. It is clear some background or higher mass resonance must be present in this region above 1.80 GeV. In any case this background must be treated very carefully if one is to obtain proper resonance parameters in a fit to this resonance. In this analysis we fit the leading edge of this resonance, and thus circumvented this background problem. Although the statistical error on this fit was rather large, we obtained a mass and width quite consistent with the energy independent partial wave analysis of P.Estabrooks et al.⁴, and the energy dependent partial wave analysis of Bowler et al.³.

Both the angular moments analysis, and the energy independent partial wave analysis discussed in this paper presented clear evidence for a new $J^P=4^+$ natural spin-parity meson resonance in the mass region around 2.08 GeV. Evidence for this state in the angular moments can be seen as bumps in the t_{60} and t_{80} angular moments, as well as a strong

interference in the t_{70} moment in this 2.08 GeV mass region (see figure 31). Evidence for the spin classification of this state is shown in figure 34 where the t_{90} and t_{100} angular moments, for a separate fit, were found to be consistent with zero within errors. Since only natural spin parity states can be seen in this reaction, the positive parity assignment follows. In the $K^-\pi^+$ elastic scattering partial waves this resonance can be seen as a small resonance loop in the G wave Argand plot in all four ambiguous solutions (see figures 50-53).

Acceptance limited statistics, as well as the small elasticity of this new 4^+ strange meson resonance made the determination of resonance parameters difficult. Table 21 presents the mass and width of this state from the three separate fits discussed in this paper. This resonance was seen with a statistical significance of greater than four standard deviations in this analysis. Additional evidence for the charge one 4^+ K^* state has recently been presented by another experimental group (see reference 44).

In chapter VIII, an energy independent partial wave analysis of the acceptance corrected angular moments was presented. This partial wave analysis extracted the $K^-\pi^+$ elastic scattering partial wave amplitudes as a function of mass. One of the most interesting results of this PWA is that one unambiguous solution was found below 1.80 GeV in mass. This is in marked contrast to the PWA of Estabrooks et al. ⁴ which displayed a four fold ambiguity from 1.5 GeV up to 1.85 GeV where the Estabrooks analysis stopped. Reexamining the region of the Barrelet zero crosses of Estabrooks et al. near 1.5 GeV, no possible crosses in our data were seen. This result can be attributed to the uniform acceptance of this

experiment compared with the forward and backward $\cos\theta$; limited data of Estabrooks et al.. The unique $K^-\pi^+$ elastic scattering partial wave solution extracted in this analysis has the same Barrelet zero structure as solution B in Estabrooks et al.. A comparison of solution B from Estabrooks et al. with our unambiguous solution up to 1.8 GeV agrees quite well in all details. Above 1.8 GeV the Estabrooks et al. analysis was severely acceptance limited. The superior acceptance properties of the LASS spectrometer allowed this PWA to extend up to 2.3 GeV.

In this PWA, a two fold ambiguity was seen in the mass region from 1.8 GeV to 2.0 GeV, and a four fold ambiguity was seen above 2.0 GeV. These ambiguities were indicated by the Barrelet zeros, $\text{Im}(z_3)$ and $\text{Im}(z_1)$, approaching zero within errors in the 1.80 GeV and 2.0 GeV mass regions respectively. Both $\text{Im}(z_1)$ and $\text{Im}(z_3)$ can be seen in figure 44 to be very nearly zero in this high mass region. Flipping the signs of $\text{Im}(z_1)$ and $\text{Im}(z_3)$ thus did little to change these partial wave solutions. Thus the four solutions extracted in this partial wave analysis were very similar in structure. This proves to be an important point since resolving these ambiguities is a very difficult experimental problem (see chapter VIII section F).

The main purpose of extracting the $K^-\pi^+$ elastic scattering partial waves in this PWA was to investigate the nonleading resonance structure hidden in our angular moments. The most prominent of these underlying structures was the S wave resonance in the 1.40 GeV region. In figure 45 the S wave magnitude and phase are seen to slowly rise in the mass region from 0.80 GeV to 1.30 GeV. Then at a mass near 1.40 GeV the S wave amplitude peaks, and then drops precipitously. In this 1.40 GeV

mass region the S wave phase also goes through a rapid phase change. This behavior of the S wave is nearly identical to the S wave behavior in the analysis of Estabrooks et al. ⁴. This structure is interpreted by Estabrooks et al. as a fairly narrow S wave resonance at ~ 1.430 GeV on top of a relatively large S wave background. No attempt is made to interpret this background. We also associate this rapid phase change with an S wave resonance in the 1.430 GeV region. As was mentioned previously, determination of the resonance parameters of this state depend strongly on the assumptions made about: 1) the nonresonant isospin $3/2$ S wave contribution, 2) the background shown dramatically by the slow rise in the S wave magnitude and phase below 1.3 GeV, and 3) the choice of the undetermined overall phase in this PWA. It is believed that any reasonable choice of overall phase will lead to nearly the same resonance parameters. Taking these cautions into account, we have used the $3/2$ parameterization from the SLAC 13 GeV $K\pi$ PWA ⁴ to isolate the isospin $1/2$ S wave (see footnote p.183). The S wave resonance mass was then estimated using the Argand plot of figure 54 to be at the position of maximum phase variation along this resonance loop. The width of this resonance was measured from the phase variation as a function of mass in this same region, and the elasticity of this resonance was evaluated by ascribing circular motion to the Argand plot of figure 54. Shown in table 22 are these estimated resonance parameters for this state. Thus we have dramatically confirmed the 0^- resonance at 1.43 GeV.

As well as this previously seen $J^P=0^+$ state at 1.43 GeV, the extracted $K^-\pi^+$ partial waves in this analysis resulted in evidence for several new underlying resonance states. In the S wave Argand plots of

figures 50-53, quite clear evidence is seen in all four ambiguous solutions for a new S wave resonance in the 1.90 GeV region. This is the first indication of this resonance in any experiment. In the P wave Argand diagrams of figures 50-53, a rather broad resonant P wave effect is seen in the 1.7 GeV mass region. This effect was previously reported in two of the four ambiguous solutions in Estabrooks et al. ⁴. In fact solution B of Estabrooks et al. quite clearly displays this P wave resonance. Here we have presented unambiguous evidence for this state. In solution A and C in these P wave Argand plots, a second P wave loop is seen, and this loop peaks in the 2.1 GeV mass region. Although this behaviour is exhibited in only two of our four ambiguous solutions, this structure could be associated with a new 1^- state at ~ 2.1 GeV. The behavior of the P wave states in these Argand plots can easily be interpreted as a single resonance but could in fact also be interpreted as two resonances spaced very close together in mass. In table 22 we have treated these structures in terms of a single resonance.

Interesting structure is also seen in the high mass region in the D, F, and G wave Argand diagrams of figures 50-53. In particular the D wave solutions display an interesting cusp at the end of the $K^*(1430)$ resonance loop in each ambiguous solution. We have attempted no interpretation of this D wave structure though.

Determination of resonance parameters for high mass states depend strongly on the choice of overall phase in this PWA; as well as the non-resonant isospin $3/2$ contributions, and the isospin $1/2$ background contributions. Taking these cautions into mind, we have made rough estimates of the resonance parameters of these new underlying states. In

TABLE 22

Estimated Parameters for the Underlying Resonances
(Masses and Widths are in MeV)

Wave	Parameter	SOLUTION A	SOLUTION B	SOLUTION C	SOLUTION D
0 ⁺	Mass	1420	seen unambiguously		
	Width	240			
	Elasticity	0.85			
0 ⁺	Mass	1880	1900	1880	1900
	Width	200	240	220	240
	Elasticity	0.45	0.35	0.45	0.35
1 ⁻	Mass	1700	1720	1700	1720
	Width	200	200	200	200
	Elasticity	0.35	0.35	0.35	0.35
1 ⁻	Mass	2100	-	2100	-
	Width	240		240	
	Elasticity	0.2		0.2	

making these estimates, the real and imaginary projections of our Argand diagrams have been used (see figures 56-60). In these plots a particular resonance is seen, in the real projection of these waves as a function of mass, as a peak followed by a valley. The mass of each particular resonance was estimated by choosing the mass halfway between the associated peak and valley. The width of the resonance was measured as the distance, along the mass scale, from the peak to the valley. Lastly the elasticity of these resonances was calculated as the distance, along the real part of the partial wave axis, from this peak to the valley. Shown in table 22 are the resonance parameters for the underlying waves estimated in this manner. It is difficult to associate a systematic error with these estimates for the resonance parameters of the underlying states. These estimates depend on: 1) our choice of overall phase, 2) the assumption that the $I=1/2$ backgrounds did not rotate the resonance masses far from the 90 degree position on these Argand diagram loops, and 3) the assumption that the $I=3/2$ and $I=1/2$ backgrounds were slowly varying functions of mass. In order to give better estimates for these resonance parameters it will be necessary to determine the isospin $3/2$ part of these $K^-\pi^+$ elastic scattering partial waves (see chapter VIII section E). Once the isospin $1/2$ part of the partial waves have been isolated, the overall phase problem and the isospin $1/2$ background problem must still be solved. Both these problems might be addressed by an energy dependent fit to the isospin $1/2$ partial waves. In such energy independent fits the resonance parameters extracted would depend only on the parameterization of the background, and not on the overall phase.

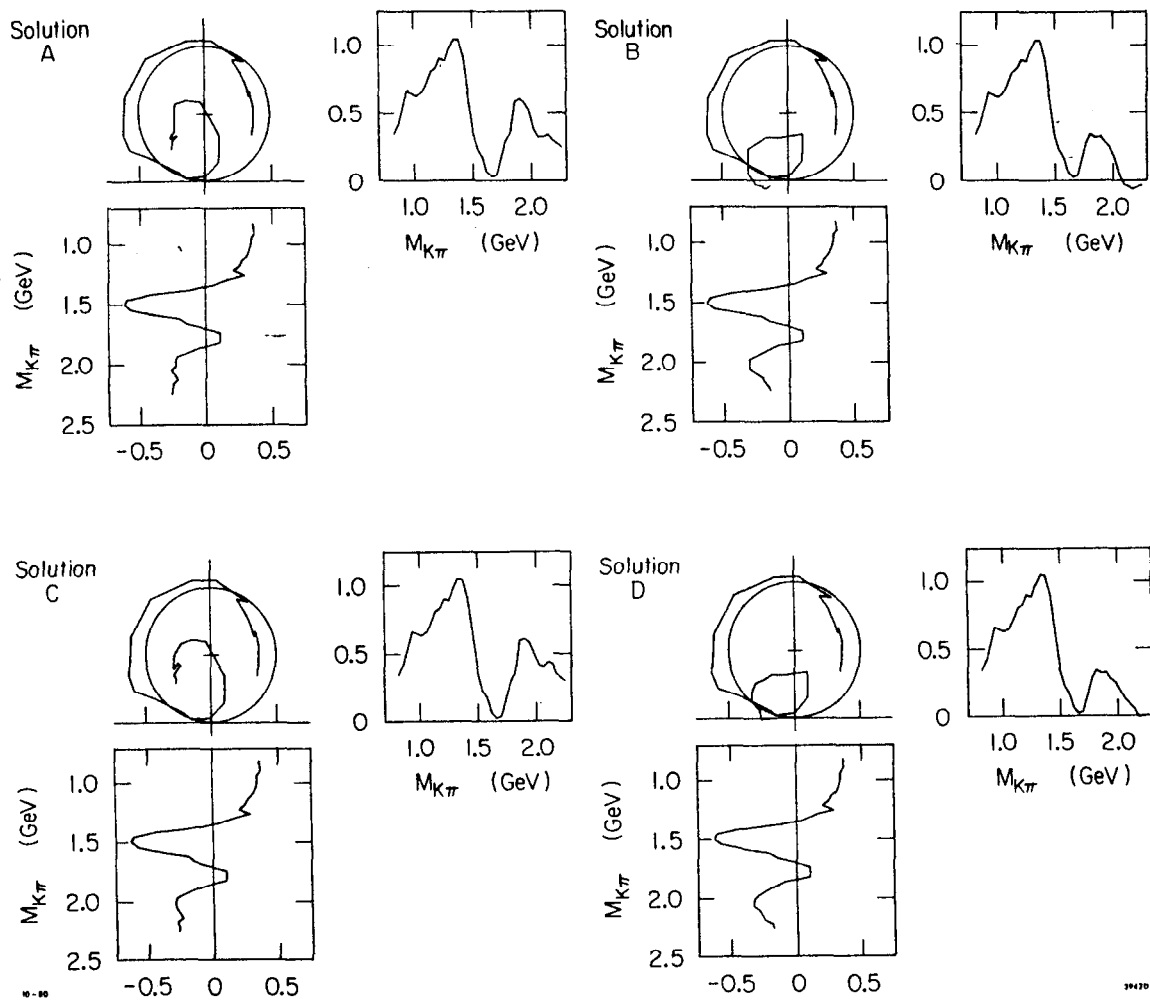


FIG. 56--Real and Imaginary projections of the S wave Argand diagrams. The diameters of these unitary circles have been normalized to one.

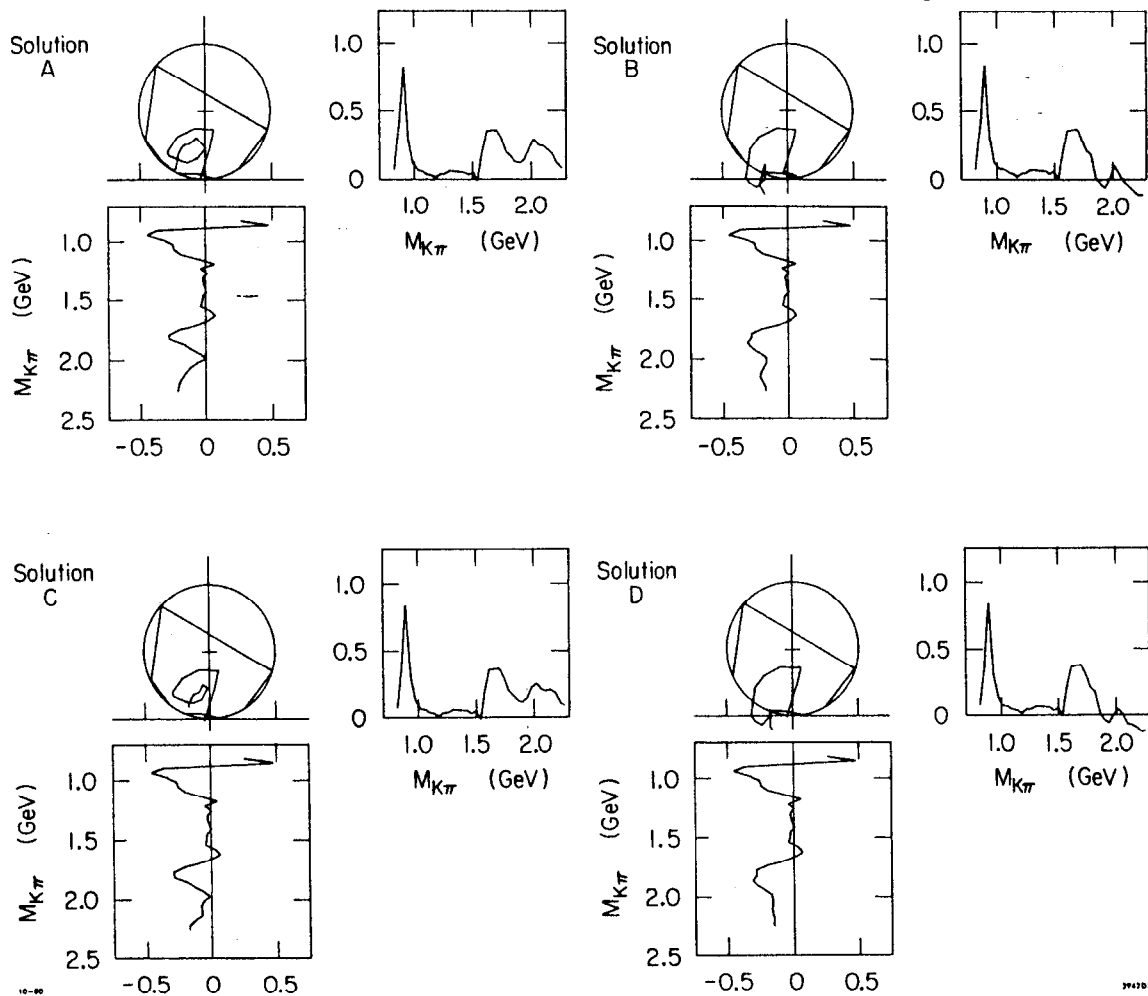


FIG. 57--Real and Imaginary projections of the P wave Argand diagrams. The diameters of these unitary circles have been normalized to one.

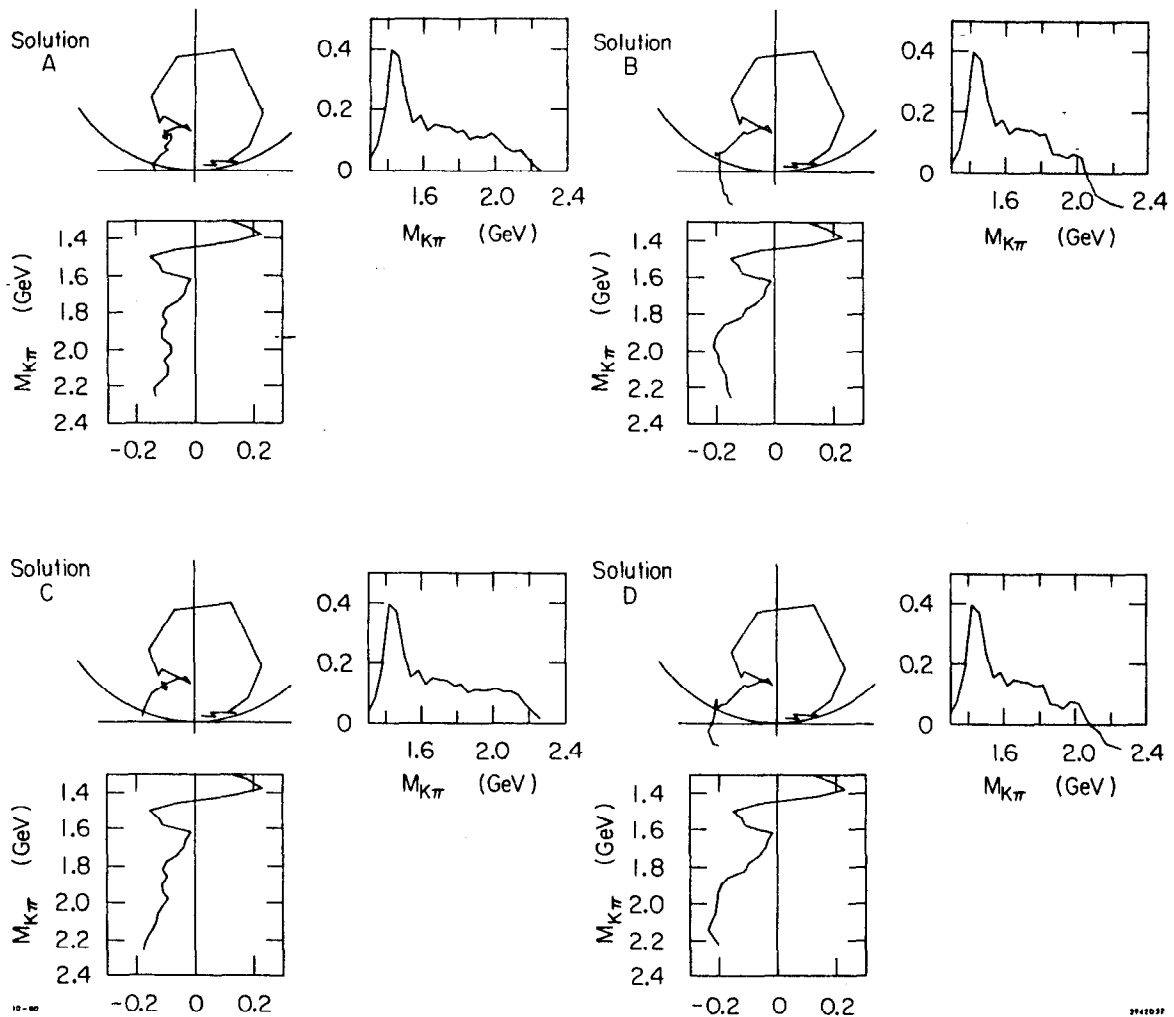


FIG. 58--Real and Imaginary projections of the D wave Argand diagrams. The diameters of these unitary circles have been normalized to one.

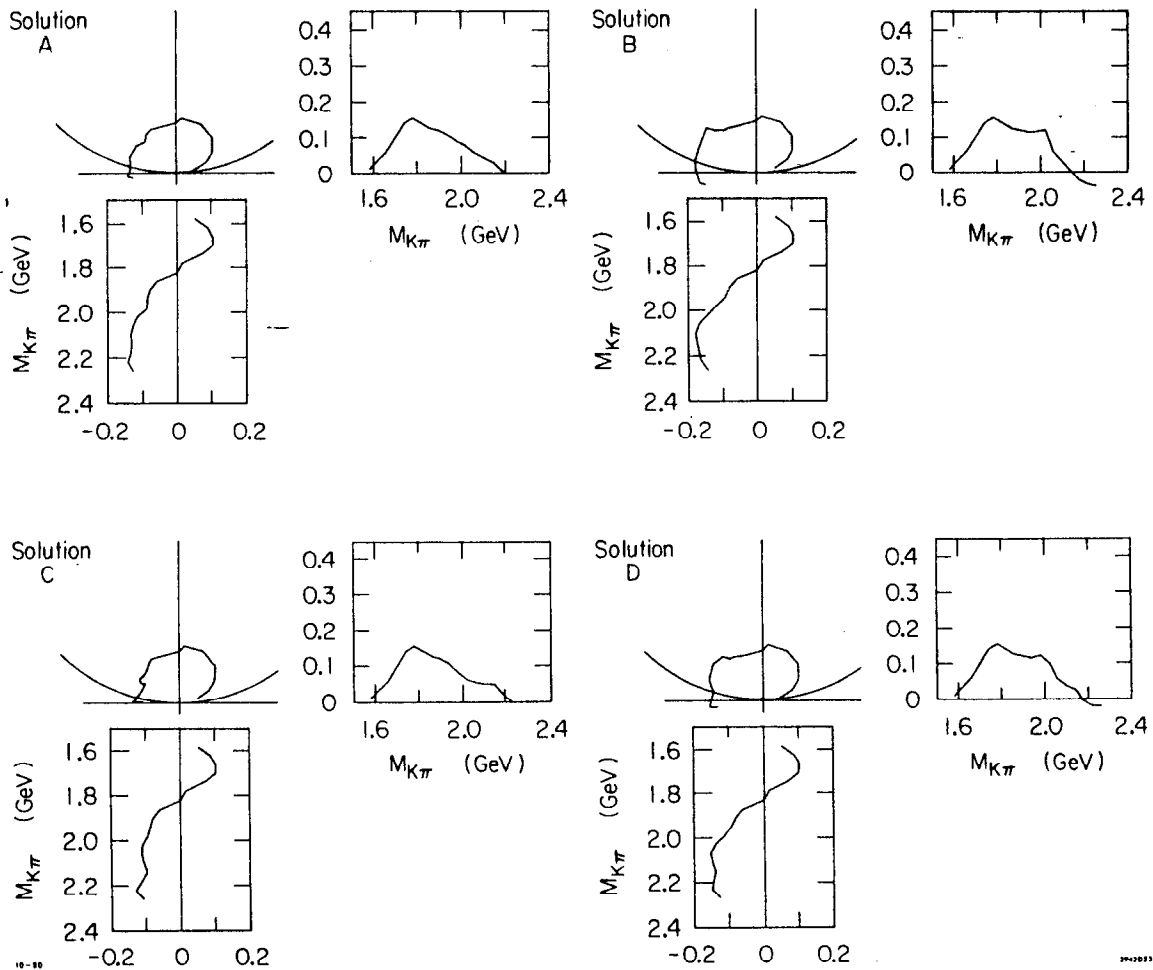


FIG. 59--Real and Imaginary projections of the F wave Argand diagrams. The diameters of these unitary circles have been normalized to one.

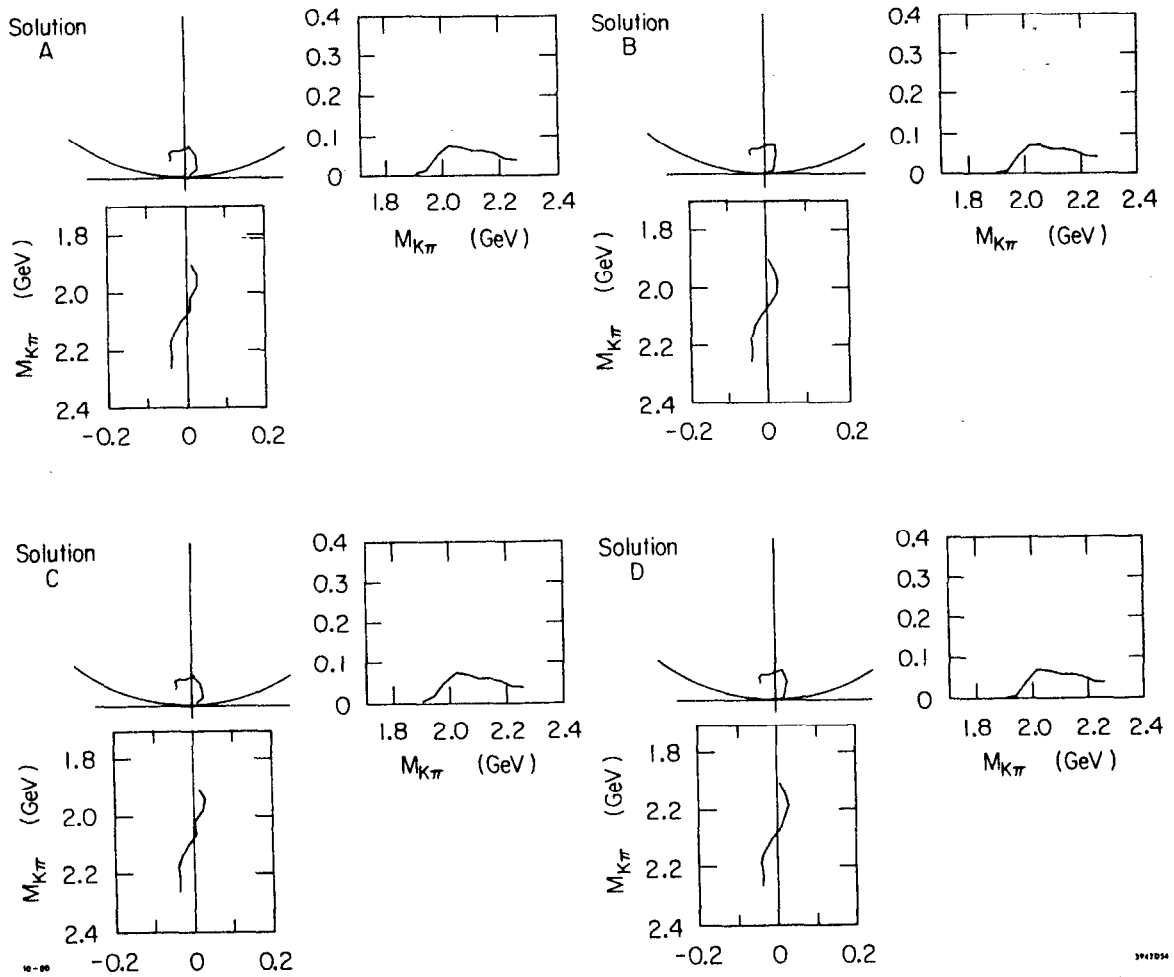


FIG. 60--Real and Imaginary projections of the G wave Argand diagrams. The diameters of these unitary circles have been normalized to one.

Thus this analysis has seen unambiguous evidence for seven resonances, and another possible resonance in two of four ambiguous solutions. Of these eight resonances four had not been seen before, or had been seen ambiguously in previous experiments. The next section of this chapter will deal with the classification of these states with the framework of a simple harmonic oscillator quark model.

B. A Simple Quark Model Interpretation of the Observed States

With the success of the preceding analysis in uncovering several new strange meson states, it is instructive to return to the simple quark model presented in chapter I, and to attempt to classify these states within this quark model. Looking once again at the Grotrian plot in figure 3, it should be remembered that only natural spin-parity ($P=(-1)^J$) states were accessible in this analysis.

Previous analysis have classified the leading $K^*(895)$, $K^*(1430)$, and $K^*(1780)$ as the highest spin members of the $S=1 L=0$, $S=1 L=1$, and $S=1 L=2$ triplets respectively. The new $J^P=4^+$ resonance seen in this analysis is naturally identified within this scheme as the 4^+ member of the $S=1 L=3$ triplet. With this classification this meson then takes its place as an $SU(3)$ partner of the $I=0$ h meson. It is interesting to plot these four leading K^* states in a slightly different manner. Shown in figure 61 (known as a Chew-Frautchi plot) are these leading states plotted as a function of spin (J) and mass squared. Remarkably all four mesons lie, to a very good approximation, on a straight line. This behavior has been observed for years in the leading natural spin-parity

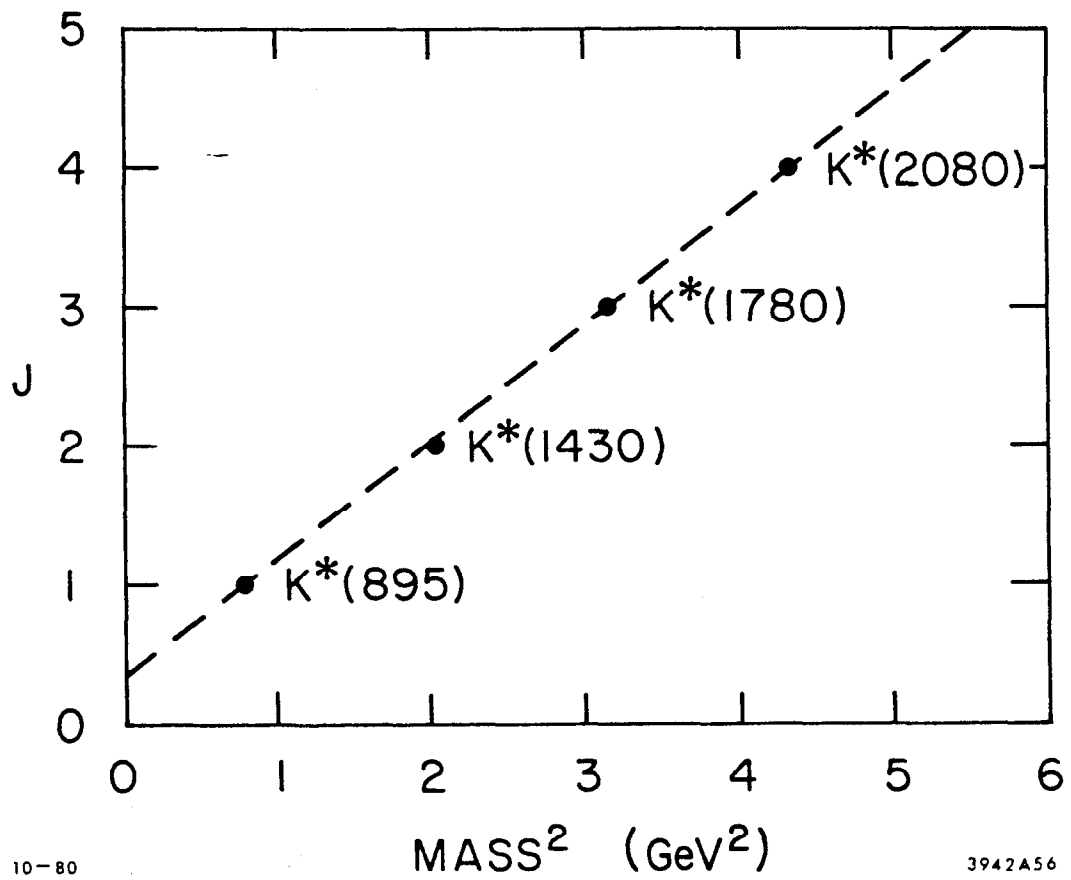


FIG. 61--A Chew-Frautschi plot of the leading natural spin-parity strange mesons.

meson states but it is noteworthy that this new 4^+ strange meson state continues along this trajectory. It is not known quantitatively what this behavior implies in terms of the quark-antiquark potential. The orbital excitations seen in this data are discussed in greater detail in reference 29.

The next states to classify within this simple quark model scheme are the two scalar mesons seen at 1.43 GeV and 1.90 GeV in mass respectively. Interpreting these states as $s\bar{d}$ resonances, the lowest mass state can be uniquely classified within this model as the 0^+ member of the $S=1$ $L=1$ triplet. The second 0^+ resonance is then naturally classified as the first radially excited recurrence of the 1.43 GeV scalar meson. This 1.90 scalar meson state is the first unambiguous evidence for a natural spin-parity strange meson radial excitation. This radial excitation will be discussed in more detail in the next section.

The 0^+ resonance at 1.43 GeV plus the 2^+ $K^*(1430)$ form the two natural spin-parity states in the lowest lying $L=1$ $S=1$ triplet. Evidence for the unnatural spin-parity member of this triplet, the $Q_A(1340)$ can be found in references 45 and 46. Thus there is a well established triplet level in this strange meson spectrum.

The two high mass vector meson states seen in this analysis are much more difficult to classify unambiguously within this quark model than the scalar mesons. The 1^- state seen near 1.70 GeV in this analysis can be classified quite naturally as either a radial excitation of the $S=1$ $L=0$ $K^*(895)$ or else as the 1^- member of the $S=1$ $L=2$ $K^*(1780)$ triplet. There is also the possibility that this 1^- state, seen in this analysis, is actually two 1^- states spaced so closely together in mass that they cannot be resolved.

The speculative second vector meson state seen at 2.1 GeV (assuming that one of the two ambiguous solutions this state is seen in is the correct solution) is even harder to classify within this simple quark model. The classification of this speculative state (or possibly two states) depends on the quark model classification of the 1.70 GeV vector meson state. There are at least four positions on the Grottrian plot where this state might be classified.

Clearly our classification of these high mass vector mesons remains very unclear. There are two questions which must be solved before a classification of even the 1^- state at 1.70 GeV can be made: 1) Is this resonance one or two states?, and 2) Should this 1^- state (or states) be classified as a radial excitation, or a triplet member within the quark model?

The first of these two questions can in principle be answered experimentally with a higher statistics partial wave analysis of this 1.70 GeV mass region. Mass dependent fits of this data might then allow resolution of two states. A study of all inelastic $K\pi$ scattering channels in this mass region might also shed some light on this problem, but such a study is beyond the scope of the present analysis.

Once the number of vector meson present in this 1.70 GeV region had been determined, an attempt could be made to classify each state as either a radial excitation, or a triplet member within the quark model. If a predictive potential model existed for strange quark mesons, it might be possible to classify this state by its observed mass. Since no successful predictive model now exists this procedure is an impossibility. Another method for experimentally determining the classification

of this state would be to measure the relative signs of the amplitudes for the reactions:

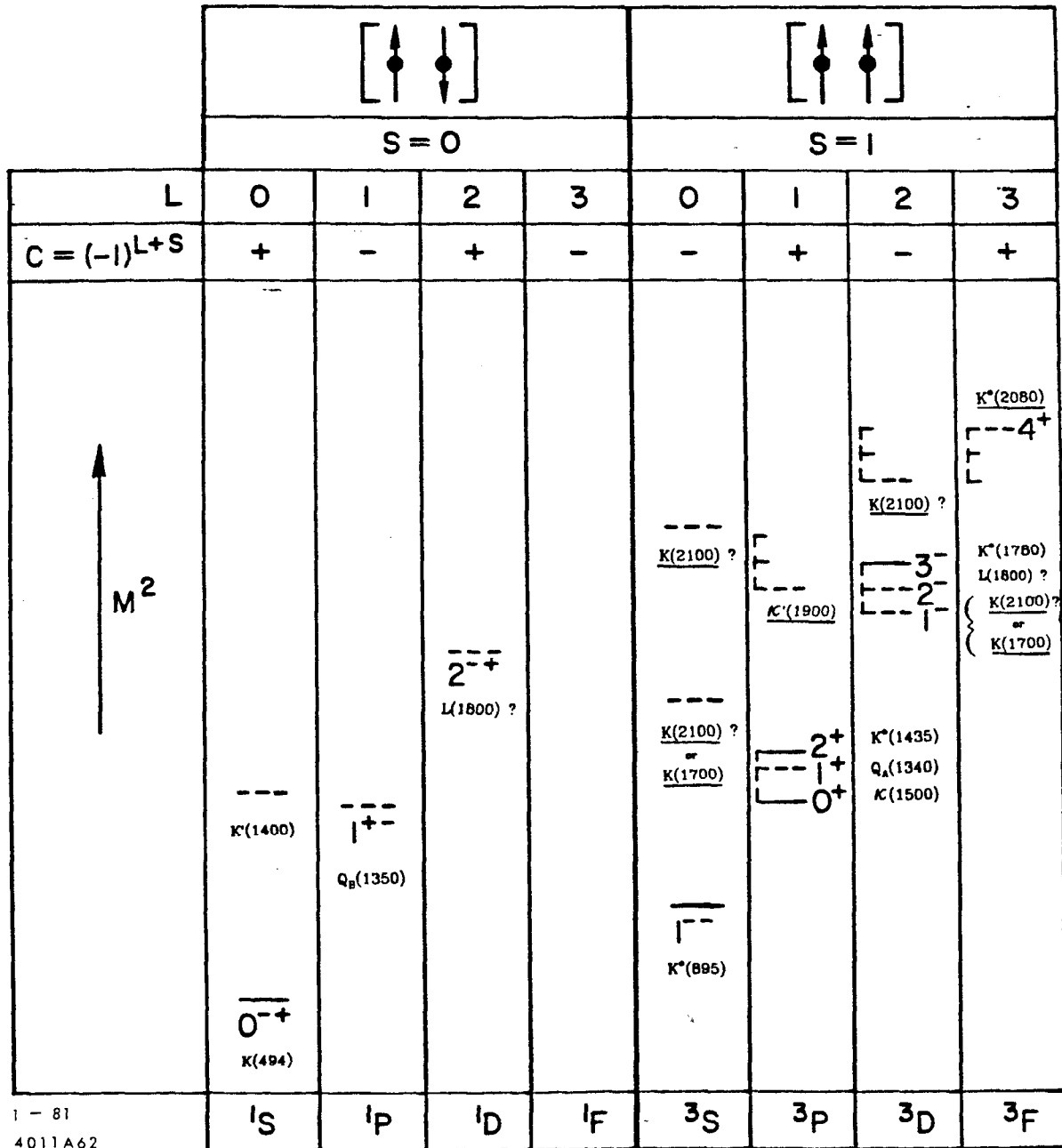
$$\begin{aligned} K\pi &\rightarrow K^*(1780) \rightarrow K^*(895)\pi \\ K\pi &\rightarrow K^{*'}(1700) \rightarrow K^*(895)\pi \end{aligned}$$

where the $K^{*'}(1700)$ represents the 1^- state at 1.70 GeV. Using an SU(6) classification scheme, an attempt could be made to classify this 1^- resonance at 1.70 GeV ⁴⁷. Such a measurement would require an extremely high statistics $K\pi\pi$ partial wave analysis.

Shown in figure 62 is a plot of the presently known strange meson states. The question mark once again means that this state has been seen ambiguously or there is some question as to its existence. States listed with a solid bar represent states whose parameters are rather well known. The other states listed on this plot are reasonably clear states which could use further study and confirmation. Classification ambiguities within this simple $q\bar{q}$ model are shown by listing the state multiple times on this plot. The states new to this analysis have been underlined. Comparing this plot with the Grotrian plot in figure 3, which represents states known previous to this analysis, it is seen that this analysis has made a great impact on our understanding of natural spin-parity strange meson spectroscopy.

With the success of the quark model's classification of these states, a discussion of the mass, widths, and elasticities of these observed resonances within a quark model framework would seem to be in order. Recently central potential bound quark-antiquark models for the nearly nonrelativistic $c\bar{c}$ and $b\bar{b}$ systems have been quite successful

($q\bar{q}$ LEVEL SCHEME)



1 - 81
4011A62

FIG. 62--A quark model level diagram showing the known strange meson states. The states new to this experiment have been underlined.

in predicting the properties of these states. Unfortunately light quark mesons are very relativistic systems, and as such prove to be much more difficult to deal with theoretically. No successful model now exists to quantitatively predict the properties of the light quark mesons. Even so light quark spectroscopy still has an important role to play in our understanding of meson spectroscopy. Experimentally certain meson states (notably high spin states) are more accessible to study in light quark meson experiments than in heavy quark meson experiments. Measurement of flavor dependences of meson parameters might also provide insight into the nature of the $q\bar{q}$ forces. In the absence of a good theory, precise experimental results could establish new regularities to aid in the development of such a theory. Moreover it is clear any comprehensive quark model theory must be able to predict the mass differences between mesons composed of different quark flavors. In anticipation of such a comprehensive theory, some of the interesting mass splittings seen in these natural spin-parity strange meson states will be discussed.

The simple quark model of chapter I suggests various mass differences which might be of interest: 1) L.S splittings, 2) orbital excitations, and 3) radial excitations. The next section of this chapter will discuss the radially excited states seen in this analysis. The triplet and orbital excitations were discussed in some detail in reference 29 with respect to the data presented in this paper.

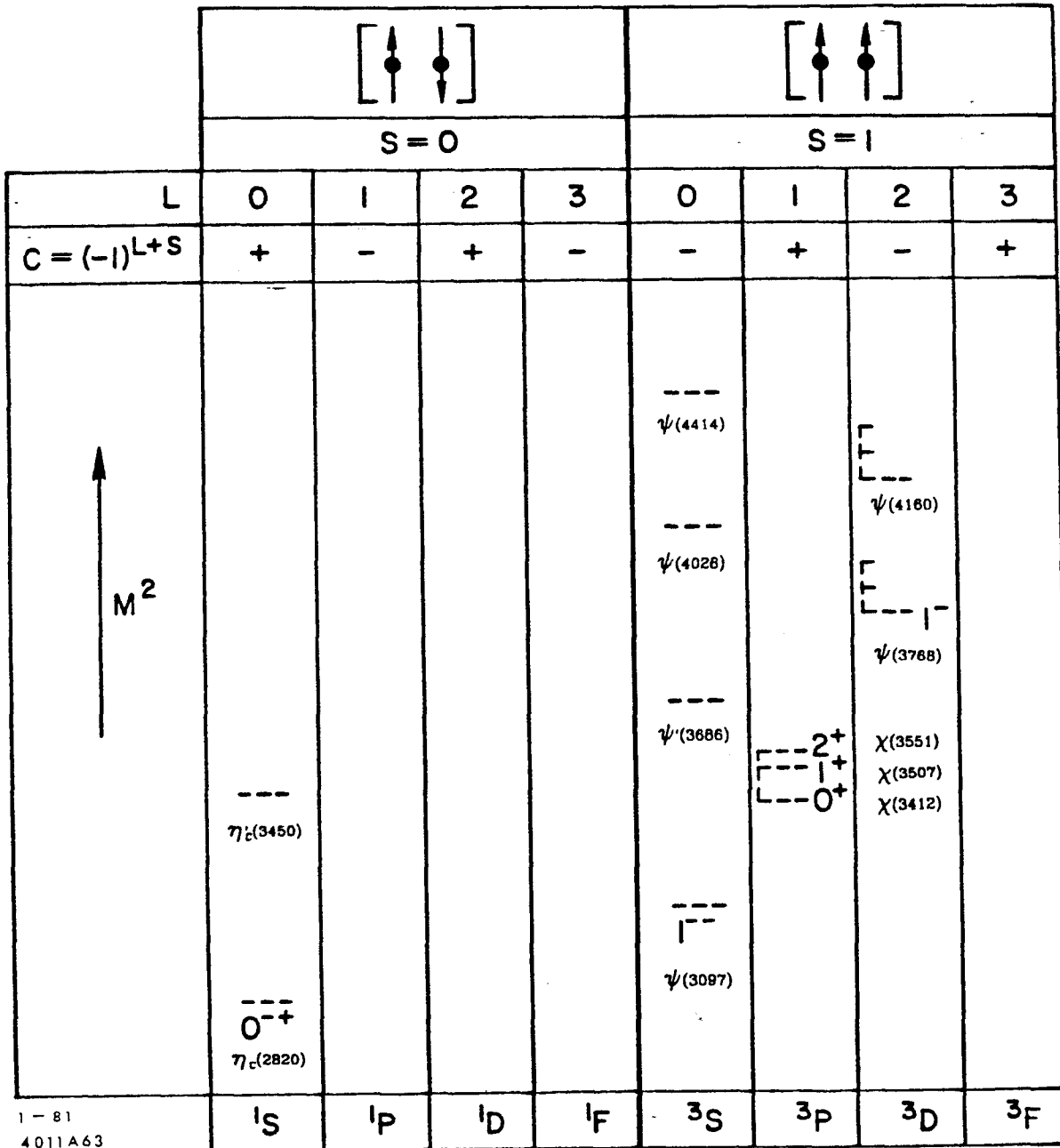
C. Radial Excitations in the Natural Spin-Parity Strange Mesons

Undoubtedly the most compelling experimental evidence for radially excited meson states comes from "charmonium" spectroscopy. Shown in figure 63 is a Grotrian plot of the presently known $c\bar{c}$ resonances and their spectroscopic assignments taken from reference 48. An impressive tower of $J^P=1^-$ $c\bar{c}$ radial excitations is evident in this plot.

The evidence for radial excitations in light quark meson spectroscopy is not as spectacular. For years the $I=1$ $J^P=1^-$ $\rho'(1600)$ was the only solid evidence for radial excitations in the light quark mesons, and some questions still exist about its precise properties. In the last few years, evidence has been presented for a 0^- strange meson radial excitation near 1.40 GeV in $K\pi\pi$ partial wave analysis. The first evidence for this state was an analysis performed by Brandenburg et al.⁴⁹ and recently this state has been confirmed by C. Daum et al.⁴⁶. Photoproduction and e^+e^- experiments have also seen a great number of possible candidates for radial excitations of vector meson states ($\rho'(1250), \rho''(1700), \omega'(1650)$) but all of these states need confirmation, and a great deal of confusion still exists as to these results⁵⁰. Thus in general very few well established radial excitations have been seen in the light quark mesons.

One of the most exciting new states discovered in this analysis is the $J^P=0^+$ strange meson resonance at 1.90 GeV. This state combined with the established 0^+ $\kappa(1500)$ presents clear evidence for a natural spin parity strange meson excitation. As was discussed earlier these two states have an unambiguous classification within a simple quark-antiquark meson model.

($q\bar{q}$ LEVEL SCHEME)



1-81
4011A63

FIG. 63--A quark model level diagram showing the known $c\bar{c}$ states.

Obtaining good resonance parameters for these two 0^+ states is a very difficult task. As was mentioned, this lower mass 0^+ state at 1.43 GeV was seen in a previous PWA performed by Estabrooks et al.⁴. P. Estabrooks⁵¹ has recently published a review of the light quark scalar mesons. In this review Estabrooks presents multiple mass dependent fits, including various background terms, to the $I=1/2$ $K^-\pi^+$ elastic scattering S wave amplitudes from this previous analysis. This data was shown to be consistent with a single 0^+ resonance in the mass range from .650 GeV up to 1.80 GeV with a mass of 1.50 GeV and a width between 120 MeV and 400 MeV depending on which ambiguous solution was fit. Since in this analysis we find solution B of Estabrooks et al. to be the correct solution, we ascertain from these fits that the mass of this 0^+ state is 1.49 ± 0.02 GeV, and the width is $400 \text{ MeV} \pm 100 \text{ MeV}$ (where systematic effects have been included in these errors)⁵¹.

Since solution B of Estabrooks et al. is so nearly identical to our unique solution in this mass region, such a fit to our data would surely lead to nearly the same resonance parameters for the 0^+ state seen in this analysis. Thus a proper treatment of background effects would appear to lead to a resonance value nearly 70 MeV above our preliminary estimates for the mass of this 0^+ object.

This result clearly justifies our caution in estimating resonance parameters for the underlying states seen in this analysis. Mass dependent fits with a proper treatment of backgrounds are essential for a detailed understanding of resonance parameters. Our estimates of the resonance parameters for this 0^+ resonance near 1.90 GeV could depend strongly on our assumptions of overall phase and backgrounds.

Thus our measurement of the mass splitting between the lower and upper 0^+ mesons seen in this analysis is very uncertain. Determination of the $I=3/2$ S wave from a PWA of $K^-p \rightarrow K^-\pi^+n$ (see chapter VIII section E), and performing mass dependent fits on this data will go a long way toward a better understanding of these resonance parameters.

The other possibilities for natural spin parity strange meson excitations seen in this data are the 1^- state at 1.70 GeV, and a possible 1^- state at 2.10 GeV. The classification ambiguities of these states has already been discussed. A great deal more work needs to be done before these two states can even begin to be unambiguously classified within a simple quark model.

Shown in figure 64 is a summary of the mass splittings of known and possible strange meson radial excitations. The masses and errors for the K and $K^*(895)$ come from the Particle Data Group tables ³. The mass and error on the 0^+ $\kappa(1500)$ come from reference 51. No error estimate has been associated with the $K'(1400)$ since none is given in either $K\pi\pi$ partial wave analysis ^{46 49} which see this state. For the other three states the mass and error estimates come from this experiment.

In viewing this table it is well worth while putting caution aside and testing a well known numeric. It is known that the differences in the squares of the masses of related pseudoscalar and vector meson states is equal to 0.58 GeV^2 to a high degree of accuracy. Although this formula does not work for the isospin zero mesons, it works quite well for the ρ and π , K^* and K, and D^* and D mesons:

$$M(\rho)^2 - M(\pi)^2 = M(K^*)^2 - M(K)^2 = M(D^*)^2 - M(D)^2 = 0.58 \pm 0.01 \text{ GeV}^2$$

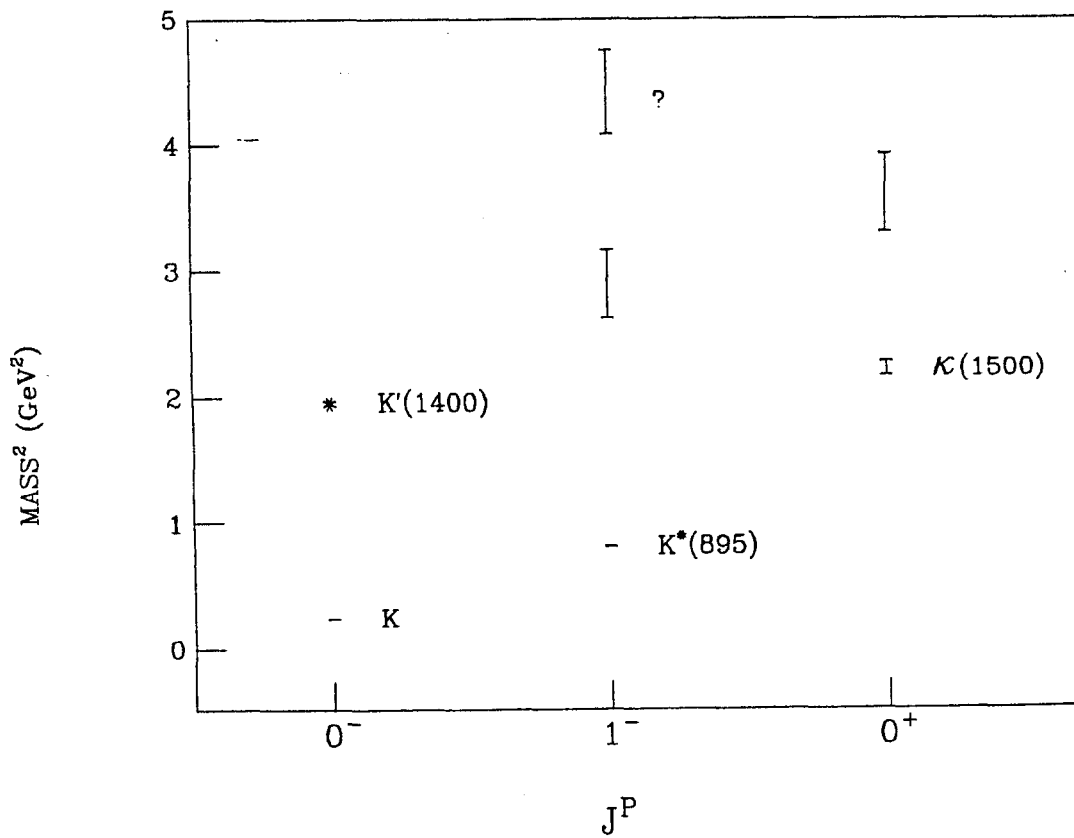


FIG. 64--A summary of the known and possible strange meson radial excitation mass splittings

Although the masses of the $K'(1400)$ and the 1^- state at 1700 MeV are not very well determined, one is immediately drawn to look at this difference for these two states assuming that the 1^- state is a single radial excitation. It is seen in figure 64 that this difference is not grossly inconsistent with $.58 \text{ GeV}^2$.

D. Conclusion

In conclusion this experiment has done much to further our understanding of natural spin-parity strange meson spectroscopy. In this analysis the well established $K^*(895)$, $K^*(1430)$, and $K^*(1780)$ were observed, and clear evidence was presented for a new $J^P=4^+$ strange meson state at a mass of 2.08 GeV. The $K^-\pi^+$ elastic scattering partial waves extracted in this PWA showed unambiguous evidence for a relatively narrow S wave resonance near 1.50 GeV. This state is a confirmation of the 0^+ $\kappa(1500)$ seen in previous partial wave analyses. A new higher mass S wave resonance was clearly seen unambiguously near 1.90 GeV. This state was quite naturally classified within a simple quark model as a radial excitation of the $\kappa(1500)$. In addition unambiguous evidence was presented for a relatively wide P wave resonance in the 1.70 GeV mass region, and ambiguous evidence was presented for a possible new second P wave state in the 2.10 GeV region.

REFERENCES

1. See for example
G.F. Chew and F.E. Low, Phys. Rev. 113, 1640 (1959)
C. Goebel, Phys. Rev. Lett. 1, 337 (1958)
2. See for example
P. Estabrooks and A.D. Martin, Nucl. Phys. B95, 322 (1975)
P. Estabrooks et al., Nucl. Phys. B133, 490 (1975)
M.J. Corden et al., Nucl. Phys. B157, 250 (1979)
3. See
R.L. Kelly et al., Particle Data Group, Rev. Mod. Phys. Vol.52,
No.2 (1980)
and the references therein
4. P. Estabrooks et al., Nucl. Phys. B133, 490 (1978)
5. G. Brandenburg et al., SLAC Group B Physics Note No.59, unpublished
6. L. Bird et al., SLAC Experimental Proposal E-132
7. F.C. Winkelmann, SLAC REPORT-160 (1973)
8. Electronics-
H.B. Jensen et al., Nucl. Inst. Meth. 125, 25 (1975)
Fabrication-
M. Marshal, Ph.D. Thesis, California Institute of Technology (1980)
9. J. Vavra et al., Nucl. Inst. Meth. 163, 415 (1979)
10. Electronics-

- S.L. Shapiro et al., IEEE Trans. Nucl. Sci. NS-23, No.1, 264
(1976)
- S.L. Shapiro et al., IEEE Trans. Nucl. Sci. NS-23, No.1, 269
(1976)
- Fabrication-
- A. Kilert et al., Paper on the LASS PWC Mechanical Properties, to
be published
- M. Davier et al., Nucl. Inst. Meth. 131, 229 (1975)
- C.L. Woody, Ph.D. Thesis, The Johns Hopkins University (1978)
- D. Blockus, Ph.D. Thesis, The Johns Hopkins University (1980)
11. G. Brandenburg et al., SLAC Group B Physics Note 59, unpublished
12. B. Bertolucci, SLAC PUB-1574 (1975)
13. C.L. Woody, Ph.D. Thesis, The Johns Hopkins University, 75 (1978)
14. G. Oakham, Masters Thesis, Carleton University; Ottawa, Can.
(1977)
15. H.H. Williams et al., Nucl. Inst. Meth. 105, 483 (1972)
16. D. Horelick, SLAC-PUB-1156
17. G.T. Armstrong et al., IEEE Trans. Nucl. Sci. NS-20, No.1, 342
(1973)
18. J. Denecke, Real-Time Note 1, SLAC Computing Services
J. Denecke et al., Real-Time Note 2, SLAC Computing Services
C. Granieri et al., Real-Time Note 3, SLAC Computing Services
J. Denecke et al., Real-Time Note 4, SLAC Computing Services
19. W.B. Johnson et al., LASS Software Documentation, to be published
20. R.J. McKee, SLAC Group B Internal Memo, unpublished
21. R. Gottfried and J.D. Jackson, CERN-TH-397 (1964)

22. V. Flaminio et al., 'Compilations of Cross Sections II- K^- and K^+ Induced Reactions', CERN-HERA 79-02, 70 (1979)
23. B.R. Martin, 'Pion-Pion Interactions in Particle Physics', (Academic Press, London, 1976), p. 411
24. G. Brandenburg, YLMFIT Writeup, SLAC Group B Internal Memo (1974), unpublished
25. G. Brandenburg, YLMFIT Addendum, SLAC Group B Internal Memo (1974), unpublished
26. G. Brandenburg, SLAC Group B Physics Note No.57, unpublished
G. Brandenburg, YLMFIT Writeup, SLAC Group B Internal Memo (1974), unpublished
27. P.H. Eberhard, Comp. Phys. Comm. 5, 163 (1973)
28. F. James, MINUIT, CERN Computer 6000 Series (1973)
29. A.K. Honma, Ph.D. Thesis, Stanford University (1980)
30. See for example
D.W.G.S. Leith, 'Experimental Meson Spectroscopy', E. Von Goeler and R. Weinstein, Eds. (Northeastern University Press, Boston, 1977), p.207
31. J. Blatt and V. Weisskopf, 'Theoretical Nuclear Physics', (Wiley, New York, 1952) p.361, p.409-410
32. D. Aston et al., Observation of a Spin 4^+ Strange Meson, to be published
33. G. Brandenburg, Group B Physics Note No.57, p.7, unpublished
34. P. Estabrooks et al., Phys. Lett. 60B, 473 (1976)
35. For a review on $K\pi$ and $\pi\pi$ partial wave analysis see

- B.R. Martin, 'Pion-Pion Interactions in Particle Physics', (Academic Press, London, 1976)
36. For an essential spherical harmonic expansion see
A. Edmonds, 'Angular Momentum in Quantum Mechanics', (Princeton University Press, Princeton, 1957) p.63
also see
B.R. Martin, 'Pion-Pion Interactions in Particle Physics', (Academic Press London, 1976) p.410-412
37. B.R. Martin, 'Pion-Pion Interactions in Particle Physics', (Academic Press London, 1976) p.413
38. P. Estabrooks, Notes on the Partial Wave Analysis Programs,
unpublished
39. E. Barrelet, Nuovo Cim. 8A, 331 (1972)
40. See for example
M. Perl, 'High Energy Hadron Physics', (Wiley, New York, 1974)
p.322
41. See for example
A. Barbaro-Galtieri, 'Advances in Particle Physics', Vol.2, R.L. Cool and R.E. Marshak, Eds. (Interscience, New York, 1968)
p.199
42. See for example
M. Perl, 'High Energy Hadron Physics', (Wiley, New York, 1974)
p.332
43. M. Bowler et al., Nucl. Phys. B126, 31 (1977)
44. C. Nef, The VI International Conference on Experimental Meson Spectroscopy, Brookhaven (1980)
45. G. Brandenburg et al., Phys. Rev. Lett. 36, 703 (1976)

- G. Brandenburg *et al.*, Phys. Rev. Lett. 36, 706 (1976)
46. C. Daum *et al.*, The VI International Conference on Experimental Meson Spectroscopy, Brookhaven (1980)
47. F. Gilman, 'Experimental Meson Spectroscopy 1974', D. Garelick, Ed., (American Institute of Physics, New York, 1974) p.369
48. J. Kirkby, 'Proceedings of the 1979 International Symposium on Photon Interactions at High Energies', T. Kirk and H. Abarbanel, Eds. (1979) p.112-113
49. G. Brandenburg *et al.*, Phys. Rev. Lett. 36, 1239 (1976)
50. See review of photoproduction and e^+e^- collisions in S.D. Protopopescu and N.P. Samios, 'Annual Reviews of Nuclear and Particle Science', Vol.29, J. Jackson, H. Grove, R. Schwitters, Eds., p.339
51. P. Estabrooks, Phys. Rev. D19, 2678 (1979)